

## ABSTRACT

TONG, ZHENGXIN. Silicon Millimeter-Wave Imaging Systems for Security and Biomedical Applications. (Under the direction of Dr. Brian Floyd).

The millimeter-wave spectrum at 30-300 GHz has been of great interest during the past few years. Applications such as high-speed communication systems, high-resolution radar, and high-resolution imaging systems are now being built in millimeter-wavelengths due to the spectrum's wide bandwidth and shorter wavelength compared to microwaves (0.3-30 GHz). Silicon technology can now provide useful gain at 50 to >100 GHz frequencies, having the potential to realize low-cost millimeter-wave solutions which are suitable for mass markets, including 60 GHz radios, 77 GHz radars, and 94 GHz imagers. In recent years, more research has focused on studying 94 GHz millimeter-wave imaging. Today, some major airports in the USA have already been equipped with full-body scanners for security checks. However, due to the active origin of these scanners, possible radiation effects are always of concern. In addition to health related issues, most of the available systems are built with discrete components and are therefore very bulky and expensive.

This dissertation addresses the aforementioned health, size and cost issues of millimeter-wave imaging systems. The primary goal is to build a low-cost, highly-integrated, silicon-based passive (no illumination provided) millimeter-wave imaging system, for the following two applications: (a) the detection of concealed objects (security); and (b) the diagnosis of dermal burn wounds (biomedical).

Towards this goal, we study electromagnetic wave and imaging phenomenology to evaluate and confirm the feasibility of the passive millimeter-wave imaging for these applications. A super-heterodyne receiving system was developed using interferometry and

synthetic aperture radio. The proposed system is the first synthetic aperture radar in the form of millimeter-wave monolithic integrated circuits. It is highly scalable and has great potential to achieve high-level integration, large aperture size, and large effective field-of-view.

The system requirements for passive imaging applications were derived, while each individual block's specifications were also designed accordingly. These blocks included a 94 GHz LNA, phase shifter, down-converting mixer, power detector, and passive electromagnetic components. Each individual block and a 4 x 1 prototype array are implemented using BiCMOS 0.13 $\mu$ m technology.

Measured hardware results are presented and all the circuits' functionality was tested and verified. Without baseband post-processing circuitry and signal-processing algorithms, an indirect method was developed to evaluate the array's potential to function as an interferometer front-end. The array output carries correct information from multiple input channels at the same time and successfully recreates the fringe patterns of an interferometer, therefore validating the multi-channel functionality of the prototype array as a front-end for a synthetic aperture radar and interferometer passive millimeter wave imager.

© Copyright 2015 by Zhengxin Tong

All Rights Reserved

Silicon Millimeter-Wave Imaging Systems for Security and Biomedical Applications

by  
Zhengxin Tong

A dissertation submitted to the Graduate Faculty of  
North Carolina State University  
in partial fulfillment of the  
requirements for the degree of  
Doctor of Philosophy

Electrical Engineering

Raleigh, North Carolina

2015

APPROVED BY:

---

Dr. Brian Floyd  
Chair of Advisory Committee

---

Dr. Griff Bilbro

---

Dr. Wesley Snyder

---

Dr. Zhilin Li

**DEDICATION**

*To my parents and wife, Yiyang*

## BIOGRAPHY

Zhengxin Tong was born and raised in Shanghai, China. He attended Shanghai Nanyang Model Middle School and High School from 1995 to 2002. In 2002, he was admitted to the Department of Electrical Engineering in Shanghai Jiao Tong University (SJTU). After his freshman year, he was awarded a three-year scholarship by the Hong Kong University Grants Committee and transferred to the Department of Electronic and Communication Engineering in the City University of Hong Kong. In 2006, he completed his Bachelor of Engineering degree with First (Highest) Class Honors.

Zhengxin began graduate studies in Department of Electrical and Computer Engineering at North Carolina State University (NCSU) in Raleigh, NC in the fall of 2006. He worked in the Bio-Electromagnetic Research Group for about 2 years and earned his Master in Science degree in 2010. In the fall of 2010, Zhengxin joined the research group of Professor Brian Floyd. Zhengxin's research interests focused on the development of passive millimeter-wave imaging systems using silicon technology. He was awarded the Analog Devices Inc. (ADI) Outstanding Student Designer Award in 2014 for his work.

In April of 2015, Zhengxin will begin his professional career by joining the RFIC group of ADI in Wilmington, MA.

## ACKNOWLEDGMENTS

First of all, I would like to thank my advisor, Professor Brian Floyd, whose teaching, endless patience, constant encouragement, and sincere friendship have been invaluable to me. Thanks also to Professors Griff Bilbro, Wesley Snyder, and Zhilin Li for their interest in my work and their time commitment while serving on my dissertation committee.

I would also like to thank all the colleagues I have worked with at NCSU: to Kevin Greene and Vikas Chauhan for their tremendous contribution to my work; to Qiaoqiao Liu, Yi-Shin Yeh, Weihu Wang, Anirban Sarkar, Charley Wilson, Jeff Bonner-Stewart, and Matthew Haentschke, whose discussion have been a great help to my work; and to Amit Qusba for his everlasting friendship and support, in good times and in bad times.

I am grateful for having made many friends during my studies in Raleigh: Yonghong Wang, Junhan Pan, Yue Zhang, Jinni Hou, John Yuan, Sheng Yi, Ruohan Sun, Entong Shen, Zhen Wang, Minyi Zhu, Lu Jin, and many others. All of those great memories with them will form my unforgettable life in North Carolina.

Last, but not the least, I would like to thank my parents for their endless love and unconditional support in every aspect, from the beginning of my life. I am grateful to my wife, Yiyang, whose love, tolerance, faith, and prayer are irreplaceable. Words cannot express my appreciation. Most importantly I thank God for letting me know Him. He is my rock, my fortress, my stronghold and my deliverer, my shield, in whom I take refuge. To him be the glory forever!

## TABLE OF CONTENTS

LIST OF TABLES .....	viii
LIST OF FIGURES .....	x
CHAPTER 1 INTRODUCTION .....	1
CHAPTER 2 ELECTROMAGNETIC WAVE PHENOMENOLOGY AT 94 GHz .....	6
2.1 Overview .....	6
2.2 EM Waves at MMW Frequency .....	6
2.2.1 EM Waves in Different Media .....	6
2.2.2 Frequency Selection for Imaging Systems .....	9
2.3 Blackbody Radiation and Emissivity .....	10
2.4 Dielectric Properties of Materials at MMW Frequencies .....	15
2.4.1 Textiles .....	15
2.4.2 Contraband Materials .....	17
2.5 Human Skin .....	21
2.5.1 Anatomy of Human Skin .....	22
2.5.2 Physiological Characteristics of Skin Burn .....	23
2.5.3 EM and Thermal Characteristics of Skin .....	27
2.6 Summary .....	34
CHAPTER 3 IMAGING PHENOMENOLOGY AND SYSTEM ARCHITECTURE .....	36
3.1 Overview .....	36
3.2 Background Knowledge .....	36
3.2.1 Active vs. Passive MMW Imaging Systems .....	36
3.2.2 Object Distance and Resolutions .....	38
3.2.3 Thermal Sensitivity .....	39
3.2.4 Image-Forming Phenomenology .....	39
3.3 State-of-Art Systems and Selection of System Architecture for this Work .....	44
3.4 Receiver System Architecture .....	50
3.5 Design of System Specifications .....	53
3.5.1 System Level Requirements .....	53
3.5.2 Security System Specifications .....	55
3.5.3 Biomedical PMMW Imager System Specifications .....	58
3.6 Summary .....	61
CHAPTER 4 MMIC IMPLEMENTATION OF THE SAR PMMW IMAGING SYSTEM .....	63
4.1 Overview .....	63

4.2 Overview of the Super-heterodyne Front-end Structure.....	63
4.3 Implementation of Individual Components .....	66
4.3.1 Low Noise Amplifier .....	66
4.3.1.1 State-of-the-Art LNA & Proposed Specifications .....	66
4.3.1.2 Design of 94 GHz LNA .....	68
4.3.2 Phase Shifter at 94 GHz.....	72
4.3.3 94 GHz to 18.8 GHz Down-Converting Mixer .....	75
4.3.3.1 LO Buffer.....	76
4.3.3.2 IFVGA .....	79
4.3.3.3 Single-balanced Gilbert Cell Mixer.....	83
4.3.3.4 Mixer Assembled and Simulation Results .....	83
4.3.4 Square-Law Power Detector .....	89
4.3.4.1 First Design.....	89
4.3.4.2 Second Design for the 4 x 1 Array.....	93
4.3.5 Passive EM Components .....	94
4.3.5.1 Design of Wilkinson Power Divider at 94 GHz .....	95
4.3.5.2 Ring-Hybrid Coupler at 94 GHz.....	97
4.3.5.3 Cascading of the Wilkinson Divider and Ring-Hybrid Coupler.....	99
4.4 Implementation of 4 x 1 Prototype Array .....	102
4.5 Summary .....	106
CHAPTER 5 HARDWARE MEASUREMENT .....	107
5.1 Overview.....	107
5.2 Definition of Various Measurement Setups.....	107
5.2.1 S-Parameter Measurement .....	107
5.2.2 Swept Power Measurement.....	109
5.2.3 Noise Measurements .....	109
5.2.3.1 Noise Figure.....	109
5.2.3.2 Y-factor Measurement .....	111
5.3 Measurement of the LNA .....	113
5.4 Measurement of the 4-bit Controlled Phase Shifter at 94 GHz .....	119
5.5 Measurement of Down-Converting Mixer from 94-18.8 GHz.....	128
5.5.1 Port Matching and SP Measurements.....	128
5.5.2 Power Measurement for the Compression Point and Conversion Gain .....	131
5.5.2.1 Power Calibration .....	131
5.5.2.2 Optimal LO Input Power .....	135
5.5.2.3 Optimal RF Input Power.....	136
5.5.2.4 Conversion Gain with Fixed LO Frequency and Swept RF Frequency.....	137
5.5.2.5 Conversion Gain when RF and LO Frequency were Simultaneously Swept.....	138
5.5.2.6 Summary of Power Measurement.....	140

5.5.3 Noise Measurement for NF.....	142
5.5.3.1 Noise Calibration .....	142
5.5.3.2 Noise Measurements and Results .....	144
5.5.4 Summary for Mixer Measurement.....	148
5.6 Measurement of the Square-Law Power Detector .....	149
5.7 Measurement of 4 x 1 Prototype Array with 1-Channel Excitation .....	153
5.7.1 Port Matching and SP Measurement.....	154
5.7.2 Power Measurement for Compression Point and Conversion Gain .....	155
5.7.2.1 Optimal LO Input Power .....	156
5.7.2.2 Optimal RF Input Power.....	157
5.7.2.3 IF Output Power during Phase Shifter Sweep .....	158
5.7.2.4 Conversion Gain Measured with a fixed LO Frequency and Swept RF Frequency .....	159
5.7.2.5 Conversion Gain Measured from Simultaneously Swept RF and LO Frequencies .....	160
5.7.3 Noise Measurement .....	161
5.7.4 Power Measurement with the Square-Law Power Detector .....	165
5.7.5 Summary of 4 x 1 Prototype Array with 1-Channel Excitation.....	167
5.8 Summary .....	168
CHAPTER 6 MULTI-CHANNEL EXPERIMENTS AND VERIFICATION OF INTERFEROMETRY.....	170
6.1 Overview.....	170
6.2 The Visibility Function & Fringe Patterns.....	170
6.3 Recreation of Fringe Pattern using Simulation Data .....	173
6.3.1 Mathematical Derivation .....	173
6.3.2 Simulation Model and Results .....	178
6.4 Recreation of Fringe Pattern using Measured Data .....	182
6.4.1 Measurement Setup.....	182
6.4.2 Measurement Results .....	184
6.4.2.1 Test 1.....	185
6.4.2.2 Test 2.....	190
6.5 Discussion.....	195
6.6 Investigation of the Four-Channel Interferometer .....	196
6.7 Summary .....	203
CHAPTER 7 CONCLUSIONS AND FUTURE WORK.....	204
7.1 Summary of Work.....	204
7.2 Key Contributions.....	205
7.3 Future Work .....	205
REFERENCES .....	207

## LIST OF TABLES

Table 2.1	Measured attenuation (dB) of common garment materials [GAT06].....	16
Table 2.2	Temperature contrasts for different ambient temperature conditions.....	21
Table 2.3	Burn depth features classified by degree of burn [TIN10] .....	24
Table 2.4	Brightness temperature of skin at different burn severities .....	32
Table 3.1	Summary of the four major techniques in forming PMMW image.....	44
Table 3.2	Comparison of recently developed PMMW imaging systems .....	47
Table 3.3	Proposed PMMW imaging system specifications for the Security and biomedical applications .....	61
Table 4.1	Comparison of recently reported LNA at about 94 GHz.....	66
Table 4.2	Comparison of two 94 GHz-input mixers for PMMW imaging applications .....	75
Table 4.3	Performance summary of the LO buffer at 75.2 GHz .....	79
Table 4.4	Performance summary of the IFVGA at 18.8 GHz .....	81
Table 4.5	Comparison of the performance between this work and that of Reynolds <i>et al</i> .....	86
Table 4.6	Simulated specifications of individual components and single-channel, end-to-end .....	104
Table 5.1	Summary of observations from Figure 5.30 .....	139

Table 5.2	Summary of the measured performance of 94-18.8 GHz down-converting mixer.....	149
Table 5.3	Summary of the prototype array's measured results.....	168
Table 6.1	Phase settings and the corresponding combinations.....	199

## LIST OF FIGURES

Figure 2.1	EM power attenuation with respect to frequency (Figure adapted from [YUJ03]) .....	11
Figure 2.2	Brightness of a blackbody at 1000 K. The Rayleigh-Jeans law approximates Planck's law better below the frequency of maximum brightness, while the Wien law approximates Planck's law better at higher frequency .....	13
Figure 2.3	Illustration of brightness temperature, no concealed object present.....	17
Figure 2.4	Illustration of brightness temperature, with concealed object .....	18
Figure 2.5	Contrast predictions for generic explosive and gun at 100 GHz (Figure adapted from [MIL07]) .....	20
Figure 2.6	Layers of normal human skin (Figure adapted from [TIN10]).....	23
Figure 2.7	Illustration of different burn degrees (Figure adapted from [TIN10]) (a) 1 <sup>st</sup> degree (sunburn); (b) 2 <sup>nd</sup> degree (superficial partial thickness); (c) 2 <sup>nd</sup> degree (deep partial thickness); (d) 3 <sup>rd</sup> degree (full thickness).....	25
Figure 2.8	Brightness temperature of different burn degrees vs. ambient temperature.....	32
Figure 3.1	Basic setup of a synthetic aperture radiometer .....	42
Figure 3.2	FOV comparison (a) Linear scan: FOV of system equals the beamwidth of antenna; (b) Rotary scan: FOV increased due to the scanning motion .....	46
Figure 3.3	(a) Antenna array layout and (b) the corresponding UV spacing .....	49
Figure 3.4	Diagram of a typical super-heterodyne receiver .....	51
Figure 3.5	Diagram of a typical direction-conversion receiver.....	52
Figure 3.6	Antenna array aims directly at the target .....	54
Figure 3.7	Antenna array aims through a lens for biomedical applications.....	55
Figure 3.8	Illustration of FOV calculation for security applications .....	56
Figure 3.9	Illustration of optics for biomedical application of PMMW imaging, displaying a large path difference .....	59
Figure 3.10	Illustration of the effect of a lens (modified from [WIK02]).....	60
Figure 4.1	Diagram of a typical super-heterodyne receiver .....	63
Figure 4.2	Diagram of the proposed 4 x 1 prototype array .....	64
Figure 4.3	Diagram of the actual 4 x 1 prototype array .....	65
Figure 4.4	Schematic of 6-stage 94 GHz LNA .....	69
Figure 4.5	Layout view of the 94GHz LNA (kit v1.2.0.1).....	70

Figure 4.6	Simulated S-Parameter of the 94 GHz LNA (with parasitics, kit v1.2.0.1) ..	71
Figure 4.7	Simulated NF of the 94 GHz LNA (with parasitics, kit v1.2.0.1) .....	71
Figure 4.8	Gilbert Cell architecture for use as a vector interpolator .....	72
Figure 4.9	Simulated S21 of the 94 GHz phase shifter, capable of 360° phase shifting (with parasitics, kit v1.3.0.3) .....	73
Figure 4.10	Simulated input and output matching of the 94 GHz phase shifter (with parasitics, kit v1.3.0.3) .....	74
Figure 4.11	Simulated conversion loss and NF of the 94GHz phase shifter (with parasitics, kit v1.3.0.3) .....	74
Figure 4.12	Schematic of LO buffer .....	76
Figure 4.13	Simulated input and output matching for the LO buffer (with parasitics, kit v1.3.0.3) .....	77
Figure 4.14	Simulated Gain & Gmax of the LO buffer (with parasitics, kit v1.3.0.3) .....	77
Figure 4.15	Simulated NF & NFmin of the LO buffer (with parasitics, kit v1.3.0.3) .....	78
Figure 4.16	Simulated linearity, input referred 1-dB compression point of the LO buffer (with parasitics, kit v1.3.0.3) .....	78
Figure 4.17	Schematic of the IFVGA .....	80
Figure 4.18	Simulated gain of the IFVGA (with parasitics, kit v1.3.0.3).....	81
Figure 4.19	Simulated NF of the IFVGA (with parasitics, kit v1.3.0.3).....	82
Figure 4.20	Simulated linearity: input referred 1-dB compression point of IFVGA (with parasitics, kit v1.3.0.3) .....	82
Figure 4.21	Schematic of the single-balanced Gilbert cell mixer .....	84
Figure 4.22	Forward transmission coefficient S21 and S31: (left) magnitude, (right) Phase (with parasitics, kit v1.3.0.3).....	84
Figure 4.23	Layout view of the down-converting mixer tape-out .....	85
Figure 4.24	Simulated RF, LO & IF port matching of the mixer break-out (with parasitics, kit v1.3.0.3) .....	87
Figure 4.25	Simulated conversion gain of the mixer break-out, RF frequency swept (with parasitics, kit v1.3.0.3) .....	88
Figure 4.26	Simulated single-sideband (SSB) NF of the mixer break-out (with parasitics, kit v1.3.0.3) .....	88
Figure 4.27	Simulated linearity, input-referred 1-dB compression point of the mixer break-out (with parasitics, kit v1.3.0.3).....	89
Figure 4.28	The first version of the RF Power Detector .....	90
Figure 4.29	Layout of the first design of the power detector. The total area = 600 x 600 $\mu\text{m}^2$ (kit v.1.2.0.1). The power consumption is only 2.4mW .....	92
Figure 4.30	Simulated responsivity of the first version power detector (with parasitics, kit v1.2.0.1) .....	93

Figure 4.31	Simulated voltage response at 94 GHz for the second version of the power detector (with parasitics, kit v1.3.0.3).....	94
Figure 4.32	Layout view of the 94 GHz Wilkinson power divider.....	95
Figure 4.33	Simulated port matching of the 94 GHz power combiner .....	96
Figure 4.34	Simulated forward transmission and isolation of the 94 GHz power combiner .....	96
Figure 4.35	Schematic of a 180° hybrid junction (Figure adapted from [PON03]).....	97
Figure 4.36	(a) A schematic of the modified ring-hybrid coupler (phase inverter circled); (b) the S-Parameter when Port 1 is excited; (c) the S-Parameter when Port 2 is excited.....	98
Figure 4.37	Cascading of two Wilkinson divider with the ring-hybrid coupler .....	99
Figure 4.38	Setup comparison to verify the EM effect of the (a) original setup, and (b) the transmission line flipped to the outside .....	100
Figure 4.39	Comparison of structure port matching .....	101
Figure 4.40	Comparison of port 1 S-parameters .....	101
Figure 4.41	Layout view of the 4 x 1 prototype array, taped-out July 2013.....	102
Figure 4.42	Simulated port matching of the single-channel, end-to-end .....	104
Figure 4.43	Simulated conversion gain of the single-channel, end-to-end.....	105
Figure 4.44	Simulated NF (DSB) of the single-channel, end-to-end.....	105
Figure 4.45	Simulated input referred 1-dB compression of the single-channel, end-to-end .....	106
Figure 5.1	Illustration of the wafer probing setup for the frequency range of (a) <70GHz, (b) >70GHz.....	108
Figure 5.2	Noise in a two-stage system.....	110
Figure 5.3	The NF measurement using a two-stage system (Figure adapted from [AGI14]).....	110
Figure 5.4	Y-factor measurement setup of (a) instrument only, and (b) DUT + the instrument .....	112
Figure 5.5	Die photo of the 6-Stage CE LNA at 94 GHz .....	115
Figure 5.6	Measured vs. simulated input port reflection coefficient (S11) of the LNA .....	116
Figure 5.7	Measured vs. simulated input port reflection coefficient (S11) in a Smith Chart .....	116
Figure 5.8	Measured vs. simulated output port reflection coefficient (S22) of the LNA .....	117
Figure 5.9	Measured vs. simulated output port reflection coefficient (S22) in a Smith Chart .....	117
Figure 5.10	Measured vs. simulated forward transmission coefficient (S21) of the LNA .....	118
Figure 5.11	Simulated polar plot for the 94GHz phase shifter .....	119

Figure 5.12	Simulated input port matching for all 16 different phase settings .....	121
Figure 5.13	Measured input port matching for all 16 different phase settings .....	121
Figure 5.14	Simulated output port matching for all 16 different phase settings .....	122
Figure 5.15	Measured output port matching for all 16 different phase settings .....	122
Figure 5.16	Simulated S21 for all 16 different phase settings .....	123
Figure 5.17	Measured S21 for all 16 different phase settings .....	123
Figure 5.18	Comparison of the measured polar plots, where $V_{\text{bias}_q} = 1.2 \text{ V}$ , and $V_{\text{bias}_i}$ varied .....	125
Figure 5.19	Comparison of the measured polar plots, where $V_{\text{bias}_i} = 1.2 \text{ V}$ , and $V_{\text{bias}_q}$ varie .....	126
Figure 5.20	EM simulated S21 and S31 for the balun of the 94 GHz phase shifter .....	127
Figure 5.21	Die photo of the 94 to 18.8GHz down-converting mixer .....	129
Figure 5.22	Measured RF & LO port matching of the down-converting mixer .....	130
Figure 5.23	Measured IF port matching of the down-converting mixer .....	130
Figure 5.24	Illustration of the mixer power measurement setup .....	132
Figure 5.25	Illustration of power calibration method described in step 1 .....	133
Figure 5.26	Illustration of power calibration method described in step 2 .....	134
Figure 5.27	Measured mixer conversion gain while sweeping LO input power .....	135
Figure 5.28	Measured mixer IF output power and conversion gain while sweeping RF power .....	136
Figure 5.29	Measured mixer conversion gain, while RF frequency is swept .....	137
Figure 5.30	Measured mixer conversion gain, with swept RF and LO, while the IF is fixed at five frequencies .....	138
Figure 5.31	The LO output power at probe tip vs. input frequency, while the output power of the signal generator is fixed at -8.5dBm .....	139
Figure 5.32	The (a) initial setup and (b) final setup of the NF measuring instrument .....	143
Figure 5.33	ENR of the noise source (top) and measured NF of instrument (bottom) .....	143
Figure 5.34	Setup of the mixer noise measurement .....	144
Figure 5.35	Measured NF for the mixer and instrument .....	145
Figure 5.36	Measured NF of the mixer at IF = 18GHz, while RF and LO frequencies swept .....	147
Figure 5.37	Measured NF of the mixer at IF = 17GHz, while RF and LO frequencies swept .....	148
Figure 5.38	Die photo of the square-law power detector .....	150
Figure 5.39	Setup for the square-law power detector measurement .....	151
Figure 5.40	DC output voltage vs. RF input power at 70, 85, 95 and 105 GHz .....	152
Figure 5.41	Responsivity of the power detector vs. the input frequency .....	153
Figure 5.42	Die photo of the 4 x 1 prototype array .....	154
Figure 5.43	Measured RF and LO port matching of the array .....	155
Figure 5.44	Measurement of the array's channel 1 conversion gain while sweeping the LO input power .....	156

Figure 5.45	The array's measured channel 1 IF output power and conversion gain while sweeping the RF power .....	157
Figure 5.46	IF output power with phase settings at 0001, 0010, 0100 and 1000.....	158
Figure 5.47	Measured conversion gain of the array at phases 1000 and 0001.....	159
Figure 5.48	Measured conversion gain of CH1 at phases 1000 and 0001 with RF & LO frequency swept and IF = 18 GHz.....	160
Figure 5.49	Measured NF of CH1 at phase 1000 with swept RF and LO and IF =18 GHz .....	162
Figure 5.50	Estimated NF for CH1 of the array, for best and worst cases.....	164
Figure 5.51	DC output voltage vs. RF input power at 70, 80, 90, 95 and 100 GHz .....	165
Figure 5.52	Responsivity of CH1 vs. input frequency .....	166
Figure 6.1	Illustration of a traditional interferometer with a correlator .....	171
Figure 6.2	Fringe pattern of an interferometric correlator for various baselines (Figure adapted from [NAN12]).....	172
Figure 6.3	Concept illustration of the interferometer system in its entirety.....	174
Figure 6.4	Illustration of a simple, two-channel interferometric radiometer .....	175
Figure 6.5	Transition between phase delay, $\phi$ , and the broadside angle, $\theta$ .....	177
Figure 6.6	Simple setup for the simulation of a two-channel phase-switched interferometer.....	178
Figure 6.7	Simulated power detector output when CH1 and CH2 excited, and the CH2 phase is swept from 0 to 720° .....	179
Figure 6.8	The fringe pattern produced by simulated data, top: $D = \lambda$ ; and bottom: $D = 2\lambda$ .....	180
Figure 6.9	The fringe pattern produced by simulated data, top: $D = 3\lambda$ ; and bottom: $D = 4\lambda$ .....	181
Figure 6.10	Illustration of the lab set up for the two-channel measurement.....	183
Figure 6.11	Test 1: the power detector output voltage vs. CH3 phase delay .....	185
Figure 6.12	The fringe patterns of the Test 1a data, top: $D = \lambda$ ; and bottom: $D = 2\lambda$ .....	186
Figure 6.13	The fringe patterns of the Test 1a data, top: $D = 3\lambda$ ; and bottom: $D = 4\lambda$ .....	187
Figure 6.14	The fringe patterns of the Test 1b data, top: $D = \lambda$ ; and bottom: $D = 2\lambda$ .....	188
Figure 6.15	The fringe patterns of the Test 1b data, top: $D = 3\lambda$ ; and bottom: $D = 4\lambda$ .....	189
Figure 6.16	Test 2: the power detector output voltage vs. the CH1 phase delay .....	190
Figure 6.17	The fringe patterns of the Test 2a data, top: $D = \lambda$ ; and bottom: $D = 2\lambda$ .....	191
Figure 6.18	The fringe patterns of the Test 2a data, top: $D = 3\lambda$ ; and bottom: $D = 4\lambda$ .....	192
Figure 6.19	The fringe patterns of the Test 2b data, top: $D = \lambda$ ; and bottom: $D = 2\lambda$ .....	193
Figure 6.20	The fringe patterns of the Test 2b data, top: $D = 3\lambda$ ; and bottom: $D = 4\lambda$ .....	195
Figure 6.21	The four-channel setup for demonstration of the prototype array .....	197
Figure 6.22	The fringe pattern of the baseline, $L_{ab} = 1\lambda$ .....	200
Figure 6.23	The fringe pattern of the baseline, $L_{bc} = 2\lambda$ .....	200
Figure 6.24	The fringe pattern of the baseline, $L_{ac} = 3\lambda$ .....	201

Figure 6.25 The fringe pattern of the baseline,  $L_{cd} = 4\lambda$  .....201  
 Figure 6.26 The fringe pattern of the baseline,  $L_{bd} = 6\lambda$  .....202  
 Figure 6.27 The fringe pattern of the baseline,  $L_{ad} = 7\lambda$  .....202

## CHAPTER 1 INTRODUCTION

The millimeter-wave (MMW) spectrum between 30-300 GHz has attracted interest over the past few years for enabling new, exciting technologies. Applications such as high-speed communication systems [MAD08], high-resolution radar, and high-resolution imaging systems [SAK08] are being built in MMW due to its wide spectral bandwidth and shorter wavelength compared to microwaves (0.3-30 GHz). Silicon technology can now provide useful gain at 50 to >100 GHz frequencies, having the potential to realize low-cost MMW solutions which are suitable for mass markets, including 60 GHz radios, 77 GHz radars, and 94 GHz imagers.

In recent years, research efforts have achieved new, promising advances in MMW imaging at 94 GHz [LOV94], [YUJ03], [YUJ06], [APP99] and [APP07]. Today, many major American airports have already been equipped with full-body MMW scanners for security surveillance purposes. However, because of the active origin (providing its own illumination source) of the scanner, there is an ongoing debate regarding possible radiation effects and health issues caused by this technology. The MMW radiation will penetrate into skin, exponentially dissipating as a function of tissue depth. This causes MMW power to mostly concentrate on the superficial layer of the skin, which may result in heating and other adverse effects [ZHA11]. In addition, the effects of active MMW systems have not been studied on pregnant women, children, or people carrying prostheses, such as pacemakers or implanted retina, nor has any long term study on health effects been conducted. Thus if a passive

millimeter-wave (PMMW) imaging system could be built, these concerns may be circumvented while still realizing the benefits of the technology.

In addition to the functionality and safety concerns of current systems, size and cost are also very important factors for enabling mass distribution. Many of today's systems are built with discrete components, which are relatively bulky and expensive. Silicon technology makes it possible to build sophisticated, highly-integrated systems operating in the MMW range. The economies of scale of silicon technology can also reduce the overall MMW system cost.

This dissertation focuses on the development of a highly-integrated, silicon-based PMMW imaging system which addresses the aforementioned health, size and cost issues. Two applications are targeted: (a) the detection of concealed objects (security); and (b) the diagnosis of dermal burn wounds (biomedical). Towards these goals, silicon-based MMW monolithic integrated circuits (MMIC) are used to implement the system in order to achieve the following advantages [NIK08]:

1. Compact form factor through high levels of circuit integration;
2. Low power consumption through power-efficient circuit design;
3. Cost effectiveness through the use of silicon technology.

The security application has a well-established theoretical foundation. MMW produced images result from differences in emissivity and reflectivity of various materials such as

metal, cloth, plastic, *etc.* The MMW radiation emitted and reflected by different materials are received and processed through the imager, which acts as a radiometer. The MMW power can be quantified and therefore provide information used for the detection of a concealed object.

For the biomedical application, the difference in healthy and injured skin tissue can be spotted based on their differences in emitted and reflected MMW radiation, which depends on the skin's water content and temperature [BOR99b]. Since the temperature difference between healthy and injured tissue is much less significant than that between metal objects and humans, the proposed biomedical application requires MMW radiation receivers with higher thermal sensitivity. An image with higher resolution is also more desirable for biomedical usage in order to resolve smaller areas of skin. Both applications have similar phenomenology and thus are proposed to operate within a similar system architecture. However, detailed design varies based on the application and will be demonstrated with the development of the proposed PMMW imaging system in Chapter 3-6.

The dissertation is structured as follows. In Chapter 2, the electromagnetic wave phenomenology is reviewed, and the reflection and transmission of wave energy between media, as well as the attenuation and emission of MMW energy by different materials are quantified in terms of media/material dielectric properties. The anatomy of human skin and the physiological characteristics of skin burns are also discussed in Chapter 2. The thermal radiation (or brightness) temperature of various burn severities are defined with regard to physical temperature and emissivity under different burn conditions. This quantitative

derivation of brightness temperature for skin burns provides motivation for potentially using PMMW imaging for the diagnosis of burn victims.

In Chapter 3, the phenomenology of an MMW imaging system is studied and a super-heterodyne phased-array receiving system is developed, using interferometry and synthetic aperture radiometer (SAR) concepts. To the author's knowledge, the proposed system is the first SAR in the form of a silicon-based MMW integrated circuit. It is also scalable and has the potential to achieve a high level of integration, larger aperture sizes, and greater effective Field-of-View (FOV). The system architecture and specifications are designed for both security and biomedical applications, with each considered for their own unique requirements.

In Chapter 4, the discussion follows the design and implementation of a SAR PMMW imaging system using IBM SiGe BiCMOS 8HP technology. Block level specifications are derived. The design and implementation of each individual block in the receiver front-end is discussed, culminating in the production of a 4x1 interferometer prototype array.

In Chapter 5, measurements of all fabricated circuits are presented. Scattering parameter, swept power and noise figure measurements are used to verify the hardware through wafer proving. These calibration and measurement procedures are reviewed, followed by detailed results for each block in the receiver prototype. The measurement results are compared to simulations and inconsistencies between the two are discussed to improve future hardware performance.

In Chapter 6, an interferometric method is proposed and demonstrated to test the prototype array while any two input channels are excited. The visibility function of an interferometer is reviewed and simulations are used to generate fringe patterns from the visibility. Based on the same method, measurement data is acquired and compared with the simulations. The measured data fits the fringe pattern created from the simulations as well as the theoretical patterns, validating the operation of the array as a MMW interferometer. Using simulations, further investigation is made for the prototype array when all four channels are excited. A method to obtain multiple brightness functions in one single sweep is proposed and verified.

Finally, chapter 7 contains the conclusion of the work and lists key contributions. Future work is summarized with aim of improving hardware performance and extending the use of the prototype array for other applications.

## **CHAPTER 2**

### **ELECTROMAGNETIC WAVE PHENOMENOLOGY AT 94 GHZ**

#### 2.1 Overview

The purpose of Chapter 2 is to determine the mechanisms of interaction between electromagnetic (EM) waves at MMW frequencies and dielectric materials that are potential targets for imaging applications. A brief background of EM wave behavior at dielectric interfaces is first given, focusing on reflections. Due to the lack of lab equipment and qualifications to perform *in vivo* or *in vitro* measurements on biological tissues, direct measurement of material dielectric properties was not possible. Instead, an extensive literature survey was conducted to collect data for dielectric properties of related materials focused on burned human skin tissue. Using this compiled data, the effective brightness temperature of different skin conditions was derived and the potential for passive MMW imaging of burns at 94 GHz is discussed.

#### 2.2 EM Waves at MMW Frequency

##### 2.2.1 EM Waves in Different Media

EM waves are the carrier for any wireless communication and remote sensing application. Depending on each case, different wave frequencies are utilized and particular characteristics of the wave are extracted. But EM waves at any frequency are defined and governed by the Maxwell Equations. To exist and propagate, EM waves need media in which to travel.

The medium can be quantitatively defined by three parameters:

- $\epsilon$ : permittivity (F/m), indicates the resistance to forming an electric field;
- $\mu$ : permeability (H/m), indicates the ability to support the formation of a magnetic field;
- $\sigma$ : conductivity (S/m), indicates the ability to conduct electric current.

The intrinsic impedance of a medium is defined as:

$$\eta = \sqrt{\mu / \epsilon} \quad (2.1)$$

Since  $\epsilon$  is a function of frequency, the intrinsic impedance of a medium also depends on the wave frequency. To design an imaging system, it is important to select a frequency at which enough signal power can be detected by the receiver. Therefore we discuss our reasoning for selecting an appropriate frequency for our MMW imaging system in the next section.

In the real world, different contacting media form boundaries between each other. When a propagating wave reaches a boundary, since the constitutive parameters ( $\epsilon$ ,  $\mu$  and  $\sigma$ ) are different on each side, the property of the wave within each medium must be also different. However the field at the boundary should encompass both media and it is therefore defined as a boundary condition. As discussed in [CHE89] and [BAL89], when a wave is incident from a dielectric medium onto a perfectly conducting medium, it is like terminating a generator with a short circuit, therefore no power is transmitted into the conducting medium and all power is reflected. Therefore our discussion will solely focus on the condition at which two different dielectric media form the boundary. Three cases exist for a

plane wave to cross a boundary between dielectric media. The corresponding reflection ( $\Gamma$ ) and transmission (T) coefficients at these different boundary cases are shown below:

1. Normally incident wave onto the boundary;

$$\Gamma = \frac{\eta_2 - \eta_1}{\eta_2 + \eta_1} \quad (2.2)$$

$$T = \frac{2\eta_2}{\eta_2 + \eta_1} \quad (2.3)$$

2. Obliquely incident transverse electric (TE) wave;

$$\Gamma_{\perp} = \frac{\eta_2 \cos \theta_i - \eta_1 \cos \theta_t}{\eta_2 \cos \theta_i + \eta_1 \cos \theta_t} \quad (2.4)$$

$$T_{\perp} = \frac{2\eta_2 \cos \theta_i}{\eta_2 \cos \theta_i + \eta_1 \cos \theta_t} \quad (2.5)$$

3. Obliquely incident transverse magnetic (TM) wave;

$$\Gamma_{\parallel} = \frac{\eta_2 \cos \theta_t - \eta_1 \cos \theta_i}{\eta_2 \cos \theta_t + \eta_1 \cos \theta_i} \quad (2.6)$$

$$T_{\parallel} = \frac{2\eta_2 \cos \theta_i}{\eta_2 \cos \theta_t + \eta_1 \cos \theta_i} \quad (2.7)$$

The reflection and transmission coefficient for TE and TM waves are different. In real scenarios, an EM wave is a superposition of TE and TM waves, and the boundary between media is typically not a flat surface, so the actual reflection and transmission of EM waves at boundaries are very complicated. No detailed EM wave derivation is made here since the purpose of this section is to re-familiarize readers with EM wave reflection and transmission

at dielectric media boundaries. Detailed derivations and results can be found in almost all electromagnetics books and are listed for reference ([CHE89] and [BAL89]).

It is also worth noting that no matter what the incident angle may be,  $\Gamma$  and  $T$  are always functions of the medium's dielectric properties, which also depend on the frequency of the wave itself. Therefore, before the EM wave phenomenology for imaging applications may be studied, the operation frequency for the chosen applications must be selected first.

### 2.2.2 Frequency Selection for Imaging Systems

To properly select the frequency range for an imaging system, there are several criteria that must be considered; first is the image resolution. The quality of an image is measured by its resolution, which is the detail an image holds [WIK01]. Similar to a camera, an imaging system in a non-optical spectrum is diffraction-limited. This means that the minimum resolvable size (or angle) of such a system is inversely proportional to the wavelength of the signal being observed [BOR99a], as described in Eq. 2.8 [LET03].

$$\alpha = C \frac{\lambda}{D} \quad (2.8)$$

where  $\alpha$  is the angle subtended by the minimum resolvable object,  $\lambda$  is the wavelength of the incident radiation,  $D$  is the diameter of the collecting optics, and  $C$  is a proportionality constant which takes into account other factors in the system. In our theoretical study,  $C = 1$  is assumed for the ideal case and such an assumption is used throughout the calculations. However, in practical cases  $C$  is greater than 1 and indicates any non-realistic factor that degrades the resolution. According to Eq. 2.8, use of a higher frequency (*i.e.* lower

wavelength) enables higher resolution to be obtained with smaller, lower weight and lower volume optics. In another words, higher frequency EM waves facilitate resolving smaller objects for a given imaging system. With a wavelength smaller than 5 mm ( $f > 60$  GHz), most objects of interest to us (*e.g.* concealed weapons, explosives, skin wound and blisters) should be properly resolved. Therefore our target spectrum is MMW in wavelength ranges from 1-10 mm ( $30\text{ GHz} < f < 300$  GHz).

The second criterion for frequency selection is wave attenuation. The attenuation of wave through a medium depends on the medium's dielectric property. Simultaneously, the dielectric property of a medium is a function of wave frequency. Within the MMW range, power transmission is subjected to significant attenuations from atmospheric absorption by molecules of water vapor, oxygen and other gaseous constituents [LET03]. However, there are certain "windows" of frequencies with lower attenuation rates. Such windows are located around 35, 94, 140 and 220 GHz, as illustrated in Figure 2.1. Current silicon technology does not yet allow the construction of low-cost imaging systems at 140 or 220 GHz, therefore 94 GHz has the greatest potential for an imaging system with good resolution that can also be realized using low-cost silicon technology.

### 2.3 Blackbody Radiation and Emissivity

While the interaction between EM waves and dielectric media has been introduced, there is still another important source of wave energy that has yet to be discussed, which is blackbody radiation (thermal radiation). All objects with a physical temperature greater than

zero emit thermal radiation [NAN12], while a blackbody is an idealized object which absorbs all incident EM radiation. According to Kirchhoff's radiation law, a blackbody emits the same amount of EM radiation as it absorbs, forming a thermal equilibrium defined at temperature,  $T$ . In thermal equilibrium, a blackbody has two notable properties [MAS05]:

1. It is an ideal emitter: at every frequency, it emits as much or more energy than any other body at the same temperature;
2. It is a diffuse emitter: the energy is radiated isotropically, independent of direction.

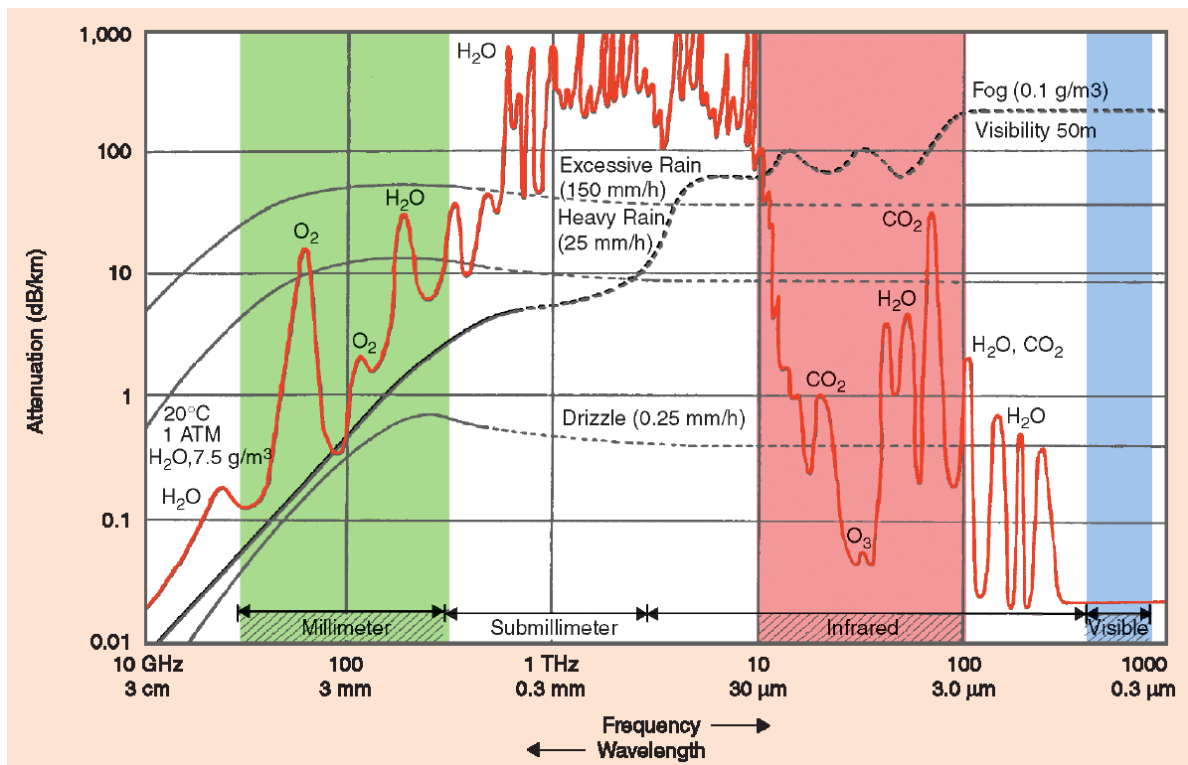


Figure 2.1 EM power attenuation with respect to frequency (Figure adapted from [YUJ03])

In such a case, blackbody radiation is described by Planck's Law:

$$B_f = \frac{2hf^3}{c^2} \cdot \frac{1}{e^{hf/kT} - 1} \quad (2.9)$$

where  $B_f$  is the spectral radiance (brightness) of a blackbody,  $h$  is Planck's constant,  $f$  is frequency,  $c$  is the speed of light,  $k$  is Boltzmann's constant, and  $T$  is the physical temperature of the blackbody in equilibrium. The radiance versus frequency is plotted as the green curve in Figure 2.2 for a blackbody at a temperature of 1000 K. At lower frequency where  $hf \ll kT$ , Eq. 2.9 reduces to:

$$B_f = \frac{2f^2kT}{c^2} \quad (2.10)$$

which is the Rayleigh-Jeans Law, indicating the brightness of a blackbody proportional to its physical temperature and the square of the frequency, shown as the red curve in Figure 2.2.

When  $hf \gg kT$ , Eq. 2.9 reduces to:

$$B_f = \frac{2hf^3}{c^2} e^{-hf/kT} \quad (2.11)$$

which is the Wien Law, accurately approximating Planck's law at higher frequencies, shown as the blue curve in Figure 2.2.

Realistically, there is no ideal blackbody that emits 100% of the energy it absorbs. The object that emits less radiation than a blackbody, is called a "greybody" [NAN12]. Referring to Eq. 2.10, the brightness of a greybody is defined as below:

$$B_{f,gb} = \frac{2f^2kT_R}{c^2} \quad (2.12)$$

where  $T_R$  is the radiometric temperature or brightness temperature of the greybody [NAN12].

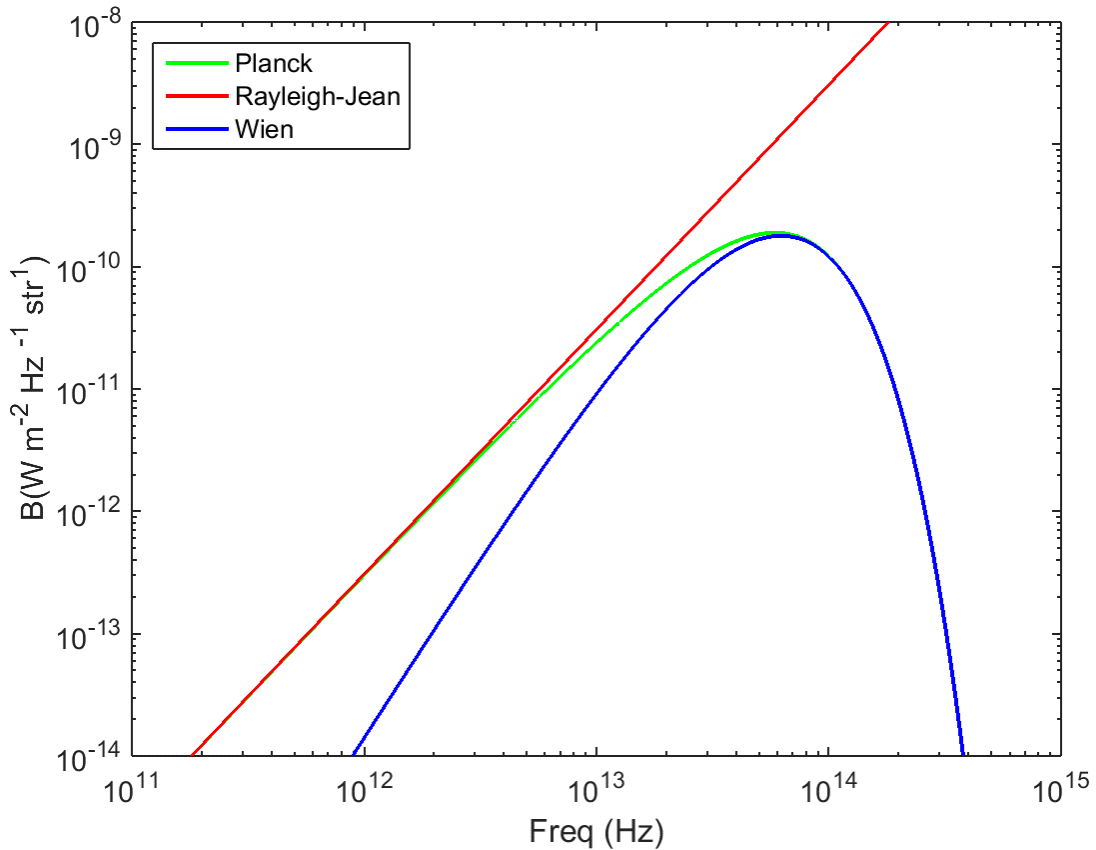


Figure 2.2 Brightness of a blackbody at 1000 K. The Rayleigh-Jeans law approximates Planck's law better below the frequency of maximum brightness, while the Wien law approximates Planck's law better at higher frequency.

The ratio of Eq. 2.10 and 2.12 gives the definition of emissivity:

$$\frac{B_{f,gb}}{B_{f,bb}} = \frac{T_R}{T} = e \quad (2.13)$$

A greybody can never radiate more than a blackbody, therefore  $0 \leq e \leq 1$ . If a greybody is homogeneous, the emissivity is only a function of frequency [NAN12]. Emissivity is also related to the reflectance and transmittance of an object. When in thermal equilibrium, the

incident flux density of an object must equal the flux density reflected, transmitted and absorbed by the object [NAN12], therefore:

$$S_{inc} = S_r + S_t + S_a \quad (2.14)$$

$$S_{inc} = rS_{inc} + tS_{inc} + aS_{inc} \quad (2.15)$$

where  $r$ ,  $t$  and  $a$  are the reflectivity, transmissivity and absorptivity of the object, respectively. Not to be confused with  $\Gamma$ , the reflection coefficient of an EM wave, reflectivity is actually the reflection rate of EM power, and is therefore the square of  $\Gamma$  [HEC01]. According to Kirchhoff's radiation law, in thermal equilibrium the power absorbed by an object is equal to the power emitted, therefore:

$$e = a \quad (2.16)$$

$$e = 1 - r - t \quad (2.17)$$

In the case of the human body, MMW energy is only able to penetrate into a very thin layer of tissue. According to Gabriel *et al* [AND97], the skin depth of human skin tissue at 94GHz is approximately 0.37 mm, which is only ~25% of the thickness of human skin at its thinnest locale (eyelid). Therefore 94 GHz waves will not penetrate through the skin which allows the human body to be opaque to the MMW wave. This means the transmissivity,  $t$ , is almost negligible, therefore the emissivity of a human can be defined as [NAN12]:

$$e = 1 - r \quad (2.18)$$

In this section, the interaction between EM waves and media has been discussed. The reflection and transmission of waves at a media boundary has been quantified in terms of dielectric properties of both media. In addition, the methodology of frequency selection for

our imaging system has been discussed. Finally the thermal radiation and emissivity of the objects have been introduced and the derivation of an object's emissivity from its dielectric property has also been elaborated.

#### 2.4 Dielectric Properties of Materials at MMW Frequencies

While the general interaction between EM waves and different media is known and the best possible frequency has been selected for our proposed imaging system, it is also necessary to determine how all the relevant materials react with waves within the spectrum. Our system's potential applications include security screening and biomedical dermal-burn inspections. Therefore, possible dielectric materials of interest for our purposes include clothing made of cotton and nylon textiles, contraband based materials such as metals, ceramics, plastics, and explosives, and of course human tissue. Imaging system receivers sense EM energy reflected off the target (either from active sources or from the ambient environment) as well as thermal radiation emitted by the target itself. So these relevant materials will be discussed in terms of their attenuation, reflectivity and emissivity in this section, while human skin will be discussed in Section 2.5.

##### 2.4.1 Textiles

Due to the increasing interest on the topic of MMW imaging of concealed weapons in recent years, several studies ([GOR00], [BJA04], [GAT06] and [XIA08]) have been conducted to measure the attenuation of MMW radiation propagating through textile based

materials, such as clothing. Generally the attenuation is very low or even negligible through textiles. In [BJA04], the MMW attenuation rate was measured for eight common clothing materials (wool, linen, leather, denim, naugahyde, silk, nylon and rayon). As frequency increases, the 3-dB attenuation point does not appear until 350 GHz, while the attenuation of these same materials below 100 GHz is so low that they can be considered effectively transparent [BJA04]. In addition, Gatesman *et al* measured the attenuation rate of six different materials using 94 GHz MMW in both perpendicular (TE) and parallel (TM) polarization [GAT06]. Complying with the thickness of normal clothing as what was presented in [BJA04], Gatesman *et al* determined that for all the studied materials and at both polarizations, the attenuation of MMW energy was less than 0.7 dB. There was minimal difference between the two polarizations of light. The results are summarized in Table 2.1. It is worth mentioning that those measurements were performed while the materials were dry, without any addition of water, such as rain or sweat, which could possibly exist in a real scenario. Textiles saturated with water could exhibit strong EM reflection, since higher water content causes higher reflectivity [BOR99b].

Table 2.1 Measured attenuation (dB) of common garment materials [GAT06]

Material	Thickness (mm)	94 GHz	
	Polarization:	TE Wave	TM Wave
Cotton Shirt	0.3	0.1	0.2
Denim	0.6	0.7	0.7
Drapery	0.9	0.5	0.3
Leather	1.3	0.6	0.7
Sweater	2.1	0.4	0.4
Sweatshirt	2.1	0.2	0.3

### 2.4.2 Contraband Materials

For the MMW imaging application of security, the low attenuation of MMW radiation through textiles will help the imager to see through the subject's clothing and find possible concealed weapons and explosives. This can be achieved by utilizing the difference in emissivity between the human body and suspicious concealed objects. Here, we define ambient temperature as  $T_s$ , The physical temperature of humans, garments and concealed objects are defined as  $T_h$ ,  $T_g$ , and  $T_c$ , respectively, and their reflectivity, transmissivity and emissivity are also respectively defined as  $r_h$ ,  $t_h$ ,  $e_h$ ,  $r_g$ ,  $t_g$ ,  $e_g$ ,  $r_c$ ,  $t_c$  and  $e_c$ . In the case of passive imaging, in the absence of a concealed object, the passive imaging receiver sees a brightness temperature of  $T_l$  [XIA08], as illustrated in Figure 2.3 and defined in Eq. 2.19:

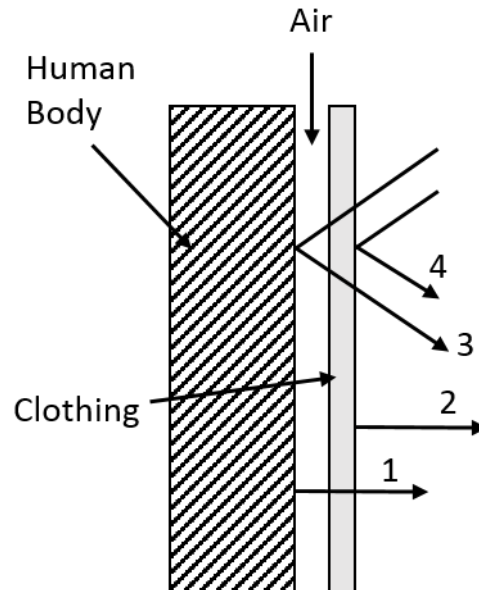


Figure 2.3 Illustration of brightness temperature, no concealed object present

$$T_1 = e_h \cdot T_h \cdot t_g + e_g \cdot T_g + t_g \cdot T_s \cdot r_h \cdot t_g + r_g \cdot T_s \quad (2.19)$$

where the first term of the right hand side stands for the human-emitted brightness temperature through the garment (arrow 1); the second term stands for the brightness temperature emitted by the garment (arrow 2); the third term stands for the ambient temperature reflected by the human, going through the garment twice (arrow 3); and the last term stands for the reflected ambient brightness temperature by the garment (arrow 4).

When the concealed object is present, the brightness temperature seen by the MMW receiver carries the same form of Eq. 2.19, but replaces the human term with an object, since the concealed object, usually made of metal, reflects all incident MMW wave energy, as illustrated in Figure 2.4 and defined in Eq. 2.20:

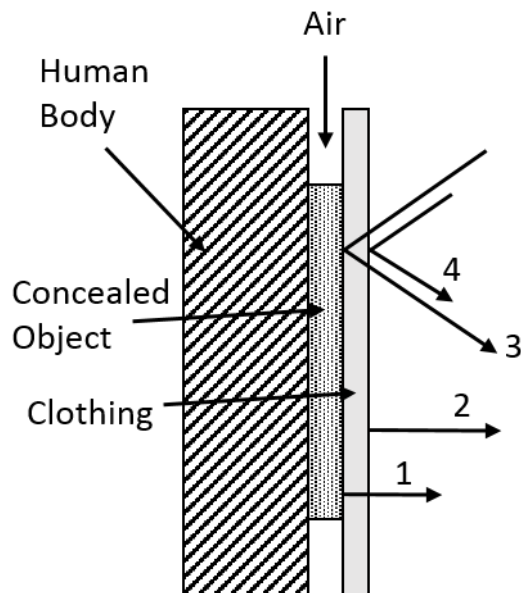


Figure 2.4 Illustration of brightness temperature, with concealed object

$$T_2 = e_c \cdot T_c \cdot t_g + e_g \cdot T_g + t_g \cdot T_s \cdot r_c \cdot t_g + r_g \cdot T_s \quad (2.20)$$

The temperature difference or contrast between two cases is:

$$\Delta T = T_1 - T_2 = (e_h \cdot T_h - e_c \cdot T_c) \cdot t_g + (r_h - r_c) T_s \cdot t_g^2 \quad (2.21)$$

When the concealed object is metal, due to the metal's high conductivity, its reflectivity is almost 1 and its emissivity approaches 0. Eq. 2.21 can thus be approximated to:

$$\Delta T = e_h \cdot T_h \cdot t_g + (r_h - 1) T_s \cdot t_g^2 \quad (2.22)$$

Invoking Eq. 2.18, we get

$$\Delta T = e_h \cdot T_h \cdot t_g - e_h \cdot T_s \cdot t_g^2 = e_h \cdot t_g \cdot (T_h - t_g T_s) \quad (2.23)$$

$e_h$ ,  $T_h$  and  $t_g$  are all characteristics of the object being imaged, and are therefore constant.

According to Appleby *et al.*, the constants in Eq. 2.23 have the following values at 100 GHz [MIL07]:

- $e_h = 0.65$
- $t_g = 0.96$
- $T_h = 303\text{K}$

Therefore Eq. 2.23 reduces to:

$$\Delta T = 189.1 - 0.6T_s \quad (2.24)$$

A greater  $\Delta T$  is favorable (*i.e.* displaying a higher contrast between the human body and concealed objects), therefore  $T_s$  in a 300 K range should be avoided. Appleby *et al.* have compared the brightness temperature of a human under a t-shirt with and without an

explosive or gun [MIL07]. As shown in Figure 2.5, the ambient temperature was sparsely swept from 100-500 K. These temperatures were relevant because 100 K is the temperature of a cold sky (the outdoor scenario) [LET03], [MIL07]; 300 K is the ambient temperature indoors [MIL07]; and 500K is artificial incoherent illumination [MIL07].

These three ambient temperatures are also used in Eq. 2.24 to calculate  $\Delta T$  and the results are shown in Table 2.2. The results suggest that the use of an MMW imaging system outdoors with artificial incoherent illumination provides a higher temperature difference, which is easier to detect. However, the results suggest that the indoor scenario of MMW imaging lacks significant temperature contrast and therefore will require a receiver with greater thermal sensitivity.

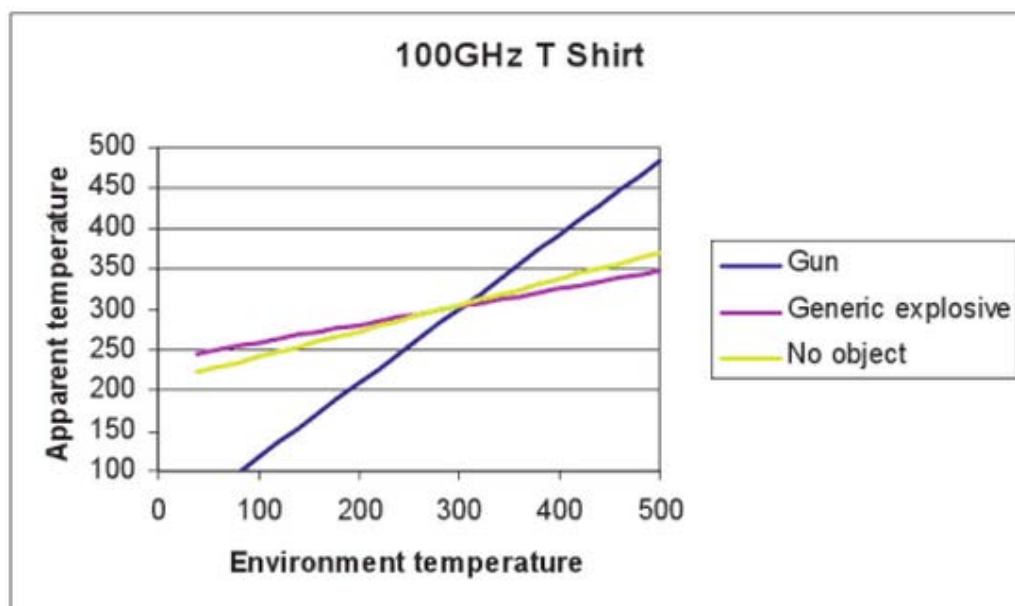


Figure 2.5 Contrast predictions for generic explosive and gun at 100 GHz (Figure adapted from [MIL07])

Table 2.2 Temperature contrasts for different ambient temperature conditions

$T_s$ (K)	100	300	500
$\Delta T$ (K)	129.1	9.1	-110.9

There are several passive imaging systems developed in 94 GHz for outdoor applications and these were able to accomplish the detection of concealed weapons ([LET05], [KIM11] and [FET08]). The features of these systems will be discussed in detail in Chapter 3.

In the case of non-metal concealed objects, such as ceramic and plastic, although they have relatively low dielectric constants, it is still possible to detect the temperature difference between these materials and the human body [NAN12]. If the object is an explosive material, an active imaging system should be used rather than passive, as most explosive materials have a similar emissivity to humans, making it difficult for a passive system to distinguish between the two [DAN09].

## 2.5 Human Skin

During treatment, dermal burn wounds are usually wrapped in medical gauze, which is essentially made of cotton. The gauze wrap minimally attenuates MMW energy emitted from or reflected off the skin [GAT06]. Therefore, an MMW imaging system could potentially replace traditional visual inspection of burn wounds, consequently eliminating the need for frequent change of the gauze, avoiding unnecessary damage to the wound and reducing

patients' pain during the healing process. At 94 GHz, the high frequency limits the depth of MMW energy penetration to very superficial layers of biological tissue [KUE99], therefore a model of the human body at MMW frequencies can be approximated in terms of the properties of the skin alone [NAN12]. Our interest is to explore the possibility of observing skin with an MMW imaging device and to distinguish different degrees skin burns. To accomplish this goal it is first necessary to discuss the anatomy of human skin in various burn conditions, followed by reviewing the physical and EM properties of skin under these conditions in order to derive the corresponding thermal brightness as seen by an MMW receiver.

### 2.5.1 Anatomy of Human Skin

The skin of an adult man covers approximately  $2 \text{ m}^2$  and has a thickness between 1.5-4 mm [GUS02]. Skin consists of three layers: epidermis, dermis and subcutaneous (or hypodermis) [TIN10], as illustrated in Figure 2.6.

The epidermis is the outermost part of the skin. It is cornified, without vessels, and normally dry [GUS02]. The epidermis protects the human body from the external environment, retains the body's temperature, blocks solar radiation, and regulates the evaporation of water. The dermis is the wet region of skin layered between the epidermis and subcutaneous layers. The dermis is composed of two layers itself: the superficial area adjacent to the epidermis is called the papillary region and the deeper, thicker region is termed the reticular dermis. The dermis consists of connective tissue and is a cushion for the

body from external stress [JAM05]. The subcutaneous layer, also known as the hypodermis, consists of loose connective tissue and fat. It is mainly for fat storage, but also contains larger blood vessels and nerves compared to those in the dermis [WIK05].

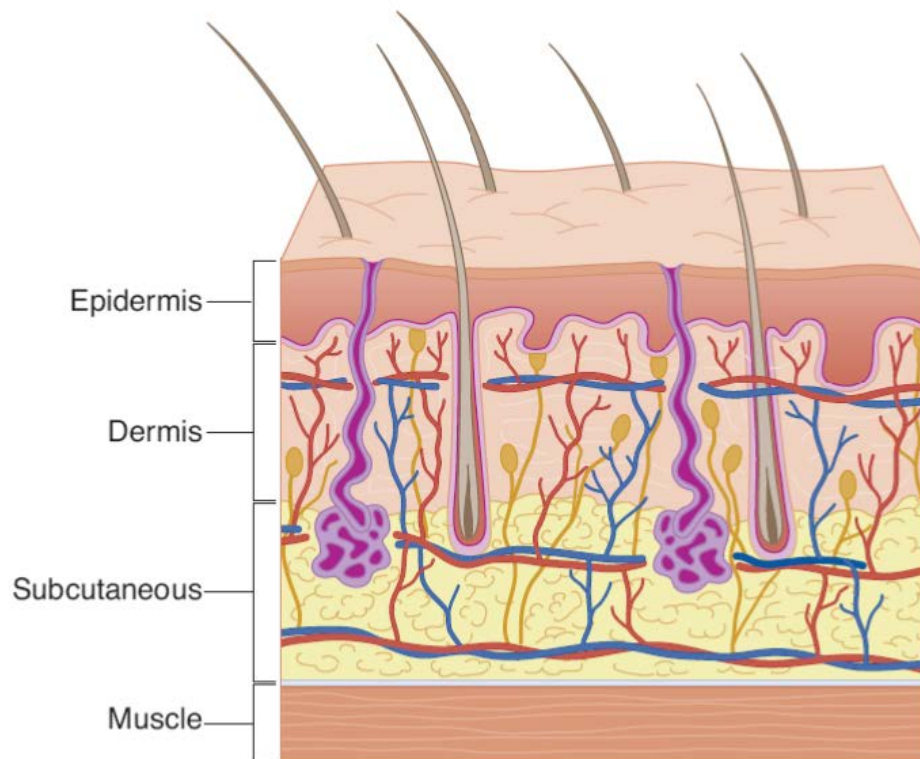


Figure 2.6 Layers of normal human skin (Figure adapted from [TIN10])

### 2.5.2 Physiological Characteristics of Skin Burns

The severity of skin burns is defined in terms of the size of the burned skin, as well as the depth of damage to the skin. The depth of the burn is usually defined in degrees: first, second, third and fourth, as shown in Table 2.3 and Figure 2.7 [TIN10]. Although, recently another classification method has emerged to define burn wounds in terms of the need for

surgical intervention, however, this method is less relevant to our work. Therefore, the traditional classification nomenclature will be used here.

Table 2.3 Burn depth features classified by degree of burn [TIN10]

Burn Depth	Histology/Anatomy	Texture	Example	Healing
First degree	Epidermis No blisters, painful	Dry	Sunburn	7 days
Superficial second degree or superficial partial thickness	Epidermis and superficial dermis Blisters, very painful	Moist	Hot water scald	14-21 days, no scar
Deep second degree or deep partial thickness	Epidermis and deep dermis, sweat glands, and hair follicles Blisters, very painful	Fairly dry	Hot liquid, steam, grease, flame	3-8 weeks, permanent scar
Third Degree	Entire epidermis and dermis charred, pale leathery; no pain	Leathery	Flame	Months, severe scarring, skin grafts necessary
Fourth degree	Entire epidermis and dermis, as well as bone, fat, and/or muscle	Dry	Flame	Months, multiple surgeries usually required

1<sup>st</sup> degree burns are usually caused by solar radiation. The burned area is red, painful, and tender but does not blister [TIN10]. The observed redness of skin is due to swelling of blood vessels and increased blood flow to dissipate heat, which creates elevated temperatures in the burned area.

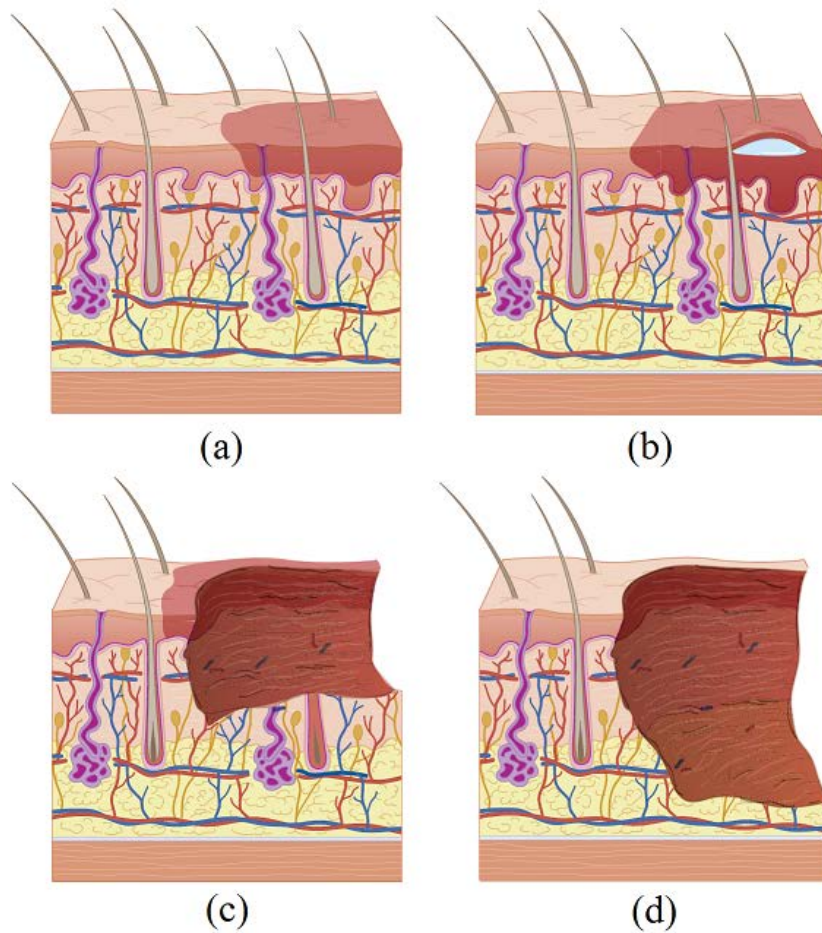


Figure 2.7 Illustration of different burn degrees (Figure adapted from [TIN10])  
 (a) 1<sup>st</sup> degree (sunburn); (b) 2<sup>nd</sup> degree (superficial partial thickness);  
 (c) 2<sup>nd</sup> degree (deep partial thickness); (d) 3<sup>rd</sup> degree (full thickness).

2<sup>nd</sup> degree superficial burns involve only the epidermis and papillary layer of the dermis, while the deeper layer of the dermis is not injured. Affected skin blisters and the exposed dermis is red and moist at the blister's base [TIN10]. Similar to the 1<sup>st</sup> degree burn, the redness in the skin indicates a surface temperature that is higher than healthy skin. However, the moisture at the blister's base differs in EM emissivity compared to that of the 1<sup>st</sup> degree burn.

The injured extent of a 2<sup>nd</sup> degree burn is deep into the dermis (reticular layer). The skin may appear blistered, while the exposed dermis is pale white to yellow due to absence of capillaries to refill blood to the area [TIN10]. Compared to 2<sup>nd</sup> degree superficial burns, wounds in the deep 2<sup>nd</sup> degree display a lower moisture content and the surface temperature is couple of degrees K lower [FOR64].

3<sup>rd</sup> degree burns involves the entire thickness of the skin, where the epidermis and dermis layers are destroyed. Skin appears charred, pale, painless and leathery [TIN10]. At this level of injury, the skin's surface temperature falls to room temperature and displays an extremely dry texture, which creates a higher emissivity than other lower degree burn wounds [BOR99b].

To diagnose the degree of burn, usually visual inspection is used and the decision follows the guideline described above. There are a limited number of studies exploring the relationship between skin surface temperature and burn severity [FOR64], [COL90]. However, since the temperature variation between different types of skin burns is only within several degrees K, which also varies with different patients and other physical and even mental factors, only a general trend of decreasing surface temperature has been observed with increasing burn severity [FOR64].

Besides the temperature difference, water content varies for different burn degrees [TIN10]. According to [BOR99b], higher water content increases the dielectric constant and consequently reduces emissivity. It is therefore possible to diagnose burn degree by

measuring the brightness temperature, which depends on both the physical temperature and emissivity of the skin.

### 2.5.3 EM and Thermal Characteristics of Skin

Extensive studies have been conducted on the dielectric properties of human tissue at frequencies below 20 GHz [GAB96a, b]. However above 20 GHz, most of the dielectric properties of normal human skin are calculated from extrapolation [GAB96b], [GAN86] or by fitting experimental data to proposed models [ALA03], [HWA03], [ALE07]. Although Gustrau *et al.* measured human tissue within the W-band (75-100 GHz) [GUS02] and their results could have been affected by many factors. No other work has been located which could be used to verify these results. Therefore in this work, we will only use the widely accepted parametric model of Gabriel *et al.* [GAB96c], [AND97].

Reusing Eq. 2.19 and for the case of no bandage or clothing present, the following approximations can be made:

- There is no energy emitted by the clothing/garment/bandage:  $T_g \rightarrow 0$
- The clothing layer in Figure 2.3 is transparent:  $t_g \rightarrow 1$ ;  $r_g \rightarrow 0$

Therefore Eq. 2.19 reduces to:

$$T = e_h T_h + r_h T_s \quad (2.25)$$

where  $T_h$ ,  $e_h$  and  $r_h$  are the physical temperature, emissivity and reflectivity of human skin, respectively, and  $T_s$  is the temperature of the environment. For an opaque object,  $r_h = 1 - e_h$ , Eq. 2.25 becomes:

$$T = e_h T_h + (1 - e_h) T_s \quad (2.26)$$

If the object is nearly a blackbody (*i.e.*  $e_h \approx 1$ ), the radiometer detects almost the temperature of the object alone, that is:

$$T \approx T_h \quad (2.27)$$

On the contrary, if the object reflects all the energy radiated from environment and produces no intrinsic radiation, indicating a reflector, (*e.g.* most metallic material), Eq. 2.26 becomes:

$$T \approx T_s \quad (2.28)$$

Eq. 2.27 and 2.28 exemplify two extreme cases for brightness temperature. Using Eq. 2.26, together with data collected from literature and by making reasonable assumptions, the brightness temperature of the following five scenarios are derived:

1. For normal human skin, at 94 GHz, using Gabriel's model, reflectivity of skin is [NAN12]:

$$r_h = 0.32 \quad (2.29)$$

While the transmissivity of skin is not "0", bulk human skin has a negligible transmissivity, therefore the emissivity of normal skin is:

$$e_h = 1 - r_h = 0.68 \quad (2.30)$$

The average surface temperature of human skin at room temperature (27°C) is about 33°C (306 K) [OLE82]. The corresponding brightness temperature is:

$$T_0 = 0.68 \cdot 306K + 0.32T_s = 208.08 + 0.32T_s \quad (2.31)$$

2. For 1<sup>st</sup> degree burns, surface temperature is increased from normal skin. Although there is no direct data quantitatively comparing the surface temperature of skin with and without a 1<sup>st</sup> degree burn, according to Forage [FOR64], the nerves in the human hand can detect a temperature difference as low as 1.5 °C. With the hand, it is possible to feel an elevated temperature on sun-burned skin, therefore a 2 °C higher than normal temperature is assumed. Additionally, the texture of the 1<sup>st</sup> degree burned skin is described as dry, so the dry skin dielectric property from Gabriel's model was used for the same calculation. Dry skin has an emissivity of 0.75, therefore the corresponding brightness temperature is:

$$T_1 = 0.75 \cdot 308K + 0.25T_s = 231 + 0.25T_s \quad (2.32)$$

3. For 2<sup>nd</sup> degree superficial burned skin, surface temperature drops by about 2 °C comparing to 1<sup>st</sup> degree burn, similar to that of healthy skin [FOR64]. However the moisture at the blister's base significantly increases the water content in the tissue. The dielectric property of a skin blister is not directly available, but since blisters are filled with a clear body fluid called serum [UCH88], the body fluid data from Gabriel's model is used to determine the skin's emissivity for superficial 2<sup>nd</sup> degree burns. The corresponding brightness temperature is therefore:

$$T_{2\_a} = 0.57 \cdot 306K + 0.43T_s = 174.42 + 0.43T_s \quad (2.33)$$

4. For deep 2<sup>nd</sup> degree burned skin, surface temperature is further decreased by about 3 °C compared to 2<sup>nd</sup> degree superficial burns [FOR64]. Skin texture is fairly dry

[TIN10], so we assume a similar emissivity as 1<sup>st</sup> degree burns, 0.74. The brightness temperature therefore is:

$$T_{2\_b} = 0.74 \cdot 303K + 0.26T_s = 224.22 + 0.26T_s \quad (2.34)$$

5. For 3<sup>rd</sup> degree burns, the texture of the skin feels leathery, therefore the measured dielectric property of natural leather [KAP12] was used to calculate emissivity, giving a value of 0.91. The physical temperature drops to room temperature, 300 K, and the brightness temperature becomes:

$$T_3 = 0.91 \cdot 300K + 0.09T_s = 273 + 0.09T_s \quad (2.35)$$

There are several assumptions that we have made to build the aforementioned mathematical model for brightness temperature of human skin under various burn severities:

- Based on the fact that the human hand can easily feel a 1.5 K temperature difference and usually we can feel a difference between sun-burned skin and normal skin, we assumed a 2 K temperature elevation for 1<sup>st</sup> degree burns;
- Based on the physiological description of how wet or dry different degrees of skin burns appear, we use dry skin and wet skin data from Gabriel's model respectively;
- The empirically derived dielectric property of leather was used to model the 3<sup>rd</sup> degree burn condition, since there is no measured data available on the leathery physiological state of a 3<sup>rd</sup> degree burn. The high emissivity complies with the physiological description, therefore we believe the assumption is reasonable.

Due to limitations of lab equipment and qualifications, these assumptions cannot be validated experimentally at this time. In the future, once PMMW imaging systems with high sensitivity are available to us, experiments should be carried out to validate our assumptions. In addition, with proper qualifications and volunteers, the surface temperature of different degrees of skin burns should also be measured, as there is no such data available now.

For the indoor, room temperature conditions (300 K), the brightness temperature of skin for the four previously described burn degrees scenarios are listed in Table 2.4. The 1<sup>st</sup> and 3<sup>rd</sup> degree burns are easy to evaluate by the naked eye through their distinctive physiological characteristics. It is the superficial and deep 2<sup>nd</sup> degree burns that need to be quantitatively distinguished, since their physiological appearance is similar. Distinguishing these types of burns is important because the deeper 2<sup>nd</sup> degree burn may require medical treatment such as skin grafting, while the superficial 2<sup>nd</sup> degree burn does not [TIN10]. At 300 K ambient temperature, the difference in the brightness temperature between the superficial and deep 2<sup>nd</sup> degree burns is about 1.2 K.

Togawa *et al.* have demonstrated a method to change the local ambient temperature by adding a thermally controlled heated hood over the studied object [TOG89], [OTS02]. The study was conducted for emissivity of skin at the 8 to 14  $\mu\text{m}$  range (21 to 37 THz). This method was verified by Boylan *et al.*, though a cooled hood was used in that instance [BOY92]. Therefore a parametric analysis was done on  $T_s$  and the results are concluded in Table 2.4 and Figure 2.8.

Table 2.4 Brightness temperature of skin at different burn severities

Condition	$T_s$ (K)	273	280	290	300
	Brightness Temperature (K)				
Normal		295.4	297.7	300.9	304.1
1st Degree		299.3	301.0	303.5	306.0
2nd Degree Superficial		291.8	294.8	299.1	303.4
2nd Degree Deep		295.2	297.0	299.6	302.2
3rd Degree		297.6	298.2	299.1	300.0

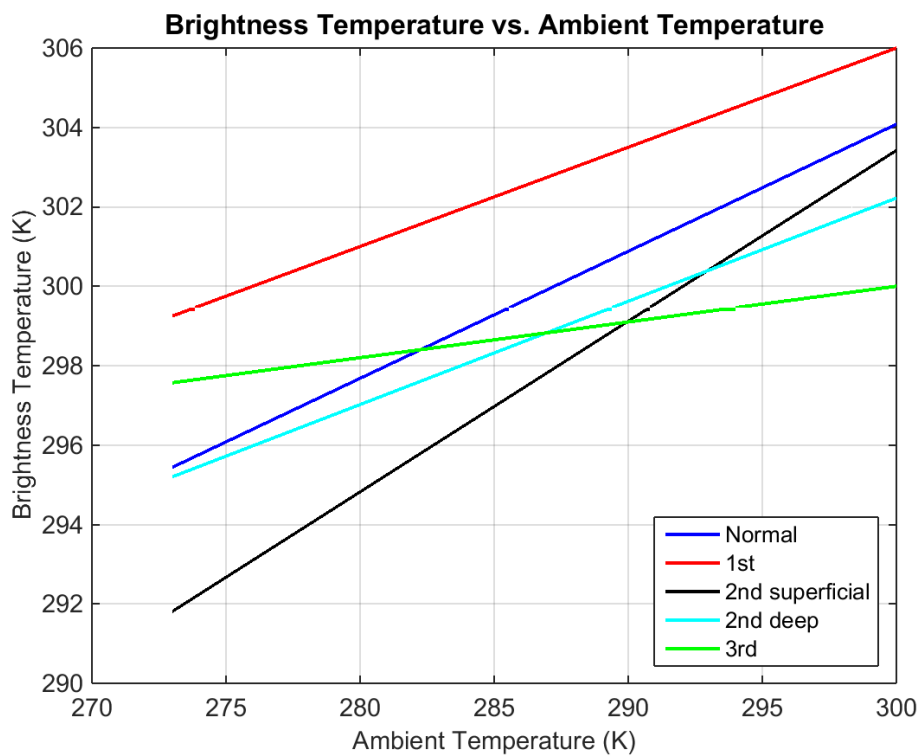


Figure 2.8 Brightness temperature of different burn degrees versus ambient temperature

The brightness temperature of all five cases are shown in Figure 2.8, where ambient temperature varies from 0-27 °C. The slope of the line indicates the dependency of the

brightness temperature on ambient temperature (*i.e.* the reflectivity). The 3<sup>rd</sup> degree burns have the driest skin texture, therefore they are the least dependent on reflectivity among the five burn scenarios. The superficial 2<sup>nd</sup> degree burn has the moistest texture, therefore brightness temperature is highly dependent on the ambient temperature.

Within our investigation range, the ambient temperature of 273 K (or 0°C) gives the greatest brightness temperature contrast between superficial and deep 2<sup>nd</sup> degree burn. Achieving this lower ambient temperature has been previously proven feasible [BOY92]. For this ambient temperature condition, the difference in brightness temperature between the superficial and deep 2<sup>nd</sup> degree burn wounds is 3.4 K. If a receiving system can resolve 0.2 K in brightness temperature, 17 steps between the superficial and deep 2<sup>nd</sup> degree burn could be resolved by the MMW imaging system, thus achieving an accurate evaluation of burn severity. In addition, using the controlled temperature hood, a series of measurements at various temperatures could be done to provide a greater amount of detail to help distinguish the burns.

It is also worth mentioning that the evaluation of burn severity using brightness temperature should be based on relative rather than absolute temperature. A system could be calibrated for a particular patient by measuring the temperature of his/her healthy tissue. Then comparing this value with the brightness temperature of his/her injured tissue over time will help to monitor the patient's healing process. It is meaningless to compare brightness temperature between patients and use one patient's severity to define another's, since the physical temperature and the dielectric value of skin varies from person to person.

In Section 2.4 and 2.5, the temperature differences ( $\Delta T$ ) for security and biomedical applications were discussed. In both applications, the ambient temperature is an important factor for providing large  $\Delta T$ . In security, outdoor or artificial incoherent illuminations could be used to provide over 100 K in  $\Delta T$ , while the indoor scenario will only create a  $\Delta T$  of 9K. For skin burns, outdoor application is not practical, but local ambient temperature could be set using a thermally-controlled hood in order to achieve a  $\Delta T$  of 3.4 K.

## 2.6 Summary

In Chapter 2, background knowledge of EM wave properties were reviewed, followed by the characterization of an EM wave in bounded media in terms of media dielectric properties, wave polarization and incident direction. The methodology of frequency spectrum selection for a passive imaging system was then discussed and the 94 GHz frequency range was selected. The application of the 94 GHz MMW imaging system is proposed for security screening and dermal burn wound inspections. 94 GHz wavelengths have the advantage of low attenuation in common clothing materials and a small enough wavelength to resolve objects in potential applications using compact antenna apertures and/or receiving optics. Additionally, current silicon technology is capable of implementing the system with low-cost IC in this frequency range.

Thermal radiation, reflectivity and emissivity of relevant materials were also discussed. It is the significant difference in emissivity between human and contraband materials that facilitates the detection of concealed objects using MMW imaging techniques. For skin burn

inspections, an extensive literature survey was conducted to study the anatomy and physiological characteristics of burn wounds in humans. Using the widely accepted extrapolated data from Gabriel *et al.*, combined with reasonable assumptions on dielectric properties of burned skin, the emissivity of skin in various degrees of burn severity was derived from which the brightness temperature was also expressed as a function of ambient temperature. Techniques of varying local ambient temperature to obtain greater contrast in brightness temperature was discussed and determined that a reasonable margin could be achieved using this technique.

Imaging phenomenology and system level design of a PMMW imager will be discussed in Chapter 3. All design specifications will comply with the brightness temperature differences derived in Chapter 2.

## **CHAPTER 3**

### **IMAGING PHENOMENOLOGY AND SYSTEM ARCHITECTURE**

#### 3.1 Overview

In this chapter, we introduce important background knowledge related to PMMW imaging systems. The difference between active and passive systems will be discussed, along with the diffraction limit and image resolution that can be achieved using a passive system. In addition, the advantages and disadvantages of PMMW imaging systems will be elaborated.

Later in the chapter, four recently developed PMMW imaging systems will be presented and compared based on their individual characteristics and specifications. Finally, state-of-the-art PMMW receivers will be introduced and our own system's specifications and anticipated results will be discussed.

#### 3.2 Background Knowledge

##### 3.2.1 Active vs. Passive MMW Imaging Systems

Both active and passive systems are common in current MMW imaging technology. Active systems illuminate the observed subject with MMW energy. Back-scattered and reflected waves are detected and processed to produce images [LAS10]. In active systems, the illuminating source is commonly a Gunn diode oscillator or a pulsed Impatt oscillator for coherent illumination [GRO03]. In such systems, interference and multi-path problems must be addressed by coherently coupling the MMW receiver with the transmitter. Active systems

excel at searching for foreign shapes on the human body, such as concealed weapons like knives and guns, but this technique can miss explosives or powders if these objects are properly disguised [LAS10].

In PMMW imaging systems, only reflected radiation from the ambient environment and some limited amount of thermal emission from the objects themselves are measured. Passive systems have the ability to sense thermal sources such as blackbody radiation, making coherent active sources of MMW illumination unnecessary if the object under observation can provide enough radiation, or has a substantially different temperature from the surrounding environment. As a result, PMMW systems are more likely to discover powder or liquid, in addition to concealed weapons. To enable detection of difference in small temperature, the receiver must contribute very little noise to the signal. Therefore a highly sensitive detector with a low-noise amplifier (LNA) is necessary for passive systems.

The receiving phenomenology for both active and passive systems can be fairly similar, but since active systems have more controllable aspects, such as polarization and direction of emitted signal, as well as the coherence that must be kept between transmitters and receivers, they typically have more sophisticated architectures than passive systems [SHE09]. Consequently, active systems tend to occupy more area and consume more power, making a system with larger pixel arrays or elements less cost-effective.

Recently, some researchers have tried using fluorescent light in indoor applications as an incoherent illumination source for better spatial resolution and contrast between different materials [MIZ05], [PER10]. Although it was mentioned in Section 2.4 that incoherent

illumination sources were used to create 500K ambient temperature for better brightness temperature contrast, there are still limited publications on similar topics and possible issues related to this method are still poorly understood [PER08].

### 3.2.2 Object Distance and Resolution

In early years, applications of MMW imaging featured a large distance between the sensor and observed objects, including such studies as “Airborne Imaging System” [VOW81] and “Earth’s Atmosphere Study.” With recent development in MMW technology, close-field applications such as security surveillance have emerged. The security camera normally operates from a distance of 1-5 meters from the target, yet 1 meter is much longer than 10 times the wavelength at 94 GHz ( $3 \text{ mm} \times 10 = 30 \text{ mm}$ ), still keeping the imaging subjects in the far field.

As stated in Section 2.2.3, PMMW imaging is diffraction-limited. At a given operating frequency with a known collecting optical diameter, the minimum resolvable angle,  $\alpha$ , is fixed. In this case, the minimum resolvable size of an object will be proportional to the distance of the object from the camera, as depicted in Eq. 3.1.

$$d = \alpha R = C \frac{\lambda}{D} R \quad (3.1)$$

where  $d$  is the minimum resolvable size and  $R$  is the distance of the object from the camera. Operating too far from the objects will cause the minimum resolvable size to increase, consequently degrading the image resolution. Additionally, at greater distances more signal diffusive attenuation will incur [OKA08], reducing the signal levels towards the noise floor.

According to Eq. 3.1, one way to reduce  $d$  is to increase  $D$ , meaning to increase the receiving optical system's diameter. For some applications, quasi-optical imaging through a focal lens is used to resolve the problem [JUN09], [LI11]. However, the major drawbacks of such systems are their large size and weight, especially due to the lens.

### 3.2.3 Thermal Sensitivity

When thermal energy is measured in PMMW imaging systems, the sensitivity of the system is defined as the lowest temperature difference it can detect, named  $\Delta T$  or the noise equivalent temperature difference (NETD). It is given by [LET03]:

$$\Delta T = C \frac{T_{SYS}}{\sqrt{B\tau}} \quad (3.2)$$

where  $C$  accounts for noise sources from the system,  $T_{SYS}$  is the noise temperature of the system,  $B$  is the RF bandwidth, and  $\tau$  is the post-detector integration time. In order to have good sensitivity (*i.e.* low  $\Delta T$ ), the system noise must be minimized, the bandwidth should be as wide as possible, and the integration time should be long enough without sacrificing the frame rate (the number of photos taken per second).

### 3.2.4 Image-Forming Phenomenology

A wide range of techniques have been developed to beam-form or scan millimeter-wave radiation. They can be generally divided into 4 categories: (1) Optical beam-forming and mechanical scanning (optomechanical scanning); (2) focal-plane array; (3) electronic beam-forming and scanning [LET03]; and (4) interferometry and SAR.

Optical beam-forming usually contains a single element detector or a small array of multiple detectors, located at the focal plane of a lens. The detectors and lens are then mounted to a mechanical scanner, which is controlled to move along the X and Y axes [YEO11]. When taking a picture, the image plane will be divided into multiple segments. The scanner then moves and stops at every segment for the receiver to detect and integrate the power received. The advantage of such a method is its relative simplicity in a system architecture. However, the system needs to scan pixel by pixel and integrate for every pixel to form an image, thus there is a trade-off between frame rate and system sensitivity. For example as in [YEO11], a 1-D array of 1 x 30 detectors is located on the focal plane. It takes 10 msec for each detector to detect and integrate, which means 1 x 30 pixels. Thus an image of 24 x 30 pixels takes 240 msec to integrate, while an image with 72 x 90 pixels could take 2.16 seconds. Another variation of this method is an optomechanical scanner, in which a planar mirror is used to scan the beam in a reciprocating or rotary motion.

For the focal-plane array (FPA) detection method, a lens is used to focus EM waves onto an array of detectors. As opposed to a mechanical scanning system, FPA utilizes a very large number of receivers on the focal plane and all receivers process the waves simultaneously, which avoids the need for scanning while still getting a comparable number of pixels in the image [DOW96]. While maintaining a comparable NEDT, FPA saves time from scanning, thereby significantly increasing the frame rate, which makes it possible for applications demanding video rate imaging ( $>30$  Hz), such as real-time surveillance. However, in FPA one receiving unit corresponds to one pixel in the image and it could

require over one thousand identical receiving units (antennas, detectors, and interconnects) to be incorporated in the system, making FPA a very expensive system solution.

Electronic beam-forming achieves scanning through phased-array technology. Even though the name implies that scanning occurs, there is actually no physically moving part in the electronic beam-forming and scanning system. A phased array contains a 2-D array of receivers. Each receiver is connected to a phase shifter and the outputs of these receivers are added in amplitude and phase to form a “pencil beam” in a given orientation [LET03]. There are also other kinds of electronic scanning systems, but most of the current ones are subjected to some similar limitations, including the number of required receivers, which is cost related, the RF bandwidth limit for high spatial resolution with a wide aperture and effective field-of-view (FOV).

Interferometry or SAR is a technique widely used in radio astronomy and remote sensing, where a very large antenna aperture is needed and the required aperture size exceeds the practical limit of manufacturing. Aperture synthesis overcomes this limitation by sparsely sampling the aperture using smaller antennas.

As illustrated in Figure 3.1, a pair of small antennas is used in conjunction with signal processing techniques to achieve the resolution of a single antenna with a larger aperture. The product of the signals from the antenna pairs is measured in the correlator and will be reconstructed in later signal processing stages. Both amplitude and phase can be measured by these antennas, thus a complex product (with a real and imaginary part) can be obtained for any combination of two antennas at various spacing.

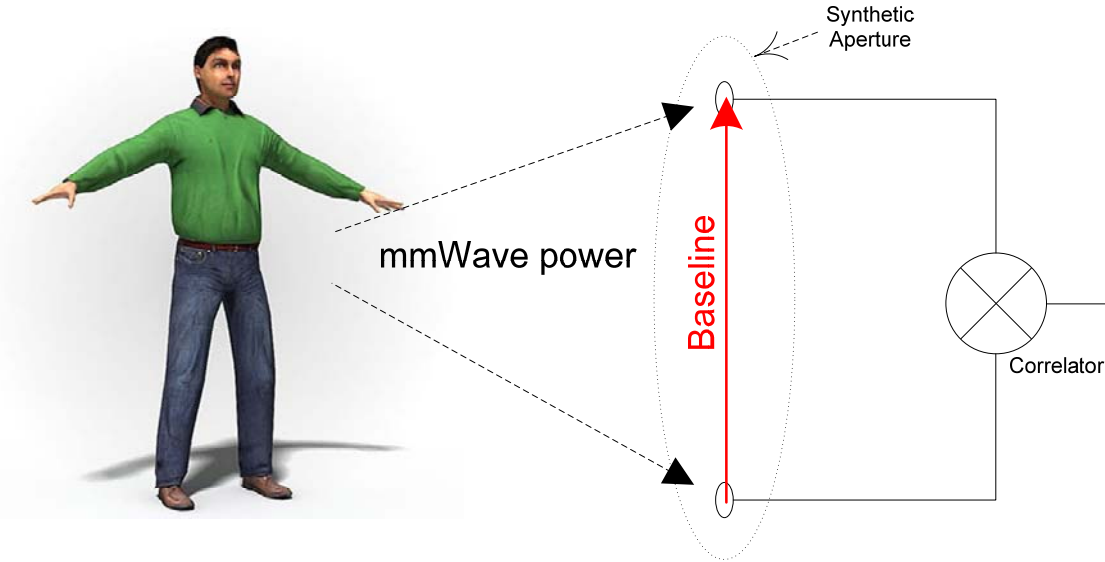


Figure 3.1 Basic setup of a synthetic aperture radiometer

A basic receiving unit, named the “baseline” as shown in Figure 3.1, is composed of two conventional receiving units, where each of the conventional unit has its own antenna, front-end receiver and subsequent circuits. The incident field is picked up by each antenna, modulated by the antenna radiation pattern and the frequency response of the front-end circuits. In this manner two received signals,  $V_1$  and  $V_2$ , will be obtained, as described in Eq. 3.3. These 2 signals will be subsequently cross-correlated (multiplied and integrated) to form the visibility (as shown in Eq. 3.4) seen by the baseline.

$$V_{1,2} = \int \int_{-\infty}^{\infty} E_{1,2}(x, y) \sqrt{A_{1,2}(x, y)} H_{1,2}(\nu) e^{j2\pi u_{1,2}} dx dy \quad (3.3)$$

$$r(\tau) = \lim_{T \rightarrow \infty} \frac{1}{2T} \int_{-T}^T V_1(t) V_2^*(t - \tau) dt \quad (3.4)$$

where  $V_1$  and  $V_2$  are defined in Eq. 3.3 with their respective subscript,  $A(\sigma)$  is the antenna power reception pattern,  $E(\sigma)$  is the incident field seen by antenna,  $H(\nu)$  is the frequency

response of the front-end circuits, and  $\tau$  is the time delay by  $V_2$  with respect to  $V_1$  ( $t_1 - t_2 = \tau$ ) [THO01]. The output of the correlator can then be calculated as below:

$$\begin{aligned}
 r(\tau) &= \lim_{T \rightarrow \infty} \frac{1}{2T} \int_{-\infty}^{\infty} \int_{-\infty}^{\infty} \int_{-\infty}^{\infty} \int_{-\infty}^{\infty} E_1(x, y) E_2^*(x, y) \sqrt{A_1(x, y) A_2(x, y)} H_1(\nu) H_2^*(\nu) e^{j2\pi\nu t_1} e^{-j2\pi\nu t_2} dx dy dt d\nu \\
 &= \int_{-\infty}^{\infty} \int_{-\infty}^{\infty} \int_{-\infty}^{\infty} I(x, y) A(x, y) |H(\nu)|^2 e^{-j2\pi\nu(xu+yv)} dx dy d\nu = \text{Visibility} \tag{3.5}
 \end{aligned}$$

Note that the squared field amplitude,  $E$ , is replaced by the source intensity  $I$ , as observed from the antennas. Eq. 3.5 indicates that the correlator output, defined as ‘‘Visibility’’, measures the Fourier transform of the field intensity distribution modified by the antenna pattern and circuit frequency response. With the knowledge of  $r(\tau)$ ,  $A(\sigma)$  and  $H(\nu)$ , source intensity can be reconstructed through an inverse Fourier transform in later signal processing stages.

One advantage of SAR over other techniques is its significantly reduced number of receivers necessary to give a comparable performance. For example, in FPA, the number of pixels in the image equals the number of receivers used. In a scanned system, the number of pixels in the images equals the number of receivers multiplied by the number of times that the scan is performed. So each receiver can acquire only 1 pixel in the image. For SAR, each distinct baseline corresponds to 1 pixel in the image, so if properly arranged and if each pair of receivers forms a distinct baseline, the number of pixels (baselines) in a system with  $N$  receivers becomes  ${}_N C_2 = \frac{N(N-1)}{2}$ . An 8-element SAR could therefore get an image with 28 pixels, almost quadruple that compared to other techniques, making SAR a very cost

effective solution for systems with a large array. As will be shown, however, there is a sensitivity penalty for SAR due to the multiplicity of detectors used to form a single pixel in the image.

All four of the major techniques in forming a PMMW image are presented above and summarized in Table 3.1.

Table 3.1 Summary of the four major techniques in forming a PMMW image

	Advantage	Disadvantage	Lens	Aperture Size
Optomechanical /Scanned Array	<ul style="list-style-type: none"> <li>· Simple architecture</li> <li>· Simple post-processing</li> <li>· Cost effective</li> </ul>	<ul style="list-style-type: none"> <li>· Long scanning time</li> <li>· Bulky and heavy</li> </ul>	Yes	Small, depends on lens
Electronic/ Phased Array	<ul style="list-style-type: none"> <li>· Faster scanning</li> <li>· No mechanical scanning</li> </ul>	<ul style="list-style-type: none"> <li>· Expensive when using many receivers</li> <li>· Complicated post-processing</li> <li>· Sidelobes</li> </ul>	No	Small
Focal Plane Array	<ul style="list-style-type: none"> <li>· High frame rate</li> <li>· Simple architecture</li> </ul>	<ul style="list-style-type: none"> <li>· Expensive when using many receivers</li> </ul>	Yes	Small, depends on lens
Interferometry & SAR	<ul style="list-style-type: none"> <li>· Cheap w/o lens</li> <li>· No scanning</li> <li>· Large aperture</li> </ul>	<ul style="list-style-type: none"> <li>· Complicated post-processing</li> </ul>	Yes/No	Big w/o lens; Bigger w/ lens

### 3.3 State-of-the-Art Systems and Selection of System Architecture for this Work

In this section, four recently developed PMMW imaging systems are presented, as shown in Table 3.2. Comparison is made with respect to their individual characteristics and specifications. Three of these PMMW imaging systems use FPA with mechanical scanning.

Two out of those three systems are used for security surveillance applications [LET05], [KIM11], and the remaining system is a SAR system used for remote sensing [FET08], [TAN07, 08].

With recent developments of semiconductor technologies, millimeter-wave monolithic integrated circuits (MMIC) have become a low-cost and dependable solution for the front-end of PMMW imaging systems [FLO05], [DOA05], [BAB06], [NAT06], [GUN05], [RAZ05].

The fact that optomechanical systems have a simpler system architecture as well as a cost-effective front-end makes it the most popular method that researchers choose to utilize in PMMW imaging. The first three systems are all optomechanical scanning systems with their receiver or receiver array located in the focal plane. They differ in the method of scanning. The MERIT system uses a large flapping mirror to produce a 2-D fan-beam scan of the scene and another concave rotating mirror which acts as the focusing element. MIRAE contains a 1-D FPA consisting of a lens which is mounted on a linear scanner, moving in the direction perpendicular to the FPA to perform a linear scan to produce a 2-D image. In the PMMW imaging system described in [FET08], there is only one receiver at the focal plane and the system is mounted on a motorized platform, which can move in a plane parallel to the image plane, thus a 2-D image can be obtained when the platform scans over the plane.

MIRAE, [FET08], and MERIT have relatively comparable performance. All three operate around 94 GHz with a system bandwidth of about 10 GHz. When the same linear scanning method is used, [FET08] has a better spatial resolution than MIRAE because of its

larger lens as described in Eq. 3.1. MERIT has a much wider FOV than the other two systems ( $60^\circ \times 20^\circ$  vs.  $17^\circ \times 17^\circ$ ), which is caused by its unique scanning mechanism. As illustrated in Figure 3.2, the FOV of a linear scanning system is primarily based on the beamwidth of a single element's antenna. The fan-beam rotary scanning system enlarges its FOV by taking advantage of the rotating flapping mirror.

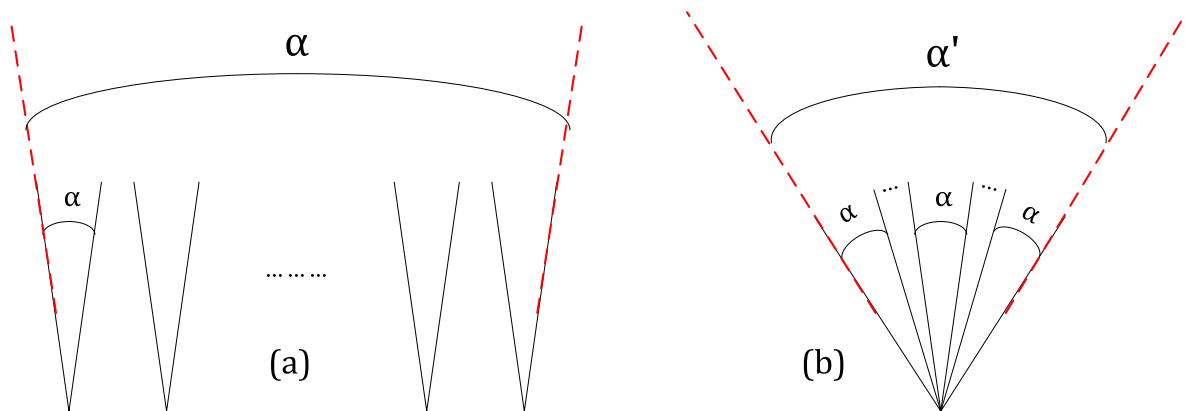
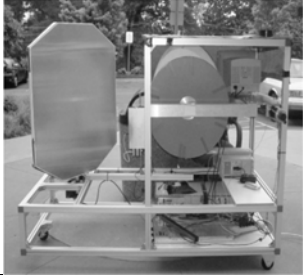
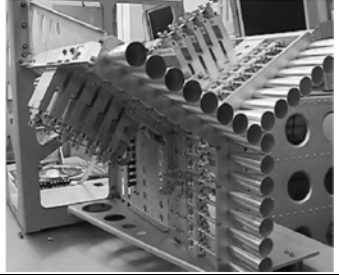


Figure 3.2 FOV comparison  
 (a) Linear scan: FOV of system equals the beamwidth of antenna;  
 (b) Rotary scan: FOV increased due to the scanning motion.

Table 3.2 Comparison of recently developed PMMW imaging systems

System	MERIT (QinetiQ)[LET05]	MIRAE [KIM11]	[FET08]	GeoSTAR Prototype [TAN07] [TAN08] [KAN08]
				
Application	Security Surveillance	Security Surveillance	Remote Sensing	Remote Sensing
Mechanism	FPA w/ mirror mechanical scan	FPA with mechanical scan	FPA with mechanical scan	Synthetic Aperture
Center Freq	94 GHz	94 GHz	95 GHz	50 GHz
BW(GHz)	12 GHz (87-99 GHz)	8 GHz	N/A*	5 GHz (50-55 GHz)
Spatial Resolution	0.52°	0.57°	0.4°	1°
FOV (H x V)	60° x 20°	17° x 17°	15° x 15°	17° Diameter Disk
Aperture Size	660 mm	500 mm	600 mm	No Lens
Sensitivity (NETD)	2 K	<1.5 K	0.9 K	1 K
# of channel	1	30	1	24
Frame Rate	10 Hz	1 Hz	1/240 Hz (4 min acquisition time)	Varies
System Noise	800 K	650 K	1-2 K/pixel (~1400 pixels calculated)	500 K

\*N/A in the table means the specification was not reported by the author.

With similar image forming phenomenology for the MIRAE, [FET08], and MERIT systems, another tradeoff could be made among NETD, bandwidth, frame rate and system noise. This has been described in Eq. 3.2 and can be confirmed with the performance of these systems. With 4/5 of the system noise, 2/3 of the bandwidth, but 10 times the acquisition time, MIRAE has a better thermal sensitivity than MERIT. Similarly, despite the noisy system, [FET08] has a 4-minute long acquisition time, which helps maintain its sensitivity to thermal contrasts.

Alternatively, SAR has the advantage of a large synthetic aperture, which allows it to generate smaller angular resolution, making it thus more desirable in applications with large distances between the object and the receivers, such as remote sensing. The system presented in Table 3.2, indicates that the PMMW imaging system with the lowest system noise at 500 K is the prototype system, GeoSTAR. It consists of three arms, with each arm containing a line of eight uniformly distributed antennas. These three arms are laid-out in “Y” shape. The “Y” configuration provides the needed baselines with a minimum number of antennas and with a fixed geometry. The 8 elements in arm1 can yield 64 unique baselines with arm2, and another 64 conjugate-symmetric baselines can be derived from arm2 to arm1. So without even considering the correlations among the elements of a common arm, this configuration, with 24 antennas, can provide 384 complex visibility samples, which is more clearly illustrated in Figure 3.3. From Figure 3.3, the minimum spacing between any 2 antennas determines the FOV, which according to [TAN07] is  $(2 / \sqrt{3})(\lambda / d_{\min}) = 17^\circ$ . The maximum spacing between any two antennas determines the smallest spatial scale that can be resolved,

which is about  $1.0^\circ$  ( $=0.53\lambda/d_{max}$ ). The projected future, scaled system will have 100 elements per arm and thus will result in a minimum spatial resolution of  $0.08^\circ$ .

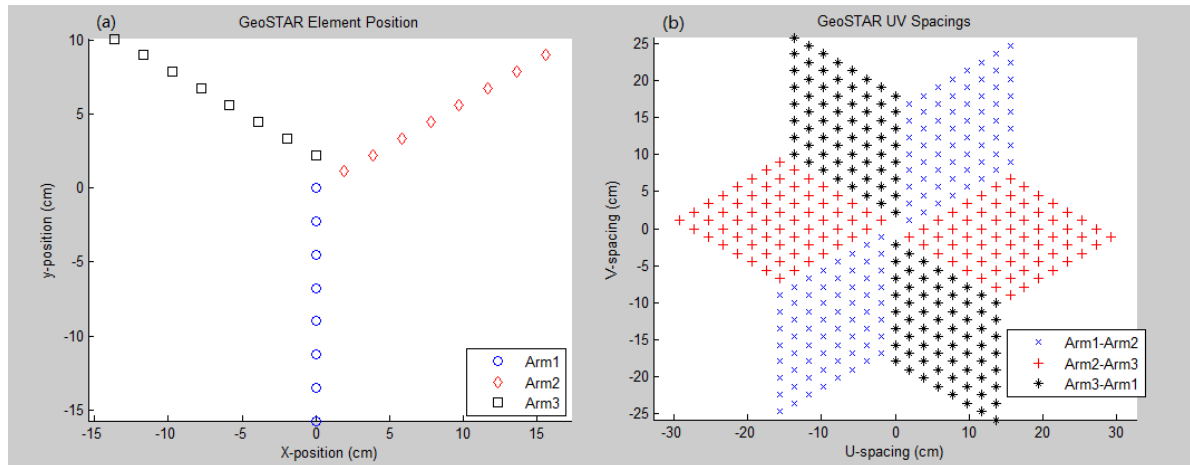


Figure 3.3 (a) Antenna array layout and (b) the corresponding UV spacing.

In Section 3.3, four state-of-the-art PMMW imaging systems were reviewed to compare their specifications. The tradeoff among these specifications has also been discussed. Optomechanical scanning systems are subjected to slow scanning and extra system noise, while a SAR, operating at only half of the scanning system frequency (double the wavelength), is only 1/4 of the size and is able to show similar technical specifications. However, out of the four PMMW imaging systems discussed, only one of them uses a SAR, and is the only system under active development. There is however, no PMMW imaging system using a SAR receiver that is also built with silicon MMICs. Even though FPAs are built with MMICs, such systems still require a large number of receivers and/or mechanical scanning devices to achieve a large aperture. SAR, in contrast, has the advantage of

synthesizing larger apertures using a smaller number of receivers and consequently the system size is smaller. If a SAR based PMMW imaging system could be built with MMIC, it would cost even less than the systems which use the FPA receiver. Furthermore, the high levels of integration in silicon will result in significantly reduced system cost and which will enable more sophisticated SAR architectures.

As stated in this section, the current PMMW imaging systems are subject to problems including bulk and weight due to the scanning mechanism, long integration times especially for images with a large number of pixels, limitations on the number of receivers used due to the high cost, aperture size of the imagers, and effective FOV, *etc.* SAR systems built in silicon MMIC show great potential in resolving one or many of these problems without trading-off other aspects in performance or incurring increased cost. Such a development would significantly contribute to the field of PMMW imaging technology. Therefore SAR is selected as the top-level system concept for this work and will be implemented in silicon MMIC.

### 3.4 Receiver System Architecture

The function of a receiver is to detect an electromagnetic signal, filter the signal into a specific frequency spectrum and provide subsequent stages with one or more measures of the input signal, so that the desired information of the EM signal can be used to reconstruct image. A receiver can provide information including amplitude, phase, power, in-phase and

quadrature version of input, *etc.* There are two major kinds of detection receivers that are widely used: (1) super-heterodyne receivers and (2) direct-conversion receivers.

The super-heterodyne receiver is a commonly used architecture for radio frequency (RF) sensors. The principle of its operation depends on frequency mixing. The input RF signal is amplified and filtered to reject image frequency. Then it is mixed with a local frequency (LO) generated by a local oscillator, shifting the signal to an intermediate frequency (IF). The IF signal (usually lower than RF) is then further processed by demodulation circuitry, as illustrated in Figure 3.4. Super-heterodyne receivers do have certain issues such as image frequency and LO or IF frequency feed through, therefore frequency filtering needs to be addressed when a super-heterodyne receiver is utilized.

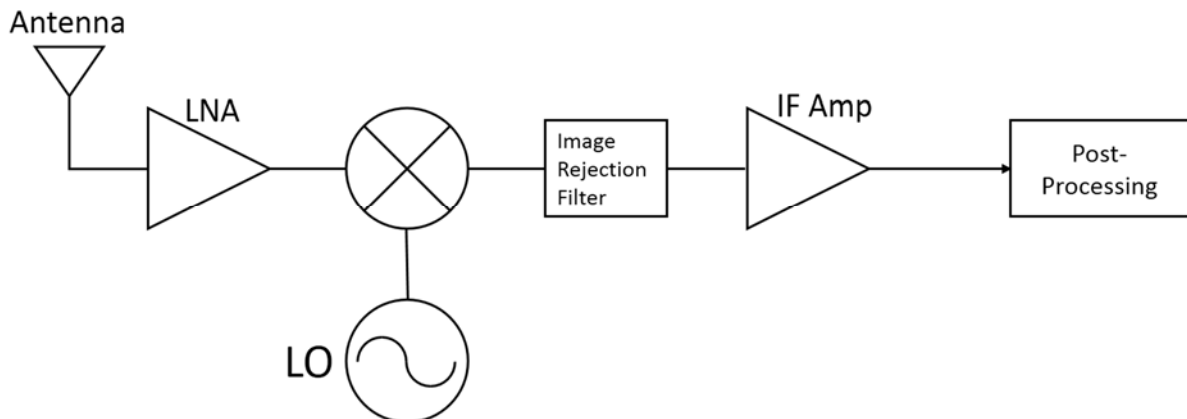


Figure 3.4 Diagram of a typical super-heterodyne receiver

On the other hand, a direct-conversion receiver (DCR), also known as homodyne or zero-IF receiver, has its own advantages over the super-heterodyne. Without the need to convert the input signal to an intermediate frequency, the DCR avoids all the complexity of

the super-heterodyne receiver, such as IF stage(s) and image rejection blocks. The input signal is directly down-converted to baseband (zero-IF) by mixing with a LO frequency identical or very close to the RF frequency. The down-converted signal is immediately ready for post-processing, as illustrated in Figure 3.5. Although seemingly much simpler than super-heterodyne, in order to match the performance a DCR still needs to accomplish certain functions at the baseband, which is addressed by the super-heterodyne receiver at IF stage with less difficulty. Besides, there are issues such as DC offset and local oscillator energy leakage, which can make DCR's production costs outweigh its benefit.

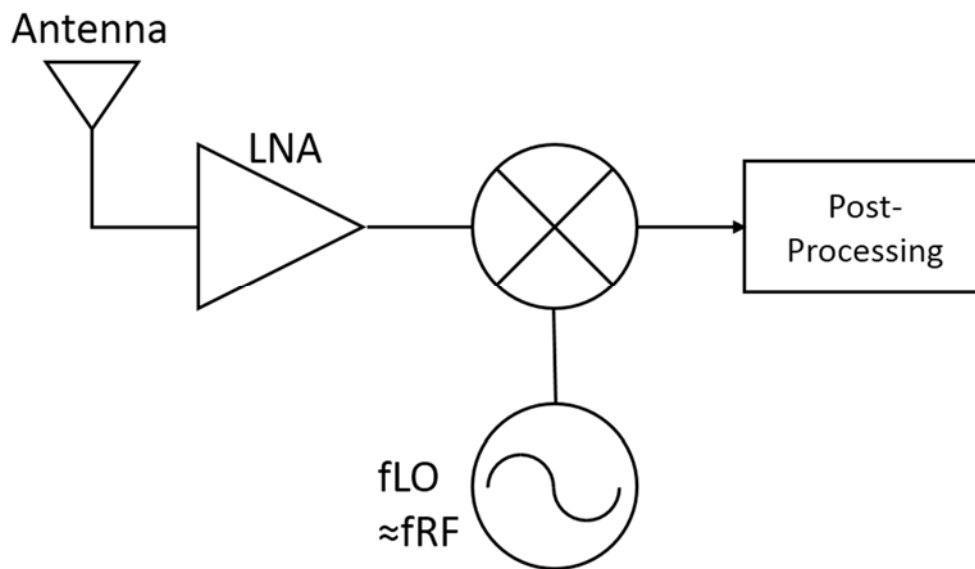


Figure 3.5 Diagram of a typical direct-conversion receiver

Therefore, after comparison of the two major RF receiver architecture, we have decided to choose the super-heterodyne receiver as the architecture for our PMMW imaging

system. However, interestingly, when we designed our prototype array, we found the total power radiometer (one kind of direct detection receiver) was useful to prove one concept of interferometry, so ultimately both kinds of receiver architectures were implemented in our system, and details can be read in subsequent chapters.

### 3.5 Design of System Specifications

The objective of the project is to design a SAR to be fabricated with MMIC technology, and to be used in two major applications: (1) the detection of concealed objects (security); and (2) the diagnosis of dermal burn wounds (biomedical). The silicon circuit prototype array and its break-out circuits are implemented in IBM BiCMOS 8HP (130 nm) technology.

#### 3.5.1 System Level Requirements

At the front-end of the SAR, an array of antennas will be fabricated and integrated on one or more printed circuit boards. These boards will be aimed towards the two targeted subjects: (1) people under security surveillance; and (2) burned skin. As learned from the phenomenology, ambient MMW radiation will be reflected from the target and the power will be received by the antenna array.

Since the temperature difference between normal and damaged skin is less than the temperature contrast between humans and concealed weapons, the biomedical application requires greater sensitivity from the receiving system. In addition, the affected skin area may

be smaller than a concealed object, which suggests that the biomedical application would also require a higher resolution. To better illustrate these facts, Figures 3.6 and 3.7 are drawn below. In these figures, depiction of a human body and a hand as imaging subjects is shown to provide a sense of scale for the size of subjects that the PMMW imaging system would target. In Figure 3.6, the interferometric antenna array is aimed directly at the subject, which is the probable configuration for the security application. Figure 3.7 depicts the arrangement of the biomedical application in which the antenna array is vertically mounted to aim the target through a focusing lens for better image resolution.

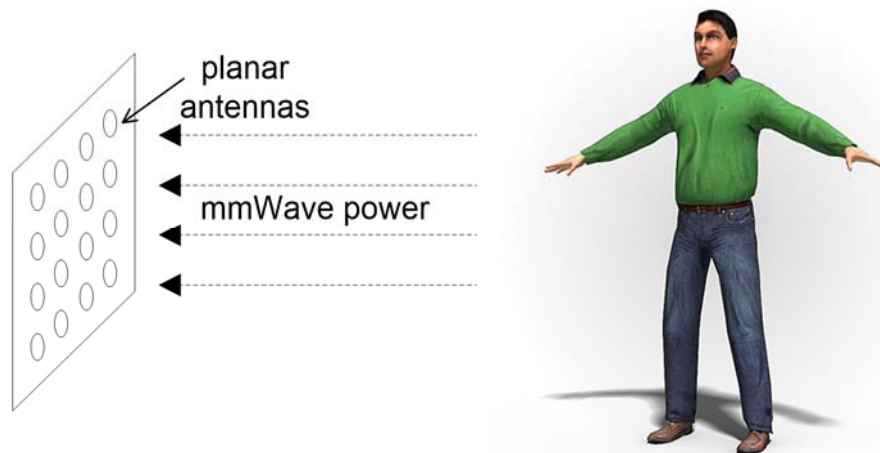


Figure 3.6 Antenna array aims directly at the target

The number of antennas and how they are arranged is out of the scope of this work. Antenna array design is outside of the scope of this particular project and would be the subject of future work. However, according to [SKO06], the “Y” shape arrangement of the arms of the SAR, as in [TAN07], is an important configuration, which minimizes the number

of redundant baselines. Therefore, the “Y” configuration is assumed throughout this work and used for all calculations. Although this is not necessarily the most mathematically efficient arrangement in terms of the number of antenna used, it is still a good choice of configuration due to its simple antenna distribution pattern and scalability for future development.

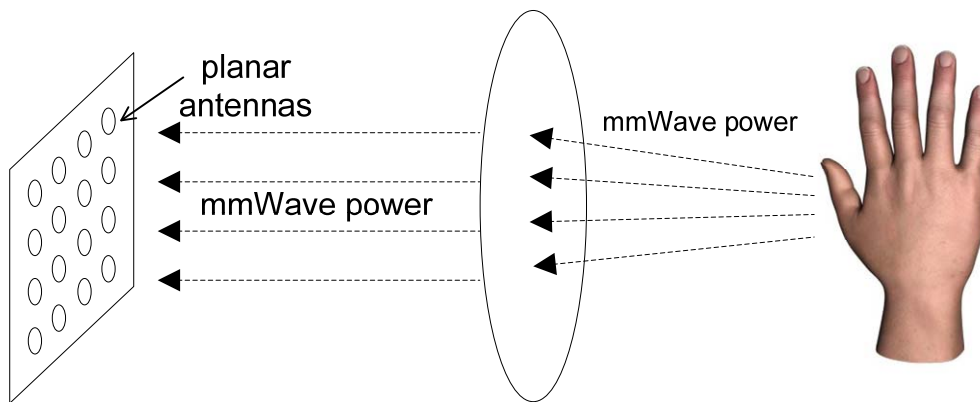


Figure 3.7 Antenna array aims through a lens for biomedical applications

### 3.5.2 Security System Specifications

In the following section, when calculations are made for the SAR system, the same mathematical model found in [TAN07] will be utilized here.

$$FOV = \theta = \frac{2}{\sqrt{3}} \frac{\lambda}{d_{\min}} \quad (3.6)$$

$$\alpha = \frac{0.53\lambda}{nd_{\min}} \quad (3.7)$$

where  $\alpha$  is the minimum resolvable angle, and  $d_{min}$  is the minimum spacing between any two antennas. The  $2/\sqrt{3}$  term comes from the “Y” layout of the antenna array [TAN07]. For security surveillance applications, the distance from the targeted object to the antenna array can be estimated at around 10 m. An average human’s height is within 2 m, thus the FOV is calculated as illustrated in Figure 3.8:

$$\theta = 2 \tan^{-1} \frac{1}{10} = 11.42^\circ \quad (3.8)$$

$$\therefore d_{min} = \frac{2\lambda}{\sqrt{3}\theta} = 5.79\lambda \quad (3.9)$$

$$\therefore \alpha = \frac{0.53}{5.79n} = \frac{0.915}{n} = \frac{5.24^\circ}{n} \quad (3.10)$$

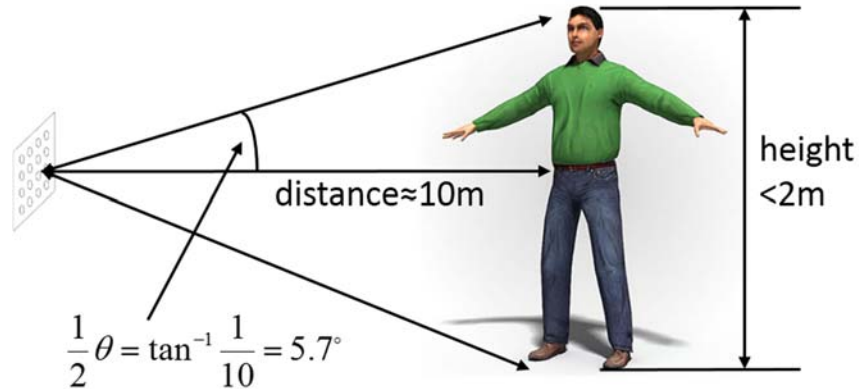


Figure 3.8 Illustration of FOV calculation for security applications

If a minimum resolution of  $0.5^\circ$  is requested, 10 elements are needed in one arm, thus the total length of the arm is  $10 \times 5.79\lambda = 185\text{mm}$  at 94 GHz. Taking the Y shape into account, the whole antenna array makes up an area of 280 mm x 280 mm.

If the observation distance is 5 m,  $\theta$  becomes  $22.6^\circ$ ,  $d_{min}$  is  $2.92\lambda$ , and  $\alpha$  is  $10.38^\circ/n$ . For a  $0.5^\circ$  minimum resolution, 20 antennas are needed in one arm. The arm's total length therefore becomes  $20 \times 2.92\lambda = 186\text{mm}$ , resulting in a similar array size of 280 mm x 280 mm. Despite the change of observation distance, in order to resolve  $0.5^\circ$ , which is comparable to FPA systems, an estimation of the proposed SAR's dimension of about 280 mm x 280 mm is necessary, and the system has a FOV of around  $22.6^\circ$  when the target is 5 meters away. For the same resolvable angle, the system with a shorter standoff distance has a better spatial resolution, but the spatial resolution comes at the expense of more necessary elements in one arm, which results in more complicated post-processing circuits and algorithms.

According to [SKO06], a limit should be imposed to make sure the effective system bandwidth can accommodate the time delay between signals arriving at pairs of antennas in the array. The limit is described in Eq. 3.11

$$\frac{L \sin(\theta)}{c} < \frac{1}{B} \quad (3.11)$$

Possible solutions to satisfy this limit are:

- Limit the effective system bandwidth
- Limit the maximum baseline, L
- Limit FOV,  $\theta$

If the 10 m stand-off distance is used,  $\theta$  is  $11.4^\circ$  and consequently the bandwidth limit will be:

$$B < \frac{c}{L \sin(\theta)} = \frac{3 \times 10^8}{185 \times 10^{-3} \times \sin(11.4^\circ)} = 8.2 \text{GHz} \quad (3.12)$$

By converting RF signal to IF, and with a reasonable bandwidth of 2 GHz, it is possible to relieve limits on  $L$  and  $\theta$ . For the assumption of  $T_{SYS}$ , a single-element receiver noise factor ( $F$ ) and its corresponding noise figure (NF) are defined as below:

$$F = 1 + \frac{T_{SYS}}{T_{REF}} = 1 + \frac{T_{SYS}}{290 \text{K}} \quad (3.13)$$

$$NF = 10 \log F \quad (3.14)$$

where  $T_{REF}$  is the reference noise temperature, defined as 290 K. A single-element receiver in SiGe BiCMOS 8HP could have a NF of around 9 dB ( $F = 7.9$ ), and consequently a  $T_{SYS}$  of 2000 K. With an assumed integration time of  $\tau = 0.5$  s, the NETD can be found as:

$$\Delta T = \sqrt{6N^2} \frac{T_{SYS}}{\sqrt{2B\tau}} = \sqrt{6 \times 10^2} \frac{2000}{\sqrt{2 \times 2G \times 0.5}} = 1.1 \text{K} \quad (3.15)$$

where  $N$  is the number of antennas in one arm,  $6N^2$  accounts for the number of conjugate baselines utilized, and the  $\sqrt{2}$  accounts for the double-counted baselines in  $6N^2$ . With the above assumptions and calculations, the synthetic aperture PMMW imaging system for security applications is developed and summarized in Table 3.3.

### 3.5.3 Biomedical PMMW Imaging System Specifications

When the proposed PMMW imaging system is applied to biomedical imaging, the system specifications have different priorities compared to the needs of a security focused system. For example, the throughput is less prioritized as it is in the case of security

surveillance. For biomedical screening, the need for higher temperature sensitivity and better image resolution for diagnostic purposes allows more time to be devoted to imaging. The wavelength at 94 GHz is 3.19 mm, so a minimum resolvable size in the 3 mm range is the best option. With a 50 cm distance from the target, an angle of  $0.5^\circ$  gives a minimum resolvable size of 4.4 mm. If we assume the target distance = 0.5 m and that  $\alpha = 0.5^\circ$ , calculations are performed as below:

$$\alpha = \frac{0.53\lambda}{nd_{\min}} = \frac{0.53\lambda}{L_{ARM}} = 0.5^\circ \frac{\pi}{180^\circ} \quad (3.16)$$

$$\therefore L_{ARM} = \frac{0.53\lambda}{\pi} 360 = 193.8mm \quad (3.17)$$

No matter what  $d_{min}$  value is chosen, in order to get a  $0.5^\circ$  resolution, the receiver arm must be as long as 194 mm, forming an angle of  $21.2^\circ$  from the boresight to each end of the arm. This may cause a problem of path delay, which results from a path difference equals to 36 mm as shown in the two dashed lines in Figure 3.9. One way to tackle this problem is to add a lens, so that the object in close range from the receiver can be viewed as if it has been placed further away. This is illustrated in Figure 3.10.

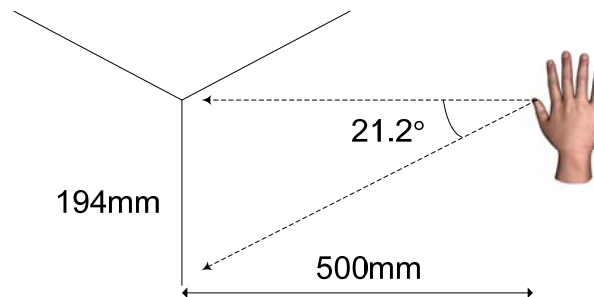


Figure 3.9 Illustration of optics for the biomedical application of PMMW imaging, displaying a large path difference

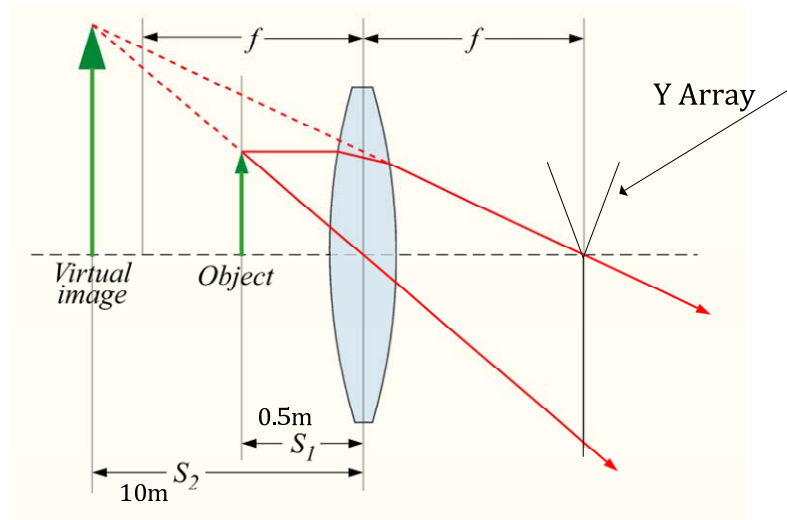


Figure 3.10 Illustration of the effect of a lens (modified from [WIK02])

Assuming a proper lens is chosen, even though the object is placed 0.5 m from the lens, the virtual image that the receivers see is as if the object were placed at a distance of 10 m from the lens. Thus an optical path from the virtual image to the receiver could be constructed similar to that which occurs in the security application of PMMW imaging. The corresponding system specifications for the biomedical application is summarized in Table 3.3.

The difference between the security and biomedical applications is the minimum resolvable size of the system with a lens. Since the minimum resolvable angle is unchanged at  $0.5^\circ$  and the minimum resolvable size for a virtual image 10 m apart is 8.7 cm, the minimum resolvable size for this actual object is  $8.7 \text{ cm}/20 = 4.35 \text{ mm}$ , which is slightly longer than the wavelength at 94 GHz, but still short enough to provide good resolution for the biomedical application of the PMMW imaging system. In order to have a better noise

temperature sensitivity, longer integration time could be applied. A 15 s integration time is 30 times longer than previously proposed, and for that reason we are expecting a theoretical 0.2 K NETD to be achieved.

Table 3.3 Proposed PMMW imaging system specifications for the security and biomedical applications

Application	Security	Biomedical
Center Frequency	94 GHz	94 GHz
Bandwidth	2 GHz	2 GHz
FOV( $\theta$ )	11.4°	11.4°
Target Distance	10 m	0.5 m
Minimum Resolvable Angle ( $\alpha$ )	0.5°	0.5°
Minimum Resolvable Size	8.8 cm	4.35 mm
Equivalent System Noise Temperature	2000 K	2000 K
Integration time ( $\tau$ )	0.5 s	15 s
NETD	1.1 K	0.2 K
# of Antennas	10/Arm, 30 in total	10/Arm, 30 in total
Antenna array dimension	280 mm x 280 mm	280 mm x 280 mm

### 3.6 Summary

In this chapter, the imaging phenomenology in MMW range was studied. Background knowledge and state-of-the-art PMMW imaging systems were reviewed and compared in order to help us choose our own system's architecture and design to meet specifications for the proposed security and biomedical applications of this work. SAR was selected to be the system architecture due to its potential in achieving high-level integration, low cost, large aperture size, and better effective FOV. Successful implementation of this work would

provide one of the first opportunities to construct a SAR PMMW imaging system using MMIC. Detailed block and circuit level design will be described in Chapter 4. The measured performance and other hardware implementation related topics will be discussed in Chapter 5 and 6.

## CHAPTER 4 MMIC IMPLEMENTATION OF THE SAR PMMW IMAGING SYSTEM

### 4.1 Overview

In this chapter, the SAR PMMW imaging system proposed in Chapter 3 is implemented with silicon MMIC, using IBM BiCMOS 8HP technology. The block level specifications are first designed by considering the system level specifications developed in Chapter 3. Each block is designed and fabricated separately, followed by the final design cascading all blocks to form the 4 x 1 prototype array. The design details are presented in this chapter while the measurement methodology and results will be discussed in Chapter 5.

### 4.2 Overview of the Super-heterodyne Front-end Structure

As discussed in Chapter 3, the super-heterodyne receiver is selected for the front-end architecture. The block level diagram is shown here again in Figure 4.1 for illustrative purposes.

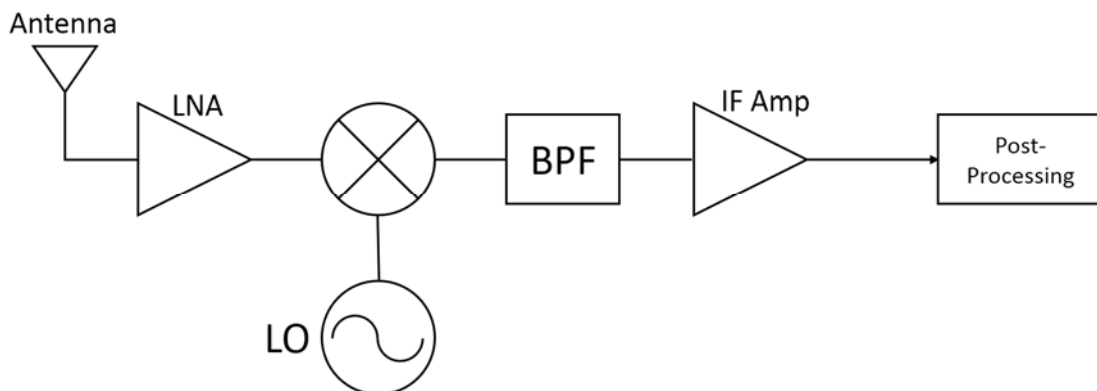


Figure 4.1 Diagram of a typical super-heterodyne receiver

There are 2 major blocks in the receiver: (1) an LNA; and (2) a down-converting mixer. Since a 4 x 1 prototype array is the final design goal, it is also necessary to include phase shifting blocks so that the output signal can be made from the combination of input signals with different phases, forming a phased-array. Through the phase switching mechanism, a simple interferometer can be implemented with two, three or four-elements. The proposed array block diagram is shown in Figure 4.2. In this proposed architecture, two stages of power combining are performed, generating one output at IF frequency from four RF input signals. It would be more power efficient if we could simply replace the combiner at the second stage with a coupler [PON03], [CHI06], which outputs the summation of two input signals as well as their difference. This gives us another degree of freedom, which swaps one input's phase between  $0^\circ$  and  $180^\circ$ . The resulting structure's diagram is shown in Figure 4.3.

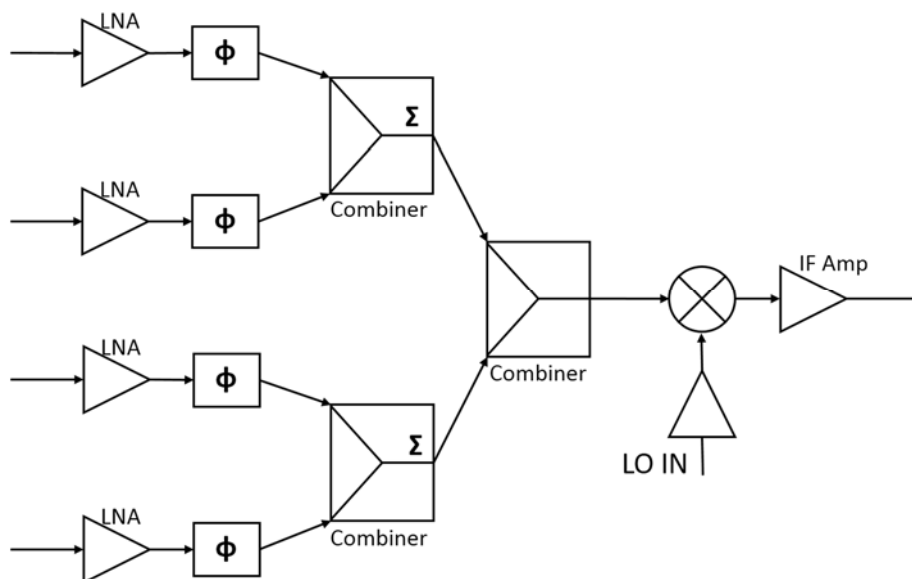


Figure 4.2 Diagram of the proposed 4 x 1 prototype array

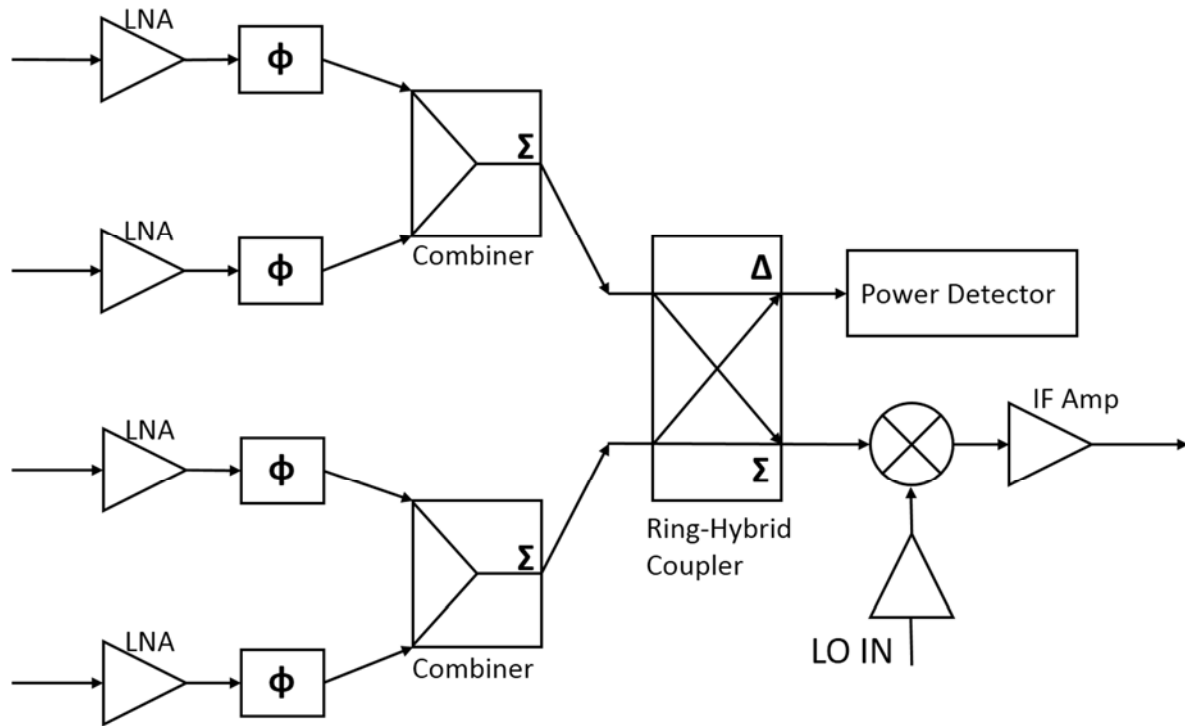


Figure 4.3 Diagram of the actual 4 x 1 prototype array

In the new structure, the circuit components that need to be designed include:

- LNA at 94 GHz
- Phase shifter at 94 GHz
- Down-converting mixer (including LO input buffer and IF output amplifier)
- Power detector
- Wilkinson power divider/combiner at 94 GHz
- Ring-hybrid coupler at 94 GHz

### 4.3 Implementation of Individual Components

#### 4.3.1 Low Noise Amplifier

##### 4.3.1.1 State-of-the-Art LNA & Proposed Specifications

In this section, some of the most recently designed LNAs will be compared to provide context for ideal LNA performance and to be used as a reference and performance benchmark for our work. Table 4.1 summarizes the performances that were reported since 2008. Although different semiconductor technologies were used, we can still make valuable comparisons between them.

Table 4.1 Comparison of recently reported LNA at around 94 GHz.

Source	Topology	Technology	Freq (GHz)	Gain (dB)	NF (dB)	Power
[SEV10]	1 Cascode	130 nm SiGe	94.7	9	8.6	13 mW
[WIN08]	2 Cascode	250 nm SiGe	94	16.2	10.6	61 mW
[MAY09]	5 CE	120 nm SiGe	98	23	8**	1.2V/29 mA
[POW08]	2 Cascode	130 nm SiGe	90	22	7	56 mW
[OJE08]	3 Cascode	250 nm SiGe	94	15	11.3**	3.3V/28 mA
[ALV08]	1 Cascode	120 nm SiGe	91	13	5.1	8.1 mW

\*\*Simulated NF, experimental results were not reported.

In all of these 6 LNA designs, only very common low-noise topologies are used, such as cascode and common-emitter (CE). Both single- and multi-stages have been utilized. Gain varies from 9 dB with single stage, to as high as 23 dB with five cascaded CE stages. For a super-heterodyne receiver, a low-noise performance is more important than gain, since IF stages can easily contribute over 50 dB of gain, thus design as seen in [ALV08] is very suitable for super-heterodyne receivers. On the other hand, May *et al* reported an LNA with a

gain of 23 dB while the NF still controlled around 8 dB, making it a good choice for the front-end of a system which needs high sensitivity [MAY09]. The noise factor (F) of a cascaded system is described in Eq. 4.1

$$F_{TOT} = F_1 + \frac{F_2 - 1}{G_1} + \frac{F_3 - 1}{G_1 G_2} + \frac{F_4 - 1}{G_1 G_2 G_3} + \dots + \frac{F_n - 1}{G_1 G_2 G_3 \dots G_{n-1}} \quad (4.1)$$

where  $F_n$  and  $G_n$  denote the noise factor and gain of the  $n^{\text{th}}$  component. In a well-designed system, only the F of the first component should be significant, which means the LNA sets the Signal-to-Noise Ratio (SNR) of the receiver and subsequent blocks do not degrade SNR. It was designed in Section 3.5.2, that our system NF would be 9 dB, giving a  $F_{TOT} = 8$ . If our LNA has an NF of 8 dB and gain of 23 dB, which matches the performance described in [MAY09],  $F_1 = 6.3$  and  $G_1 = 199.5$ , giving an  $F_2$  as large as 340, or  $NF_2 = 25$  dB, which is much higher than the typical NF of silicon 94 GHz mixers. Even if  $NF_1 = 8.5$  dB,  $NF_2$  can still be 22.4 dB. To implement this system, the very first component, the LNA, is designed to have the following specifications: center frequency = 94 GHz, Gain = 23 dB and  $NF < 8$  dB. Other characteristics such as bandwidth and power consumption are not set to a target. But bandwidth for the LNA needs to be as wide as possible in order for maximum power to be delivered to the detection circuits, while power consumption needs to be as low as possible (even at the expense of trading off for some gain), since the scalability of the system must be taken into account. In future developments, the number of front-end element could reach 64 or more, therefore lower power consumption for the LNA is favorable.

#### 4.3.1.2 Design of a 94 GHz LNA

To design the LNA with the target specifications suggested in the previous section, the following design steps were used [FLO06]:

1. Simulate noise measurement (NM) vs. collector current density ( $J_C$ ) to choose the optimal range of  $J_C$ ;
2. Scale the emitter length such that  $R_{opt} = 50 \Omega$  (increase the emitter length to reduce  $Z_{opt}$ );
3. Add an emitter degeneration inductor to create a real input impedance for power match;
4. Complete the input match with transmission lines.

In order to obtain the lowest possible noise, a traditional CE topology was chosen. Six similar CE stages were cascaded in order to achieve a gain higher than 20 dB, although early stages were tuned in favor of low noise and later stages for increased gain. Several other techniques were applied during the design of the LNA:

1. *Current Reuse*: As shown in Figure 4.4, the 6 stages were divided into three groups. Each group contains two stacked-CEs. The 2.5 V supply voltage can be equally distributed to each stage, making each stage use 1.25 V DC supply. Although it appears to be a single cascode stage, the output of the lower transistor is not connected to the emitter of the top one. The lower transistor's collector will be connected to a load and the other end of the load is an AC

ground, making it a pure CE. This lower CE's output will be routed to the base of the higher transistor.

2. *Staggered Tuning*: For the application of millimeter-wave imaging, the target may emit power within a wide range of frequencies near, though not specifically at 94 GHz. Therefore a flatter frequency response of gain within the band is more desirable. Each amplifier stack was targeted to a different center frequency: the first stack for 88 GHz, the second for 94 GHz and the last stack for 100 GHz. With this technique, a 3 dB bandwidth of over 22 GHz was achieved in simulation.

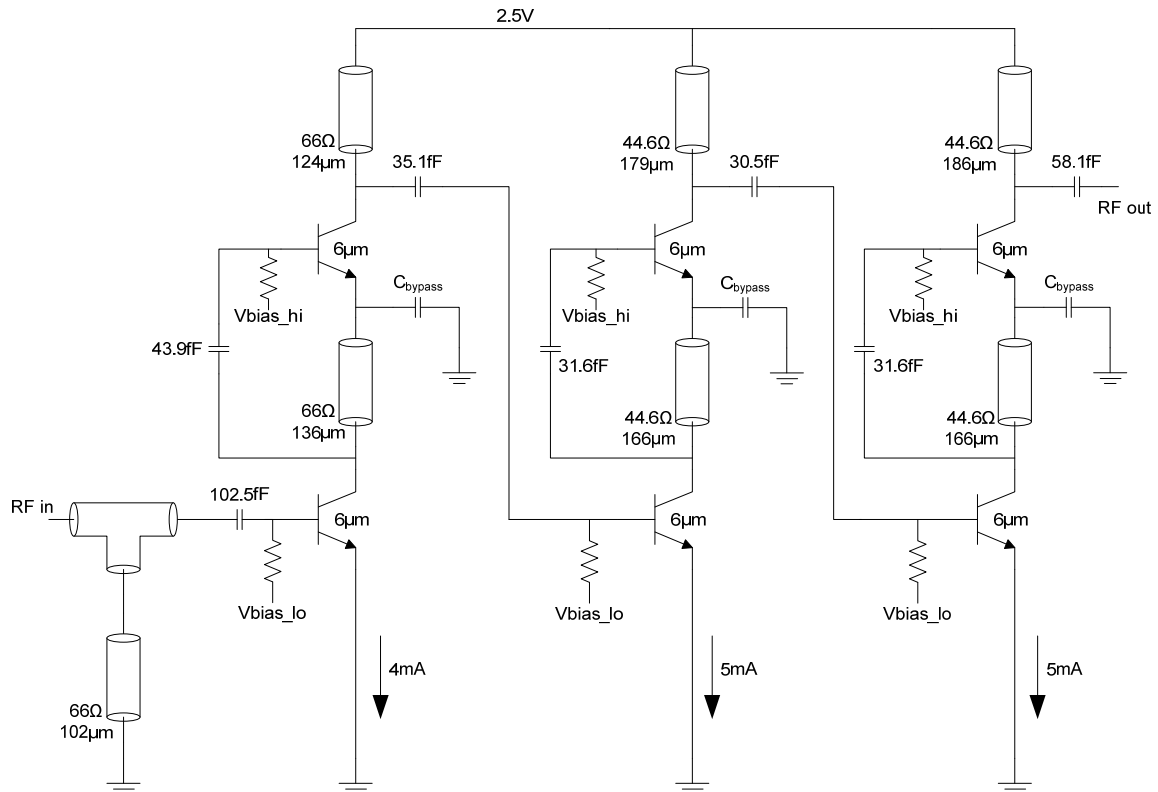


Figure 4.4 Schematic of a 6-stage 94 GHz LNA

Figure 4.5 shows the LNA layout view. The total size of the LNA, including bond pads is  $635 \times 581 \mu\text{m}^2$ . In simulation, a peak gain of 26 dB, with 3d B bandwidth of 23 GHz (82.5-105.5 GHz) was achieved. The simulated NF reaches a minimum at 93.2 GHz for 7.7 dB, while from 83.7-104.6 GHz, the NF is below 8 dB. Both input and output ports are matched to  $50 \Omega$ . A layout with SiGe BiCMOS 8HP 130 nm technology was also designed for the schematic. Due to the unavoidable parasitic capacitance and inductance, slightly degraded but more practical results were obtained and presented below.

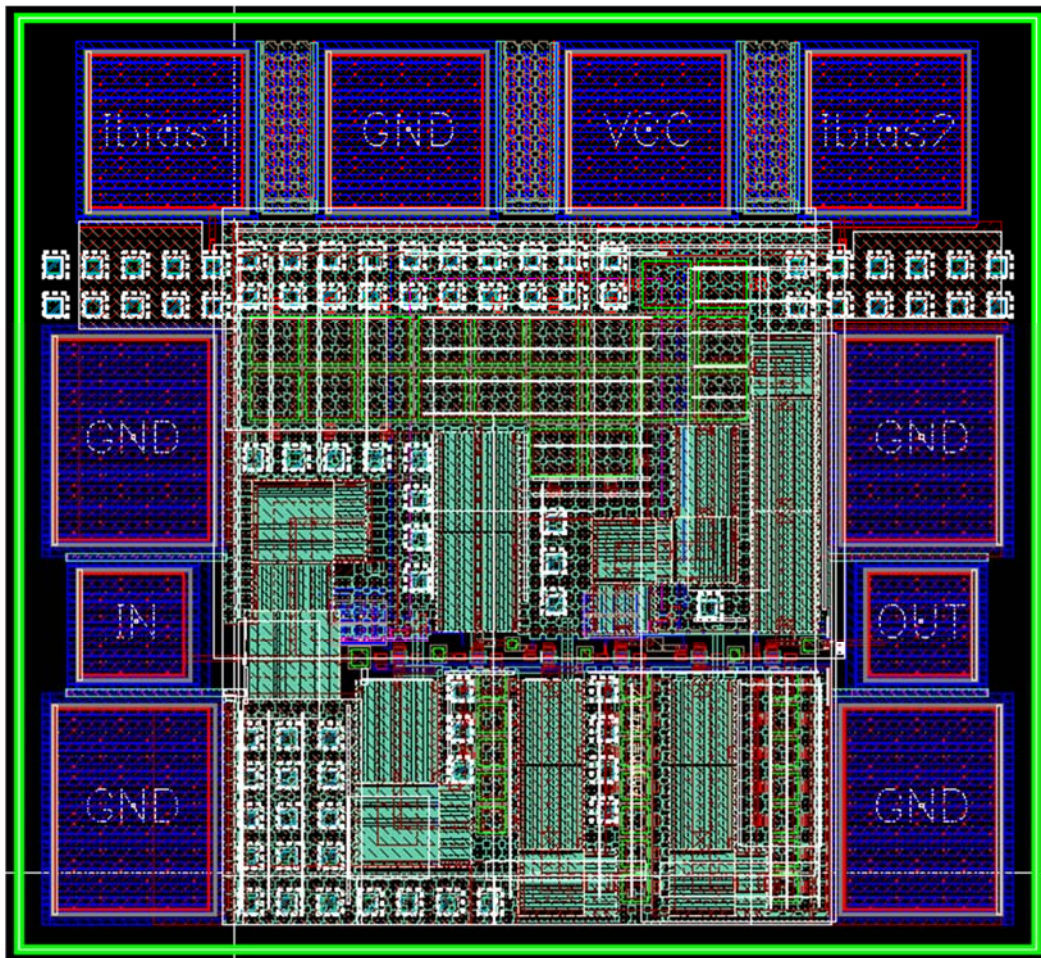


Figure 4.5 Layout view of the 94 GHz LNA (kit v1.2.0.1)

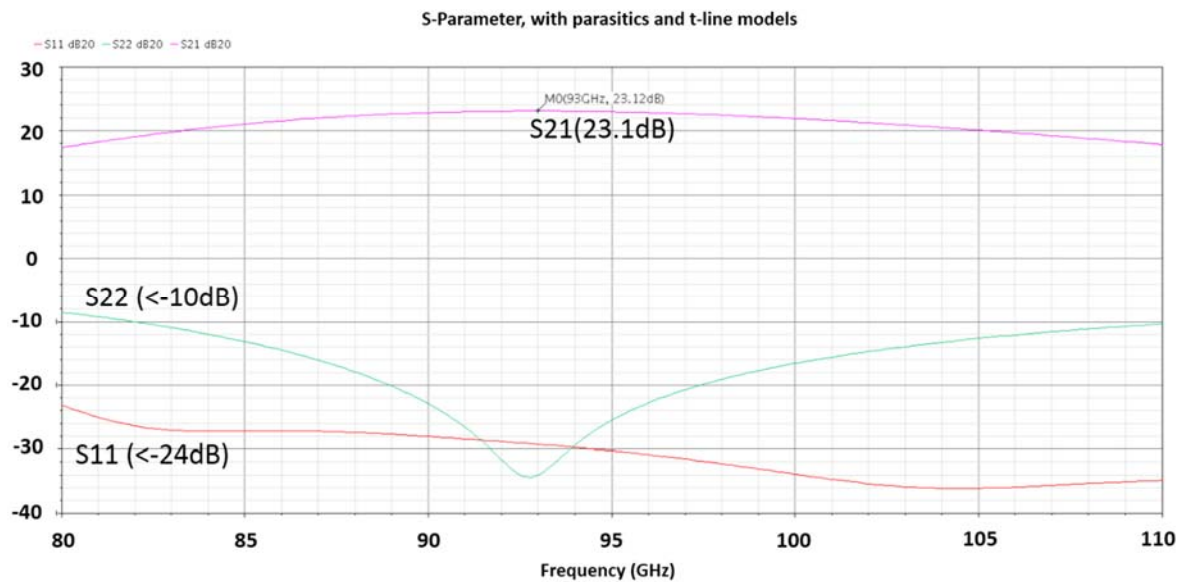


Figure 4.6 Simulated S-Parameter of the 94 GHz LNA (with parasitics, kit v1.2.0.1)

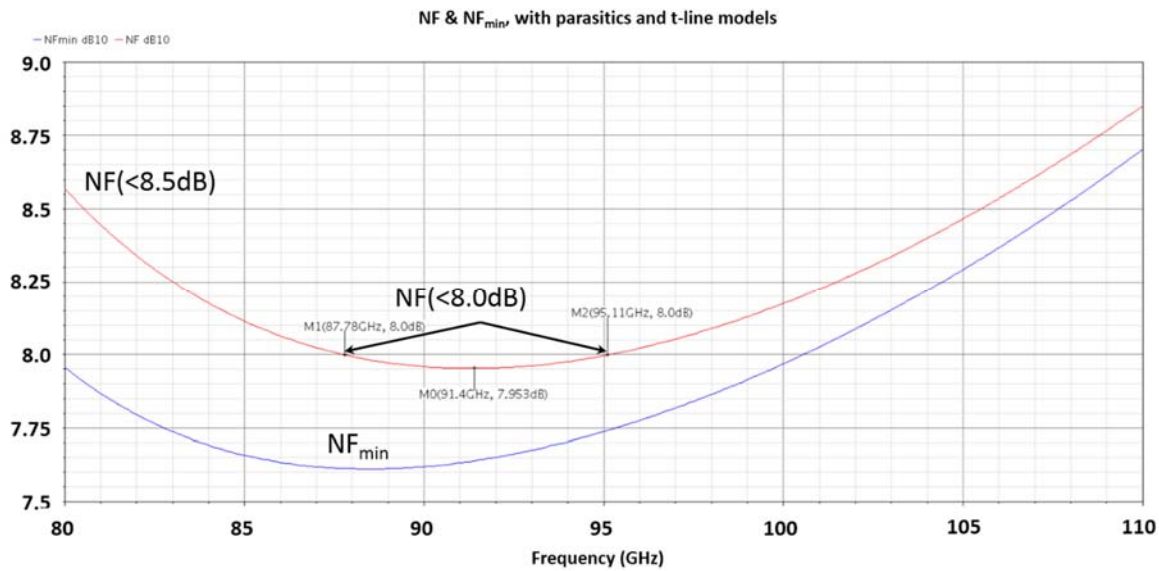


Figure 4.7 Simulated NF of the 94 GHz LNA (with parasitics, kit v1.2.0.1)

In summary, the post-layout LNA has a 23.1 dB peak gain at 93 GHz, with a 3d B bandwidth from 83-105 GHz. NF of less than 8 dB was achieved from 87.8-95.1 GHz, a 7.3 GHz span. Both the input and output ports are well matched, with a reflection coefficient below -10 dB. The LNA consumes 36.6 mW of power and is operating in an unconditionally stable manner (simulated from 1 GHz to 1 THz for stability).

#### 4.3.2 Phase Shifter at 94 GHz

A 4-bit (16-state) active phase shifter was designed by Mr. Kevin Greene, a research assistant within Prof. Brian Floyd's research group. The phase shifter was realized using a vector-interpolator topology, very similar to that described in [SAR14]. A single-ended input signal is passed through a quadrature Lange coupler, followed by a balun to obtain differential quadrature signals and achieve a  $360^\circ$  phase shift range. The schematic of the phase shifter is shown in Figure 4.8.

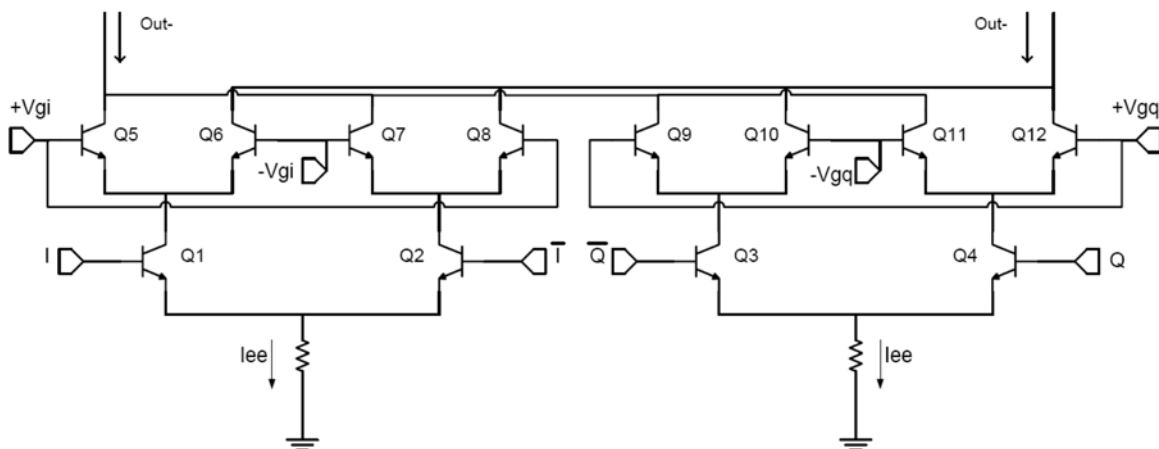


Figure 4.8 Gilbert cell architecture for use as a vector interpolator

The bottom four transistors (Q1-Q4) are controlled by the RF differential quadrature inputs:  $I$ ,  $\bar{I}$ ,  $Q$  and  $\bar{Q}$ . These were generated using a passive differential quadrature hybrid coupler. The DC current through these transistors is held constant (*i.e.* tail current  $I_{ee}$  is constant). This reduces the change in input impedance for different phase settings, eliminating the need for buffer between the input hybrid coupler used to generate quadrature signals and the vector interpolator. Instead of adjusting the current through  $I$  and  $Q$  branches, the current is steered in the top transistors (Q5-Q12) using control voltages  $V_{gi}$  and  $V_{gq}$ . One drawback of this design is the current consumption. For example, if the phase setting is 0 degrees even though only the  $I$  path is necessary for the output vector, the  $Q$  path will still be consuming power, though its current is equally split between Q9-Q12, causing no  $Q$ -current to flow into the output load [FLO12]. Simulation results are illustrated in Figure 4.9 to 4.11.

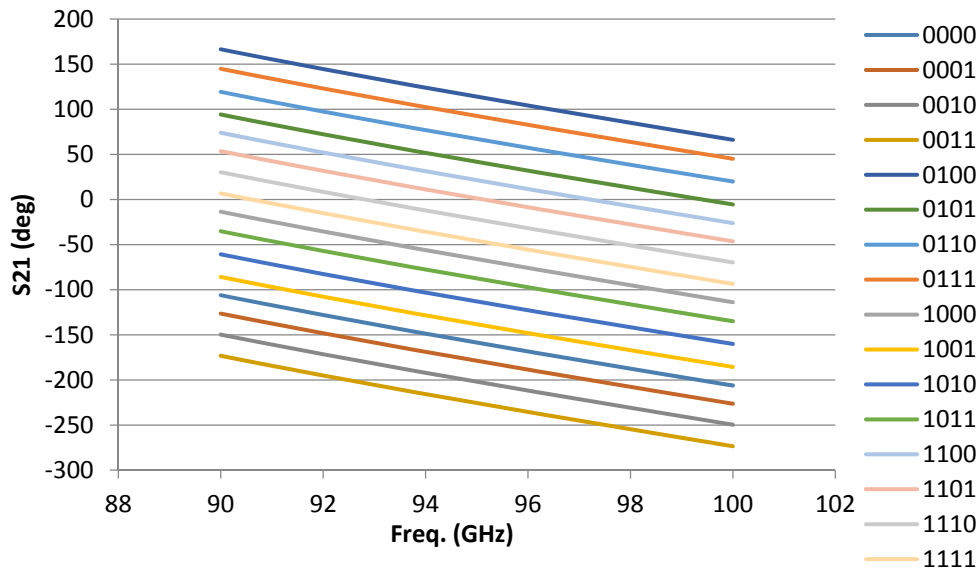


Figure 4.9 Simulated S21 of the 94 GHz phase shifter, capable of 360° phase shifting (with parasitics, kit v1.3.0.3)

Figure 4.9 shows the phase shifter is able to cover 360° phase shift by the 4 controlling bits. The input port is well matched, while the output port has some slight mismatch from 50 Ω Z<sub>o</sub>, as shown in Figure 4.10. There is a conversion loss of about 7 dB and a 17.5 dB NF (with variance among phase settings).

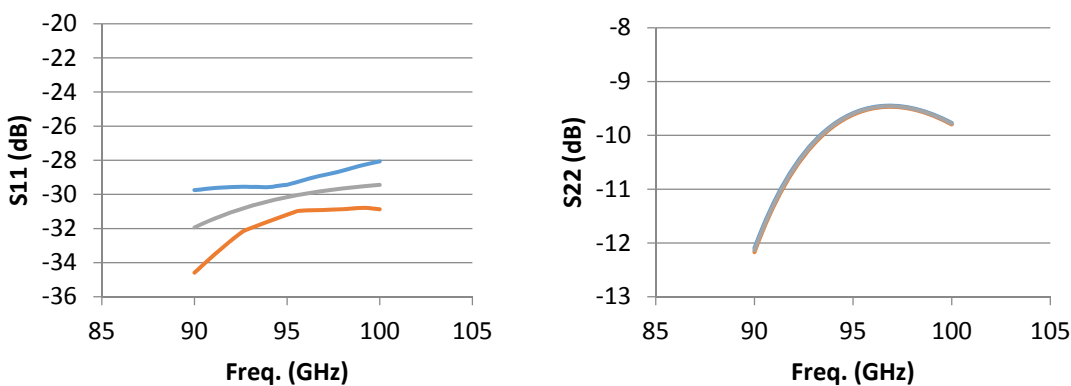


Figure 4.10 Simulated input and output matching of the 94 GHz phase shifter (with parasitics, kit v1.3.0.3)

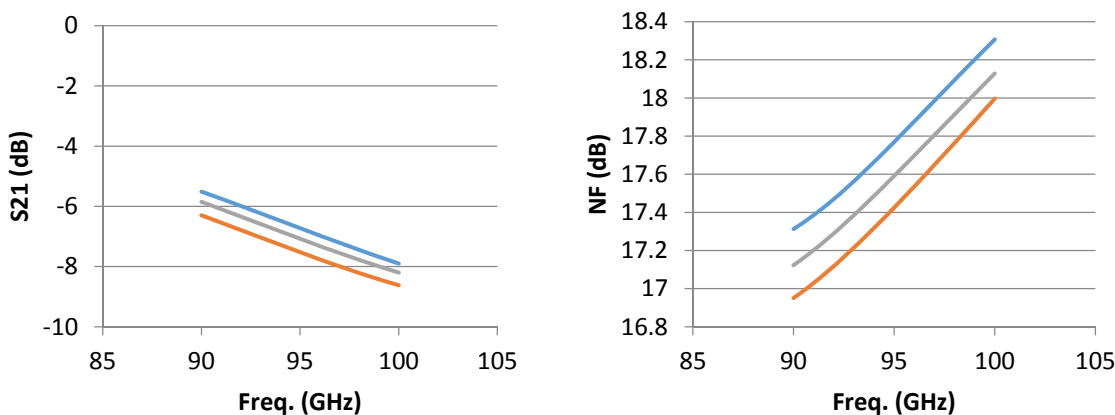


Figure 4.11 Simulated conversion loss and NF of the 94 GHz phase shifter (with parasitics, kit v1.3.0.3)

### 4.3.3 94 GHz to 18.8 GHz Down-Converting Mixer

During the design of the 94 GHz down-converting mixer, two papers were referred to as benchmarks, [REY06] and [OJE08]. Their performance is summarized in Table 4.2. Both mixers are able to obtain more than 15 dB conversion gain, while achieving less than 17.5 dB SSB NF. Although the mixer reported by Reynolds *et al* [REY06] appears to have inferior performance in gain and NF than that by Öjefors *et al* [OJE08], it does operate at a higher IF frequency. For our imaging application, we want an IF bandwidth of at least 2 GHz. To make it more realizable, assuming 10% bandwidth, we choose our mixer's IF frequency to be around 19 GHz, which is approximately 1/5th of the RF frequency, 94 GHz. The single-balanced Gilbert Cell topology was selected since there is no need to avoid RF feed-through to reject image signals (with a 94 GHz RF and 75 GHz LO, the image signal would be at 56 GHz, which will be naturally filtered by the matching networks). The single-balance topology also significantly facilitates the layout process.

In addition to the single-balance mixer core, there are other components included in the whole circuit to be considered for a mixer, such as an LO Buffer with balun and IF variable gain amplifier (IFVGA). The design details are described in the following subsections.

Table 4.2 Comparison of two 94 GHz-input mixers for PMMW imaging applications

Source	I/O (GHz) Frequency	S/D Balanced	Conversion Gain	SSB NF (dB)	1dB Compression
[REY06]	94/8.8	Single Balanced	15 dB	17.2	-10.7 dBm
[OJE08]	94/2	Double Balanced	20 dB	15	-31 dBm

### 4.3.3.1 LO Buffer

The LO Buffer is designed to drive the LO inputs of the mixer. In our measurement setup, not enough LO power could be directly generated (details explained in Chapter 5), and for the mixer to work in its maximum conversion gain region, this LO buffer is used to supply enough swing at the mixer LO to be multiplied with the RF current produced by the transconductance transistor. An ordinary cascode topology was used and the bipolar devices were biased similarly to an LNA, however they tend to have slightly higher current density, since more gain is desirable. The schematic of the LO buffer is shown in Figure 4.12, while the simulation results are presented in Figure 4.13 to 4.16 and summarized in Table 4.3.

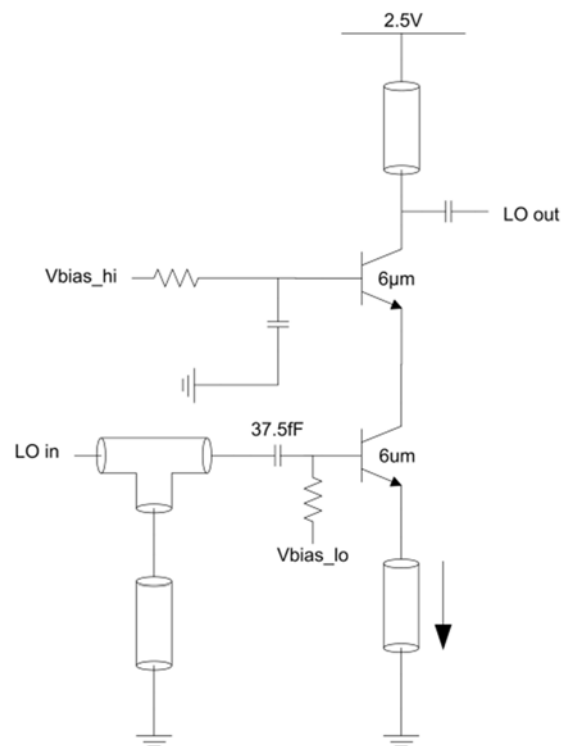


Figure 4.12 Schematic of the LO buffer

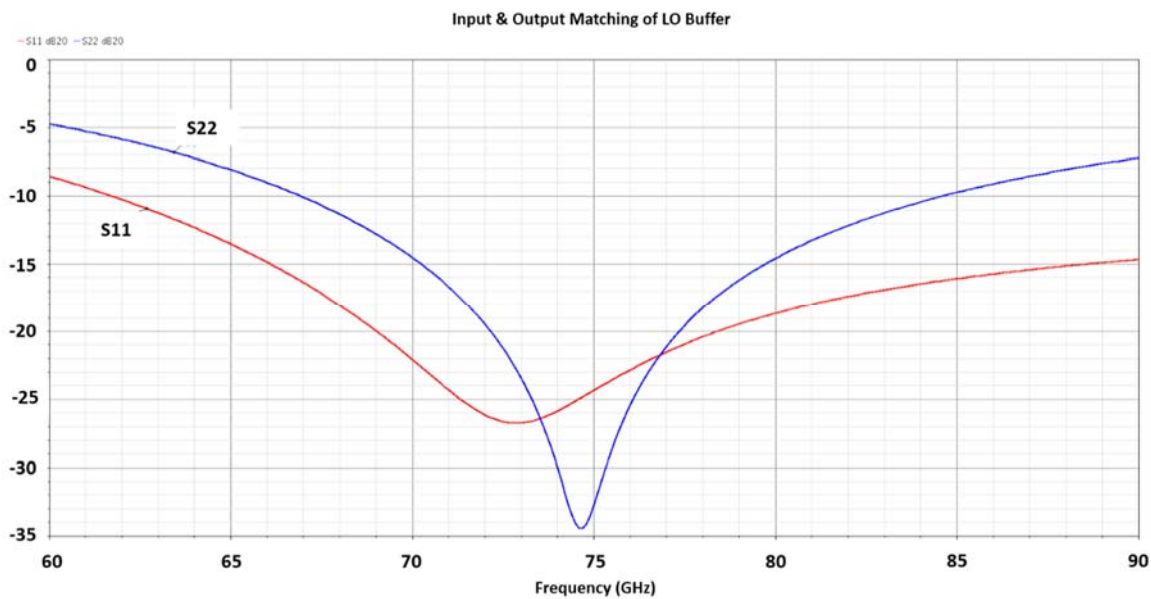


Figure 4.13 Simulated input and output matching for the LO buffer (with parasitics, kit v1.3.0.3)

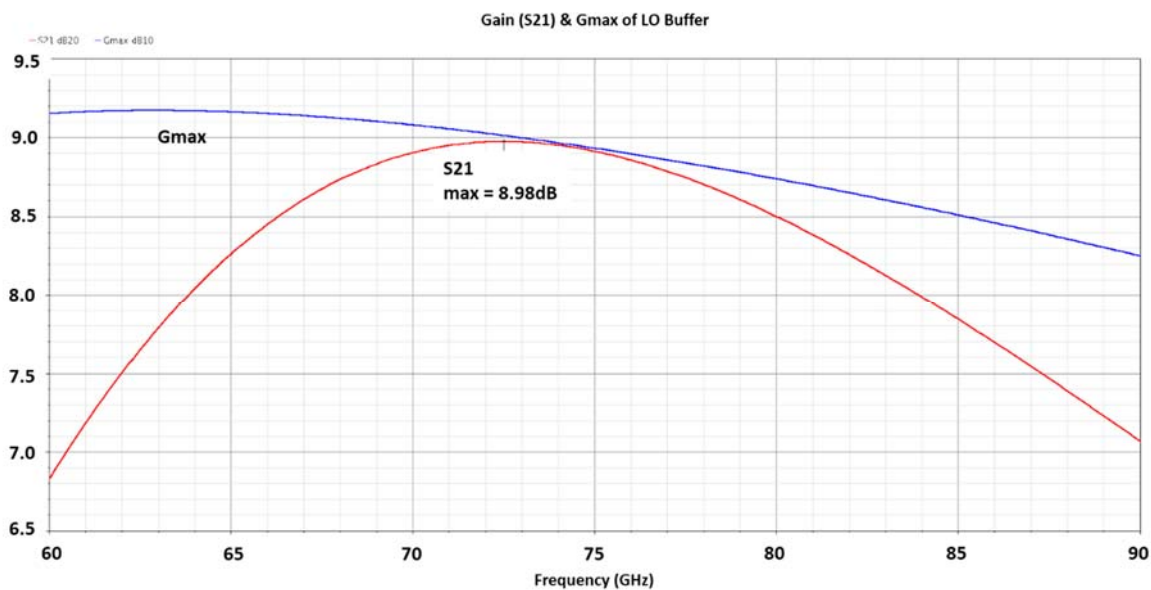


Figure 4.14 Simulated Gain & Gmax of the LO buffer (with parasitics, kit v1.3.0.3)

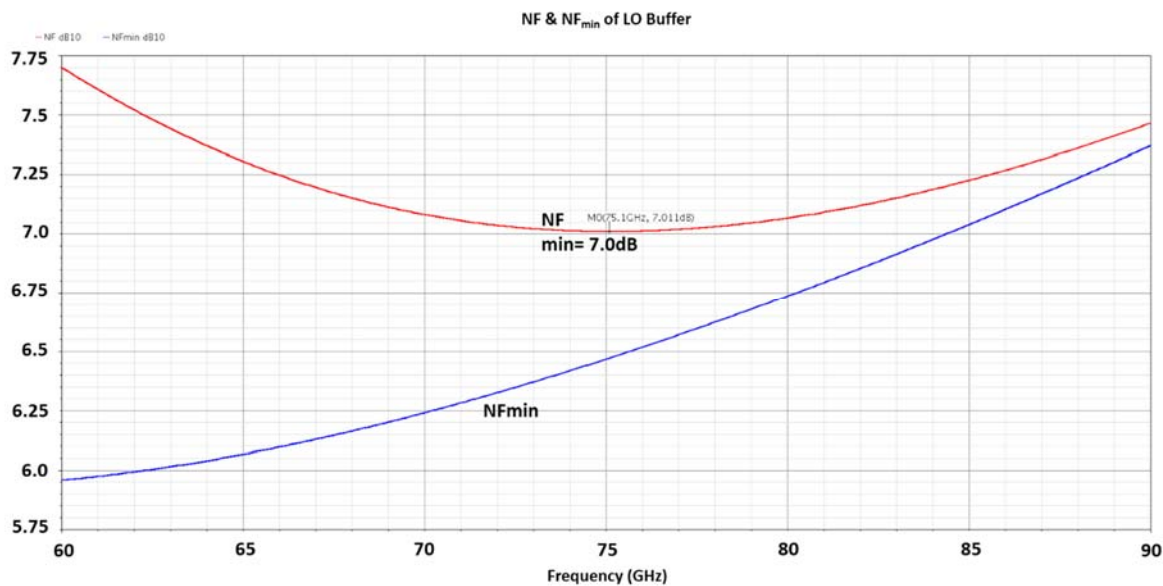


Figure 4.15 Simulated NF & NFmin of the LO buffer (with parasitics, kit v1.3.0.3)

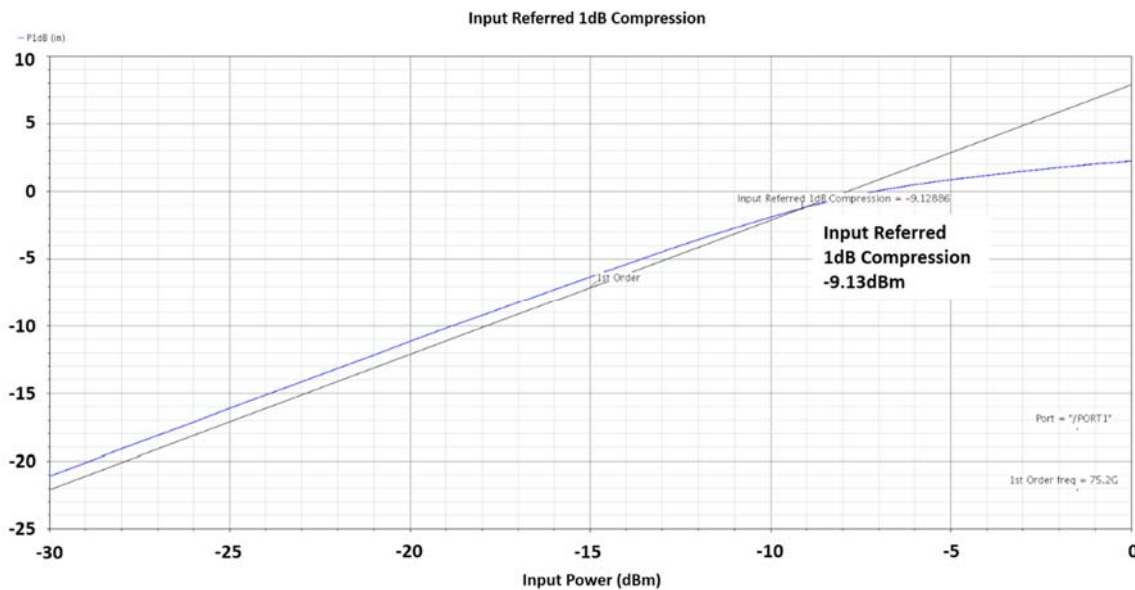


Figure 4.16 Simulated linearity, input referred 1-dB compression point of the LO buffer (with parasitics, kit v1.3.0.3)

Table 4.3 Performance summary of the LO buffer at 75.2 GHz

Frequency	75.2 GHz
Gain	9 dB
3 dB BW	Within 3 dB across 60-90 GHz
NF	7 dB minimum @ 75 GHz, <7.5 dB across 62-92 GHz
P1dB (in)	-9.12 dBm

#### 4.3.3.2 IFVGA

A differential IFVGA is designed at the output of the mixer to increase the conversion gain. Since the operating frequency is at 18.8 GHz, which is much lower than the RF frequency at 94 GHz, the initial design used many inductors in matching networks and also the load, rather than the use of transmission lines in 94 GHz circuits. Also it utilized a pre-distortion circuit for conditioning of the control voltage to make the IFVGA gain linear-in-dB versus the control voltage. We found it extremely difficult, however, to lay the components out due to excessive use of inductors as well as the increased design complexity from the pre-distortion, whose function is not a crucial part of the block. Therefore the IFVGA was re-designed, targeting a higher gain and a better port matching mechanism with the mixer core output. The size of the transistors were chosen in consideration not only for the performance in gain and noise, but also the matching between stages so that the least amount of inductor and transmission lines needed to be used in order to keep the layout condensed, consequently reducing the parasitics.

The schematic of the IFVGA is shown in Figure 4.17. It was implemented in a very similar way to a double-balanced mixer, while the bottom two transistors act as the

transconductance, converting the input IF voltage to a current. There are four identical transistors on top, forming the outer pair and the inner pair. The outer pair is biased by a fixed DC voltage, ( $V_{bias\_hi}$ ) and has no load component, while the inner pair is biased by the gain-controlling voltage ( $V_{agc}$ ) and is loaded by a symmetric inductor of 833 pH inductance. When  $V_{agc}$  is less than  $V_{bias\_hi}$ , current in the branches is steered into the outer pair of transistors, causing attenuation to dominate the circuit. While  $V_{agc}$  is larger than  $V_{bias\_hi}$ , current steers back to the inner pair, and the IFVGA acts like a differential cascode amplifier. Therefore  $V_{agc}$  controls the amount of current steered into the outer and inner branches. Consequently, it controls the gain of the circuit.

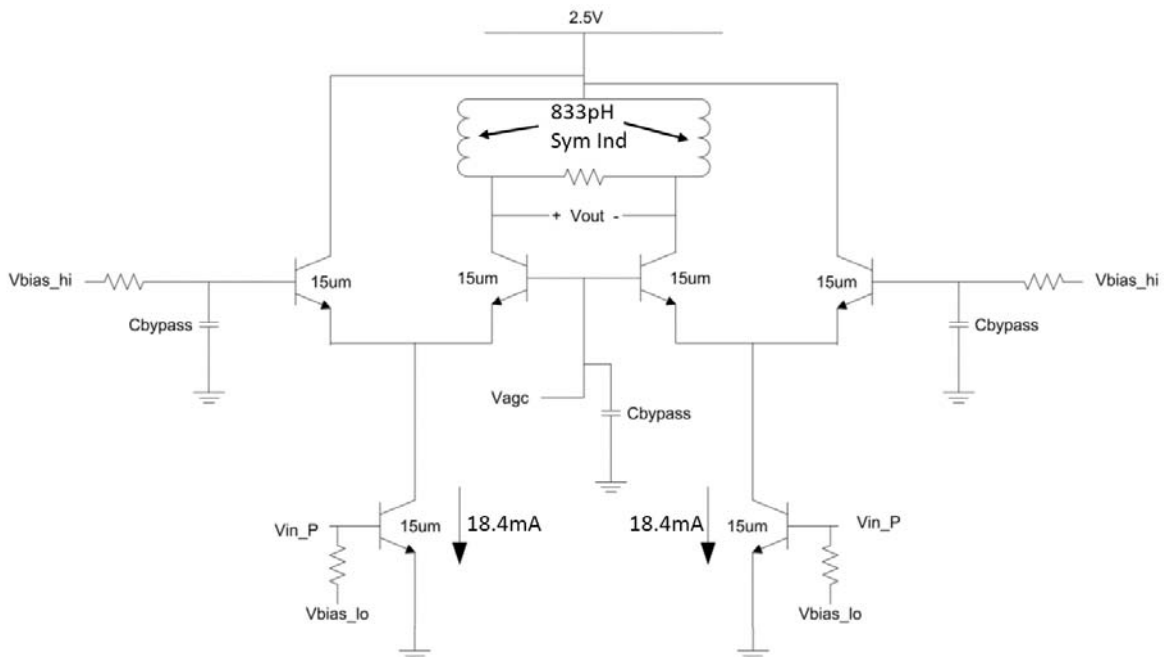


Figure 4.17 Schematic of the IFVGA

The IFVGA alone is able to achieve a controllable range of gain from -20 dB to 20 dB, while at a maximum gain setting, it reaches an 8.2 GHz 3 dB bandwidth. NF across the bandwidth is below 3 dB. Simulation results of gain, NF and linearity are presented in Figure 4.18 to 4.20 and the standalone specifications are summarized in Table 4.4

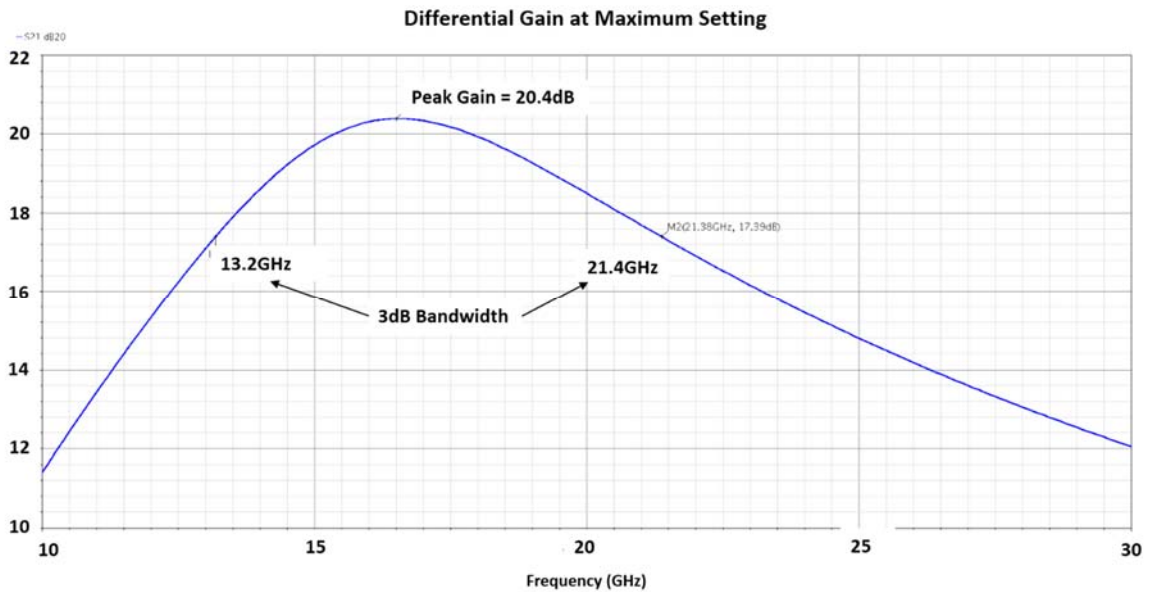


Figure 4.18 Simulated gain of the IFVGA (with parasitics, kit v1.3.0.3)

Table 4.4 Performance summary of the IFVGA at 18.8 GHz

Frequency	18.8 GHz
Gain vs. $V_{agc}$	-20 dB to 20 dB ( $V_{agc}$ varies from 0 V to 4 V)
3 dB BW	13.2 – 21.4 GHz
NF	<3 dB whole bandwidth
P1dB (in)	-13.17 dBm

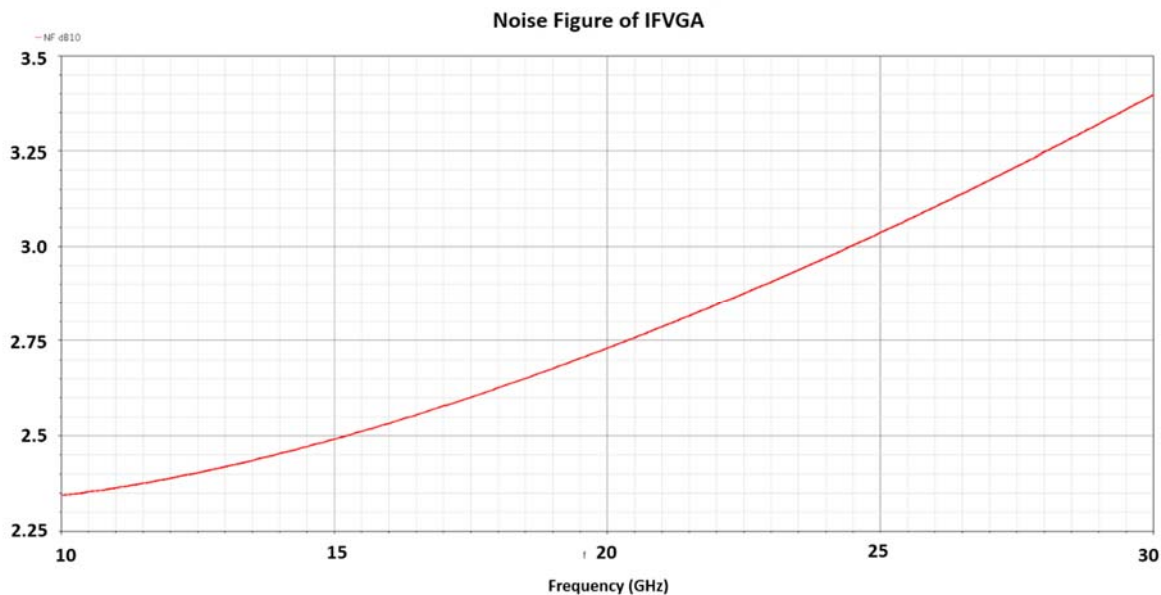


Figure 4.19 Simulated NF of the IFVGA (with parasitics, kit v1.3.0.3)

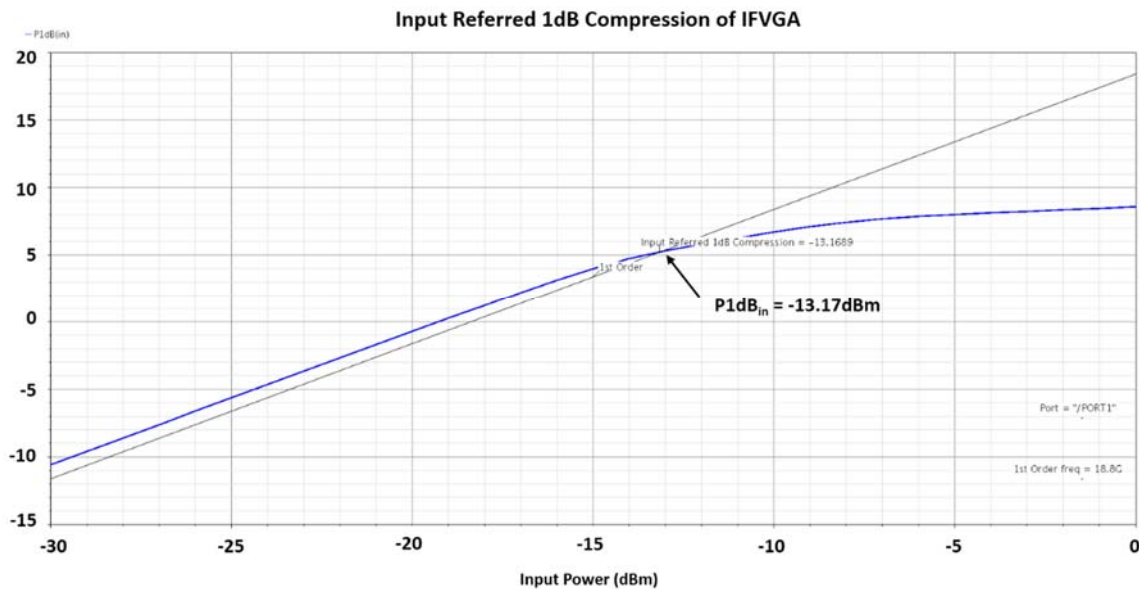


Figure 4.20 Simulated linearity: input referred 1-dB compression point of the IFVGA (with parasitics, kit v1.3.0.3)

#### 4.3.3.3 Single-balanced Gilbert Cell Mixer

At the beginning of Section 4.3.3, it was explained why a single-balanced Gilbert Cell was selected for the topology. The design was initially implemented with a symmetric inductor (SymInd) at the top transistor pair's collector node to save space. One SymInd acts like two inductors sharing one common node. However, for the sake of the circuit symmetry (due to its differential nature), the SymInd needs to be put at the center of the mixer core, resulting in very long wires routing around it to pass the output signal to the IFVGA. Therefore, the initial design was abandoned and the SymInd was replaced by two identical inductors in the final design as shown in Figure 4.21. As a result, the parasitic capacitance and inductance caused by long wires was eliminated.

#### 4.3.3.4 Mixer Assembled and Simulation Results

With all the aforementioned components, the 94 GHz to 18.8 GHz down-converting mixer was assembled. A Marchand balun was used to convert the single-ended output of the LO buffer to a differential signal needed to drive the mixer. This balun was designed by Mr. Kevin Greene using the simulation tool, Sonnet. The balun's EM simulation results are shown in Figure 4.22.

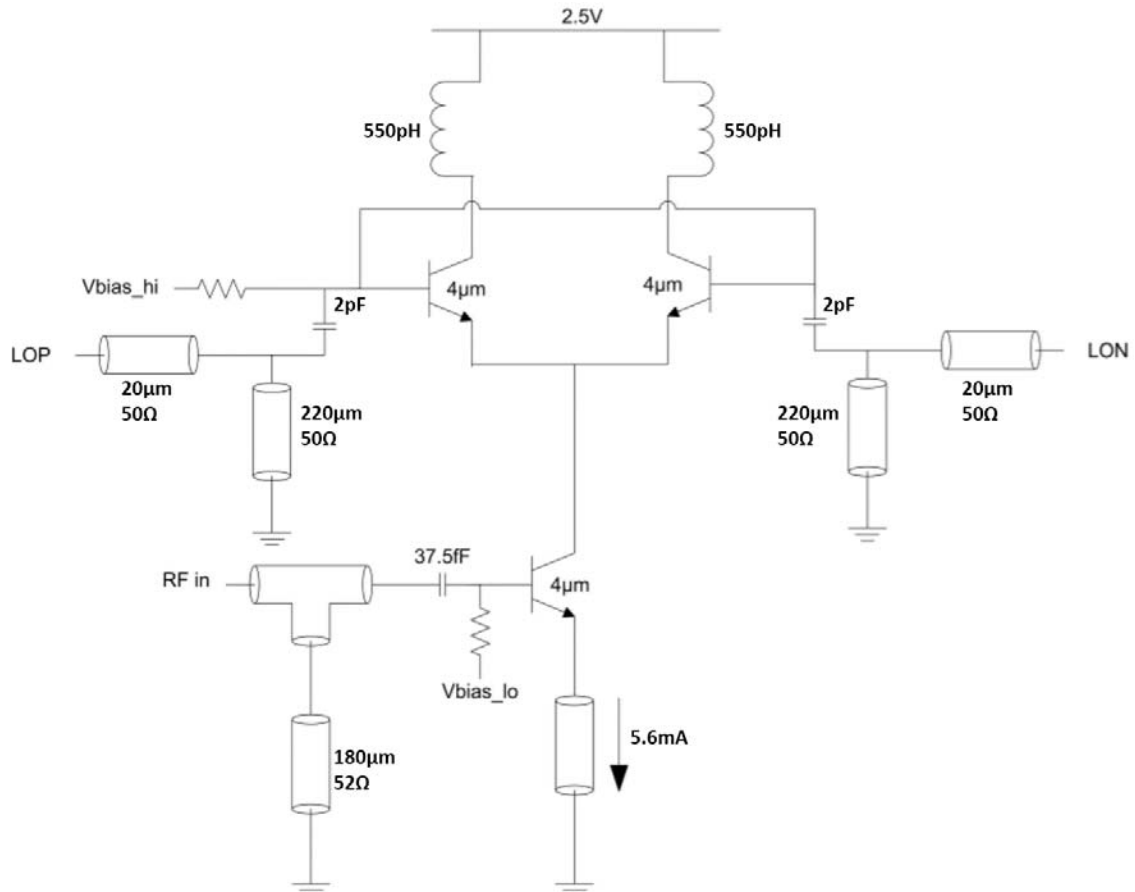


Figure 4.21 Schematic of the single-balanced Gilbert cell mixer

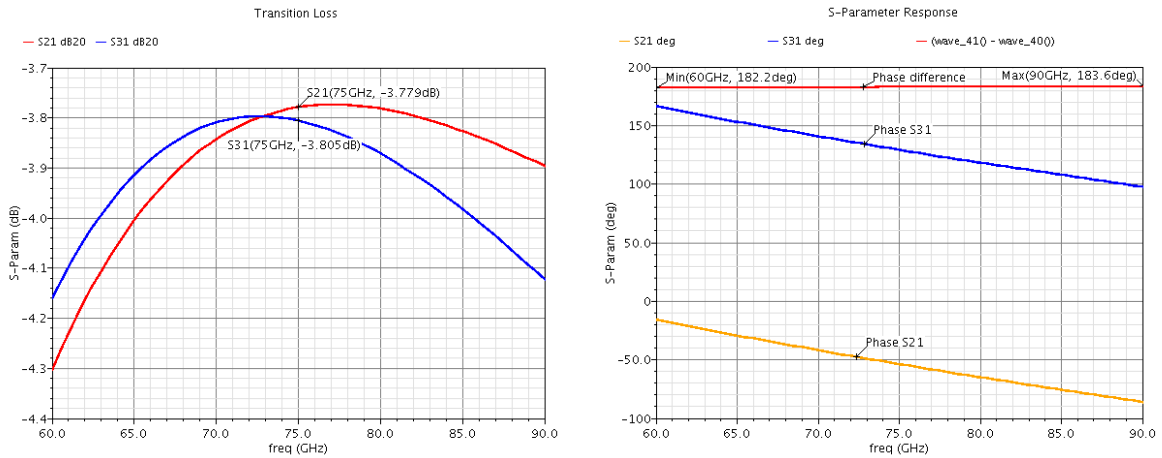


Figure 4.22 Forward transmission coefficients S21 and S31: (left) magnitude, (right) phase (with parasitics, kit v1.3.0.3)

The structure of the Marchand balun is designed according to the actual layout profile of other components. With less than 0.1 dB in gain difference from the balanced and the unbalanced side, an almost constant phase difference between the differential outputs of approximately  $183^\circ$  can be achieved, making this design a very good fit for the work. Figure 4.23 shows the final tape-out version of the down-converting mixer, which consumes an area of  $800 \times 770 \mu\text{m}^2$ .

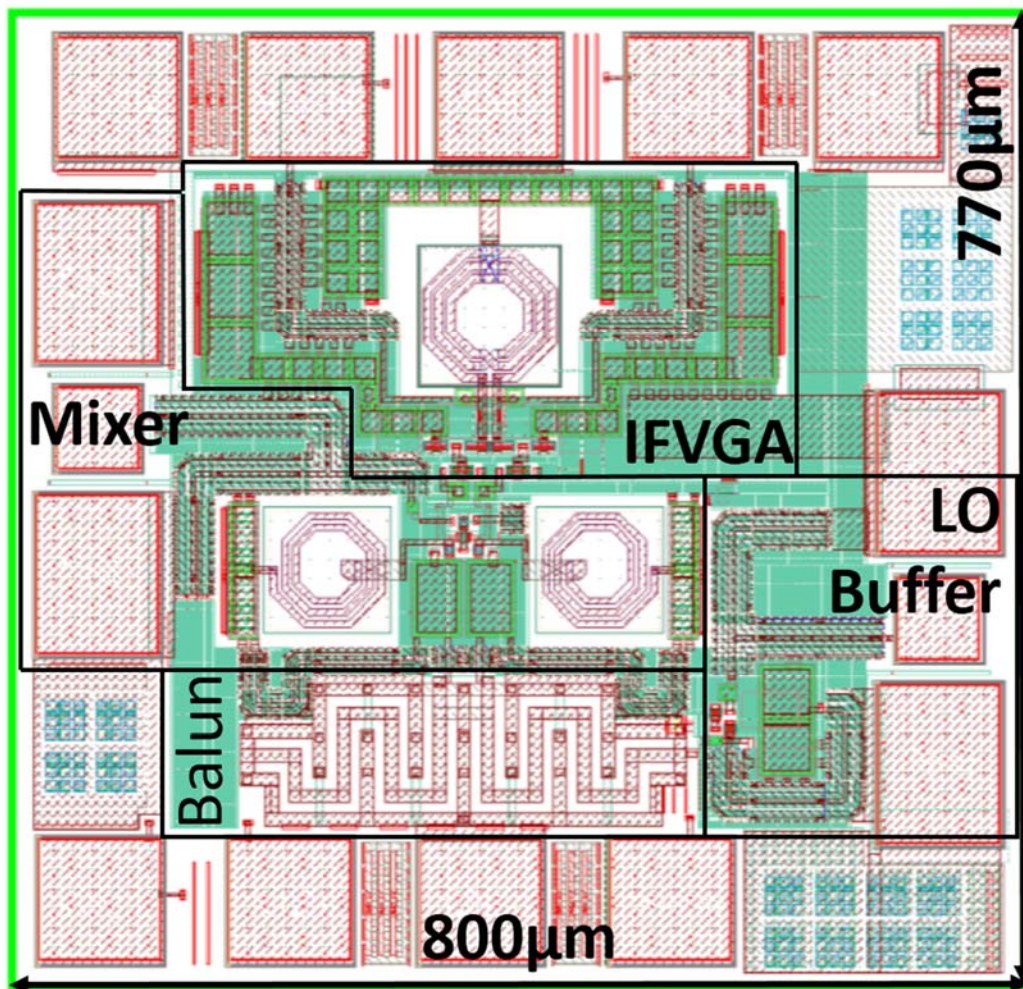


Figure 4.23 Layout view of the down-converting mixer tape-out

Simulation results with all parasitics considered are summarized in the Table 4.5. Also included, is a comparison between this work and the work of Reynolds *et al* [REY06]. All simulation results of the completed mixer circuit are plotted from Figure 4.24 to Figure 4.27.

Table 4.5 Comparison of the performance between this work and that of Reynolds *et al*

Specification	[REY06]	This Work
IF Frequency	8.8 GHz	18.8 GHz
NF	16.6-17.7 dB (89-97 GHz)	15-17 dB (84-107 GHz)
Conversion Gain	5 dB (for Mixer) Total 15 dB (mixer + VGA)	20.23 dB peak @ 92.2 GHz input 3 dB BW (89.3-95 GHz = 5.7 GHz)
P1 db (input)	-10.7 dBm	-12.1 dBm
Power Consumption	3 V 120 mA (mixer + VGA)	2.5 V 40.25 mA (LO + mixer + VGA)

From the end-to-end simulation results, it can be observed that a 5.7 GHz IF bandwidth was achieved, while the original pre-layout result was wider than 8 GHz. The loss of bandwidth is caused by parasitics and also the difficulty in matching the output of the IFVGA to the 100  $\Omega$  differential, in order to mimic the actual measurement environment. However both RF and LO have achieved a really wideband matching.

In noise performance, the mixer achieves a minimum of 15 dB at 20.6 GHz, while across the whole bandwidth, the NF is well below 16.6 dB, which is the minimum NF from Reynolds's work. To reach a higher gain, a relatively high current density and large bipolar device was used in the IFVGA, making our final conversion gain 5 dB higher than

Reynolds's work at the 20.23 dB peak, although we did sacrifice the linearity to achieve this. Since our input signal power at 94 GHz is expected to be lower than -35 dBm, and our front-end LNA and phase shifter have a combined gain of less than 20 dB, the mixer is sure to perform in the linear region. Simulation results of the mixer break-out are shown in Figure 4.24 to 4.27.

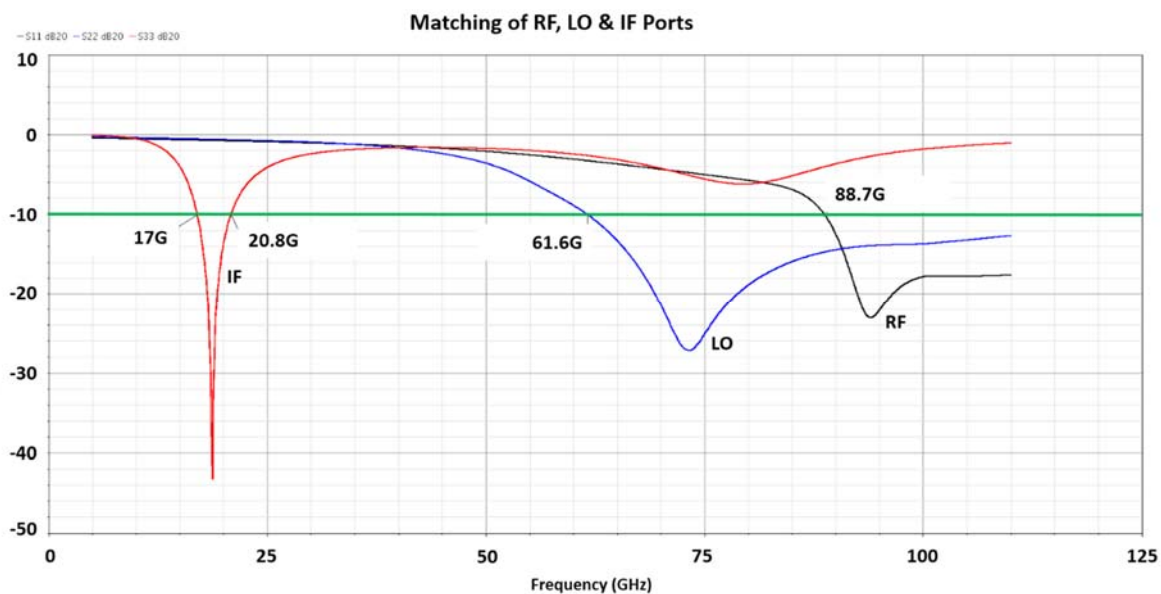


Figure 4.24 Simulated RF, LO and IF port matching of the mixer break-out (with parasitics, kit v1.3.0.3)

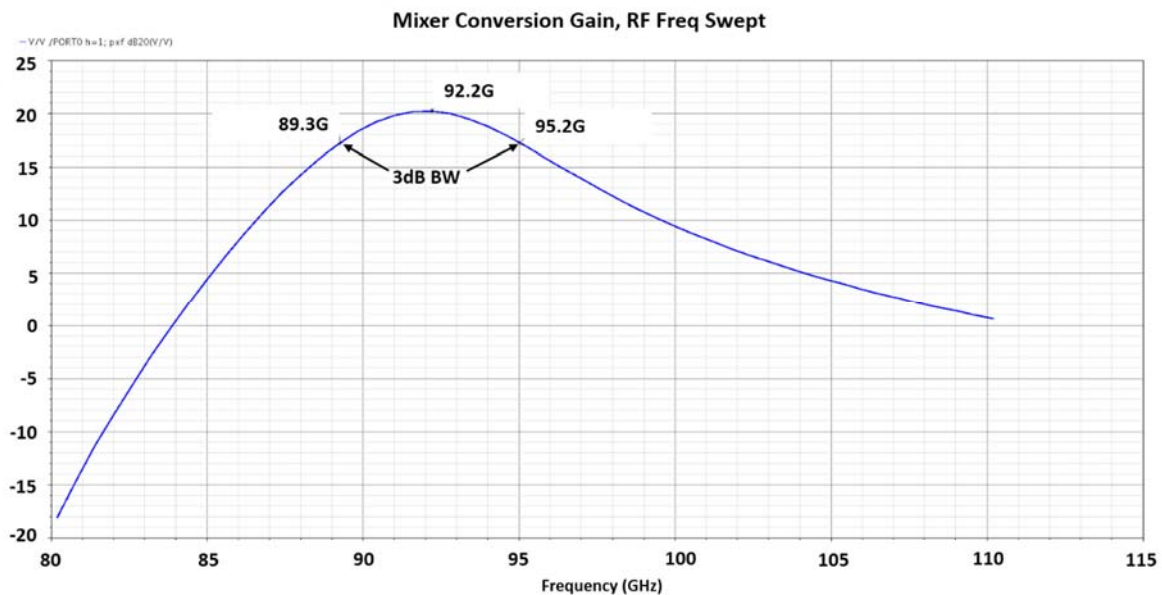


Figure 4.25 Simulated conversion gain of the mixer break-out, RF frequency swept (with parasitics, kit v1.3.0.3)

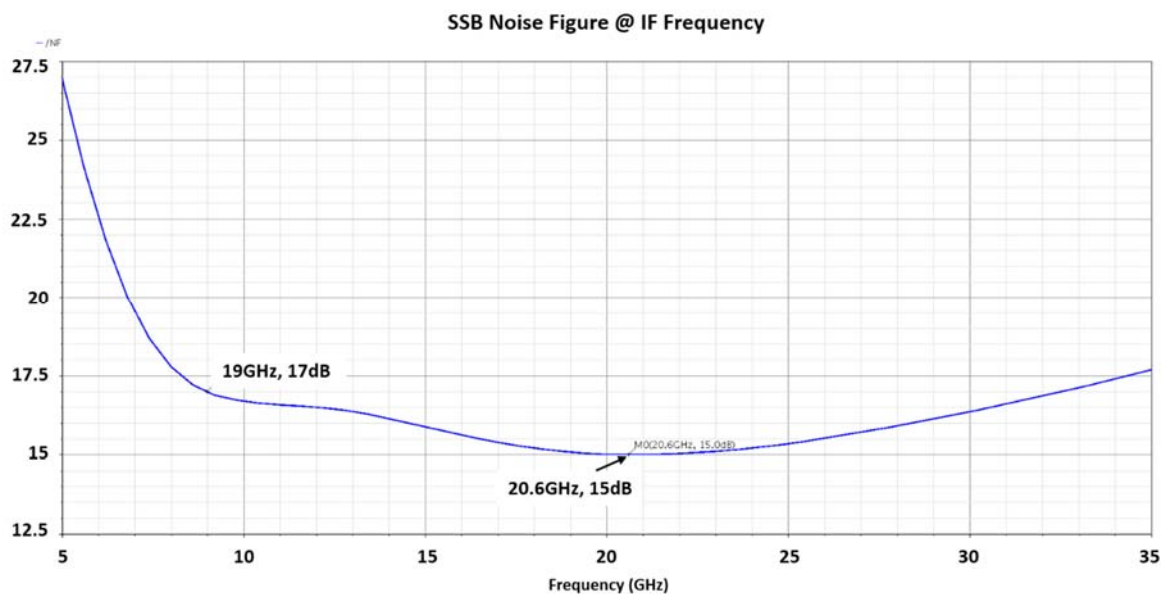


Figure 4.26 Simulated single-sideband (SSB) NF of the mixer break-out (with parasitics, kit v1.3.0.3)

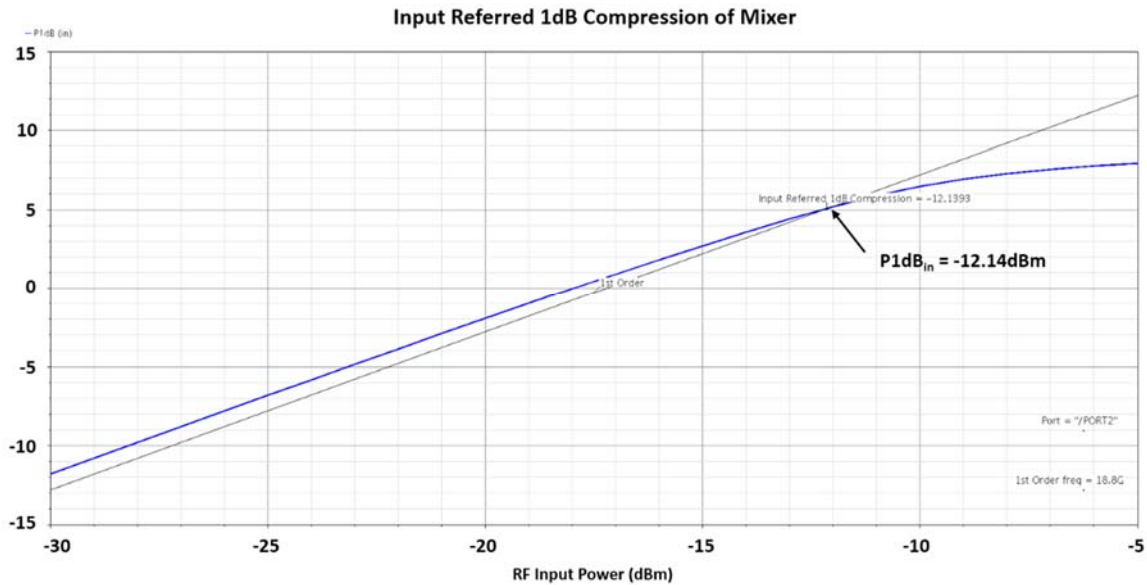


Figure 4.27 Simulated linearity, input-referred 1-dB compression point of the mixer break-out (with parasitics, kit v1.3.0.3)

### 4.3.4 Square-Law Power Detector

#### 4.3.4.1 First Design

The output of the mixer designed in Section 4.3.3 will give an IF signal of around 19 GHz. However, without proper baseband post-processing circuitry and application of a DSP algorithm, there is no intuitive way to interpret the down-converted signals. Before investing more resources to develop post-processing blocks, it is necessary to verify that the RF signals retrieved by the prototype array are useful as inputs for interferometry imaging. Two components are used to describe a single-tone signal: (1) amplitude and (2) phase. A time and cost effective way is to have a power detector that converts the input signal power to a voltage reading, which can be easily measured by a cheap multimeter. A square-law power

detector, similar to what has been previously described ([MEY95], [ZHA05] and [ZHA06]), was designed by Ms. Qiaoqiao Liu, targeting at 94 GHz. The schematic is shown in Figure 4.28.

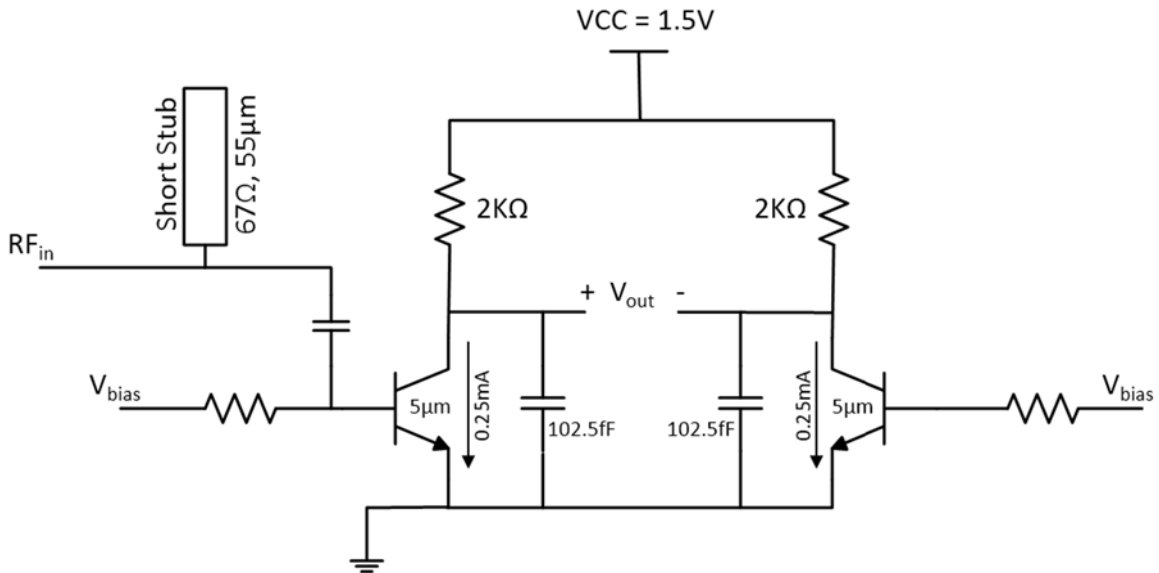


Figure 4.28 The first version of the RF power detector

The design utilizes a differential BJT pair, identically biased, although only the left BJT is connected to the RF input while the right BJT acts as a DC reference.

$$\begin{aligned}
 V_{OUT}^+ &= VCC - I_{C1} \cdot R_L \\
 V_{OUT}^- &= VCC - I_{C2} \cdot R_L \\
 V_{OUT} &= V_{OUT}^+ - V_{OUT}^- = (I_{C2} - I_{C1}) \cdot R_L
 \end{aligned} \tag{4.2}$$

where  $I_{C1} = I_S e^{\frac{V_{BE1} + V_{RF}}{V_T}}$ ,  $I_{C2} = I_S e^{\frac{V_{BE2}}{V_T}}$ . According to [ZHA05],  $V_{RF} = \sum_{i=1}^N V_{RFi} \cos(\omega_i t + \phi_i)$ , so

$I_{C1}$  can be written as:

$$I_{C1} = I_S e^{\frac{V_{BE1}}{V_T}} \prod_{i=1}^N e^{\frac{V_{RFi} \cos(\omega_i t + \phi_i)}{V_T}} \quad (4.3)$$

For small-signal detection,  $I_{C1}$  can be further simplified to:

$$I_{C1} \cong I_S e^{\frac{V_{BE1}}{V_T}} \prod_{i=1}^N \left( 1 + \frac{V_{RFi}^2}{4V_T^2} \right) \quad (4.4)$$

using  $e^x \approx 1 + x$ ,

$$V_{OUT} = -\frac{I}{4V_T^2} e^{\frac{V_{BE1}}{V_T}} \sum_{i=1}^N V_{RFi}^2 = C_o \sum_{i=1}^N V_{RFi}^2 \quad (4.5)$$

where  $\sum_{i=1}^N V_{RFi}^2$  is the sum of the square of all the harmonics' amplitude, which corresponds to

the total power. Therefore, the absolute value of the output voltage reading is proportional to the RF input power. From the schematic, a pair of 102.5fF capacitors, along with other parasitic capacitors, act as a low-pass filter so only DC response will be observed at the output port. The layout is shown in Figure 4.29. With parasitics, the responsivity of the power detector is simulated and shown in Figure 4.30.

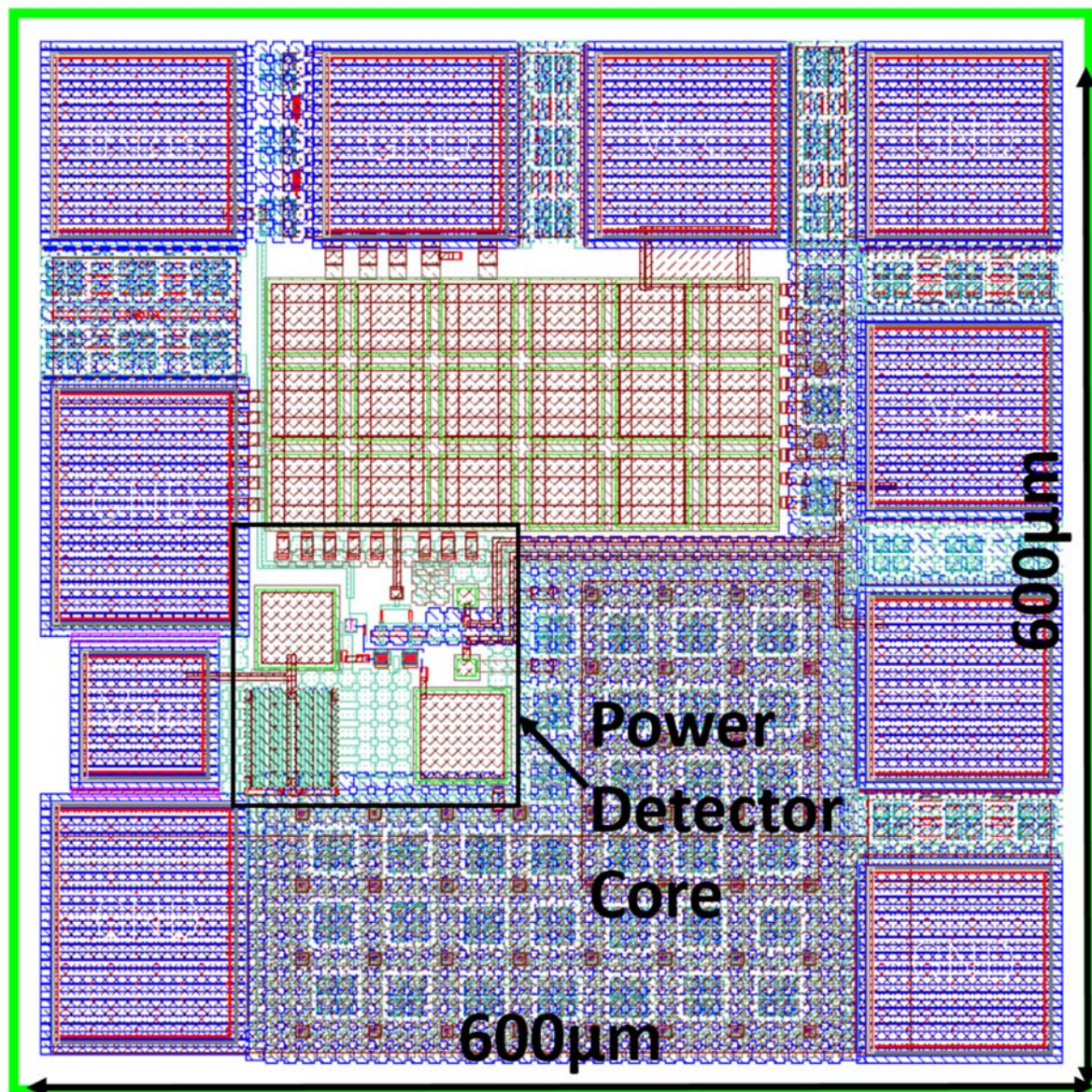


Figure 4.29 Layout of the first design of the power detector. The total area =  $600 \times 600 \mu\text{m}^2$  (kit v.1.2.0.1). The power consumption is only 2.4 mW.

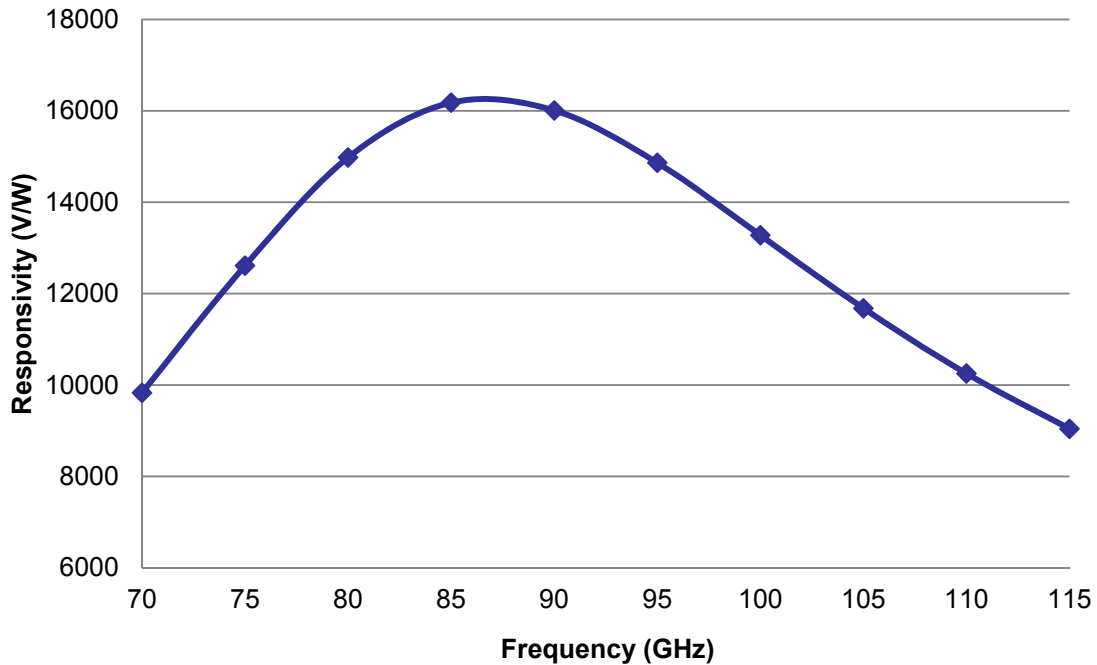


Figure 4.30 Simulated responsivity of the first version power detector (with parasitics, kit v1.2.0.1)

#### 4.3.4.2 Second Design for the 4 x 1 Array

Since the first design by Ms. Liu was taped-out as a trial, it uses a 1.5 V VCC, which is not compatible with other circuit components in the array. Therefore, during the final tapeout of the array, the power detector was redesigned. The circuit topology was not changed, however, two cascoded CMOSs were used to attenuate the universal VCC from 2.5 V to 1.5 V. The layout was optimized to fit into the small space between the pair of power combiners. The layout was totally redesigned in order to make the differential pair appear as symmetric as possible. The simulated output voltage response to the 94 GHz input power is plotted in Figure 4.31. The corresponding responsivity is calculated to be 16.2 kV/W.

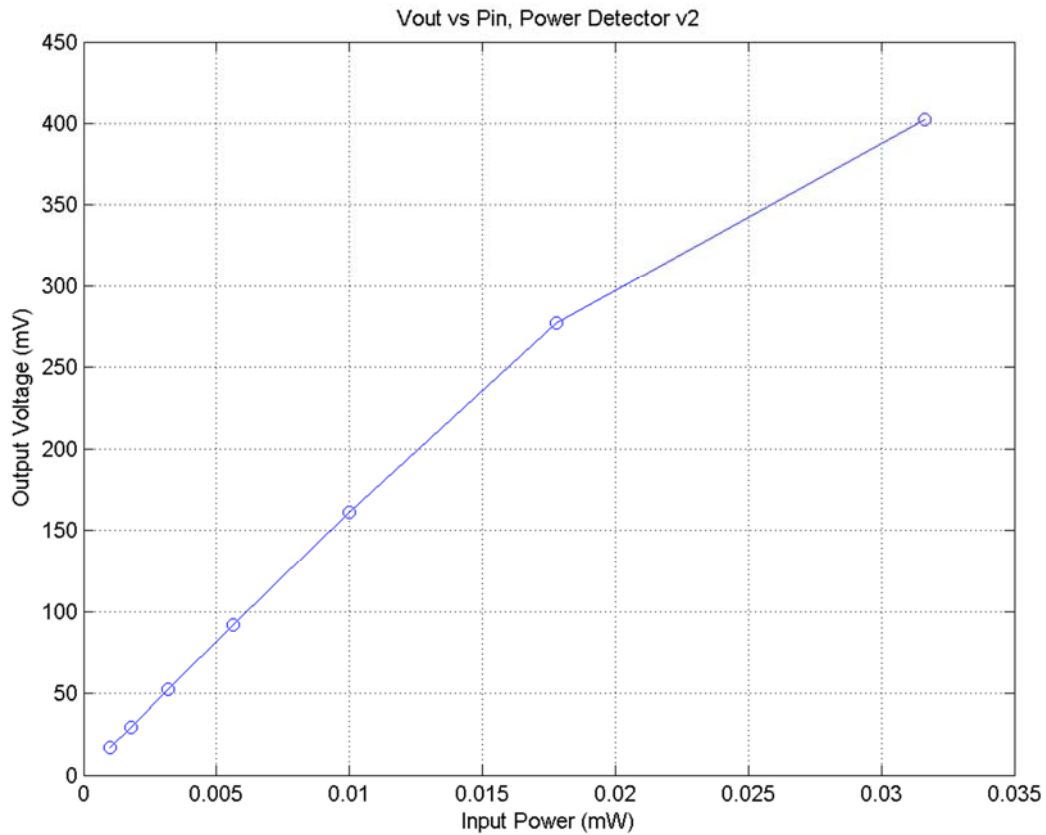


Figure 4.31 Simulated voltage response at 94 GHz for the second version of the power detector (with parasitics, kit v1.3.0.3)

#### 4.3.5 Passive EM Components

As illustrated in Figure 4.2, two stages of power combining are performed in the 4 x 1 array. The first stage includes two identical Wilkinson power dividers, while the second stage is a single ring-hybrid coupler. Details of the design and their simulation results are presented in the following subsections.

#### 4.3.5.1 Design of the Wilkinson Power Divider at 94 GHz

The objective of the design is to achieve a compact size and minimum insertion loss. To connect the input and output of this divider to other designed components without having to adjust the transmission line width, a standard 4  $\mu\text{m}$  width was used across the whole divider, while only the gap between the signal line and the ground shield was varied to achieve both 50  $\Omega$  and 70  $\Omega$  characteristic impedances that the divider requires. Due to the use of a ground shield, the lines could be meandered and squeezed as tightly as possible without having EM interaction between nearby lines.

The structure of this divider consists of multiple segments of pre-existing interconnection models found in the BiCMOS 8hp design kit, except for two kinds of tees, which connect lines with different  $Z_0$ . These tees were analyzed through EM simulation with Sonnet. A final layout view of this 94 GHz Wilkinson power divider is shown in Figure 4.32 (rotated 90° to save space). The corresponding simulation results are plotted in Figure 4.33 and 4.34.

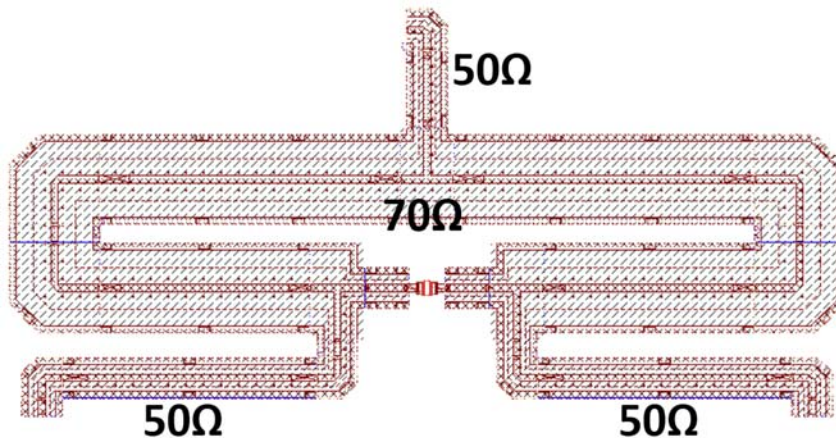


Figure 4.32 Layout view of the 94 GHz Wilkinson power divider

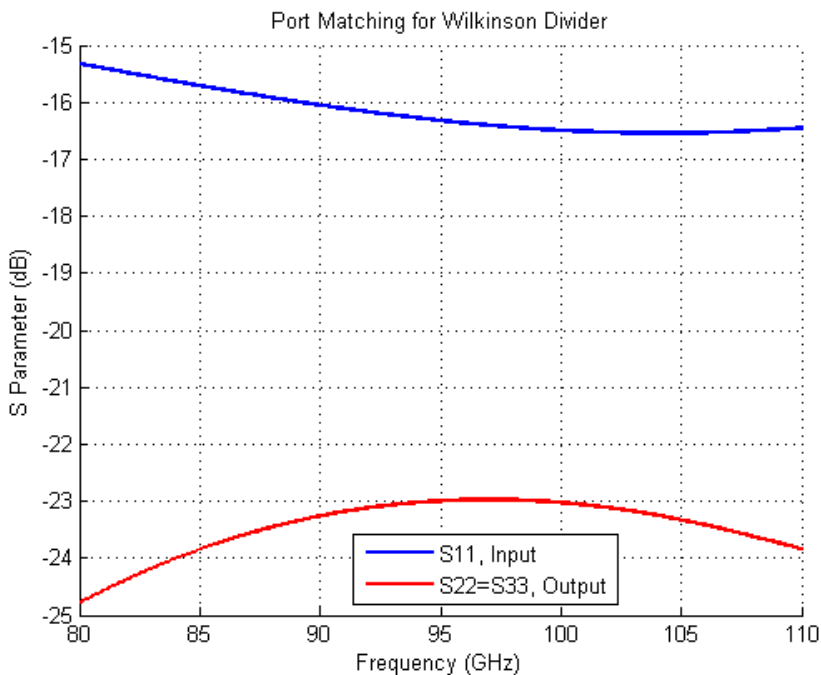


Figure 4.33 Simulated port matching of the 94 GHz power combiner

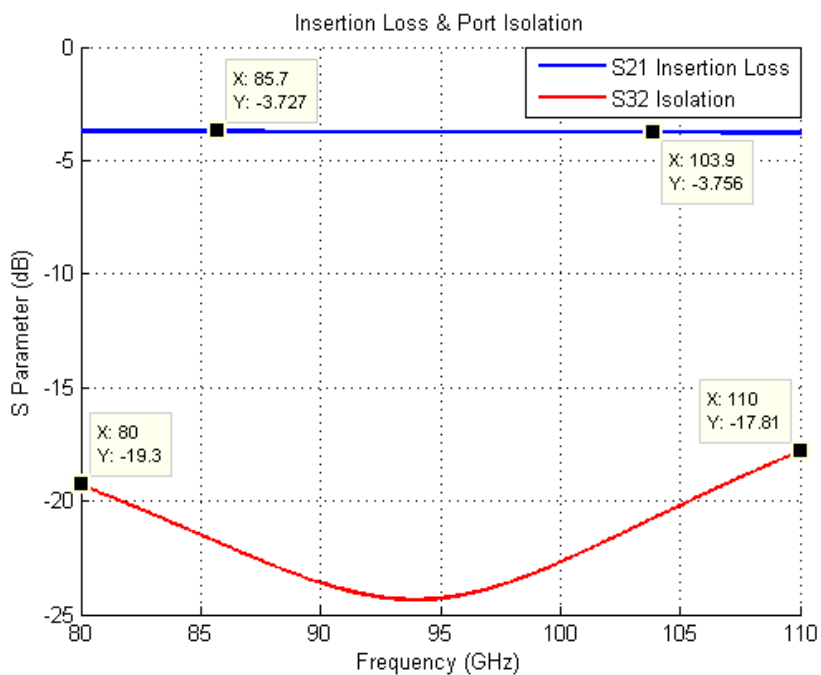


Figure 4.34 Simulated forward transmission and isolation of the 94 GHz power combiner

All ports are well matched over a wide bandwidth and good isolation between the two output ports is also achieved. Insertion loss from both ports are maintained at a relatively flat value of -3.73 dB, where the -3 dB comes from the theoretically equivalent power splitting. Therefore, only a 0.73 dB power loss is observed from this design.

#### 4.3.5.2 Ring-Hybrid Coupler at 94 GHz

The ring-hybrid coupler is a 4-port bilateral device as illustrated in Figure 4.35 [PON03]. When Port 2 and Port 3 are excited, Port 1 becomes the summation port, while Port 4 becomes a difference port. It is the  $\lambda/2$  path difference between Port 2 and Port 3 towards Port 4 that causes the wave between Port 2 and 4 to travel  $\lambda/2$  more, therefore the signal's phase is shifted by  $180^\circ$ .

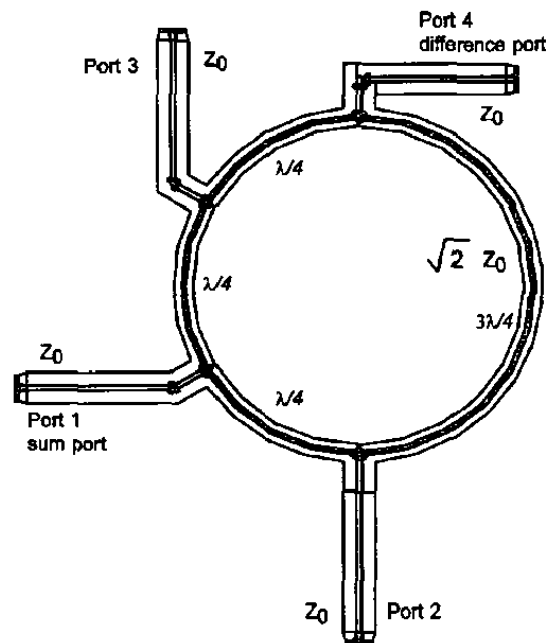


Figure 4.35 Schematic of a  $180^\circ$  hybrid junction (Figure adapted from [PON03])

In this configuration, the whole ring is about  $1.5\lambda$  long. Even at 94 GHz, the ring is about 1.6 mm in length, including the large space inside the ring which largely goes to waste, making the design very expensive, considering its size and simple function. [CHI06] developed a method, which could reduce the ring by about  $\lambda/2$ . Following this path, we further minimized the structure and constructed it as shown in Figure 4.36(a), while the s-parameter simulation results are plotted in (b) and (c).

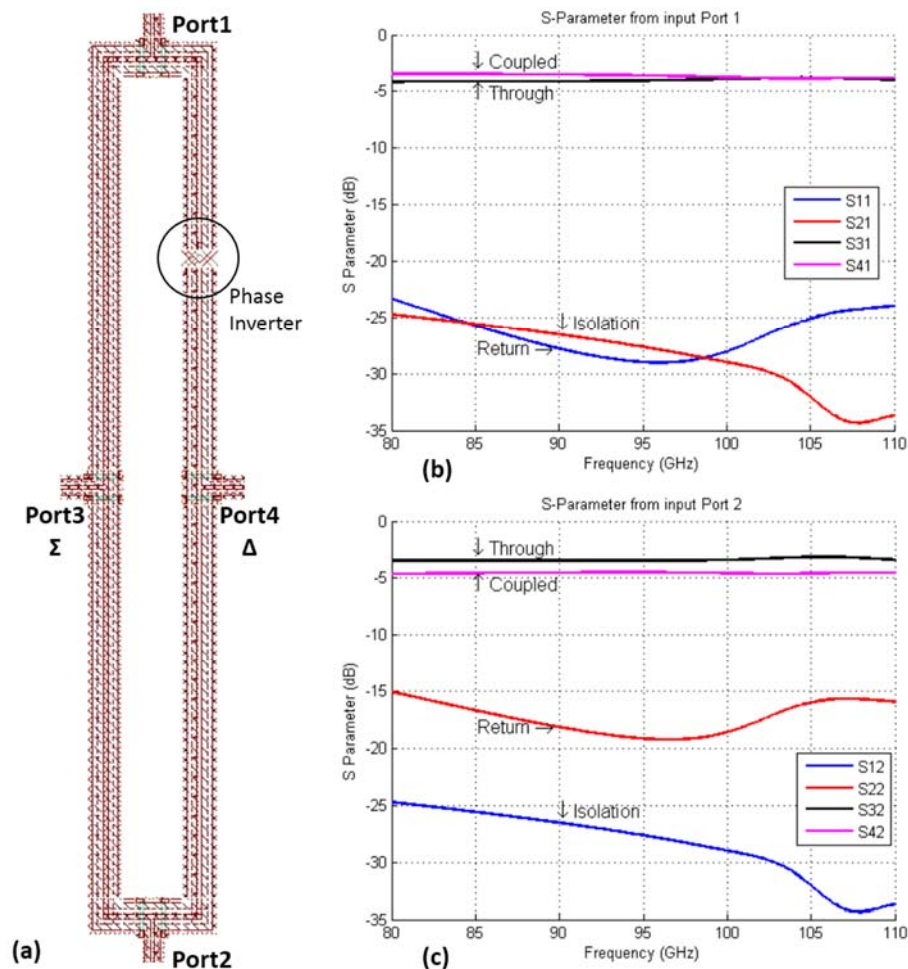


Figure 4.36 (a) A schematic of the modified ring-hybrid coupler (phase inverter circled); (b) the S-Parameter when Port 1 is excited; (c) the S-Parameter when Port 2 is excited

The simulation results show that all ports are well matched. The isolation between the two input ports is very good as well. There is some slight difference in S31 and S41, as well as S32 and S42, at a maximum of 1.5 dB. The difference in power level is nearly negligible when it is measured by the power detector.

#### 4.3.5.3 Cascading of the Wilkinson Divider and Ring-Hybrid Coupler

Although the ring-hybrid coupler was implemented with “singlecpw” (single wire with a co-planar waveguide as a ground shield), due to the phase inverter (which reduces the wire length by half of a wavelength), both the inside signal wire and outside ground shield are actually used as signal lines. Therefore, it is necessary to verify that an EM component in close proximity will not have coupling effects with the ring-hybrid coupler. The original cascading setup is shown in Figure 4.37.

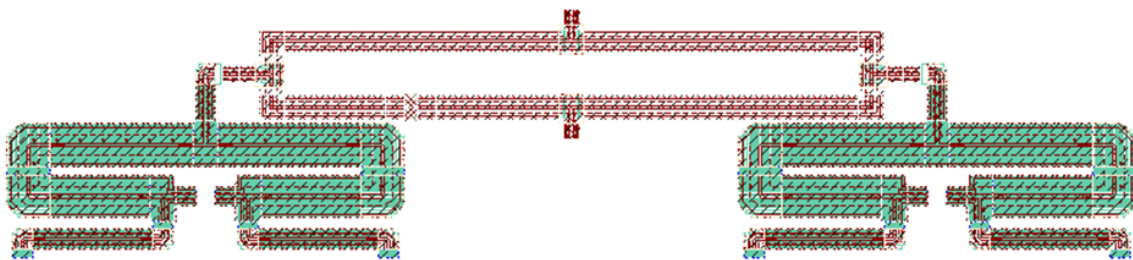


Figure 4.37 Cascading of two Wilkinson dividers with the ring-hybrid coupler

The inside corner of the Wilkinson divider is very close to the coupler, therefore it was necessary to simulate the whole structure for the overall port characteristics. However due to limitations in computational resources, we reduced the EM simulation size so that only the

parts in close proximity to the coupler were included. Two simulations were performed for comparison and their setups are illustrated in Figure 4.38.

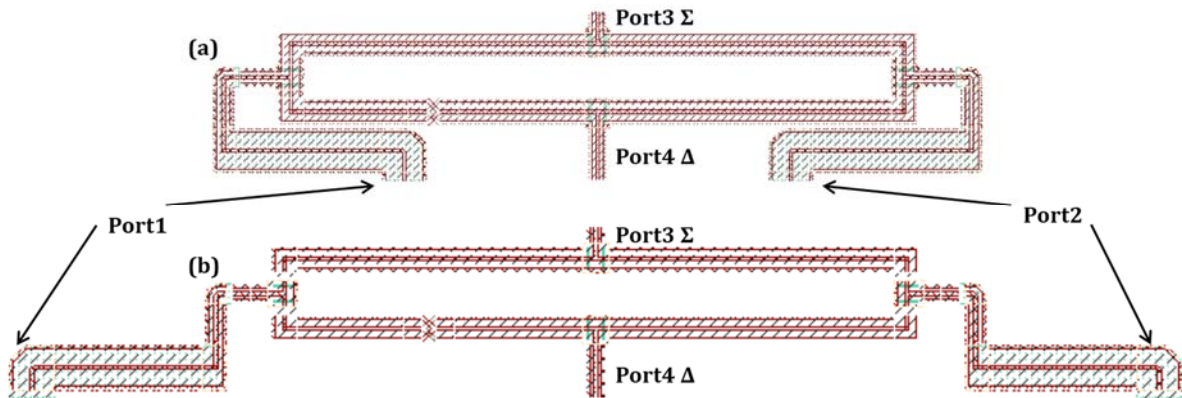


Figure 4.38 Setup comparison to verify the EM effect of the (a) original setup, and (b) the transmission line flipped to the outside

The EM simulations on the different setups in Figure 3.38 were performed in the exact same grid size to minimize any software or calculation error. The results of the simulations are shown in Figure 4.39 and 4.40. Figure 4.39 compares all four ports' matching between the original design (blue) and the flipped design (red). For all four ports, the original design displayed better matching and achieved wider bandwidth. In Figure 4.40, all S-Parameters from port 1 were compared, including isolation, through and coupled. It shows that the original design has a better port isolation from port 2 and flatter curves are observed for the original design on both through and coupled S-parameters. Therefore, we conclude that the close proximity of the Wilkinson divider lines to the coupler will not affect their corresponding EM performance, while giving a better performance in port matching and coupling.

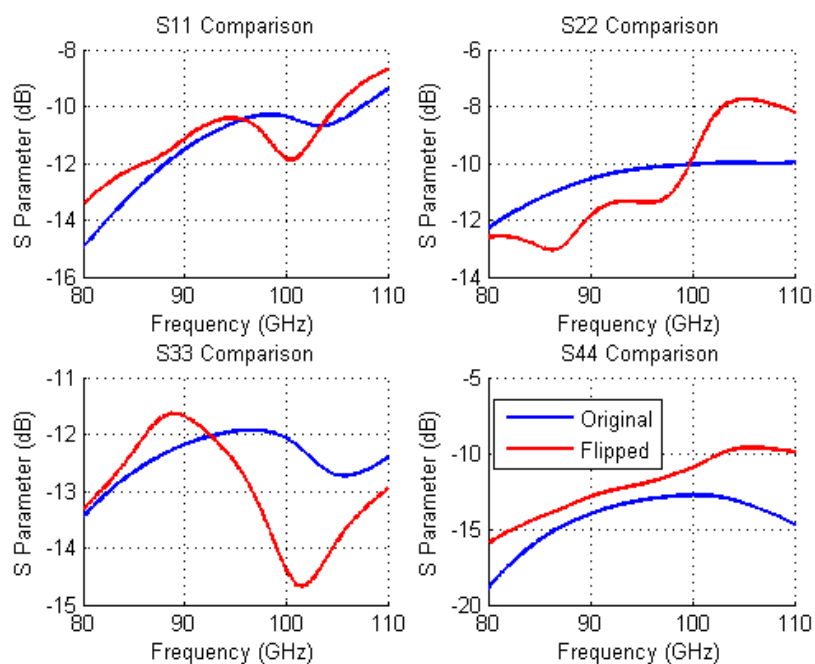


Figure 4.39 Comparison of structure port matching

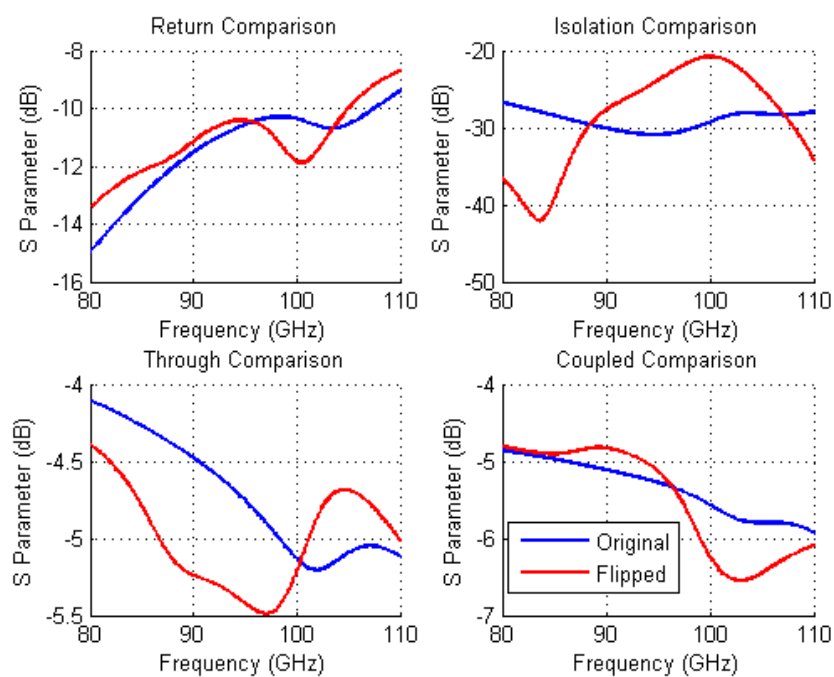


Figure 4.40 Comparison of port 1 S-parameters

#### 4.4 Implementation of a 4 x 1 Prototype Array

After all individual components were designed and simulated, they were cascaded together and an end-to-end simulation was performed. Only one channel of the components was included in the simulation due to limited computational resources and time.

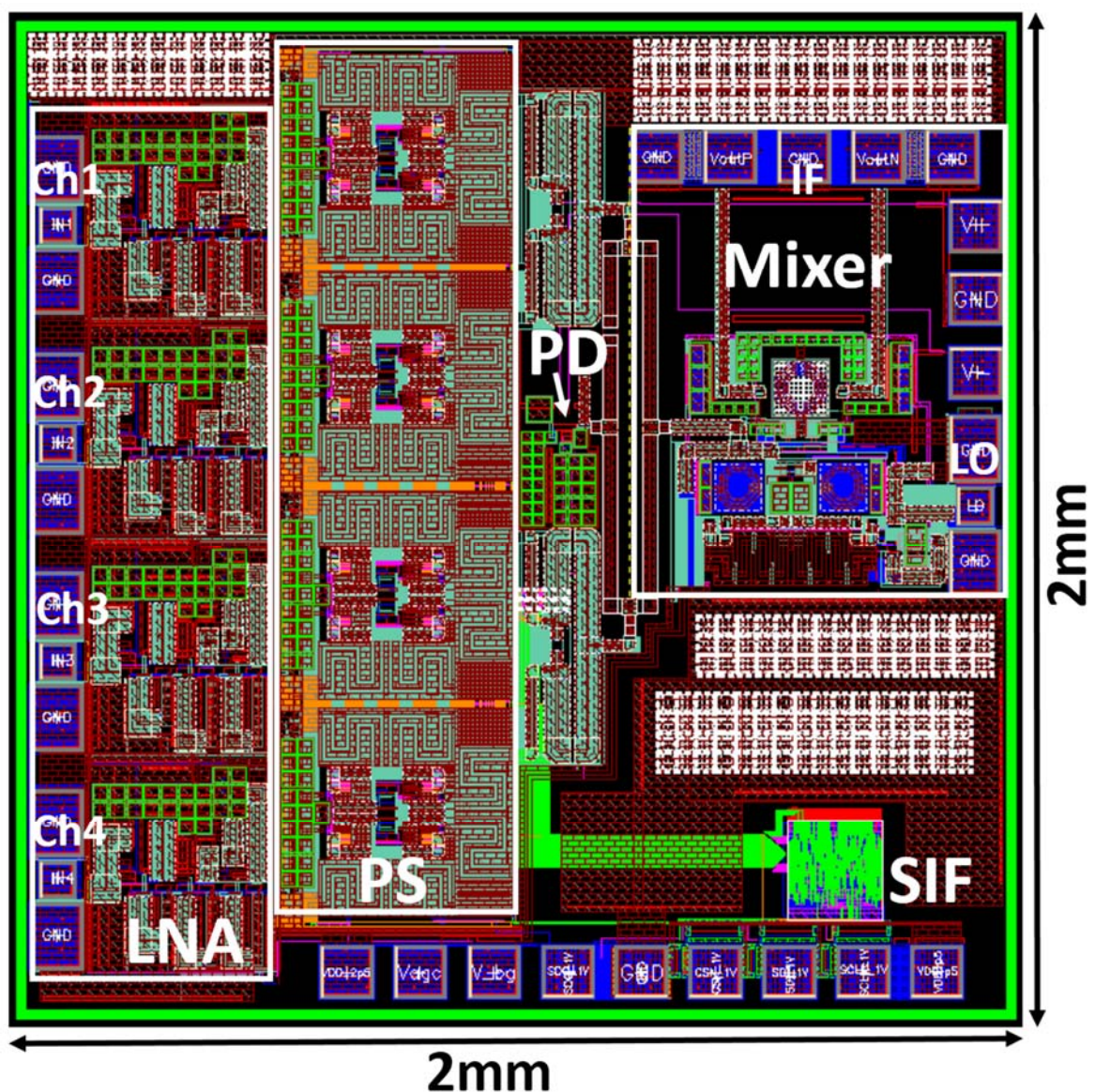


Figure 4.41 Layout view of the 4 x 1 prototype array, taped-out on July 2013

As illustrated in Figure 4.41, the July 2013 tape-out takes up an area of  $2 \times 2 \text{ mm}^2$  and includes everything highlighted. However, the corresponding end-to-end simulation only includes the first element (LNA1 + PhaseShifter1 + Wilkinson + coupler + mixer + power detector + serial interface). The serial interface (SIF) was originally designed by the Asahi Kasei Microdevices Corporation. We obtained permission to use it in our project through a cooperative agreement. Phase shifting on all four channels was controlled by the SIF and an on-chip code modulation function (designed by Mr. Vikas Chauhan) was also included in the array. However, since it is not relevant to this work, it will not be discussed in this dissertation.

Simulation results are plotted in Figure 4.42 through 4.46. Similar to the mixer, both the RF and LO ports can be matched with wide bandwidth. The IF port has only a 3.7 GHz bandwidth, which is still adequate for our system's application. Conversion gain peaks at 30.7 dB differential with input frequency at 91.6 GHz and a 5.4 GHz, 3 dB bandwidth is achieved. Double-sideband NF is below 11 dB across the bandwidth and the input referred 1 dB compression point is -26 dBm, well above our anticipated input signal power at 94 GHz. The specifications are summarized in Table 4.6. Note that the power of 186 mW from the end-to-end simulation contains only one channel. If the whole  $4 \times 1$  array is considered, the total power consumption is at about 481.3 mW.

Table 4.6 Simulated specifications of individual components and single-channel, end-to-end

	LNA	Mixer	End-to-End
Frequency	<80 to 99.2 GHz (3 dB BW)	RF = 94 GHz LO = 75.2 GHz IF = 18.8 GHz	RF = 94 GHz LO = 75.2 GHz IF = 18.8 GHz
Gain	Peak 25.1 dB @ 88 GHz = 24.1 dB @ 94 GHz	Peak 20 dB @ RF = 92 GHz >17 dB, RF = 88-96 GHz	Peak = 30.7 dB @ RF = 91.6 GHz >27.7 dB RF = 88.6-94 GHz
NF	<8 dB within BW	<13 dB DSB w/i IF BW	<11 dB DSB w/i IF BW
P1dB <sub>in</sub>		-12.14 dBm	-26 dBm
Power	36.6 mW	112.18 mW	186 mW
Total power of 4 x 1 array: 481.3 mW			

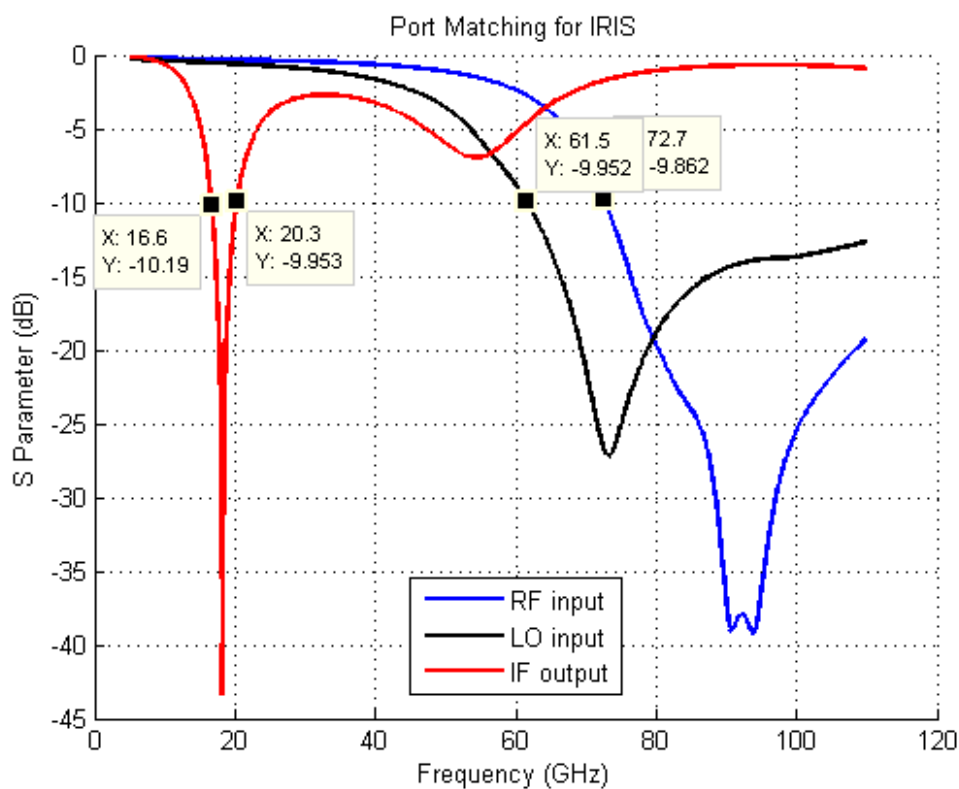


Figure 4.42 Simulated port matching of the single-channel, end-to-end

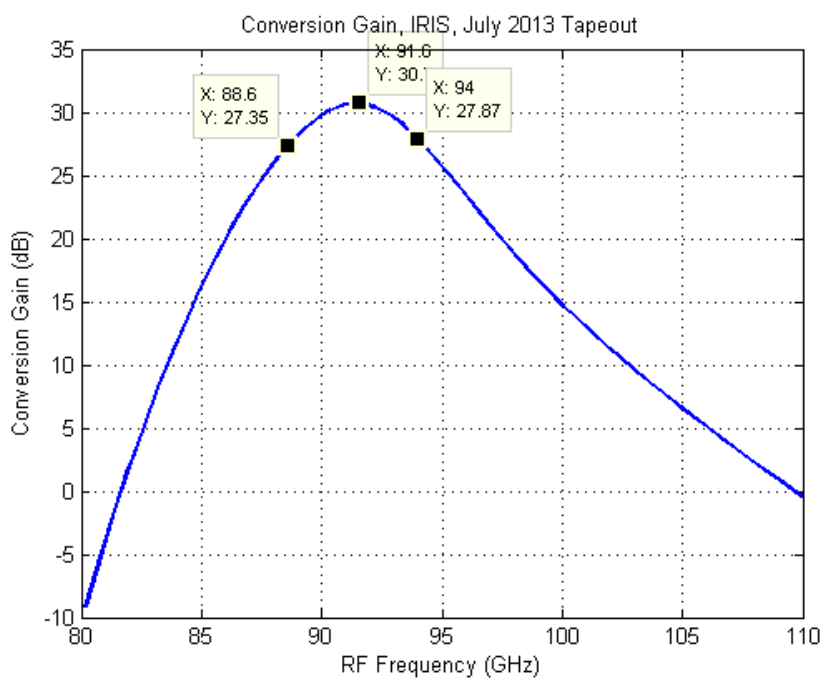


Figure 4.43 Simulated conversion gain of the single-channel, end-to-end

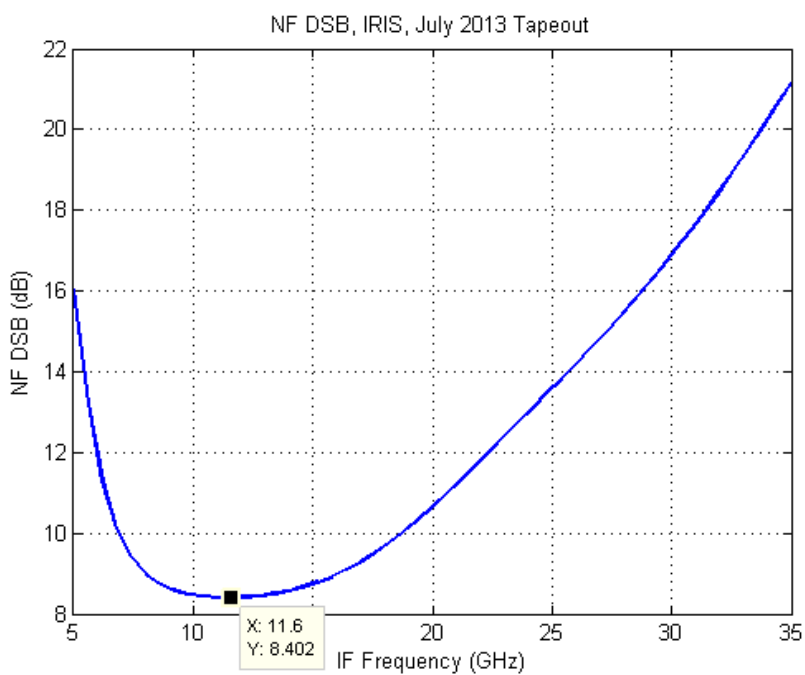


Figure 4.44 Simulated NF (DSB) of the single-channel, end-to-end

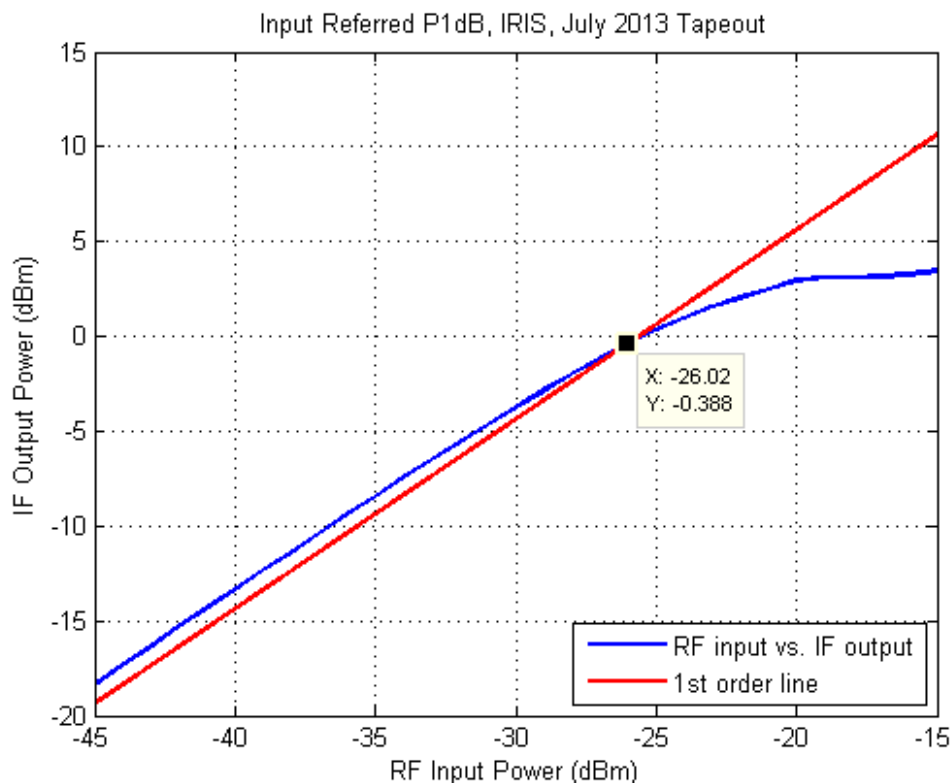


Figure 4.45 Simulated input referred 1-dB compression of the single-channel, end-to-end

#### 4.5 Summary

In Chapter 4, the SAR PMMW imaging system proposed in Chapter 3 was implemented with silicon MMIC, using IBM BiCMOS 8HP technology. Block level specifications were developed first, followed by the design of each individual block, with design details and simulation results presented. The final design cascaded all blocks to form the 4 x 1 prototype array, named IRIS (stands for Imaging using Reconfigurable millimeter-wave phase arrays in Silicon). Measurement methodology and results will be discussed in Chapter 5.

## **CHAPTER 5 HARDWARE MEASUREMENT**

### 5.1 Overview

In this chapter, the methods used to characterize the PMMW imaging components will be briefly introduced. Power, noise and linearity results from the individual components presented in Chapter 4 (*e.g.* the LNA, phase shifter, mixer, power detector, as well as the 4 x 1 prototype array) will be reported. Device calibration and verification methodologies were used to demonstrate that the results are accurate and dependable. Comparison between simulations and measurement will be made and the reasons for any discrepancies will be analyzed.

### 5.2 Definition of Various Measurement Setups

#### 5.2.1 S-Parameter Measurement

The equipment used for the measurement of the S-Parameter (SP) includes:

- Agilent E8361C PNA Microwave Network Analyzer (10 MHz-67 GHz range)
- Agilent 75 to 110 GHz Millimeter Wave VNA Extender with head controller (covers 75 to 110 GHz)
- Agilent N4694-60003 10 MHz – 67 GHz Electronic Calibration Module (ECal)
- Hewlett-Packard W11644A WR-10 Calibration Kit
- V band (40-75 GHz) and W band (75-110 GHz) Cables and Probes
- GGB CS-5 Calibration Substrates

All SP measurements and calibration are performed on the PNA instrument. There are two kinds of SP measurements: 1-port and 2-port. Pre-measurement calibration is required for both port setups. For the 1-port measurement, the only SP we care about is S11, or the return loss of port 1, which is an indication of how well the port is matched to the system's characteristic impedance,  $Z_0$  (usually 50  $\Omega$ ). While in 2-port configuration, it is necessary to measure S11 (port 1 return loss), S21 (forward transmission coefficient), S12 (reverse transmission coefficient), and S22 (port 2 return loss). All our circuits were measured by wafer probing, so we set the reference plane at the tip of the probe(s) when calibrating.

Proper cables and probes need to be selected, corresponding to the different frequency ranges of the measurement. Probes were connected through cables directly to the PNA for the low frequency study (<70 GHz), while for conditions >70 GHz, the VNA extender was connected to the PNA on one side, with the other side of the extender connecting to the probe through adapters and cables as illustrated in Figure 5.1. Green and black lines are cables and the arrows indicate probes.

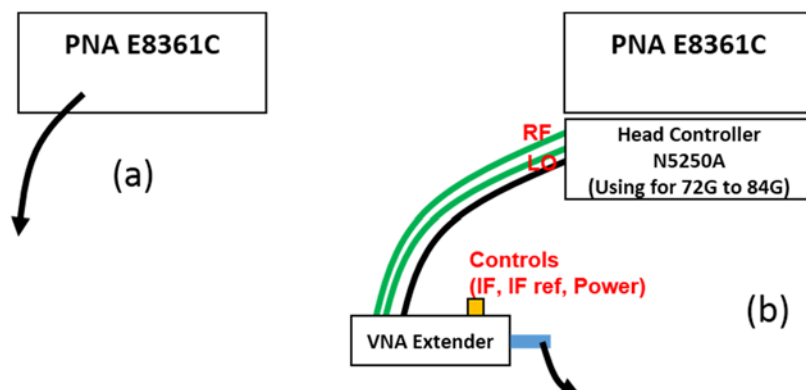


Figure 5.1 Illustration of the wafer probing setup for the frequency ranges of (a) <70 GHz, and (b) >70 GHz

In both cases, the probe(s) were landed on to the CS-5 calibration substrate and the calibration was performed using instructions from the software built into the PNA. After successful calibration, probe(s) were landed on the device under test (DUT) and the measured SP results were observed from the PNA.

### 5.2.2 Swept Power Measurement

For power measurement, the goal is to determine how output power relates to input power as the input power is swept, allowing measurement of the 1 dB compression point. De-embedding loss associated with any cables, probes, adaptors, *etc.* must be done to move the reference plane to the probe tips. Swept power measurements were performed on the mixer breakout, the array, and the power detector breakout. Details will be discussed in sections 5.5.2 (mixer power section) and 5.7.2 (array power section).

### 5.2.3 Noise Measurements

#### 5.2.3.1 Noise Figure

Noise measurements were performed to determine the NF (dB) or the F of the DUT. F and NF are defined in Eq. 5.1 and 5.2.

$$F = \frac{SNR_{in}}{SNR_{out}} = \frac{S_{in} / N_{in}}{S_{out} / N_{out}} \quad (5.1)$$

$$NF = 10 \log_{10} F \text{ (dB)} \quad (5.2)$$

In the case of a two-stage system as shown in Figure 5.2, each stage is defined by their corresponding gain and  $F$ , while the total system  $F$  is defined as in Eq. 5.3.

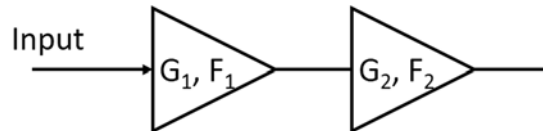


Figure 5.2 Noise in a two-stage system

$$F_{tot} = F_1 + \frac{F_2 - 1}{G_1} \quad (5.3)$$

From the above equation, we can derive:

$$F_1 = F_{tot} - \frac{F_2 - 1}{G_1} \quad (5.4)$$

If we replace stage 1 with the DUT and stage 2 with the instrumentation connected to the output of the DUT, a basic measurement setup can be established as illustrated in Figure 5.3 [AGI14]. Two measurements need to be performed: (1) without the DUT, just the stage-2 instruments alone, and (2) with the DUT and all stage-2 instruments. Properly de-embedded (calibrated), the NF of the DUT can be accurately derived.

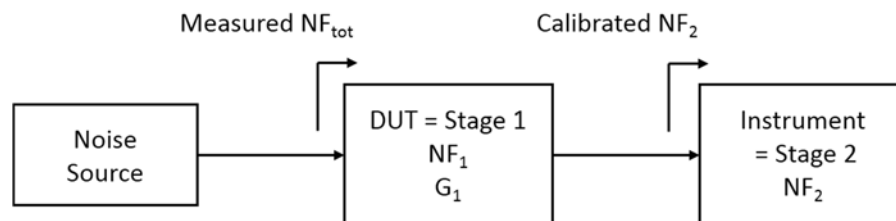


Figure 5.3 The NF measurement method using a two-stage system (Figure adapted from [AGI14])

### 5.2.3.2 Y-factor measurement

To determine the NF for the instrument and the total system, a method called Y-factor technique was applied. It requires the use of a noise source as shown in Figure 5.3. The noise source is pre-calibrated and the calibration is defined as the Excess Noise Ratio (ENR), which is unique for every single noise source and is mathematically defined as in Eq. 5.5 and 5.6,

$$ENR = \frac{(T_S^{ON} - T_S^{OFF})}{T_0} \quad (5.5)$$

$$ENR_{dB} = 10 \log_{10} \left[ \frac{(T_S^{ON} - T_S^{OFF})}{T_0} \right] \quad (5.6)$$

where  $T_S^{ON}$  and  $T_S^{OFF}$  are the noise temperature of the noise source when it's ON and OFF,  $T_0$  is the reference temperature of 290 K. Usually in calculations, we equate  $T_S^{OFF}$  to  $T_0$ , based on the assumption that the noise temperature of the noise source is room temperature.

On the other hand, the Y-factor itself is the ratio of two noise power levels, measured by a spectrum analyzer when the noise source is ON and OFF, as illustrated in Figure 5.4. Figure 5.4(a) shows the setup for measuring the Y factor of the instrument, which in our case includes an LNA at 20 GHz cascaded by a spectrum analyzer. While in Figure 5.4(b), the DUT is inserted between the noise source and the instrument, therefore the Y factor obtained with this setup is for the DUT and the instrumentation together. In either case, the noise power seen by the spectrum analyzer is proportional to the total noise temperature, so the Y factor for each case is described in Eq. 5.7 and 5.8.

$$\text{Case (a)} \quad Y = \frac{N^{ON}}{N^{OFF}} = \frac{T^{ON} + T_{SA}}{T^{OFF} + T_{SA}} \quad (5.7)$$

Case (b) 
$$Y = \frac{N^{ON}}{N^{OFF}} = \frac{T^{ON} + T_{DUT+SA}}{T^{OFF} + T_{DUT+SA}} \quad (5.8)$$

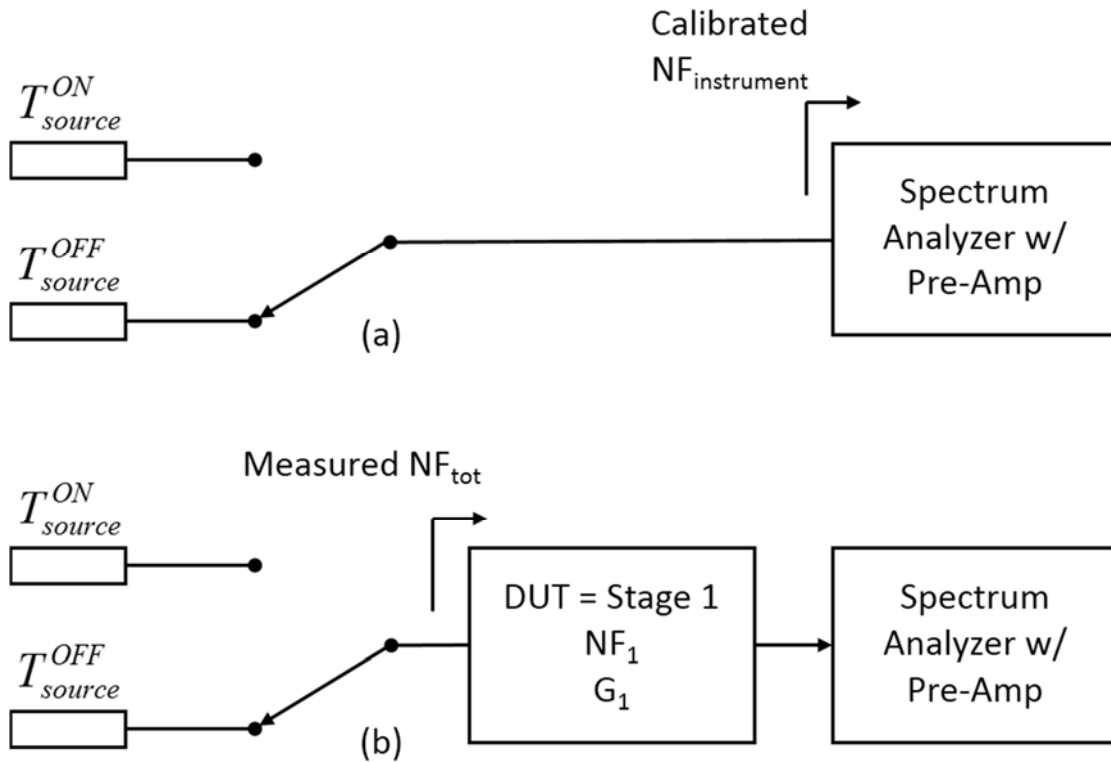


Figure 5.4 Y-factor measurement setup of (a) instrument only, and (b) DUT + the instrument

The relationship between F and the noise temperature ( $T$ ) of a device is defined as:

$$F = 1 + \frac{T}{T_0} \quad \text{or} \quad F_{dB} = 10 \log_{10} \left( 1 + \frac{T}{T_0} \right) \quad (5.9)$$

Since Eq. 5.7 and 5.8 have the same format, we use  $T$  to denote  $T_{SA}$  and  $T_{DUT+SA}$  in each case:

$$T = \frac{T^{ON} - Y T^{OFF}}{Y - 1} = T_0 (F - 1) \quad (5.10)$$

In general, we assume  $T^{OFF} = T_0 = 290$  K, thus from Eq. 5.10 and 5.5 we get:

$$F = \frac{T^{ON} - T^{OFF}}{(Y - 1)T^{OFF}} = \frac{ENR}{Y - 1} \text{ or } F_{dB} = ENR_{dB} - 10\log_{10}(Y - 1) \quad (5.11)$$

With the Y-factor technique, the F of both cases ( $F_{DUT}$  &  $F_{DUT+SA}$ ) can be found. Recalling Eq. 5.3 and 5.4,  $F_{SA}$  is de-embedded and  $F_{DUT}$  is calculated as below:

$$F_{DUT} = F_{DUT+SA} - \frac{F_{SA} - 1}{G_{DUT}} \quad (5.12)$$

With our measurements, both the mixer and the prototype array's noise will be measured. An 18 GHz noise source is first used to determine the F of the instrument at an IF frequency ( $F_{SA}$ ), while a 94 GHz noise source used to excite both circuits and the down-converted noise power will be detected by the spectrum analyzer to obtain  $F_{DUT+SA}$ . The DUT's F can be calculated with additional knowledge of its gain. Therefore, a logical order for the measurements of the mixer and array would be gain measurement followed by noise measurement. The detailed results and analysis of these two components will be presented in Section 5.5 and 5.7.

### 5.3 Measurement of the LNA

The main purpose of an LNA is to detect a low-power input signal and amplify the signal without adding much noise to degrade it. Several of the most important specifications that define an LNA include: (1) gain, (2) NF, and (3) linearity. In our lab, we measured the SP of the LNA. The NF was not measured because only harmonic down-conversion mixers were available. These harmonic mixers introduce too much noise, making it impractical to

measure the NF of the LNA alone. As a result, we estimate that the NF will be similar to circuit simulations and similar to that reported in [MAY08]. Linearity has not been measured due to inaccuracy of the power detector at the low power levels associated with the LNA output. However, the linearity of the array can be measured and give us an idea of how linear the LNA is.

Figure 5.5 shows the die photo of the fabricated LNA. The steps described in section 5.2.1 were used to take the data in both the  $<70$  GHz and  $> 70$  GHz ranges. These results are plotted in the same graph, covering the frequency from 20-110 GHz. Input port matching is shown in Figures 5.6 (rectangle form) and 5.7 (Smith Chart). The output port matching is displayed in Figures 5.8 and 5.9, while the forward transmission coefficient S21 (gain) is shown in Figure 5.10.

From Figure 5.6 to 5.9, we observe that both the input and output ports are well matched over a broad band that ranges from slightly below 70 GHz all the way up to 110 GHz and beyond. There is a mismatch in resonant frequencies. At the input side, the original two resonances still exist, but are shifted to lower frequency by about 10 GHz. Observing from the Smith Chart, the measured curve is an elongated and clockwise rotated version of the simulation. This may indicate an underestimated parasitic capacitance and interconnection length during parasitic extractions. On the other hand, at the output port matching, the measured curve appears as a shrunken version of the simulation, indicating a slight overestimation of the loss. However, the actual output matching provides a much wider bandwidth than originally estimated.

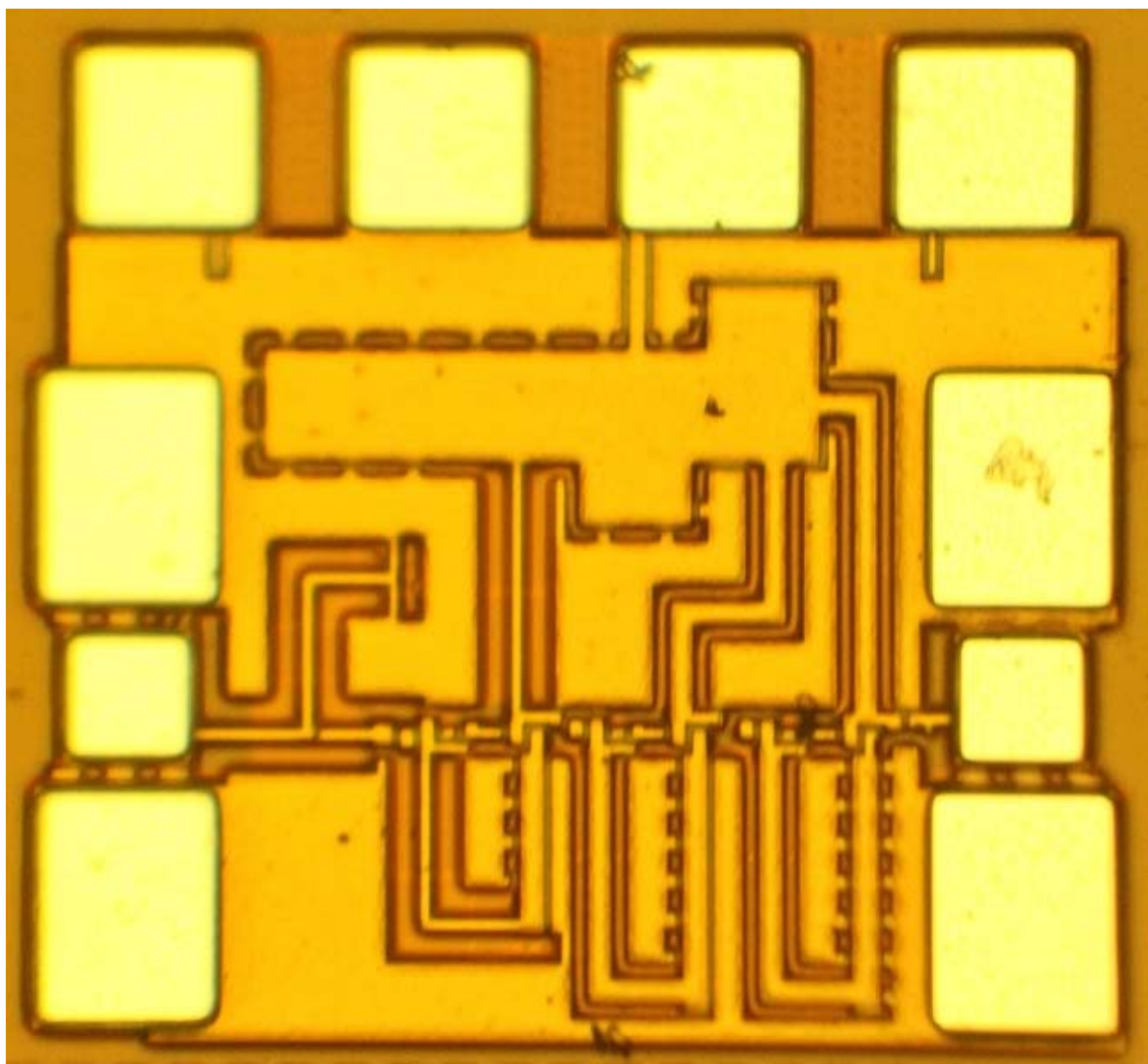


Figure 5.5 Die photo of the 6-Stage CE LNA at 94 GHz

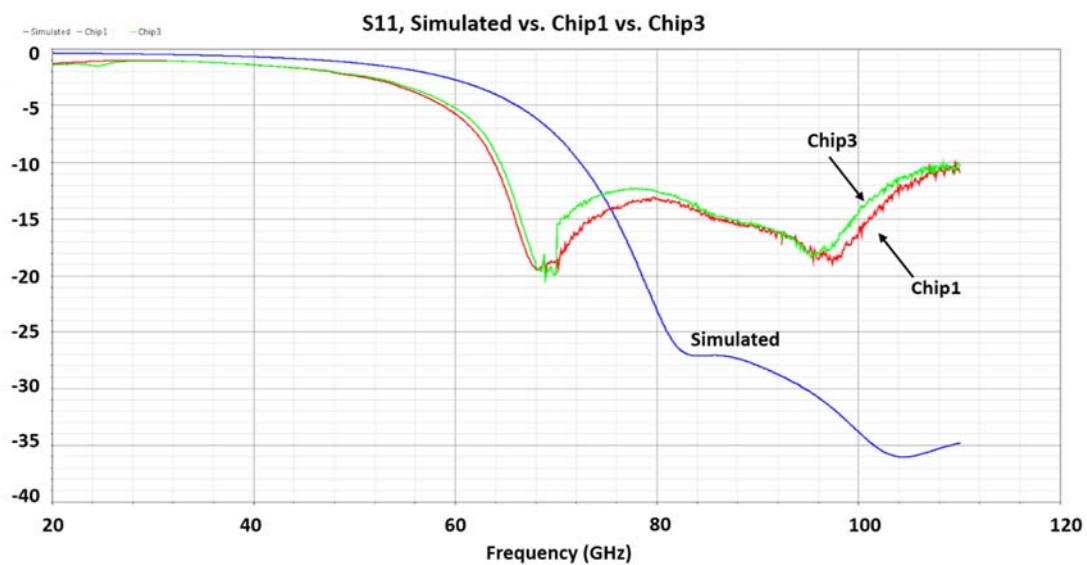


Figure 5.6 Measured vs. simulated input port reflection coefficient (S11) of the LNA

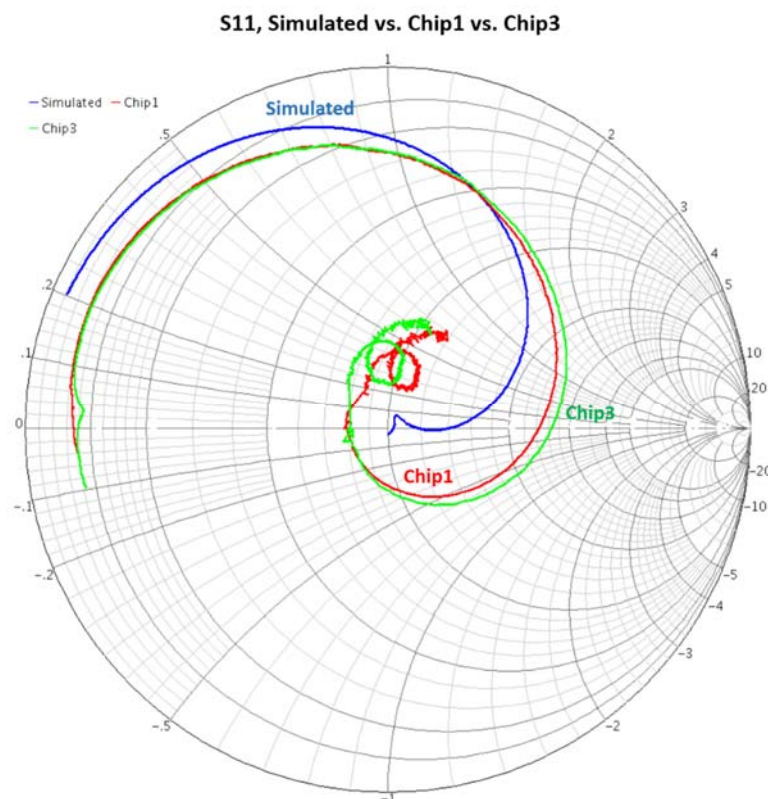


Figure 5.7 Measured vs. simulated input port reflection coefficient (S11) in a Smith Chart

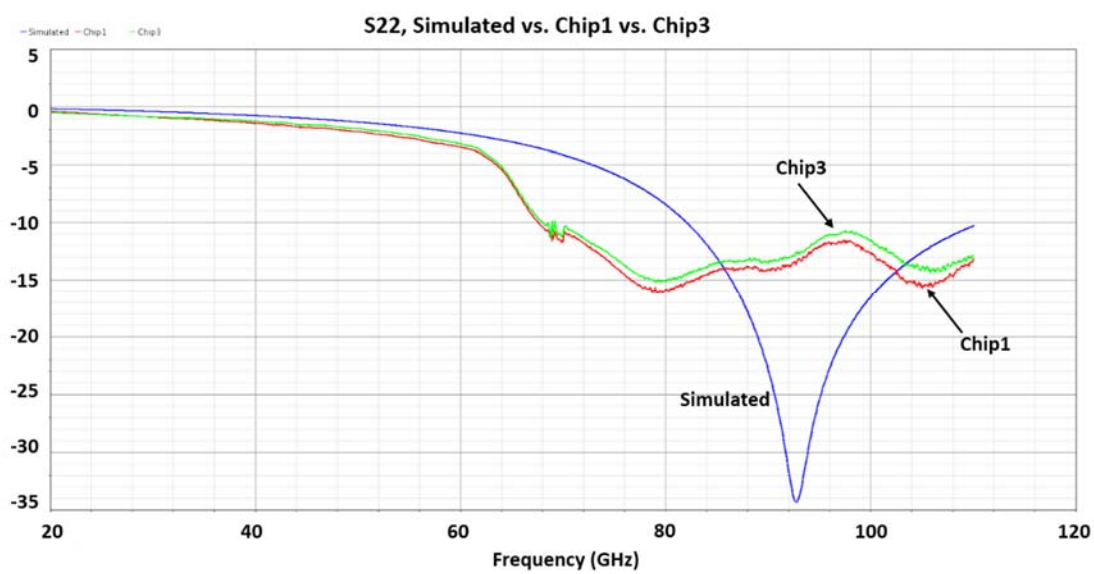


Figure 5.8 Measured vs. simulated output port reflection coefficient (S22) of the LNA

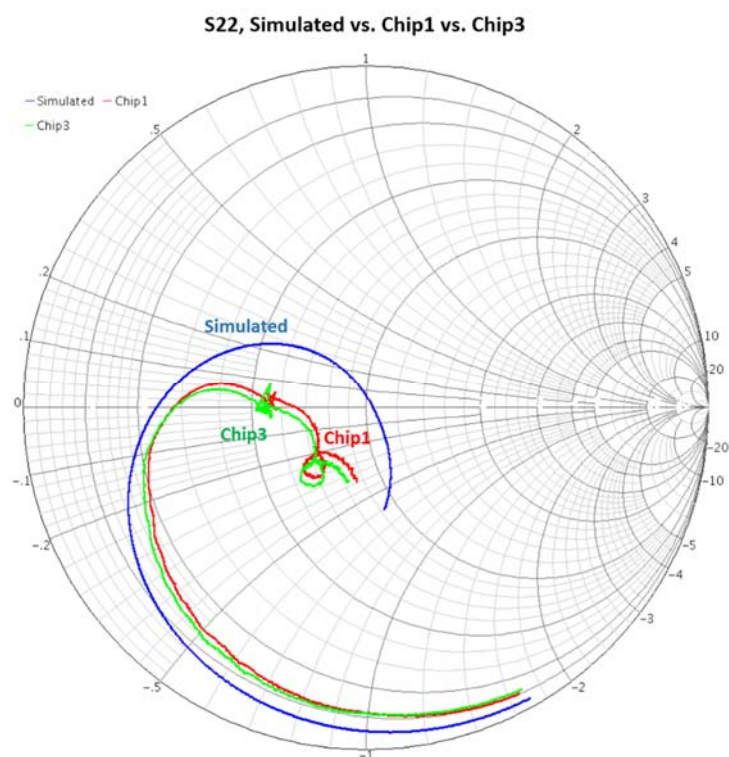


Figure 5.9 Measured vs. simulated output port reflection coefficient (S22) in a Smith Chart

In Figure 5.10, a comparison between measured and simulated LNA gain is made. The results coincide with what we have seen from the input port matching, in which resonances are shifted to a lower frequency. Two peaks can be observed from the measured curve, at 68.1 GHz and 94.25 GHz, and both have a peak gain of above 20.5 dB. The original staggered-tuned stages target three frequencies: 88 GHz, 94 GHz, and 100 GHz. The corresponding simulation results give a single peak at 94 GHz, valued at 23 dB gain.

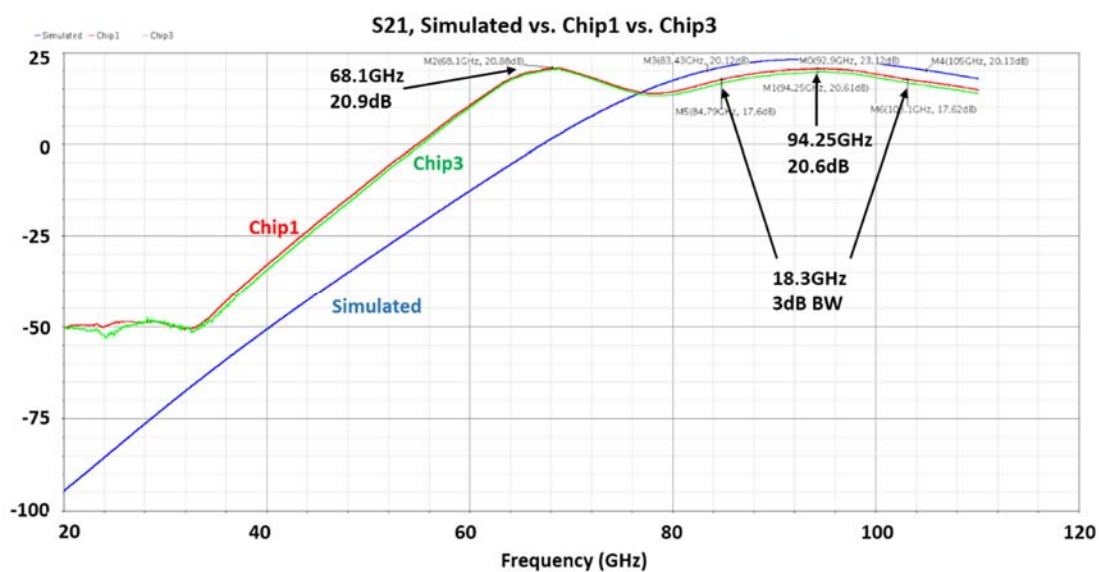


Figure 5.10 Measured vs. simulated forward transmission coefficient (S21) of the LNA

We can conclude from the input and gain measurements that the frequency shift is apparent, but the estimated gain holds its value since the peak is split in two, but the peak value decreases by only 3 dB, just half of the original single peak value. Although frequency shift is not desirable, we found a way to utilize this mismatch and created a two-channel measurement presented in Chapter 6.

Originally we used a 2.5 V VCC, however during measurements it was not able to provide enough swing headroom for the signals. Therefore we tuned the VCC to 3 V and the expected DC bias current was achieved, which enabled the presented data to be measured. When putting the LNA into our prototype array, the inter-stage matching networks were slightly changed to tune up the resonant frequency, but similar frequency response was still observed from the array measurement.

#### 5.4 Measurement of the 4-bit Controlled Phase Shifter at 94 GHz

In Mr. Kevin Green's design, with a 2.5 V VCC and 1.2 V bias voltage for both in-phase and quadrature circuits, an ideal polar plot like Figure 5.11 is expected.

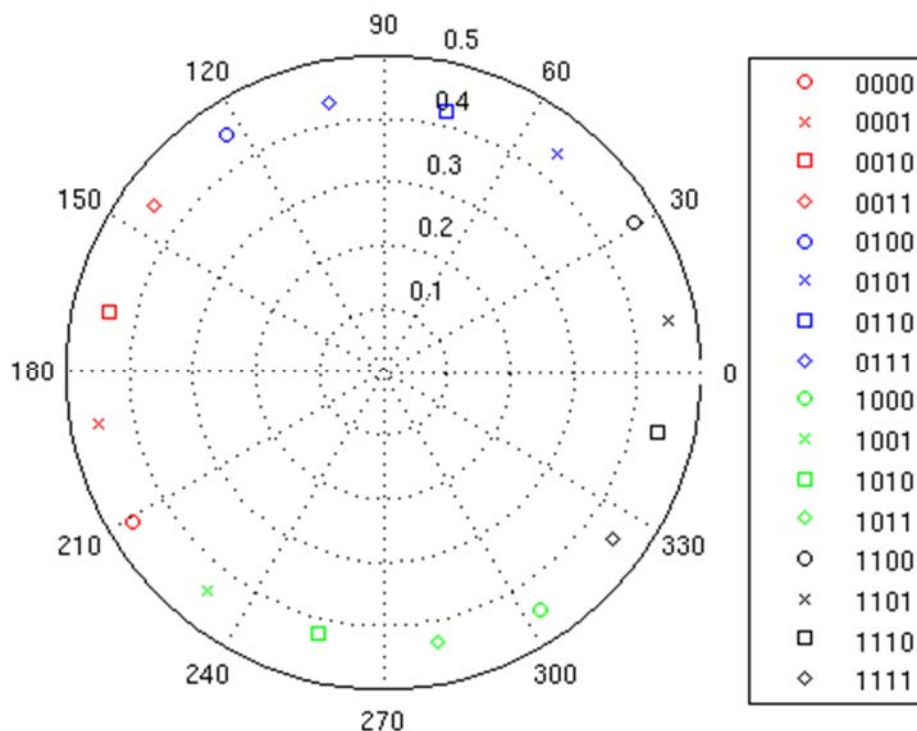


Figure 5.11 Simulated polar plot for the 94 GHz phase shifter.

Multiple measurements in different DC biasing conditions were performed. To achieve a similar DC operating current as in the simulation, the VCC was set to 2.7 V rather than the original 2.5 V. Bias voltage for the in-phase and quadrature circuits were varied around 1.2 V to eliminate any mismatch between them for an optimally symmetric polar plot. The best results we obtained occurred for the conditions when VCC equaled 2.7 V and 1.2 V for both the in-phase and quadrature circuits.

The input and output matching are plotted in Figures 5.12 through 5.15, with both simulated and measured results displayed. In simulations, the input port was well matched at 94 GHz, however the measured results show that the input port is only matched below 91 GHz for all 16 phase settings, a noticeable down shift of resonance compared to the simulation. On the output side, the original design was matched from 81.5-94 GHz, having relatively narrower band matching than the LNA. The measured results matches the simulation in frequency reasonably well, with very close resonance both at around 86 GHz. However, the amplitude of the reflection coefficient had some degradation, with only 80-89 GHz matched below -10 dB, a reduction in bandwidth of about 30%.

As far as the forward transmission coefficient, the simulated and measured S21 are plotted in rectangular form in Figure 5.16 and 5.17. Two kinds of discrepancy from the simulation were observed: (1) significant loss in amplitude of S21 for all 16 phase settings (about 9-12 dB loss); and (2) the S21 variance was increased across 16 phase settings. For the loss in S21 amplitude, underestimation of the parasitic capacitance, resistance and inductance could play a part. However, we also found there is a great discrepancy between

the EM simulation-generated component models used in the simulation and their actual performance in the silicon circuits.

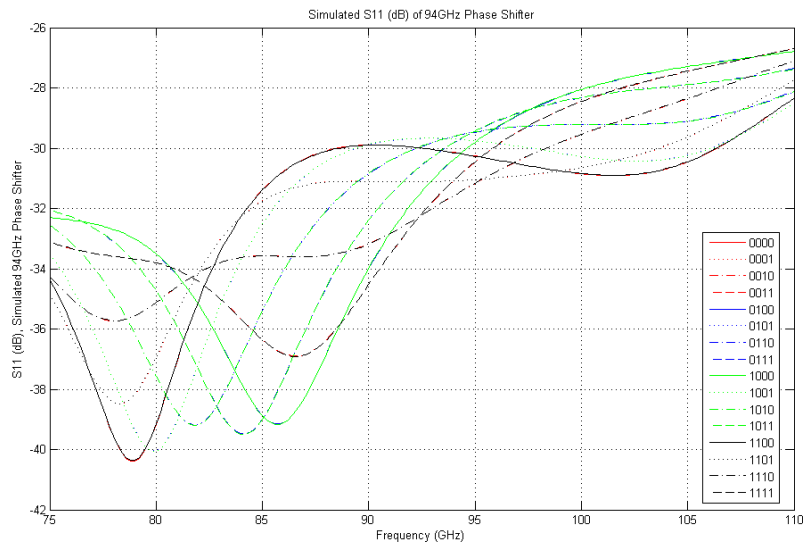


Figure 5.12 Simulated input port matching for all 16 different phase settings

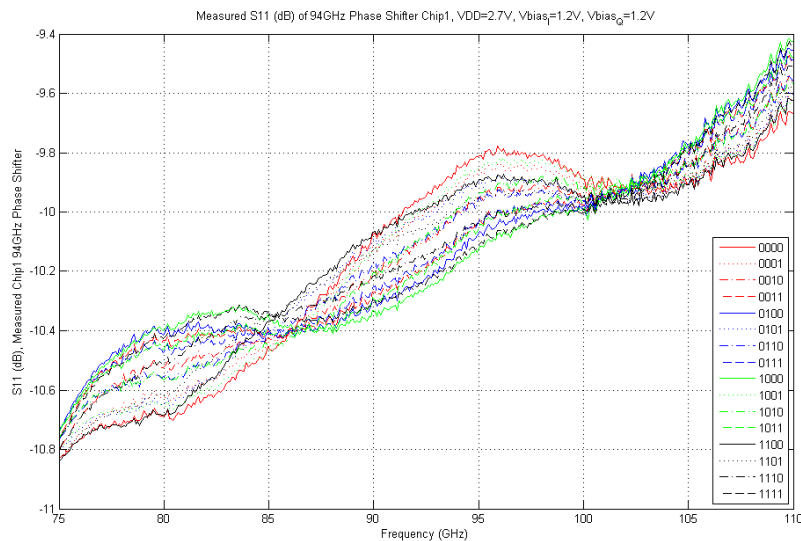


Figure 5.13 Measured input port matching for all 16 different phase settings

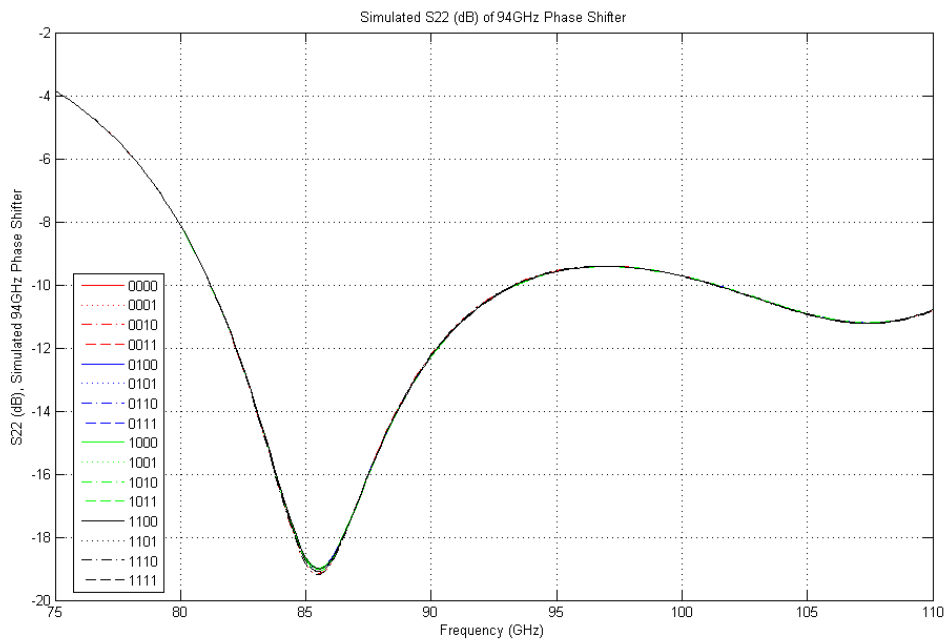


Figure 5.14 Simulated output port matching for all 16 different phase settings

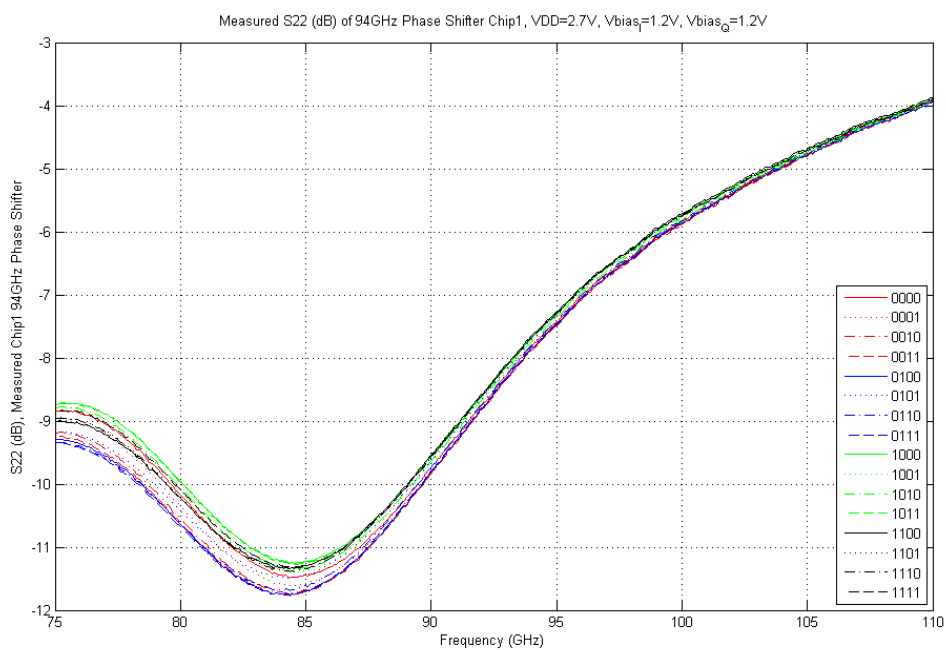


Figure 5.15 Measured output port matching for all 16 different phase settings

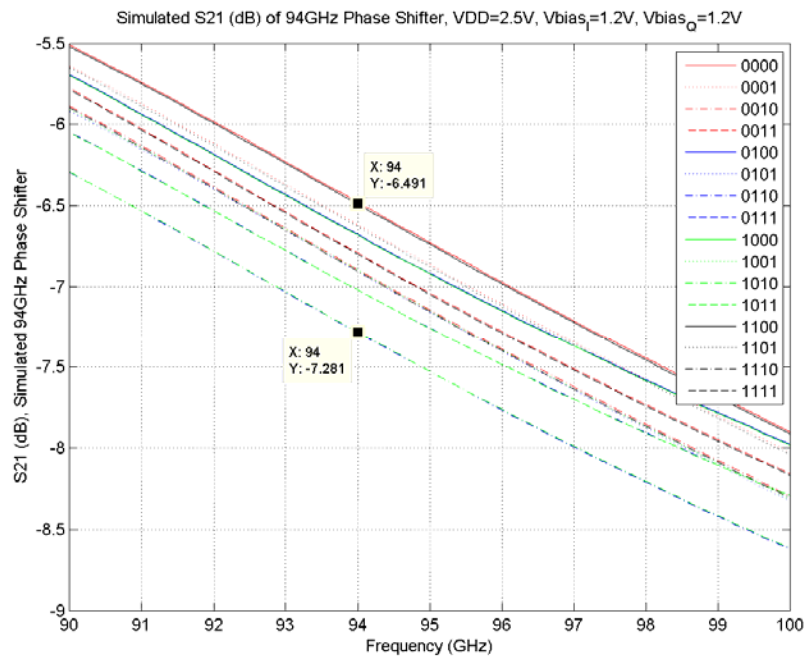


Figure 5.16 Simulated S21 for all 16 different phase settings

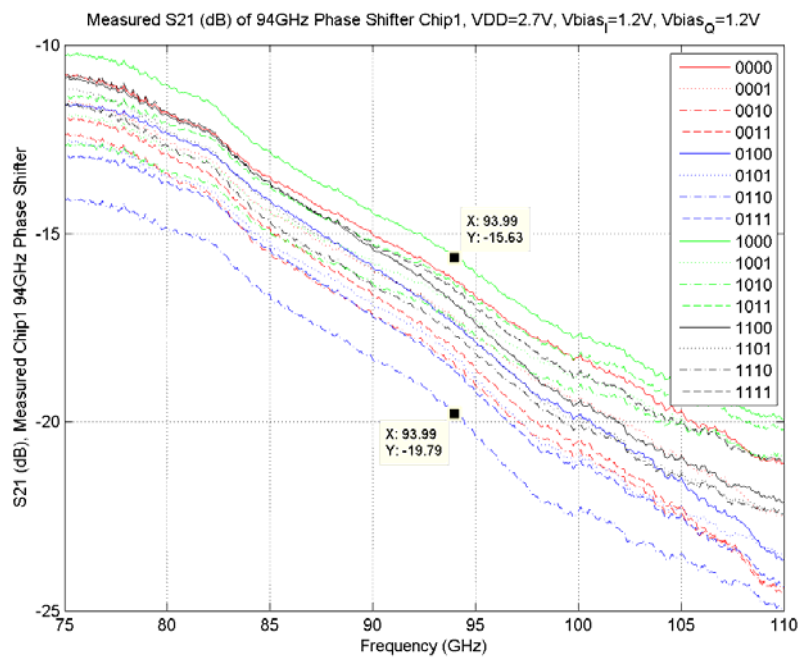


Figure 5.17 Measured S21 for all 16 different phase settings

Mr. Greene designed several vector-interpolator phase shifters in the following frequencies: 28 GHz, 60 GHz, and 94 GHz. All these designs used similar topology and design method, therefore a consistent discrepancy from designs in other frequencies is also found. At the input of the phase shifter, there are two back-to-back EM components: (1) a Lange coupler; and (2) a Marchand balun. Both components were designed and simulated in Sonnet. After comparing the same structures in Sonnet, Momentum and HFSS, Mr. Greene found that in some cases Sonnet was not consistent with the EM results determined with the other two software programs. An over-estimation of  $S_{21}$  in these two EM components could consequently cause the whole circuit's  $S_{21}$  to be overestimated. Other supporting evidence for our explanation comes from the  $S_{11}$  and  $S_{22}$  comparison. There is a large difference between the modeled  $S_{11}$  and the measured hardware, while the  $S_{22}$  featured reasonably consistent results between the modeled and empirical data. Therefore, it is highly possible that the EM characteristics of the Lange coupler and/or the Marchand balun were not accurately modeled by Sonnet, causing our overestimation of  $S_{21}$ .

On the other hand, there is an increase in  $S_{21}$  variance across the 16 phase settings. This comes from the mismatch and asymmetry in the layout between the in-phase and quadrature circuits. We constructed polar plots for six different cases, divided into two groups to investigate the effect of bias voltage on the in-phase and quadrature circuits. Three cases are shown in Figure 5.18, where the quadrature bias voltage,  $V_{\text{bias}_q}$  is fixed while the in-phase bias voltage,  $V_{\text{bias}_i}$  is swept from 0.8-1.6 V. The other three cases are shown in Figure 5.19, where the  $V_{\text{bias}_i}$  is fixed while the  $V_{\text{bias}_q}$  varies in the same fashion. We

observed that  $V_{\text{bias}_i}$  controls the phases near  $90^\circ$  and  $270^\circ$ , and  $V_{\text{bias}_q}$  controls the phases near  $0^\circ$  and  $180^\circ$ . Therefore these two biasing voltages need to be properly paired to get a uniform distribution of the S21 amplitude.

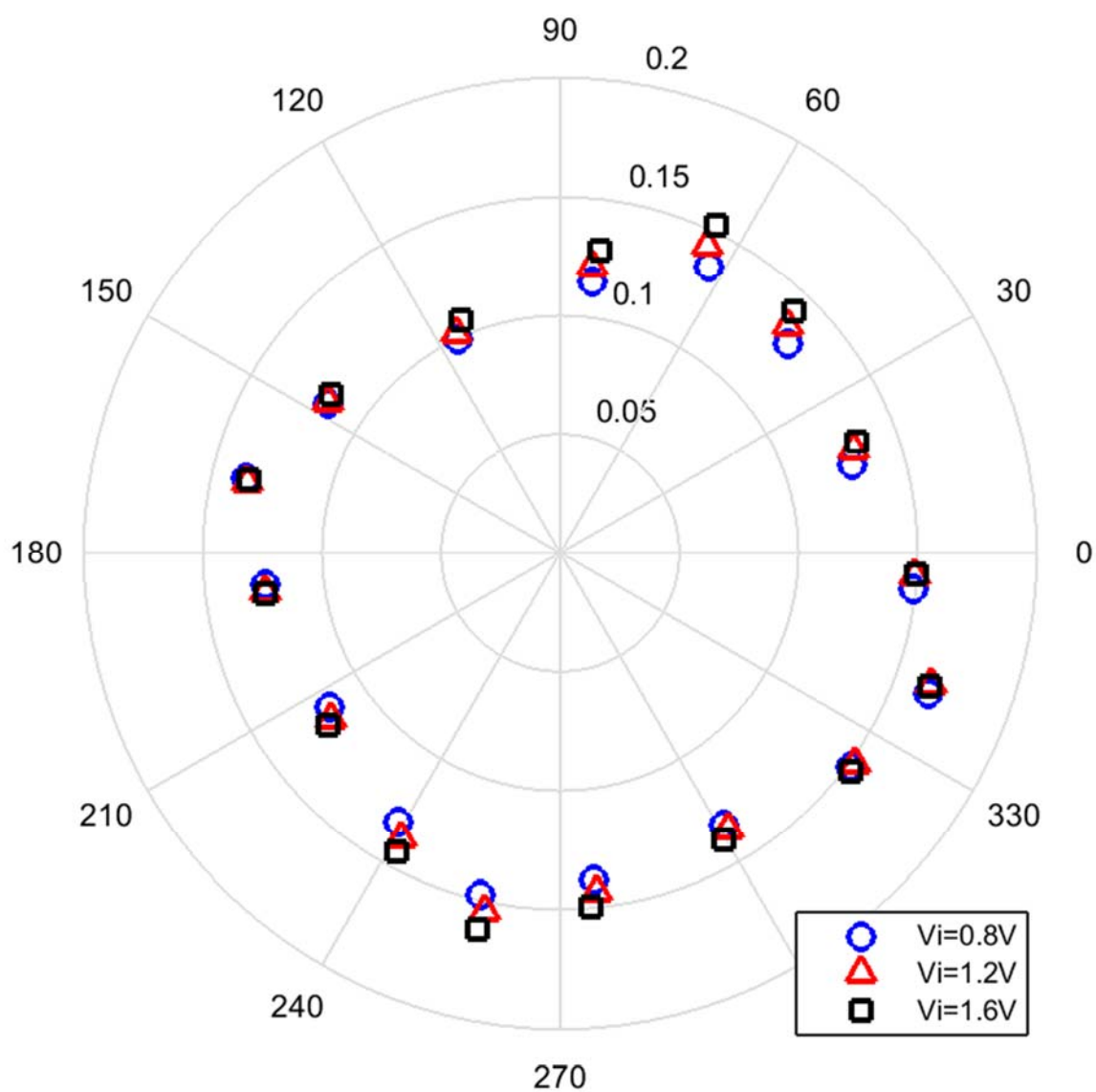


Figure 5.18 Comparison of the measured polar plots, where  $V_{\text{bias}_q} = 1.2\text{ V}$ , and  $V_{\text{bias}_i}$  varied

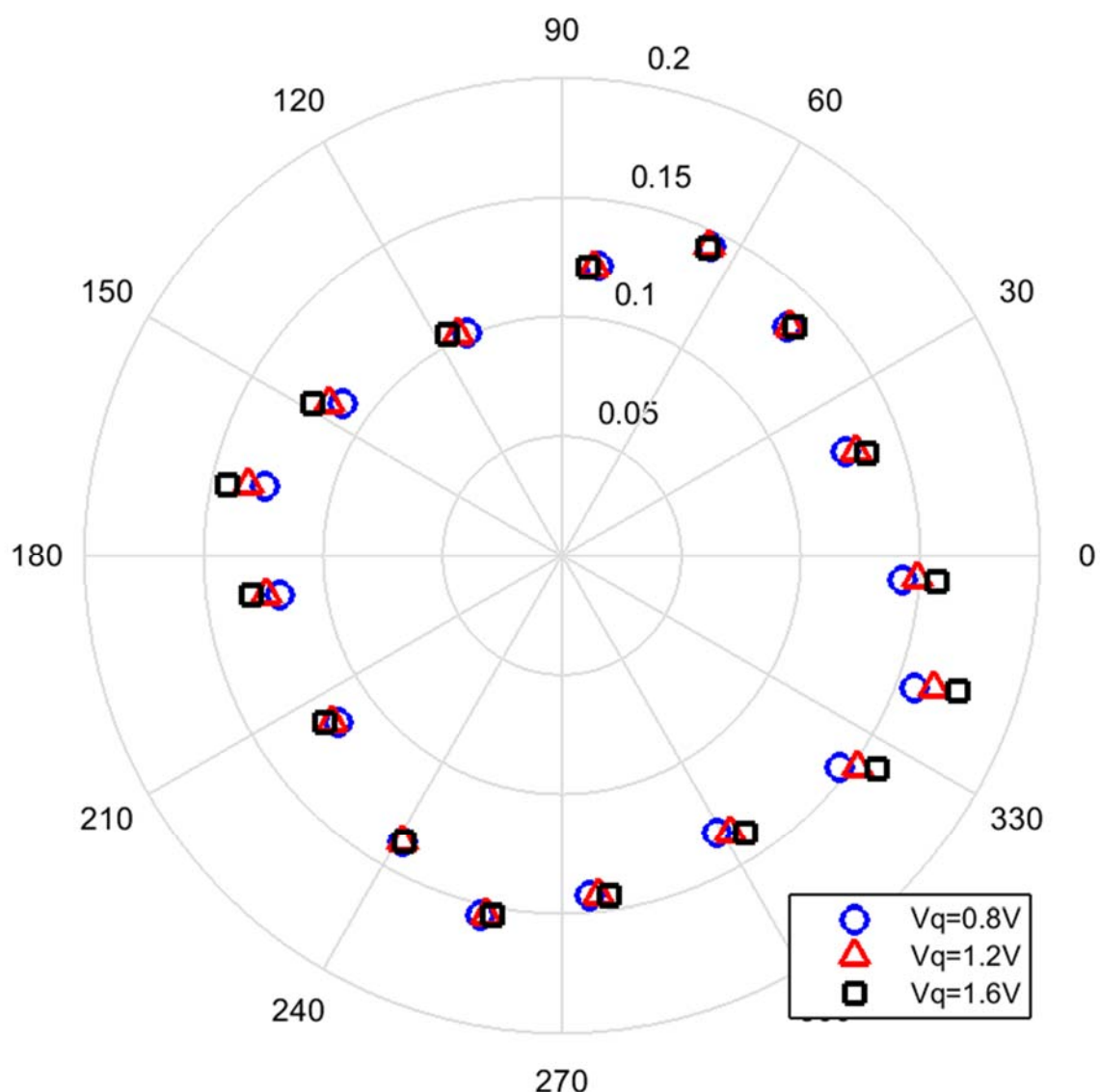


Figure 5.19 Comparison of the measured polar plots, where  $V_{\text{bias}_i} = 1.2\text{ V}$ , and  $V_{\text{bias}_q}$  varied

Since there are 16 phase settings controlled by four bits,  $V_{\text{bias}_i}$  and  $V_{\text{bias}_q}$  only have a dominant effect on the  $0^\circ$ ,  $90^\circ$ ,  $180^\circ$ , and  $270^\circ$  phases. Phases close to  $45^\circ$ ,  $135^\circ$ ,  $225^\circ$ , and  $315^\circ$  don't respond to these two bias voltages. Another degree of freedom should come from the balun at the very front of the circuit, which separates the input signal and feeds it into a

different quadrature. This balun was designed through EM simulation and the power level at its two outputs are not identical. From EM simulation, the result shows a difference of 0.25 dB between these outputs (as shown in Figure 5.20), however as we discussed above, the actual performance of the balun might deviate from the simulation. An extra 2-3 dB difference in the actual hardware performance compared to the EM model is possible.

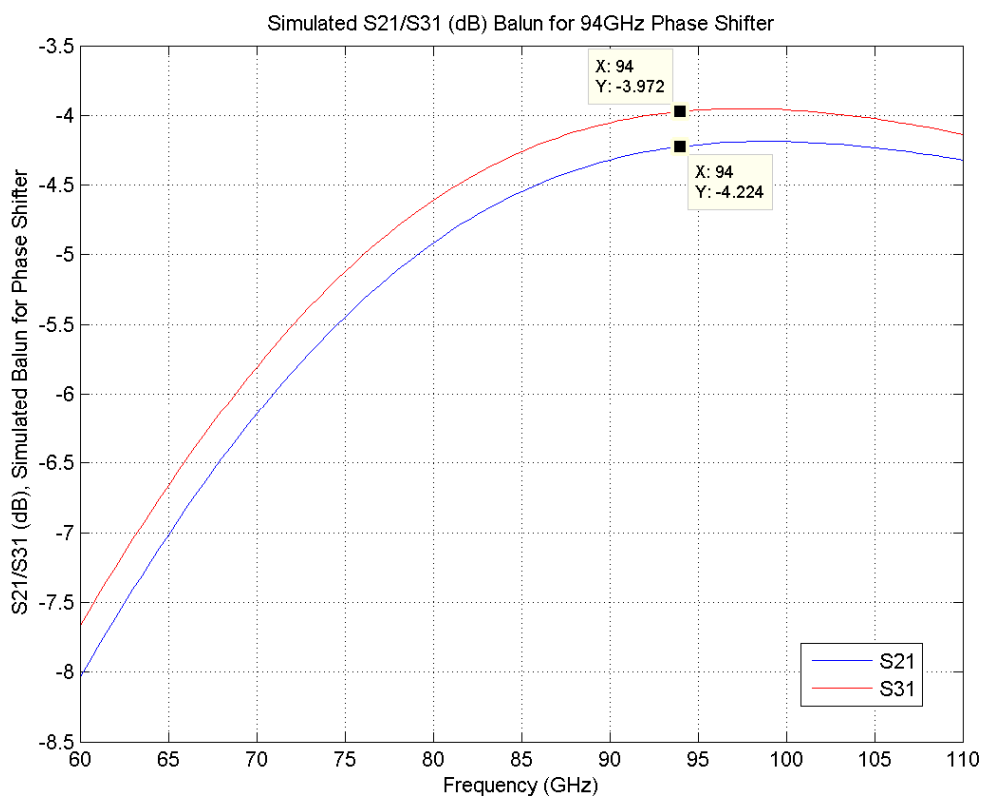


Figure 5.20 EM simulated S21 and S31 for the balun of the 94 GHz phase shifter

In summary for the 94 GHz phase shifter, the measured hardware performance has an obvious degradation compared to the simulation. The S21 for all 16 phase settings

unanimously decreases from the original estimate, which is dominantly caused by the first two stages of the EM simulated components: the Lange coupler and the Marchand balun. Other small effects come from the parasitic extraction.

### 5.5 Measurement of the Down-Converting Mixer from 94-18.8 GHz

In this section, the results of the down-converting mixer measurements are presented. The mixer's function is to take input signals at 94 GHz and multiply them with a 75.2 GHz LO signal, and finally amplify at the IF frequency. The actual hardware die photo is shown in Figure 5.21, with the RF port on the left, the LO on the right, the DC on the bottom, and the IF on the top. The following characteristics are important in defining a mixer and are therefore measured: (1) port matching; (2) input power compression point; (3) conversion gain; and (4) NF. Details of the calibration, measurement and comparisons of hardware and modeled results are discussed.

#### 5.5.1 Port Matching and SP Measurements

The mixer takes two input signals, RF at 94 GHz and LO at 75.2 GHz, and down-converts them to 18.8 GHz. It is important to make sure each port is well matched to their corresponding frequency band in order to filter out unwanted signals at the image frequency. Therefore an SP measurement was performed to measure the reflection coefficient at the ports. Unlike in the LNA and phase shifter, no transmission coefficient needs to be measured here, since the frequency conversion is involved. 1-port calibration was performed to set the

reference plane at the probe tip, as depicted in Figure 5.1. Case (a) was used for the LO and IF ports while case (b) was used for the RF port. The results are shown in Figures 5.22 and 5.23.

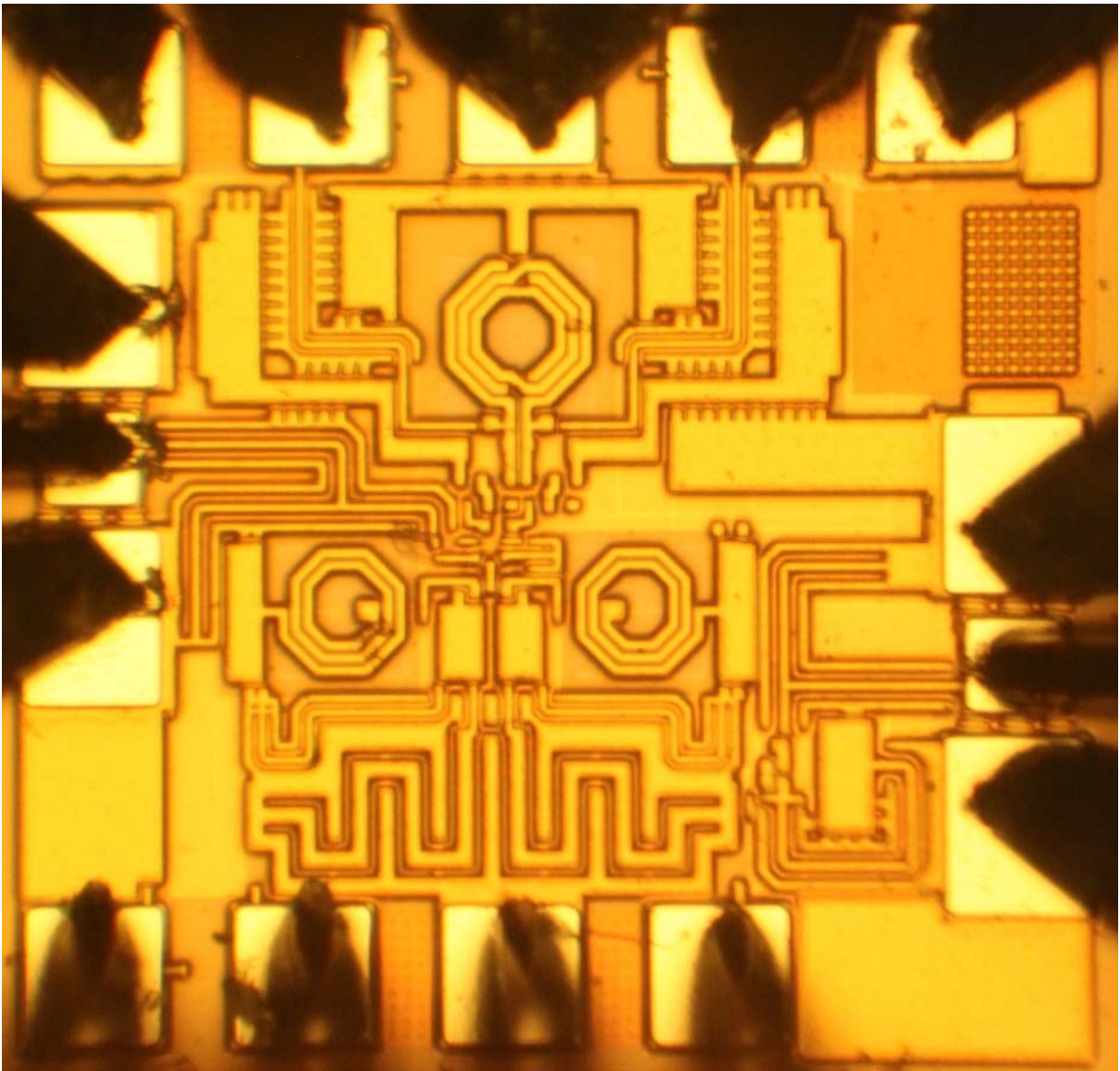


Figure 5.21 Die photo of the 94 to 18.8 GHz down-converting mixer

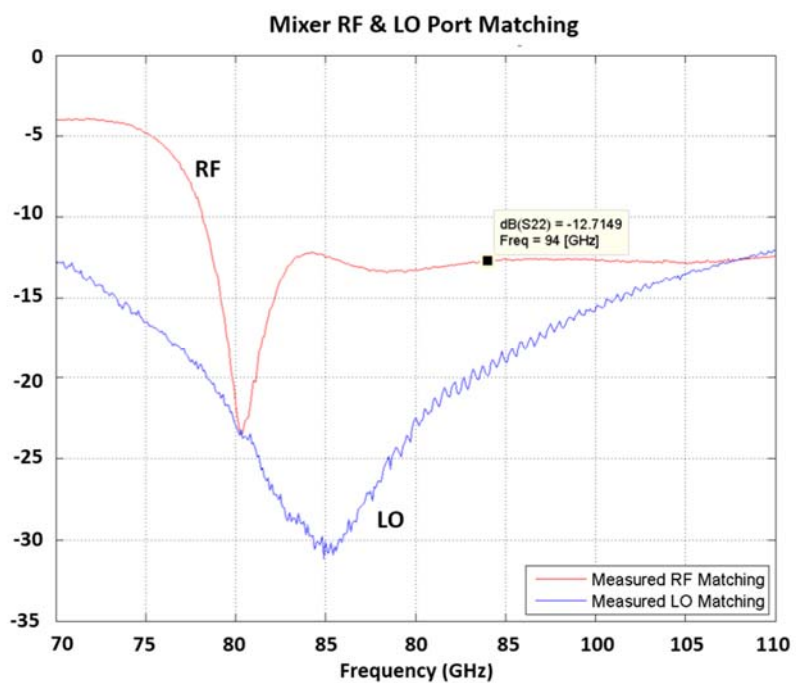


Figure 5.22 Measured RF and LO port matching of the down-converting mixer

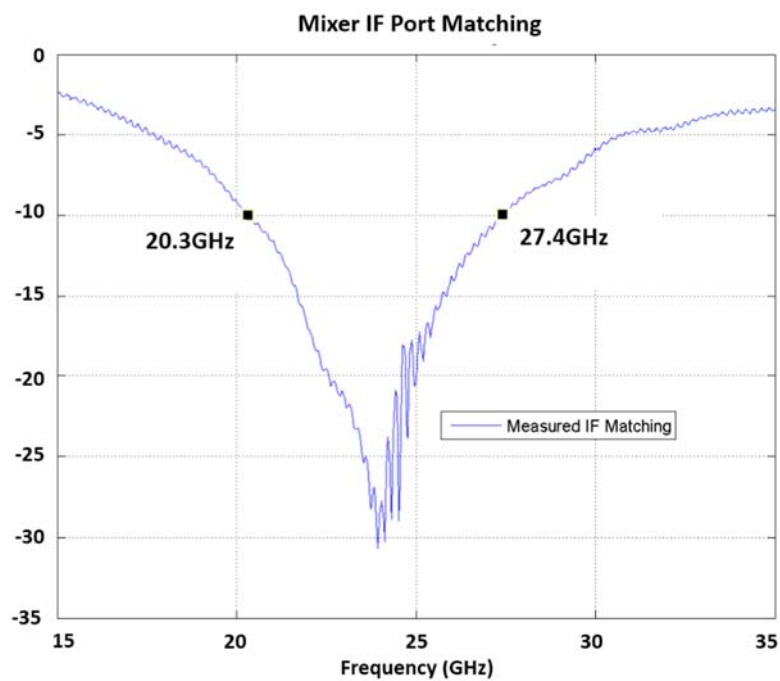


Figure 5.23 Measured IF port matching of the down-converting mixer

Compared to the simulation results shown in Figure 4.24, both RF and LO ports are well matched at their corresponding frequencies with just a shift in resonant frequency caused by minor differences between the extracted and actual parasitics. The measured results show that the matched ( $<-10$  dB) frequency range is even wider than originally estimated. For the IF port, the simulation shows a 3.8 GHz matched bandwidth, while the matched bandwidth of the experimental results is 7.1 GHz. Although the measured frequency range of the matched ( $<-10$  dB) shifted up, it was found out that during parasitic extraction for the mixer, the exact same bond pad model used at 75 GHz was used at IF port, thereby overestimating the parasitic capacitance for the 19 GHz IF port, causing the frequency shift. On the other hand, in the prototype array, the RF input pads were removed, so this error was naturally eliminated.

## 5.5.2 Power Measurement for the Compression Point and Conversion Gain

### 5.5.2.1 Power Calibration

Figure 5.24 illustrates the setup for a mixer power measurement. Since both RF and LO frequency are above 70 GHz, 75-110 GHz frequency extenders were used for up-conversion, which takes an input and multiplies its frequency by six. Therefore, both the PNA and signal generator include a multiplier factor of six in their configurations. Before building the whole setup as in Figure 5.24, two calibration steps were first performed:

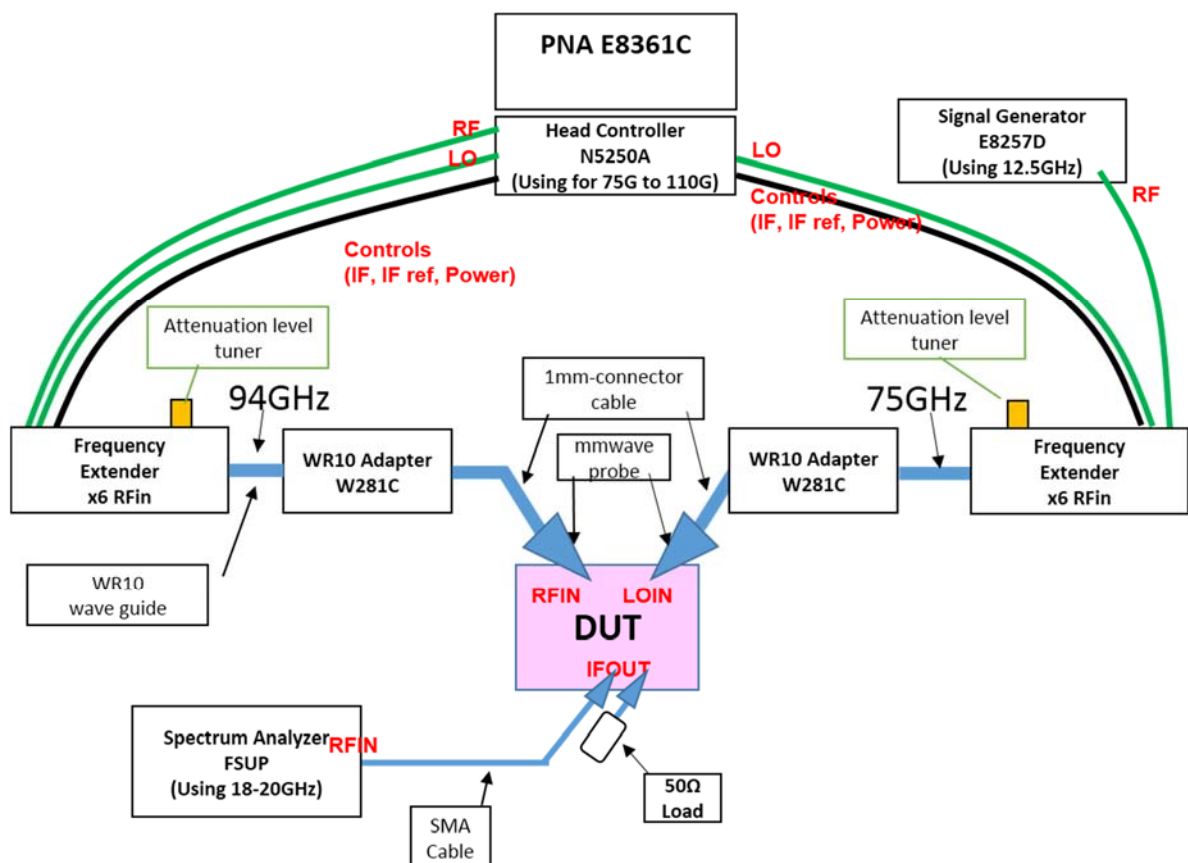


Figure 5.24 Illustration of the mixer power measurement setup

1. Measure the absolute power at the nodes where the “94 GHz” and “75 GHz” arrows point, which are the output ports of the frequency extender. The method is illustrated in Figure 5.25. The power meter with a connected sensor was able to find the absolute power at the aforementioned “nodes” The output power level was no longer controlled by the equipment, rather by the “attenuation level tuner” on the frequency extender;

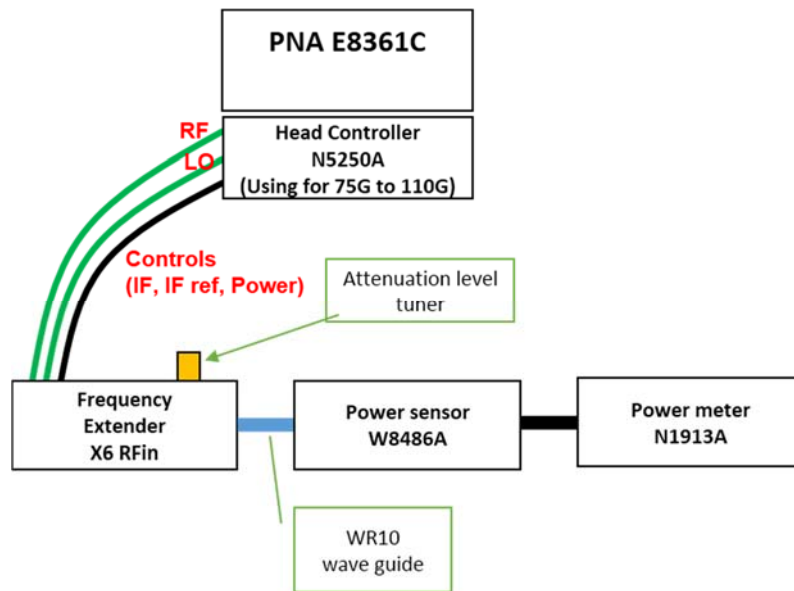


Figure 5.25 Illustration of the power calibration method described in step 1

2. The path loss between the “nodes” and their corresponding probe tip can be measured using the configuration in Figure 5.26. Since this path only contains three passive components: WR10 adapter; 1 mm cable; and the MMW probe (we define them as Path1 for the RF side and Path2 for LO side), it was possible to use SP information to determine their loss in the following steps:
  - a. With the reference plane already at the output of the frequency extenders, both probes were landed on to the “THRU” pattern in the CS-5 calibration kit (as shown in position (a) in Figure 5.26). The S21 seen from the PNA was the aggregated path loss including Path1 and Path2;
  - b. Both probes were removed from the pattern, leaving both paths open in air (as shown in position (b) in Figure 5.26). The S11 reading is the back and forth loss of Path1 and S22 is the same for Path2.

c. Loss of both paths were then calculated through the following equations:

$$Loss_1 = \frac{S11}{S11 + S22} \cdot S21 \quad (5.13)$$

$$Loss_2 = \frac{S22}{S11 + S22} \cdot S21 \quad (5.14)$$

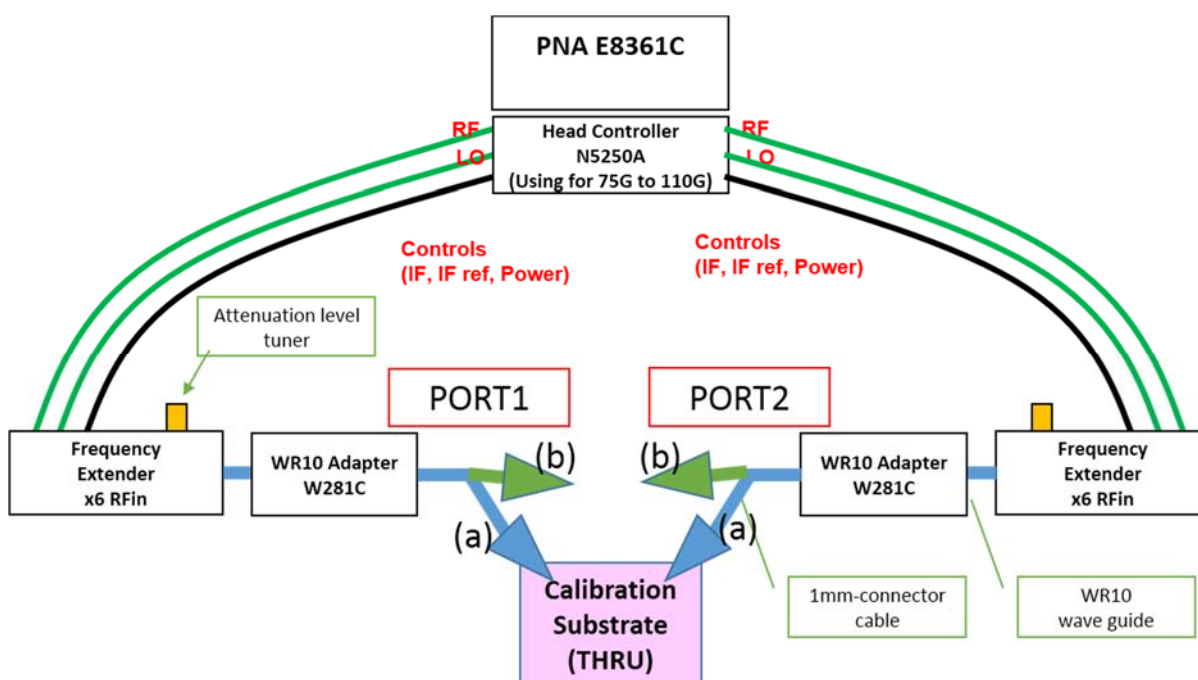


Figure 5.26 Illustration of the power calibration method described step 2

With step 1 and 2 of the calibration process, we were able to find the absolute power at both the RF and LO probe tips. For the IF port, since we measured the power of only several frequencies, the loss was directly calculated using the manufacture specifications for the SMA cable, two adapters, and the IF probe. Thus, the power level referred to the probe tips for all three ports was available.

### 5.5.2.2 Optimal LO Input Power

In order to find the best possible conversion gain, the optimal LO input power needs to be determined first and used thereafter. In the meantime, the RF input power was set very low so as to ensure no signal compression would occur. Figure 5.27 shows the results of the conversion gain while the LO power was swept. The conversion gain is calculated as shown in Eq 5.15. The same calculation is applied throughout the rest of the work.

$$G(\text{dB}) = P_{IF}(\text{dBm}) - P_{RF}(\text{dBm}) \quad (5.15)$$

As the results in Figure 5.27 show, when the LO power is at -8.1 dBm, the mixer gives a peak conversion gain of 6.2 dB. The compression point is about 1 dB higher than the simulated. From this point on, all the mixer measurements were performed when the LO power was set to -8.1 dBm.

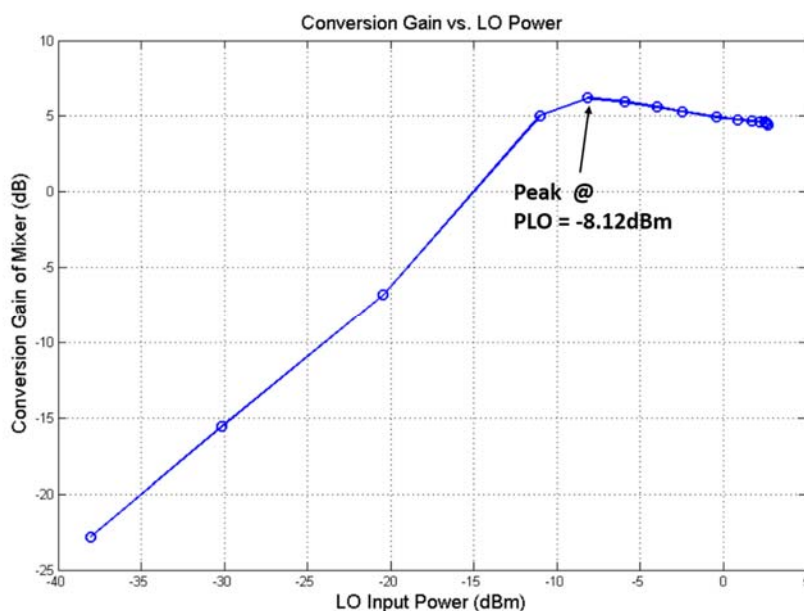


Figure 5.27 Measured mixer conversion gain while sweeping the LO input power

### 5.5.2.3 Optimal RF Input Power

In last section, we set the RF input power very low to insure that there was no signal compression within the signal path. With the optimal LO power determined, we swept the RF power to find the input referred 1 dB compression point for the mixer, as shown in Figure 5.28. The measured  $P_{1dBin}$  was  $-10.8$  dBm, which is  $1.3$  dB higher than to our simulated results shown in Figure 4.27. The linearity of the actual mixer worked as projected, and from this point on, the RF power was set to around  $-25$  dBm to ensure no compression occurred. In the meantime, the IF output level was kept above the spectrum analyzer's noise level as much as possible.

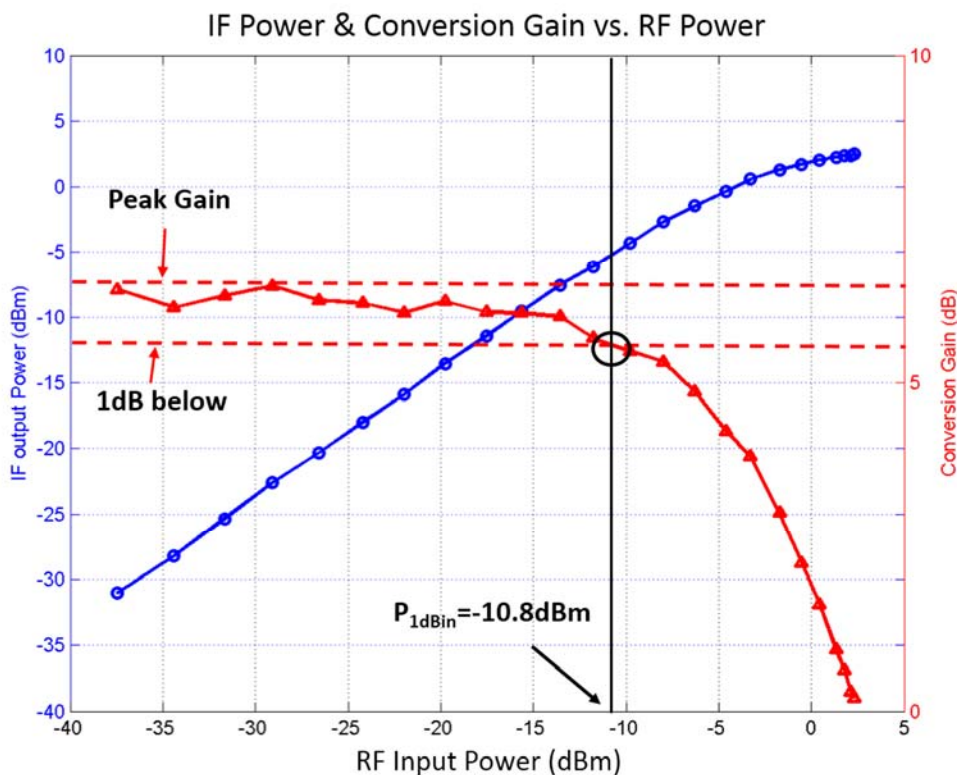


Figure 5.28 Measured mixer IF output power and conversion gain while sweeping RF power

#### 5.5.2.4 Conversion Gain with Fixed LO Frequency and Swept RF Frequency

After finding both the optimal LO and RF input power level, multiple frequency sweeps were performed to observe the frequency response at all three ports. In this subsection, the LO frequency was fixed at 75 GHz first, while the RF frequency was swept. Results are plotted in Figure 5.29. A peak gain of about 95 GHz was achieved, with a value of 9.3 dB. This was measured through a single-ended setup, therefore 3 dB should be added for a 12.3 dB differential gain. Compared to the 20.2 dB simulated value, the actual circuit produces 8 dB less gain than expected, while the 3 dB bandwidth shrinks by about 2 GHz. On the other hand, since the RF and LO ports were both well matched, the frequency response curve should have reflected the IF port matching. In Figure 5.26, the 3 dB band corresponds to the IF from 17-22 GHz, which coincides with the up-shifted IF frequency band found in the SP measurements.

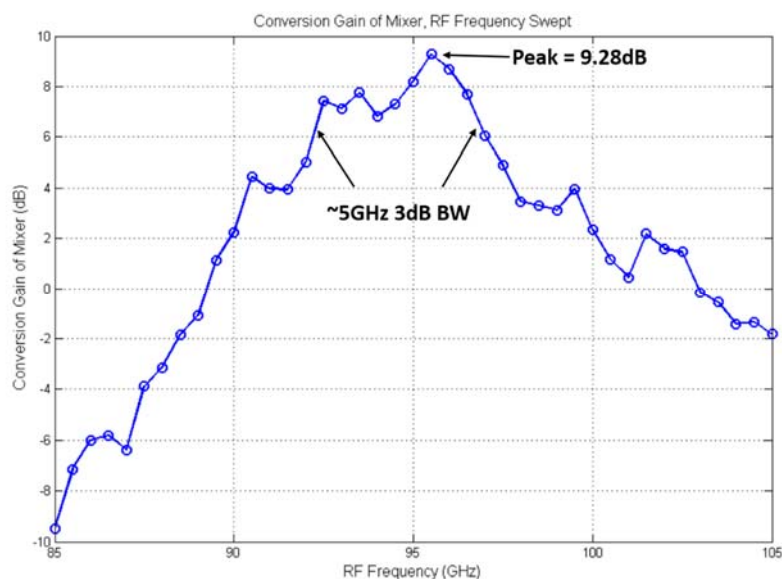


Figure 5.29 Measured mixer conversion gain, while the RF frequency is swept

### 5.5.2.5 Conversion Gain when RF and LO Frequencies were Simultaneously Swept

From the last measurement, we found that the IF frequency response coincides with what we found from the SP measurement. Next we varied the IF frequency at five discrete values (16, 17, 18, 19, and 20 GHz), and observed the frequency response at the RF and LO ports. The parametric measurement results are shown in Figure 5.30.

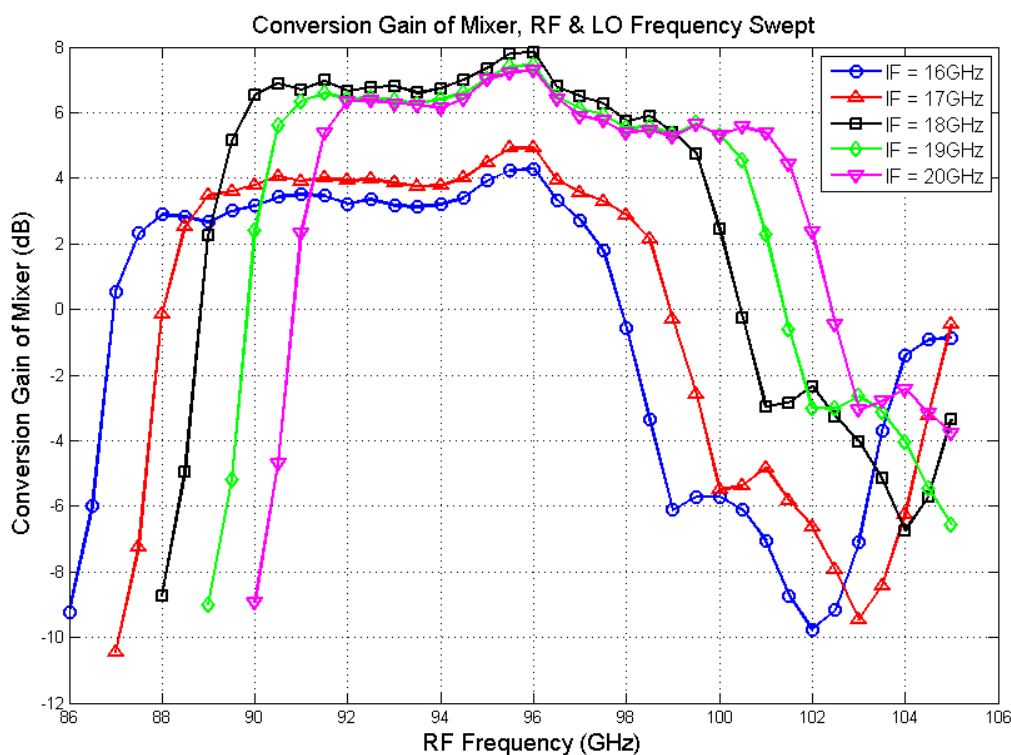


Figure 5.30 Measured mixer conversion gain, with swept RF and LO, while the IF is fixed at five frequencies

There are some interesting observations from Figure 5.30. First, we observed the peak gain varied with IF frequency. It was low when the IF frequency was outside of its measured

operation band, while it increased when the IF frequency was set within the operation band (*e.g.* when IF = 18, 19, and 20 GHz).

Secondly, we found that the frequency response of each individual curve moved along with the LO frequency. The observations are summarized in Table 5.1.

Table 5.1 Summary of observations from Figure 5.30

Color, IF (GHz)	Corner 1 (Low Frequency)		Corner 2 (High Frequency)	
	RF (GHz)	LO (GHz)	RF (GHz)	LO (GHz)
Blue, 16 GHz	88	72	97	81
Red, 17 GHz	89	72	98	81
Black, 18 GHz	90	72	99	81
Green, 19 GHz	91	72	100	81
Pink, 20 GHz	92	72	101	81

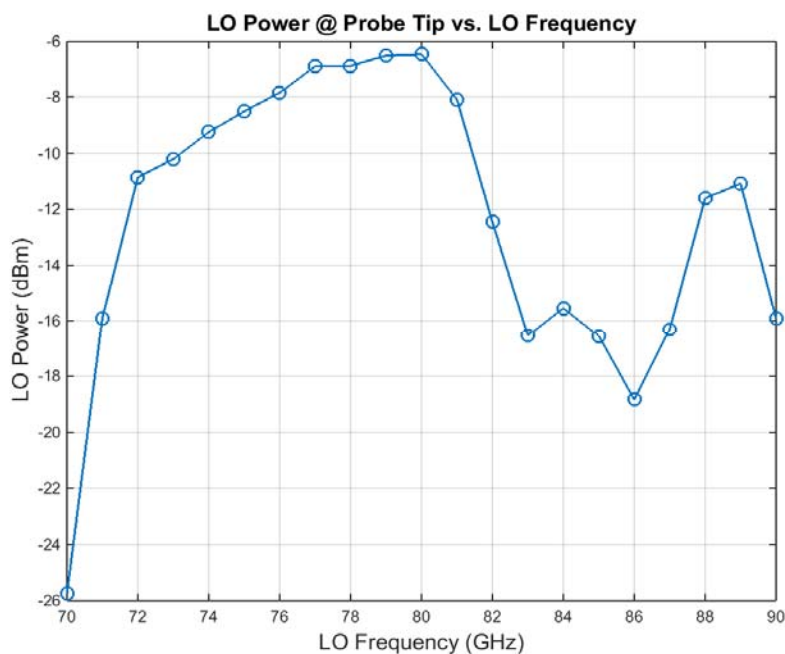


Figure 5.31 The LO output power at the probe tip *vs.* the input frequency, while the output power of the signal generator is fixed at -8.5 dBm

The observations in Table 5.1 apparently show that the frequency response was not limited by the RF band, rather by the LO port response. All 5 measurements indicate that the conversion gain of the mixer was at its optimal performance when the LO ranged from 72-81GHz. However it is not fair to directly conclude that our LO port is only matched at that the 9 GHz range. Rather, we looked again at the actual LO power at the probe tip. The LO power, as illustrated in Figure 5.1, was generated from Agilent E8257D signal generator, while its output power level was fixed at -8.5 dBm. The LO signal passed through the VNA frequency extender, cables and provided its power to the probe tip. The actual LO power measured versus frequency is plotted in Figure 5.31. The curve looks very similar to all five curves shown in Figure 5.30, implying that when the LO power is not sufficient at the probe tip, the conversion gain of the mixer drops. The LO power raises back up at 88 GHz, and the corresponding raise in conversion gain is also be observed in Figure 5.30. Therefore, we draw a conclusion that the frequency response showing only 9 GHz LO bandwidth is caused by the frequency band limit from the VNA frequency extender, not the LO circuitry in our mixer. The LO buffer still provides a relatively wide bandwidth for the mixer to work in its designed frequency range.

#### 5.5.2.6 Summary of Power Measurement

In the power measurement section, the power calibration method was introduced first. Then two power sweeps were performed to find the best LO and RF input power for the mixer to function properly. This was followed by several frequency swept measurements and

the observed results were consistent with the frequency response derived from the simulation.

The actual DC biasing condition for the mixer in all these measurements should be discussed. The VCC was set to 3.3 V to make the whole mixer consume 37 mA of current to facilitate comparisons with the 40 mA simulated value using a 2.5V VCC. The higher VCC provided a larger headroom for the signals and improvement in the conversion gain was observed. The IFVGA's  $V_{agc}$  has been tested as well and gain variance can be achieved. However maximum gain setting was used for all the measurements to compensate for the unexpected loss in conversion gain.

The big issue we found for the mixer was its significant reduction in conversion gain. There may be several reasons that caused this to happen:

1. The topology chosen for the LO buffer is a cascode, which works well as an LNA. However its stacked transistor topology could cause a swing headroom issue, thereby limiting the swing ability of the LO signal. A possible solution would be to add a cascaded stage of emitter-follower and would be included as a future work if there were an opportunity for another tape-out.
2. The Marchand balun following the LO buffer was also designed based on the EM simulation modeled in Sonnet. The simulation results in Figure 4.25 shows it a very well designed balun, however we have seen and confirmed that two EM components in the phase shifter designed in a similar manner show extra loss in the actual

hardware measurements. Therefore, it is also very likely that the balun here leads to additional attenuation of the LO signal.

### 5.5.3 Noise Measurement for NF

#### 5.5.3.1 Noise Calibration

As described in Section 5.2.3, de-embedding of the measuring instruments needs to be performed. The Y-factor technique was used to measure the NF of the instruments first. Data was recorded with the noise source in the ON and OFF status. One initial measurement on the instrument (Rohde & Schwarz FS-Z60 Spectrum Analyzer) was performed as illustrated in Figure 5.32(a). However the instrument itself had a high noise and the reading between the ON and OFF status was not distinguishable, causing a small Y-factor and non-trustworthy NF data. Therefore an ultra-wideband amplifier with at least 20 dB gain and less than 5.5 dB NF was used at the input port of the spectrum analyzer to reduce the NF of the instrument (from now on, the measuring instrument refers to the spectrum analyzer with the pre-amplifier). After the alteration, the instrument was re-measured as illustrated in Figure 5.32(b). The measured Y-factor, together with the provided ENR of the noise source was used to calculate the NF. With proper pre-amplification, the instrument had a measured NF of less than 7.2 dB. The ENR of the noise source and the NF of the instrument are plotted in Figure 5.33.

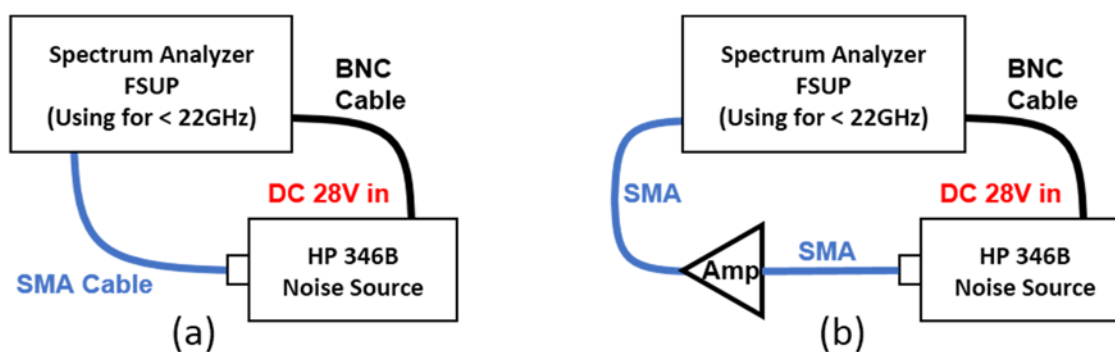


Figure 5.32 The (a) initial setup and (b) final setup of the NF measuring instrument

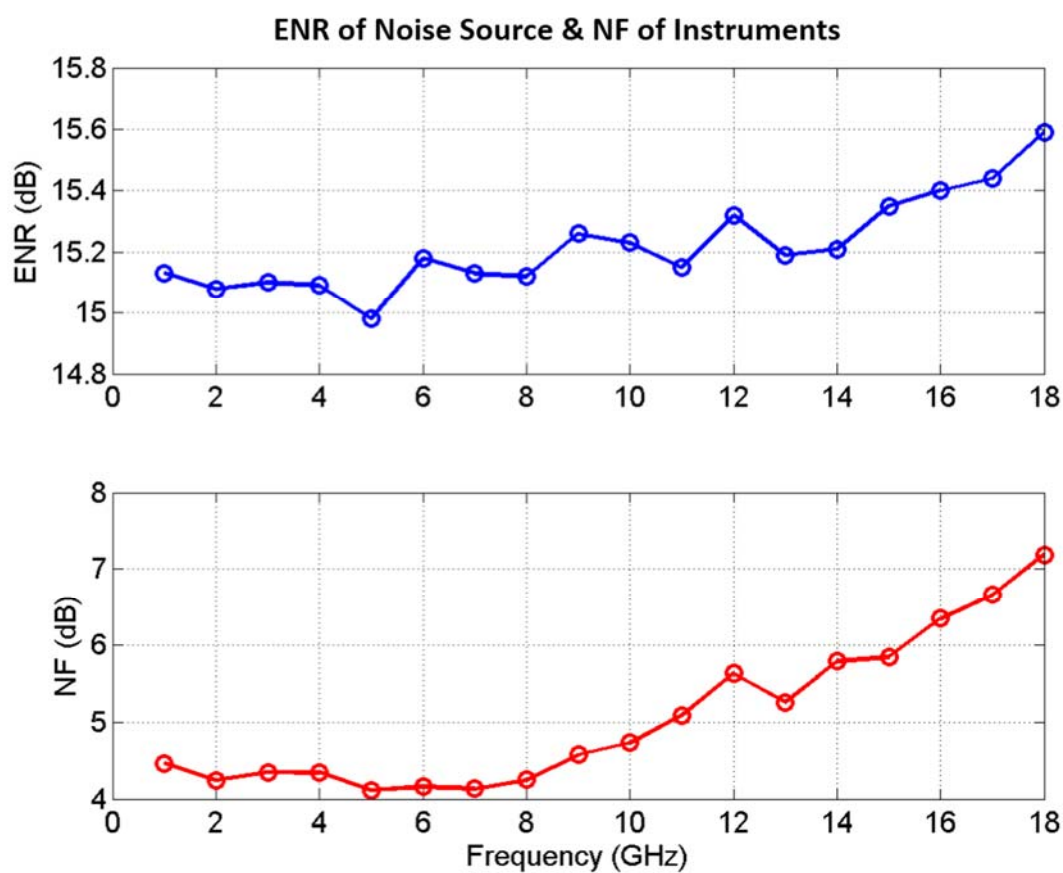


Figure 5.33 ENR of the noise source (top) and the measured NF of the instrument (bottom)

### 5.5.3.2 Noise Measurements and Results

In this section, measurement of the mixer NF was performed. The setup is illustrated in Figure 5.34. A different noise source (QuinStar QNS-FB12LW) at the W-band was used to excite the mixer RF port, while the LO port maintained the same setup as in the power measurement. The Y-factor was measured and the corresponding NF for the DUT followed by the measuring instrument was calculated. Then de-embedding of the measuring instrument was performed with the NF of the instrument and other passive connection accessories. The NF results are shown in Figure 5.35.

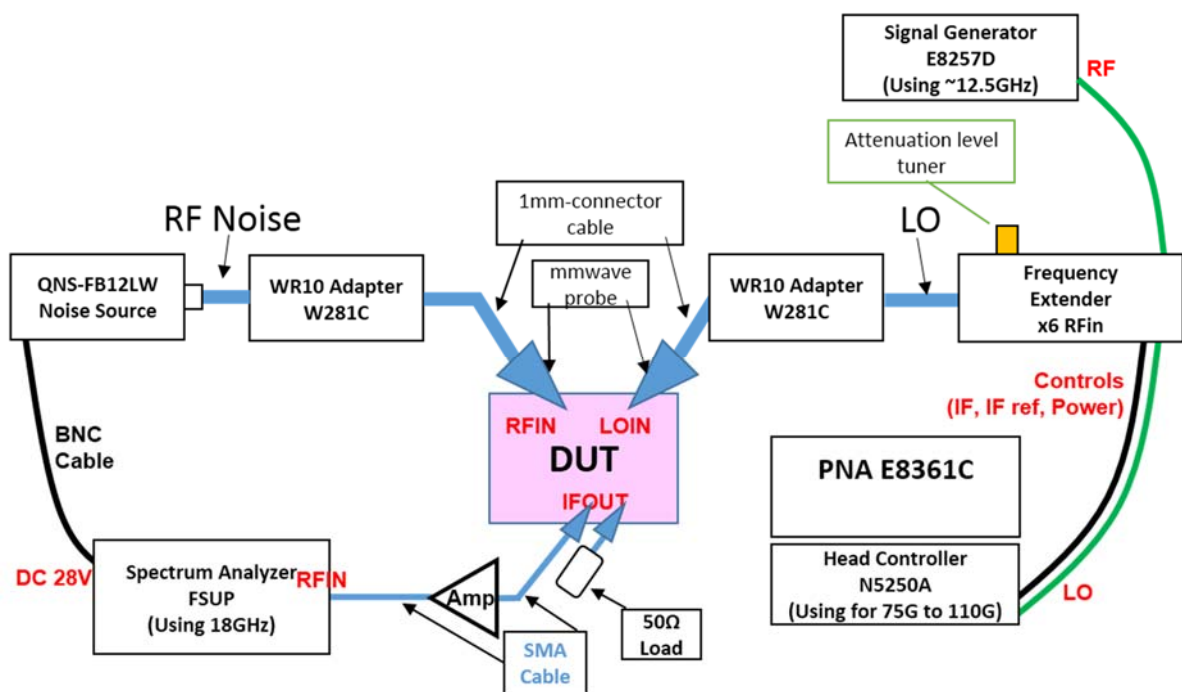


Figure 5.34 Setup of the mixer noise measurement

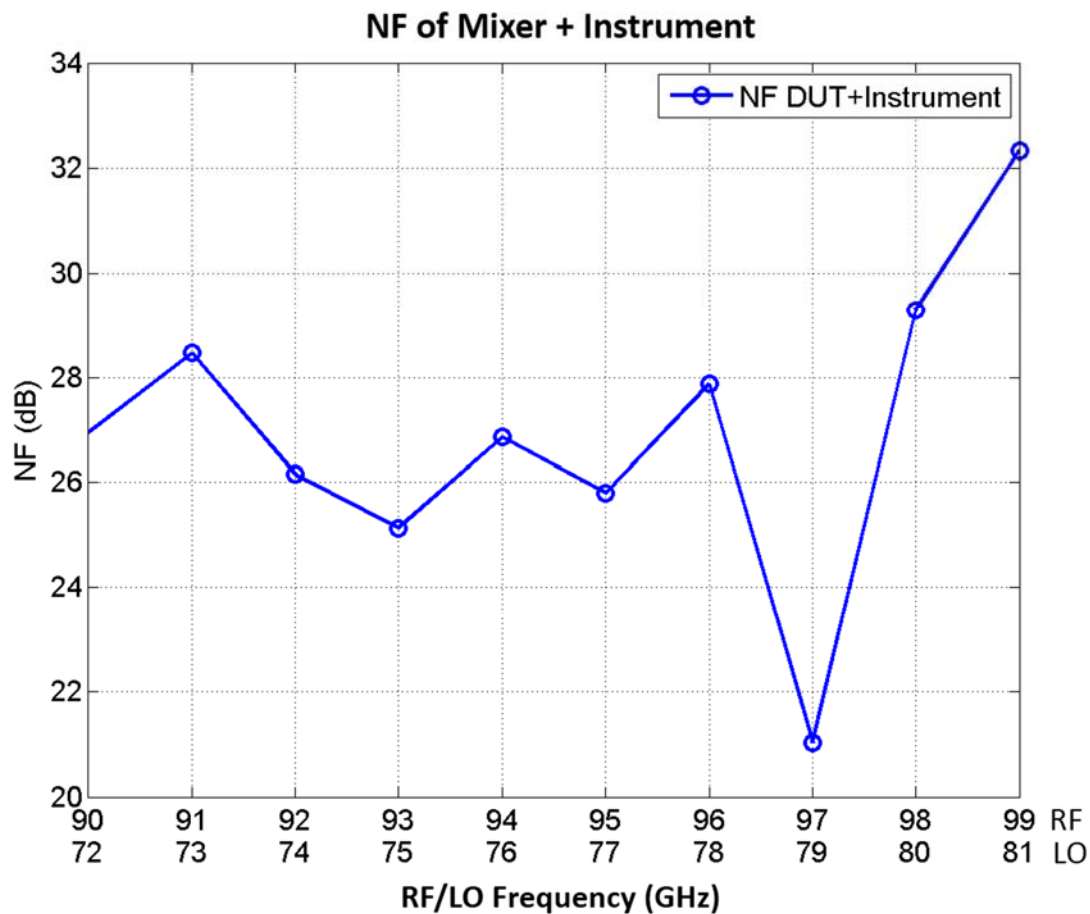


Figure 5.35 Measured NF for the mixer and instrument

According to the setup shown in Figure 5.34, there are several components that need to be de-embedded and the details are described below. Components will be grouped in several stages, and “Stage n” has its corresponding gain and noise factor defined as “ $G_n$ ” and  $F_n$ ”.

Stage 1: WR-10 to 1 mm adapter + 1 mm cable + w-band probe

Stage 2: Mixer

Stage 3: IF probe + SMA Cable

Stage 4: Instrument (Amp + SMA Cable + Spectrum Analyzer)

The total noise factor including all four stages is define as:

$$F_{TOT} = F_1 + \frac{F_2 - 1}{G_1} + \frac{F_3 - 1}{G_1 G_2} + \frac{F_4 - 1}{G_1 G_2 G_3} \quad (5.16)$$

Stage 1 is purely passive, so:

$$F_1 = L_1 = 1/G_1 \quad (5.17)$$

where  $G_1$  was measured during power calibration. Stage 2 is the DUT, which is the mixer in this case, whose gain was measured in Section 5.5.2.5. To be more precise for this case,  $G_2$  used here is exactly the black curve shown in Figure 5.30. Stage 3 is also purely passive and the conversion loss data was acquired from the component's specifications. Stage 4's  $F$  was obtained in the last section. Therefore we have found all parameters in Eq. 5.16, so  $F_1$  can be derived as below:

$$F_{TOT} = F_1 + F_1(F_2 - 1) + \frac{F_1(F_3 - 1)}{G_2} + \frac{F_1 F_3(F_4 - 1)}{G_2} \quad (5.18)$$

$$F_{TOT} = F_1 F_2 + \frac{F_1(F_3 F_4 - 1)}{G_2} \quad (5.19)$$

$$F_{mixer} = F_2 = \frac{F_{TOT}}{F_1} - \frac{F_3 F_4 - 1}{G_2} \quad (5.20)$$

Mixer NF was calculated and plotted in Figure 5.36. The measured NF is about 5-7 dB higher compared to simulation results shown in Figure 4.26. Additionally, the data points were not as stable as the NF measured for the instrument. The reason for this is due to the significant loss in conversion gain for the actual mixer circuit. When measuring  $F_{TOT}$ , the aggregated conversion gain from Stage 1 through Stage 3 is less than 0 dB, which indicates a

conversion loss. The noise power from the noise source is actually attenuated rather than amplified by the mixer. The attenuated signal is then compared to that when the noise source is OFF by the instrument. Excessive attenuation makes it more difficult for the instrument to distinguish the difference between the ON and OFF states, which is quantitatively interpreted by a very small Y-factor, approaching 1. We also observed an increased NF at higher frequency, which should come from further reduced conversion gain at the higher LO frequency, as stated in Section 5.5.2.5.

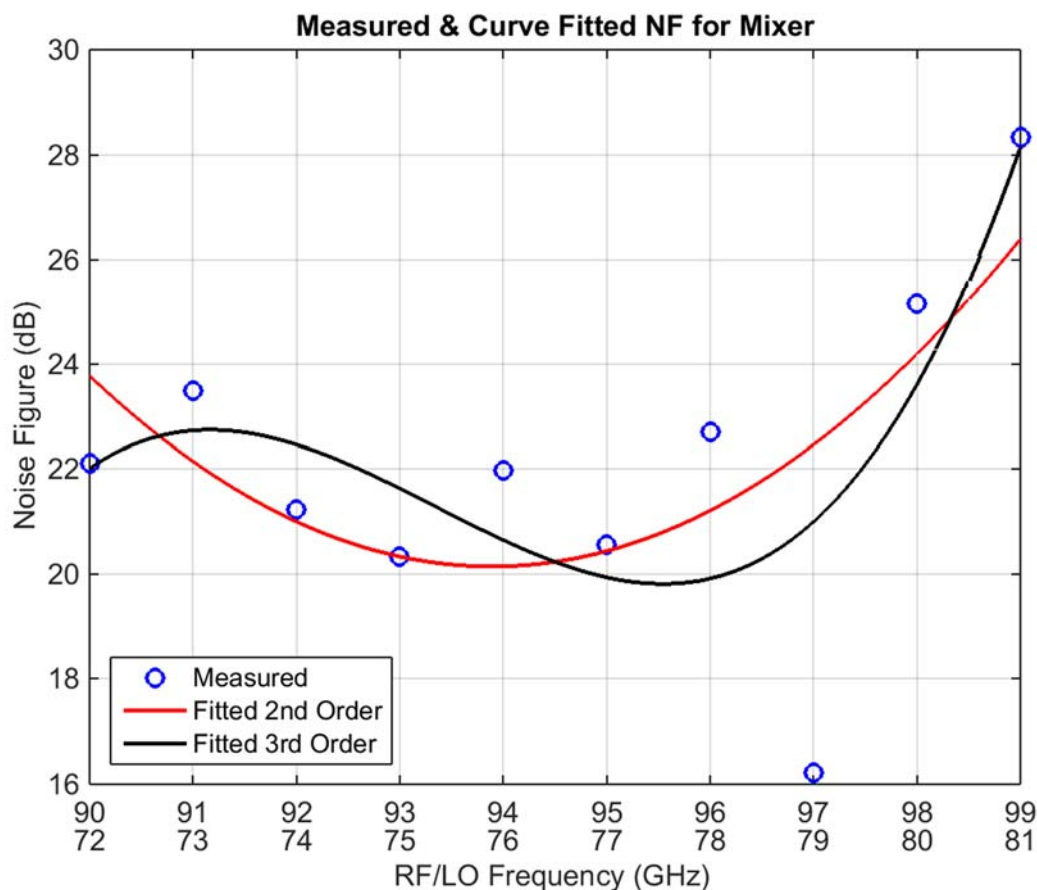


Figure 5.36 Measured NF of the mixer at IF = 18 GHz, while RF and LO frequencies swept

The hypothesis was confirmed by making another mixer NF when the IF frequency was 17 GHz, shown in Figure 5.37. Nonetheless, the results still demonstrate that the instrument has difficulty distinguishing the noise power between the ON and OFF status.

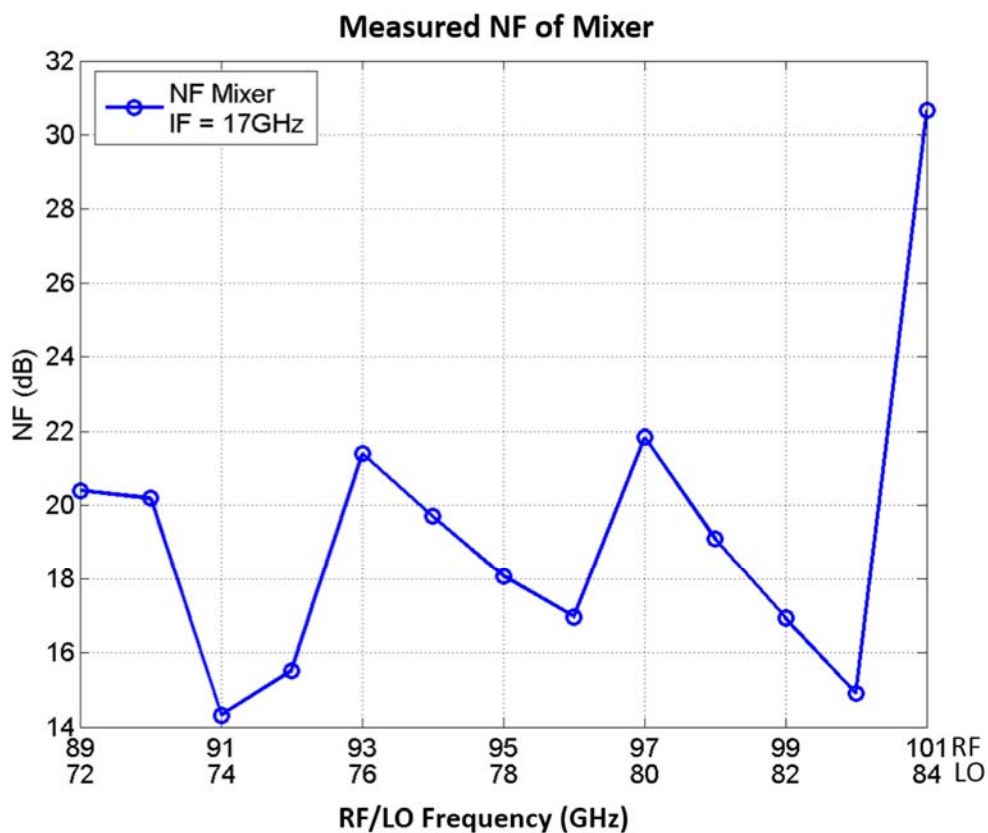


Figure 5.37 Measured NF of the mixer at IF = 17 GHz, while RF and LO frequencies swept

#### 5.5.4 Summary for Mixer Measurement

Three sets of measurements were performed on the mixer. SP measurements proved this 94-18.8 GHz down-converting mixer matched all three ports, however with some frequency shift at the RF port, which can be removed during assembly of the prototype array.

In the power measurement, the optimal RF and LO input power for the best conversion gain was found first and these values were used in all the following power and noise measurements. Conversion gain of the mixer was measured while sweeping the RF and LO frequency, showing good agreement with the frequency response that was determined with the SP measurements. However, the lack of LO swing and the misestimation of the EM components caused significant loss in conversion gain, which consequently, results in extreme difficulty in precise measurement for the noise figure of the mixer. The measured mixer NF is about 5 dB higher than the simulated results, but the degree of confidence for this data is not high, because the combination of the mixer with the cables and adapters creates a conversion loss for the DUT. The measured performance of the mixer is summarized below:

Table 5.2 Summary of the measured performance of the 94-18.8 GHz down-converting mixer

Specification	This Work
IF Frequency	18.8 GHz
NF	20-23 dB (89-97 GHz)
Conversion Gain	9.2 dB peak @ 95 GHz input 3d B BW (5 GHz)
P1db (input)	-10.8 dBm
Power Consumption	3.3 V 37 mA (LO + mixer + VGA)

### 5.6 Measurement of the Square-Law Power Detector

The die photo of the square-law power detector is shown in Figure 5.38. The measurement setup is illustrated in Figure 5.39. The RF path was configured the same way as

the previous power measurements, so that the power level at the RF probe tip can be obtained. On the output side, the DC probe was directly connected to a multimeter to record the DC output voltage level.

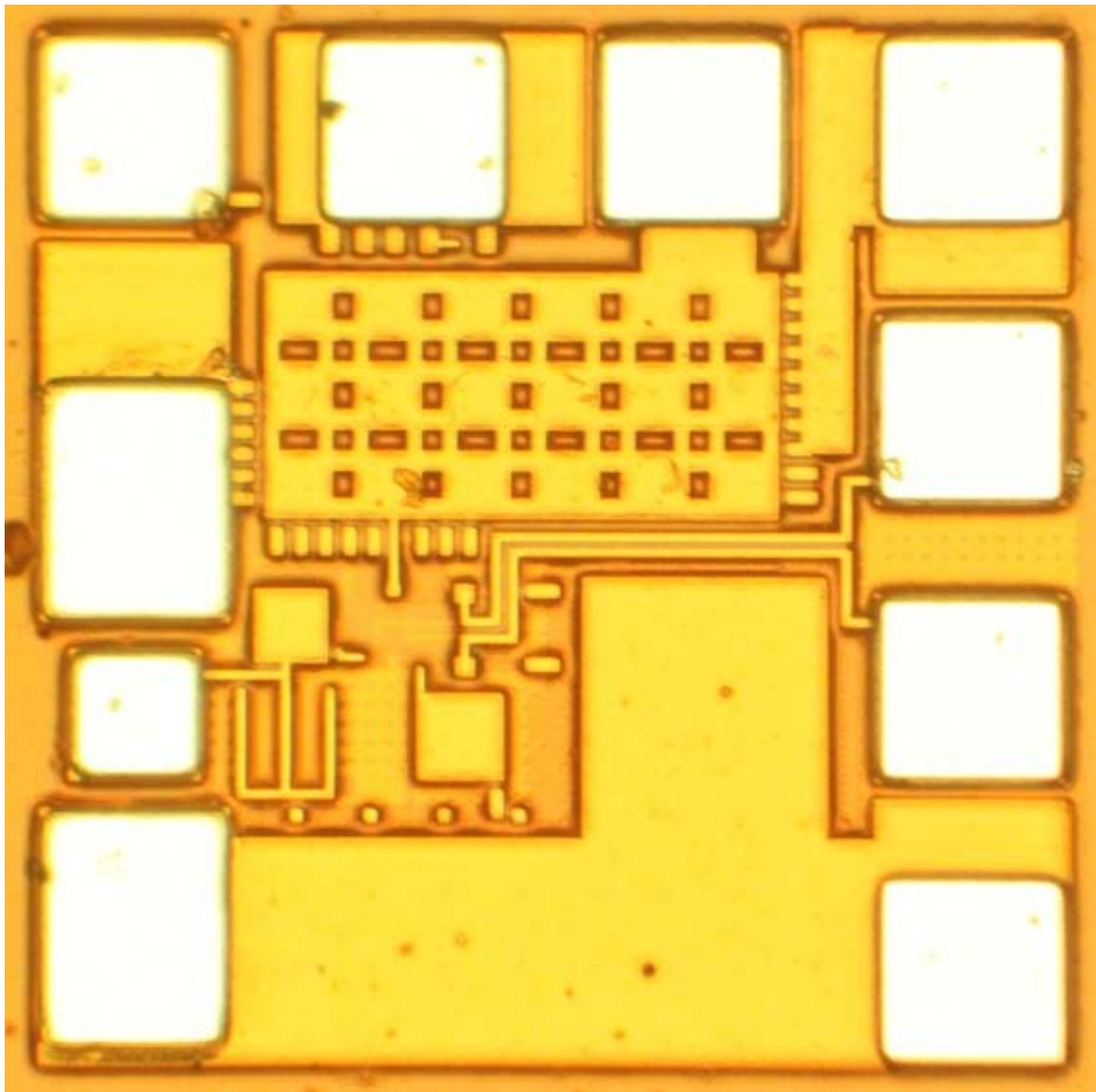


Figure 5.38 Die photo of the square-law power detector

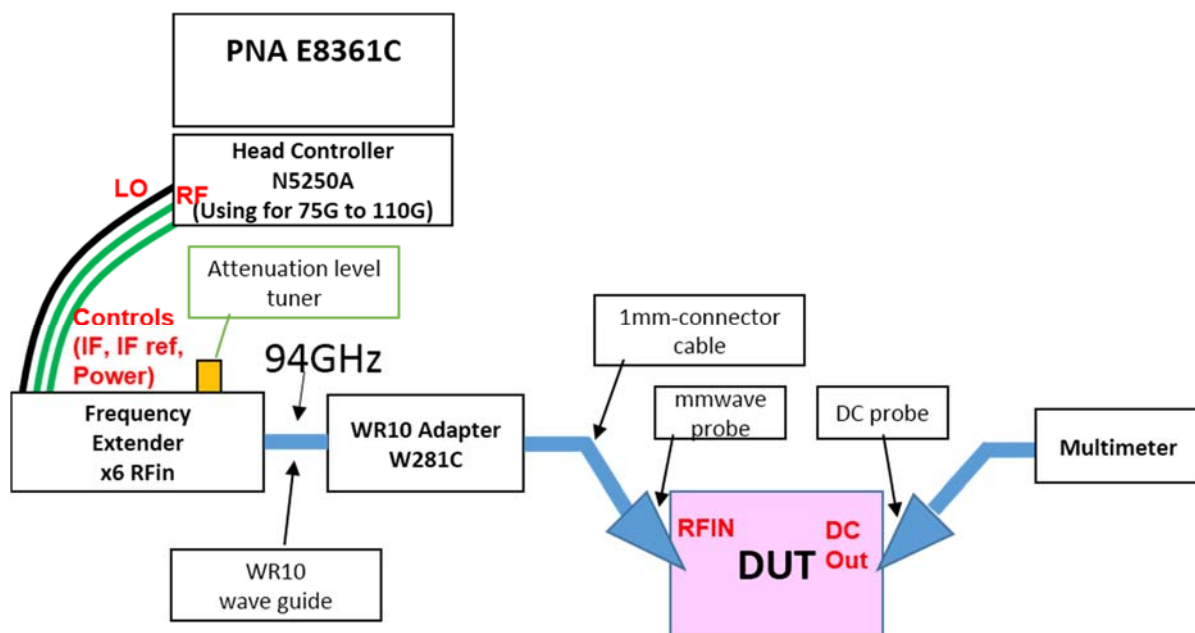


Figure 5.39 Setup for the square-law power detector measurement

The output DC voltage was recorded while the input frequency and power were swept. Figure 5.40 shows the output voltage versus the input power at several selected frequencies (70, 85, 95, 105 GHz). The x-axis represents the input power in the units of mW, and the y-axis is in units of V. At input power below 0.025 mW, which is about -16 dBm, creates plots that appear to be straight lines, indicating that the output voltage is linearly proportional to the input power, which is how the power detector should behave. On the other hand, the difference in the slope of the four plots means that the output voltage responds with a different sensitivity to the input power, which is termed “responsivity”. In the four selected frequencies, 85 GHz appears to have the highest responsivity. To have a complete picture of responsivity with regards to input frequency, a plot is shown in Figure 5.41. Compared to Figure 4.30, the measured results match the simulation in frequency response. In both cases,

the responsivity peaks at around 85 GHz. However, there are differences between the measured and simulated responsivity value, which possibly results from the difference in the DC biasing current. Since the original simulated current data was not available, only the same DC biasing voltage from the simulation was used to bias the circuit in the measurement. It was not possible to determine from the comparison whether the current consumed by the circuit was the reason for the discrepancy in responsivity. It is not very likely that the error was introduced by power calibration or instrument error. Since responsivity is the ratio of voltage (in the mV range) to power (in the mW range), both of these variables are actually incremental values rather than absolute values, so even if there is error in the instrument or calibration, it should be offset when the increment is calculated.

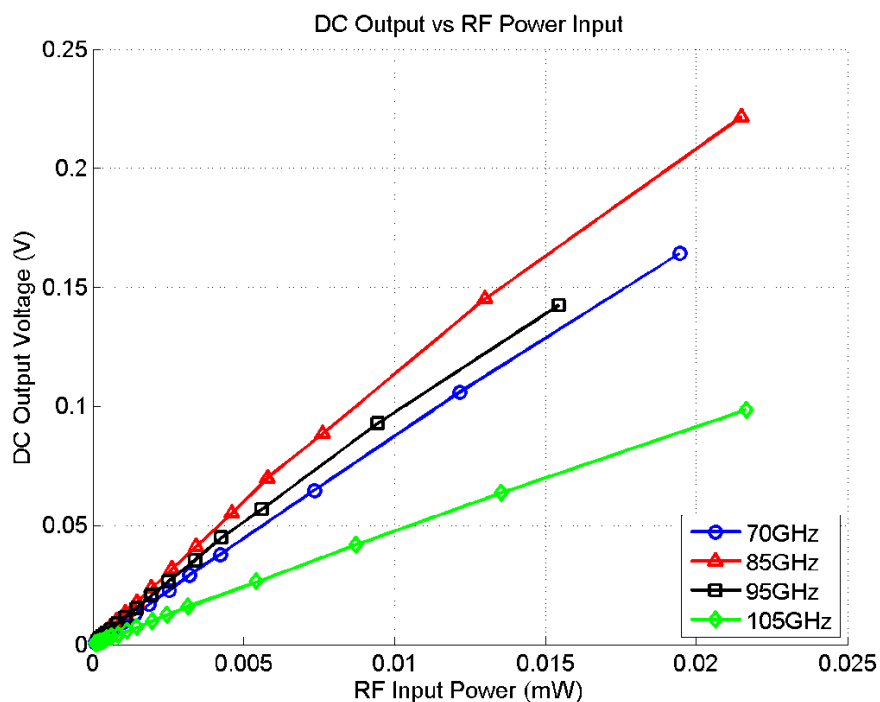


Figure 5.40 DC output voltage vs. the RF input power at 70, 85, 95, and 105 GHz

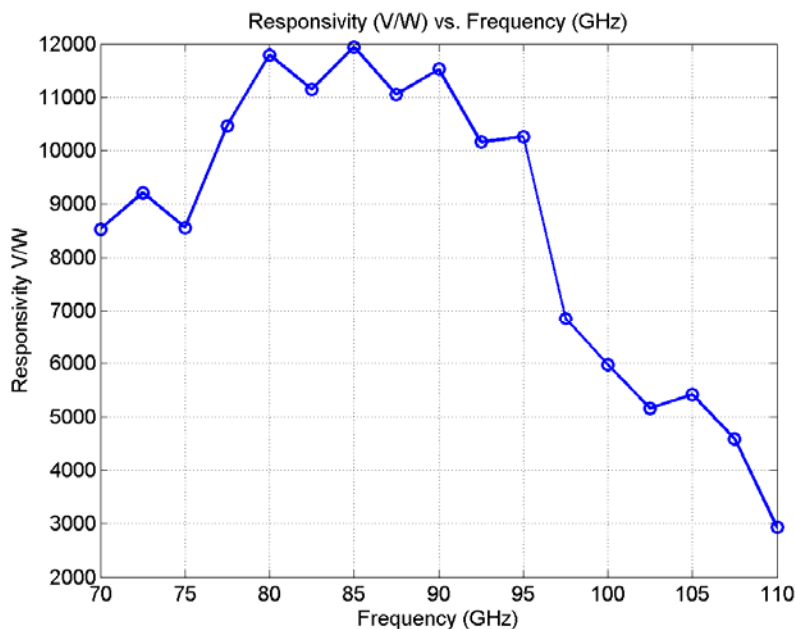


Figure 5.41 Responsivity of the power detector vs. the input frequency

### 5.7 Measurement of the 4 x 1 Prototype Array with 1-Channel Excitation

In this section, the 4 x 1 prototype array is thoroughly tested when only one of the four RF channels is excited. Similar to the testing method applied to the down-converting mixer, SP measurements were performed for port matching, power measurements were done to determine conversion gain, and linearity and noise measurements were made to determine the NF of the array. During power measurement, the phase shifter was swept to observe the conversion gain under different phase settings. In addition, the square-law power detector's output was also measured when the array was excited using only one input. We are also very interested in the performance of the prototype as an interferometer, where at least two channels need to be excited simultaneously. Those results will be separately presented in Chapter 6 and more in-detail analysis will be discussed.

### 5.7.1 Port Matching and SP Measurement

A die photo of the 4 x 1 prototype array is shown in Figure 5.42. The measurement setup for the SP test is the same as for the mixer in Section 5.5.1, only the probes are calibrated for one port measurement only. Since the array IF output is simply the mixer output, and due to the complexity of calibrating a differential probe on a CS-5 calibration substrate, the IF port reflection coefficient was not measured, but it should look very similar to Figure 5.23.

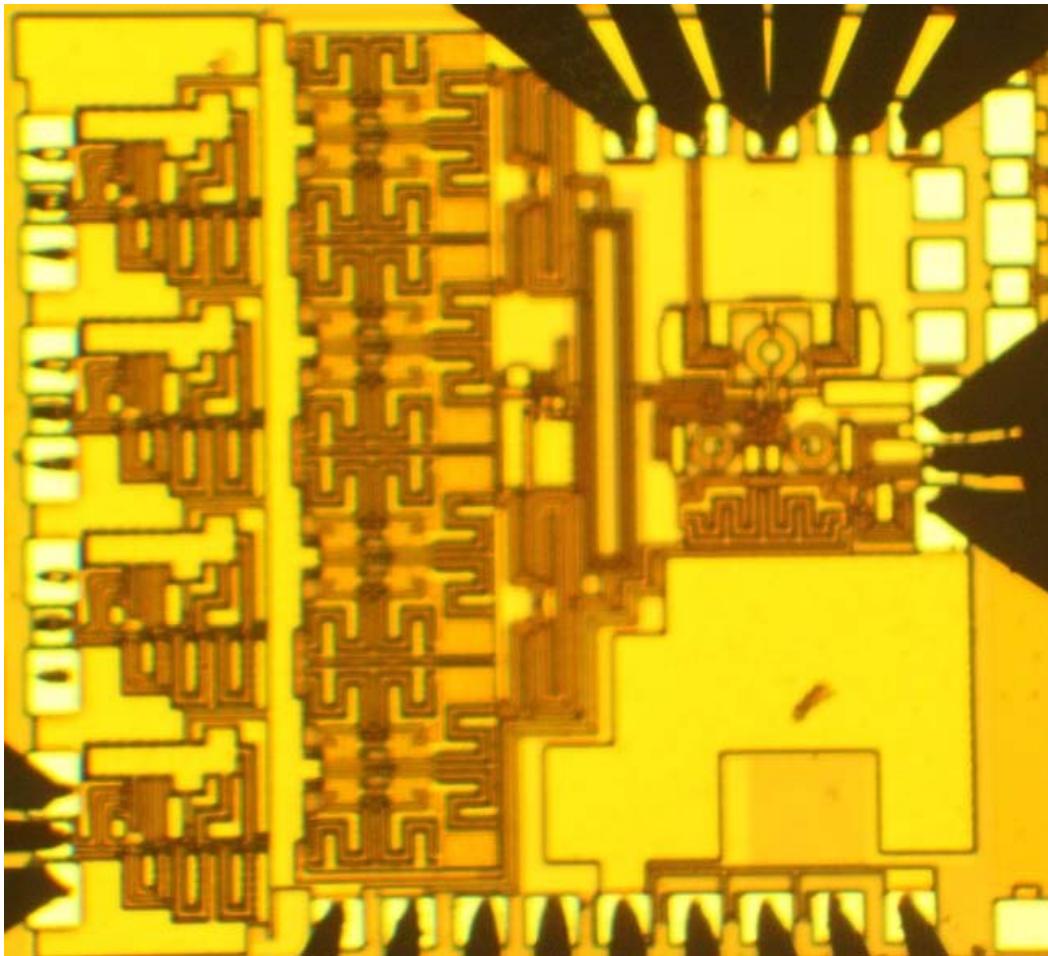


Figure 5.42 A die photo of the 4 x 1 prototype array

The return loss of RF and LO are plotted in Figure 5.43. Since all four LNAs at the RF input are exactly the same, only one reflection coefficient is plotted. Compared to the LNA input matching in Figure 5.6 and mixer LO matching in Figure 5.22, all array ports are still well matched as expected, with no degradation in bandwidth.

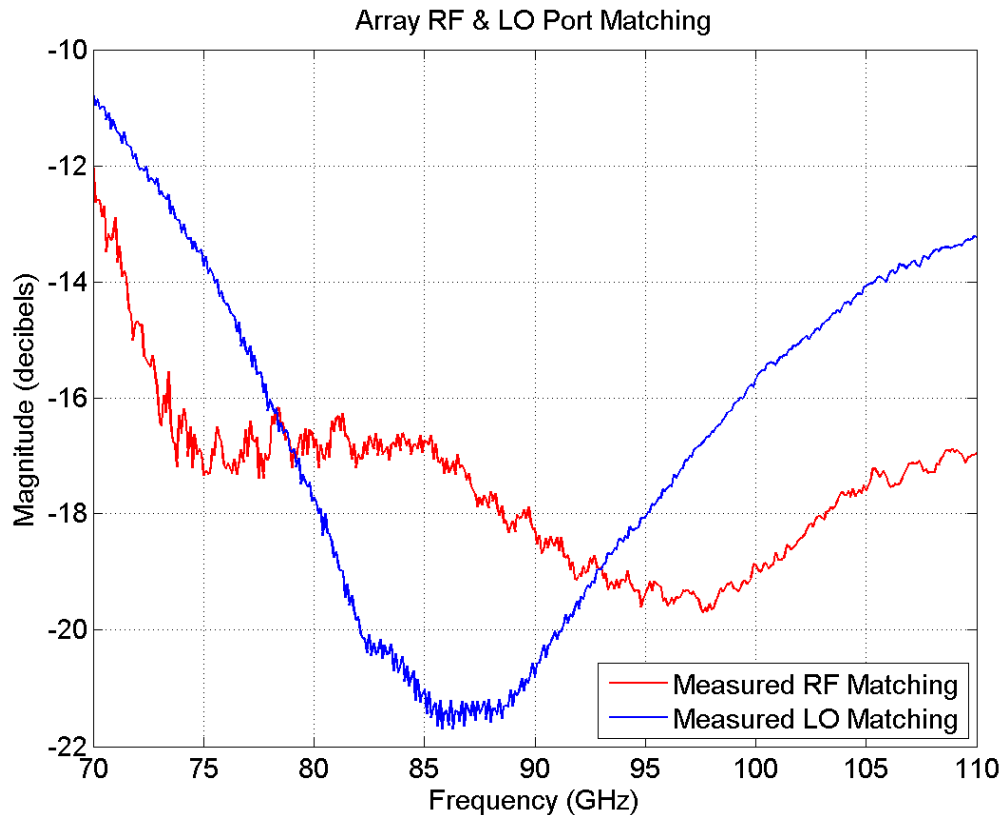


Figure 5.43 Measured RF and LO port matching of the array

### 5.7.2 Power Measurement for Compression Point and Conversion Gain

The power measurement of the array uses the same setup and calibration method as the mixer, while the only additional aspect is the phase shifter's control bits. Before frequency

sweeping, the optimal LO and RF input power were determined first by power sweeping. Then RF and LO frequency were swept to produce similar conversion gain plots as shown in Section 5.5.2.

### 5.7.2.1 Optimal LO Input Power

Using Channel 1 as a sample, the LO power was swept and the resulting conversion gain is plotted in Figure 5.44. Almost the same curve is observed as what was seen in Figure 5.24, because the optimal LO power for the array was set to -8.12 dBm as well and used throughout the whole measurement.

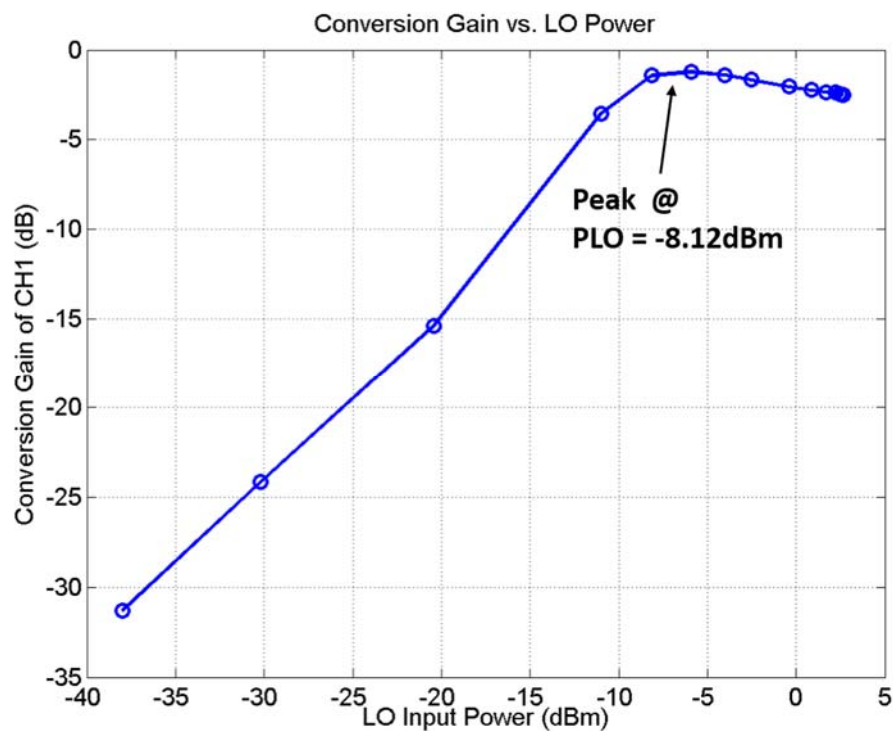


Figure 5.44 Measurement of the array's channel 1 conversion gain while sweeping the LO input power.

### 5.7.2.2 Optimal RF Input Power

With the LO power set to -8.12 dBm, the RF input power was swept to determine the input compression point for the input channels. Figure 5.45 shows the IF output power and conversion gain versus the RF input power. The input referred 1-dB compression point was measured at -17 dBm, about 9 dB higher than the simulated results shown in Figure 4.45. The improved linearity results from the loss of conversion gain compared to the simulations. However, the MMW input power level should be significantly lower than -17 dBm, therefore the array should work linearly for its proposed applications.

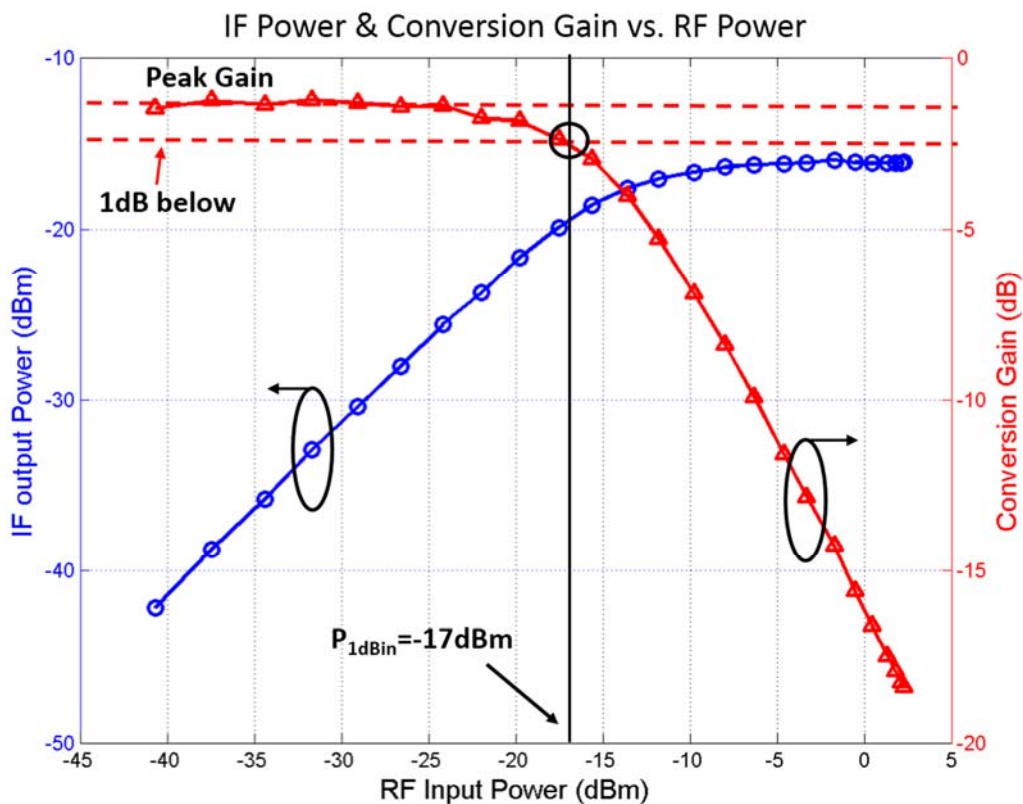


Figure 5.45 The array's measured channel 1 IF output power and conversion gain while sweeping the RF power

### 5.7.2.3 IF Output Power during Phase Shifter Sweep

When the 94 GHz phase shifter was measured, we noticed that S21 was not the same for all 16 phase settings. The maximum difference between the two phase settings was 4 dB. We have also found low conversion gain can cause NF measurements to be inaccurate, therefore it is crucial for us to find the phase setting with the maximum IF output power (*i.e.* conversion gain) for more reliable NF measurements. To remain consistent with the previous measurements, we used Channel 1 (CH1) again for this test. With a fixed LO and RF input power, the IF power at 16 phase statuses was measured. To make it easier to read, only four of the states were picked and plotted in Figure 5.46.

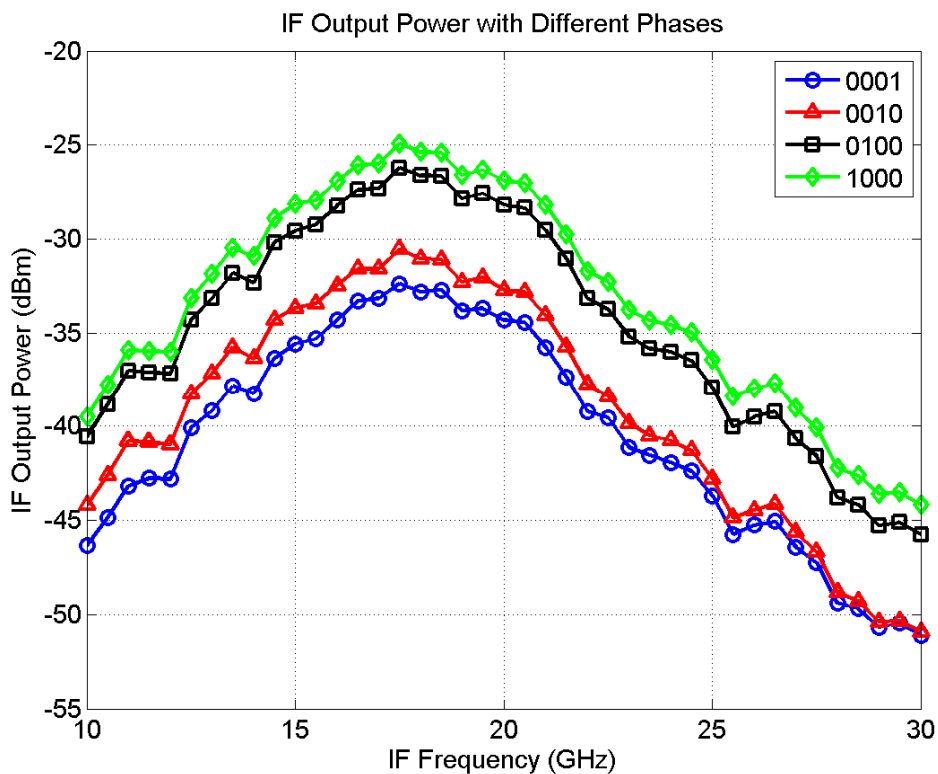


Figure 5.46 IF output power with phase settings at 0001, 0010, 0100 and 1000

Phase 1000 gives the highest IF output power, while phase 0001 is among the lowest; their difference is about 8 dB. For comparison, both Phase 1000 and 0001 will be used for the noise and conversion gain measurements. All other phase statuses' curve should stay between these two settings.

#### 5.7.2.4 Conversion Gain Measured with a Fixed LO Frequency and Swept RF Frequency

Using the very same setting as we used in mixer measurement, the conversion gain of the array versus the RF frequency was measured. Both phases, 1000 and 0001, are plotted in Figure 5.47. A very similar frequency response to the mixer (Figure 5.29) is observed, with peak gain located at our target frequency range and 3-dB bandwidth is wider than 5 GHz.

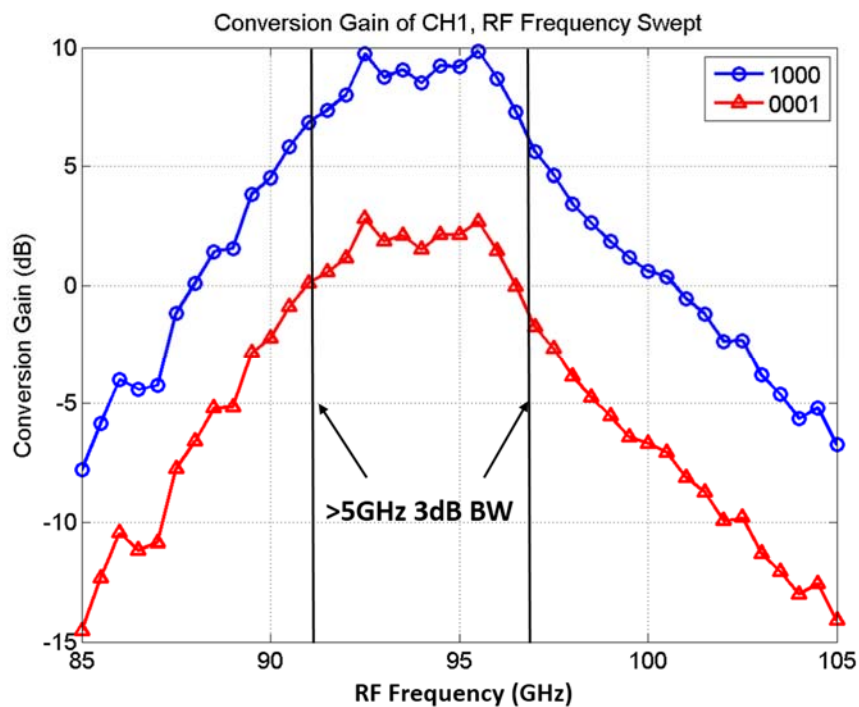


Figure 5.47 Measured conversion gain of the array at phases 1000 and 0001

### 5.7.2.5 Conversion Gain Measured from Simultaneously Swept RF and LO Frequencies

When measuring the mixer, multiple IF frequencies were tested to investigate the frequency response of all ports and compare them to those measured with SPs. For the array, we focused on IF=18 GHz, because 18 GHz is the highest frequency that the noise source can cover while still being close to our target frequency of 18.8 GHz. In the measurement, RF frequency was swept from 88-106 GHz, while LO was swept from 70-88 GHz, keeping a constant 18 GHz IF frequency. The conversion gain is plotted in Figure 5.48.

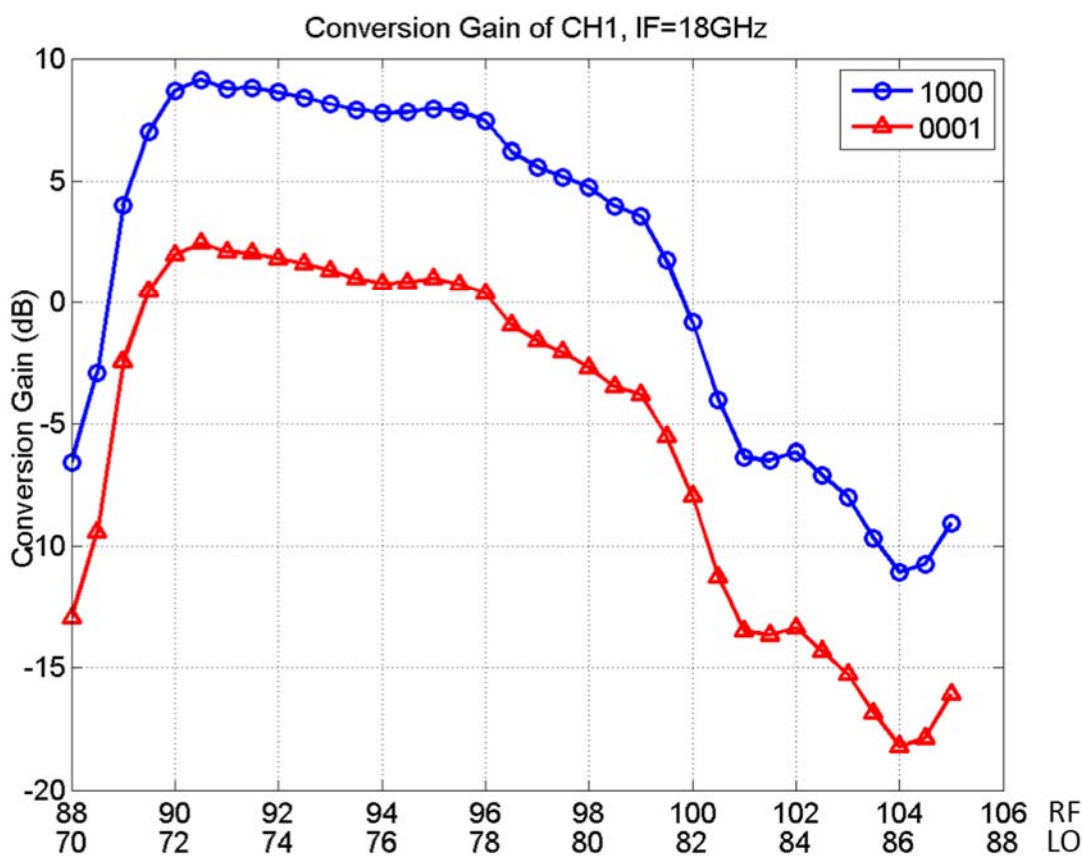


Figure 5.48 Measured conversion gain of CH1 at phases 1000 and 0001 with RF & LO frequency swept and IF = 18 GHz.

The gain of phases 1000 and 0001 still have a difference of about 7 dB. The curves' shape, resembling those for the mixer in Figure 5.30, show apparent corners at LO=72 and 81 GHz, which we concluded in Section 5.5.2.5 was a consequence caused by the VNA frequency extender not being able to provide enough power below 72 GHz or above 81 GHz. Since our LO circuitry is the same as in the mixer, the same explanation applies to the array. Therefore it is reasonable that we can see corners at 72 and 81 GHz. On the other hand, the curve for the array does not hold at its peak value for the whole bandwidth. Rather, the gain value gradually drops as frequency moves higher. This comes from the aggregated frequency response of the LNA and phase shifter, where the LNA's gain reaches a peak at 94 GHz and drops beyond that point, and the phase shifter's S21 has a negative slope all along in the RF bandwidth.

### 5.7.3 Noise Measurement

After determining the array's conversion gain at IF=18 GHz, we used the same method as described earlier to measure the NF of the array, particularly CH1 with the maximum gain setting. Although the 16 phase settings generate different conversion gains, the circuit itself is still identically biased under those 16 circumstances; therefore the NF of the 16 phase settings should be the same. The highest gain phase setting was used to facilitate the measurement and make the results more reliable. The measured NF is plotted in Figure 5.49. Similar to the mixer NF, the array NF value was not stable during measurement, an indication of the difficulty in resolving the difference in the output noise power when the

noise source is ON and OFF. As a result, we cannot trust the measured NF results for the array.

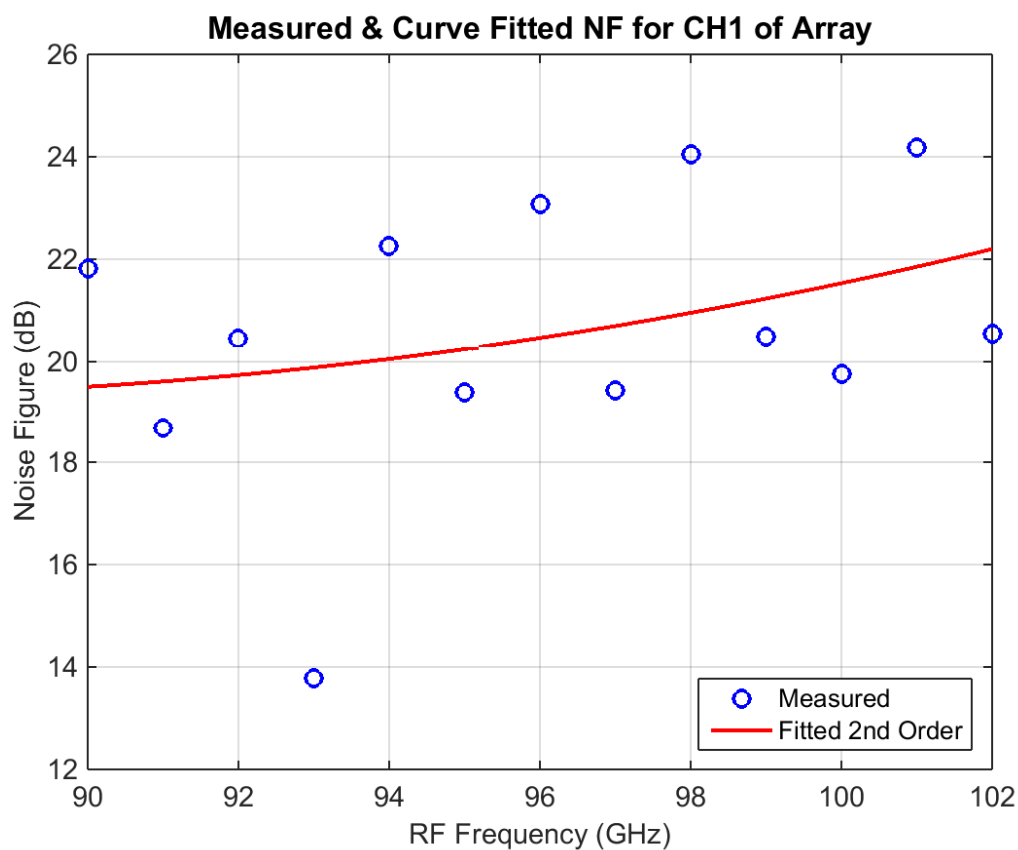


Figure 5.49 Measured NF of CH1 at phase 1000 with swept RF and LO and IF = 18 GHz

Because the direct noise measurement does not work due to unexpected loss in the conversion gain, an indirect method was used to estimate the NF of the array using as many measured results as possible. As described in Eq. 5.16, the NF of a system with multiple stages can be calculated with each stage's individual gain and noise information. Therefore, without losing generality, empirically measured data was chosen for each block of this

calculation. If no direct measurement data was available, generous but reasonable assumptions were made. A list of data, all from 85-105 GHz, was selected and provided below for reference:

#### 1. LNA

- i)  $G_1$ : S21 measured as shown in Figure 5.10;
- ii)  $F_1$ : Simulation results in Figure 4.7 shows  $NF < 8.5$  dB from 81-106 GHz, therefore assuming a constant  $NF = 8.5$ .

#### 2. Phase shifter

- i)  $G_{2a}$ : For phase 1000, S21 measurement shown in Figure 5.17;
- ii)  $F_{2a}$ : Simulation results show  $NF < 20$  dB from 85-105 GHz, therefore assuming a constant  $NF = 20$  dB;
- iii)  $G_{2b}$ : For phase 0001, although minimum S21 in Figure 5.17 is only 4.2 dB below the maximum, we still observe a 7.5 dB difference in Figure 5.43 for the array conversion gain, therefore we assume  $G_{2b}$  7.5 dB below  $G_{2a}$ ;
- iv)  $F_{2b}$ : Assumed to be the same as  $F_{2a}$ , 20dB.

#### 3. Wilkinson divider + ring hybrid coupler

- i)  $G_3$ : Worst case for simulated forward transmission is -8 dB, therefore -8 dB is assumed across the spectrum;
- ii)  $F_3$ : based on  $G_3$ ,  $F_3$  is  $1/G_3$ .

#### 4. Mixer

- i)  $G_4$ : Not needed for the NF calculation;

- ii) F4: Simulation results in Figure 4.26 shows  $NF < 17$  dB, therefore assuming a constant  $NF = 17$  dB

With data listed above, the estimated NF for CH1 of the array is plotted in Figure 5.50.

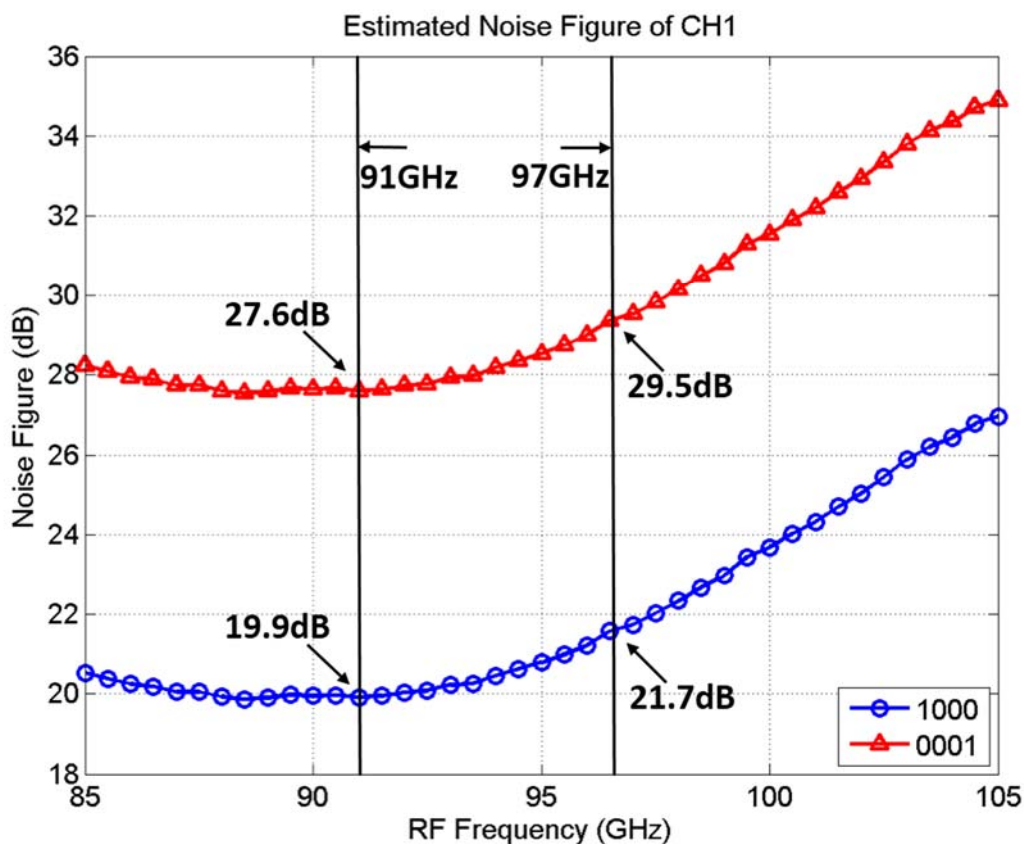


Figure 5.50 Estimated NF for CH1 of the array, for best and worst cases

The best and worst cases are shown, where the only difference between these two estimated extremes is the gain (or conversion loss) of the phase shifter under different phase settings (*i.e.* 1000 for best case and 0001 for the worst). Intuitively, for an RF front end, it is important to make the very first component (*i.e.* the LNA) high gain and minimal noise. In

this case, although measured gain of the LNA is only 3 dB below expected, the phase shifter attenuated almost 80% of the amplified signal, while the worst case has more attenuation than what the LNA amplified. In addition, following the phase shifter is another 8 dB of loss in passive components. This makes the whole front end very lossy, and therefore noisy as well.

#### 5.7.4 Power Measurement with the Square-Law Power Detector

CH1 is used to measure the output voltage of the square-law detector, while both input power and frequency are swept. Figure 5.51 shows the output voltage in response to the input power at various frequencies.

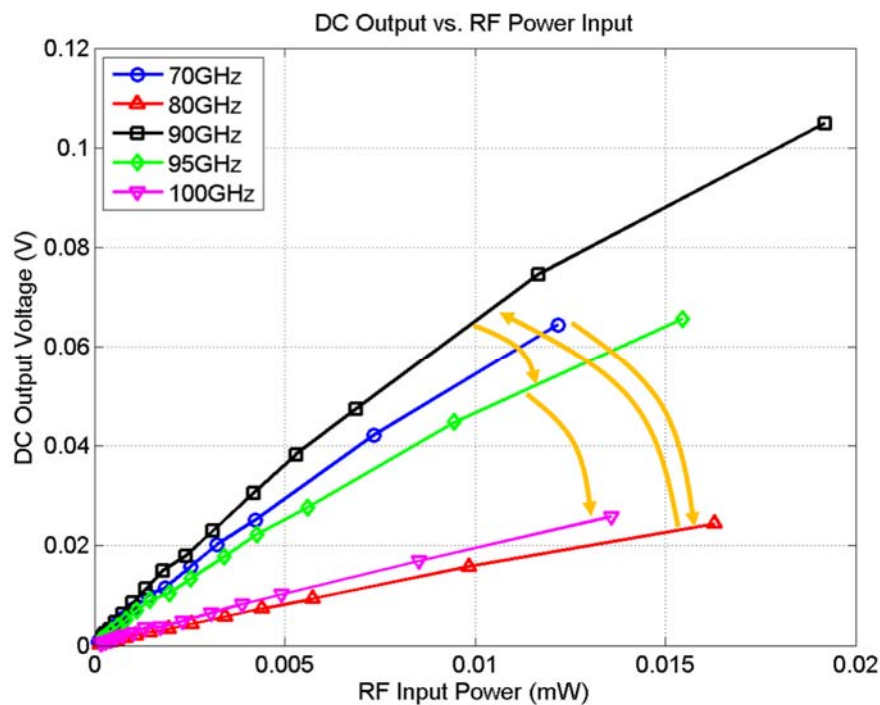


Figure 5.51 DC output voltage vs. RF input power at 70, 80, 90, 95 and 100 GHz

Similar to the plot of the standalone power detector (Figure 5.40), different slope (*i.e.* responsivity) is observed from frequency to frequency. What is interesting is the slope starts at 70 GHz with a relatively high value, then decreases as frequency moves to 80 GHz followed by another increase in slope at 90 GHz. After that, the slope gradually decreases. This observation was also confirmed by Figure 5.52, which shows the responsivity as a function of frequency. From the trend in the curve, there should be another peak somewhere below but close to 70 GHz. This characteristic is expected since we kept the original LNA's double peak design, which peaks at 68.1 GHz and 94.3 GHz. The high responsivity at around 70 GHz facilitates the prototype to be tested with two-port excitation, since our lab is only equipped with a differential RF probe up to 67 GHz.

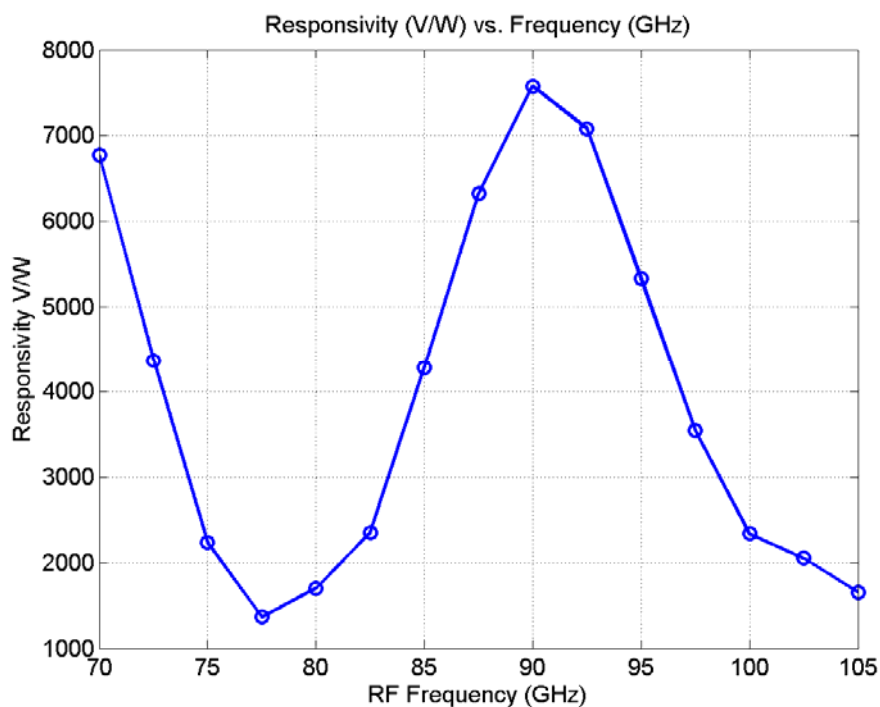


Figure 5.52 Responsivity of CH1 vs. input frequency

### 5.7.5 Summary of 4 x 1 Prototype Array with 1-Channel Excitation

In Section 5.7, measurement results were presented of the 4 x 1 prototype array excited by only one RF port. All four RF ports, LO port, and IF port inherited the original break-out circuits' design, therefore are well matched to the system characteristic impedance at their designed frequency. The conversion gain for all channels was less than simulation, which is an aggregated result of loss of gain in all components, including the LNA, phase shifter, and mixer, while within the 16 phase settings of one channel, the conversion gain varies as well. This symptom can be oriented to the mismatch and unbalance within the phase shifter in-phase and quadrature circuits. As a result, the attenuated gain makes noise measurements impossible. Although measured data was presented, it should not be considered reliable. In such circumstances, the array NF was evaluated using theoretical equations and measured data from each constitutional block. In addition to the measurement of the super-heterodyne path, the direct-detection path was tested as well. The square-law detector's output voltage is linearly proportional to the input power applied to each channel, however the responsivity value from each channel is lower than the standalone detector, due to the attenuation from the phase shifter and combining passive components. On the other hand, thanks to the double peak frequency response of the LNA, the direct-detection circuit has responsivity peaks at two frequencies: 68 GHz and 94G Hz, making it favorable for the interferometry proof-of-concept in Chapter 6.

Table 5.3 summarizes the array measurement results and compares it with the simulations. With the target frequency achieved, the actual circuit's conversion gain is

significantly under-performing, as is the NF. To push the circuit to reach its maximum possible gain, 3.3 V was used instead of 2.5 V for VCC and the  $V_{bg}$  was set to 1.9 V, 0.7 V higher than in the simulation. The overall power consumption, therefore is much higher than expected.

Table 5.3 Summary of the prototype array's measured results

	Simulated (1 Channel)	Measured (Channel 1)
Frequency	RF = 94 GHz LO = 75.2 GHz IF = 18.8 GHz	RF = 94 GHz LO = 75 GHz IF = 19 GHz
Gain	Peak = 30.7 dB @ RF = 91.6 GHz >27.7dB RF = 88.6-94GHz	Highest Setting: Peak = 10 dB (1000) Lowest Setting: Peak = 3 dB (0001)
NF	<11 dB DSB w/i IF BW	Lowest Setting: <22 dB (1000)* Highest Setting: < 29.5 dB (1000)*
P1dB <sub>in</sub>	-26 dBm	-17 dBm
Power	481.3 mW (Array)**	735.9 mW (Array)***

\* NF is evaluated using theoretical equations and measured results of single elements

\*\* Simulation VCC = 2.5 V,  $V_{bg}$  = 1.2 V

\*\*\* Measurement VCC = 3.3 V,  $V_{bg}$  = 1.9 V

## 5.8 Summary

Chapter 5 began with an introduction of the background knowledge for MMW wafer-probing measurements, which included descriptions of the measurement design, calibration method, and theory. After that, every fabricated silicon circuit was tested and their measured results were compared to corresponding simulations. The reasons for hardware-to-model mismatch were extensively discussed. Although the overall measured specifications were not

as good as expected, the 4 x 1 prototype array still functions as designed. Improvement on the hardware performance could be made in future works to meet the design specifications.

## **CHAPTER 6**

### **MULTI-CHANNEL EXPERIMENTS AND VERIFICATION OF INTERFEROMETRY**

#### 6.1 Overview

In Chapter 5, the prototype array's single channel performance was evaluated. The actual chip underperforms compared to the simulated projections in terms of system specifications, however the array does work as expected as far as functionality. In this chapter, we will evaluate the prototype array's potential as an interferometer. To help readers better understand how an interferometer works, more details about the visibility function and its relationship with each array channel will first be explained. Then simulations will be used to generate the visibility function, followed by implementing the same method on the actual chip. Both simulated and measured data was able to successfully recreate fringe patterns of the interferometer in various baselines, therefore demonstrating that this chip is a potential prototype for an interferometer front-end implemented with silicon IC. Further post-processing algorithms and functioning circuitry remain to be designed to complete the system.

#### 6.2 The Visibility Function and Fringe Patterns

In a traditional interferometer, the correlation of a pair of receiver's output voltages is used to create a visibility function, as defined in Eq. 3.4, re-written in Eq. 6.1, and illustrated in Figure 6.1.

$$r(\tau) = \lim_{T \rightarrow \infty} \frac{1}{2T} \int_{-T}^T V_1(t) V_2^*(t - \tau) dt = \langle V_1(t) V_2(t) \rangle \quad (6.1)$$

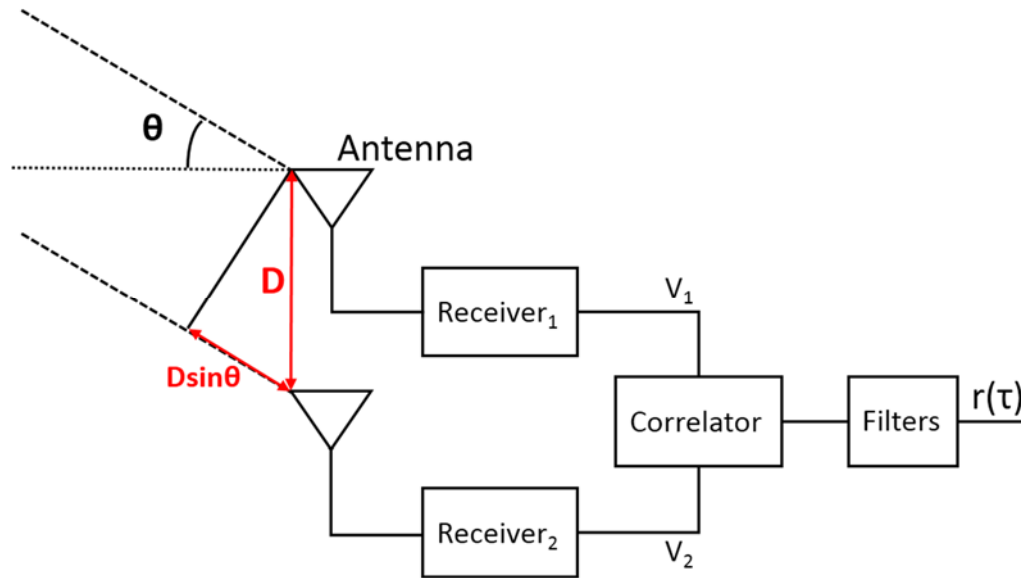


Figure 6.1 Illustration of a traditional interferometer with a correlator

where according to [NAN12],  $V_1$  and  $V_2$  can be written as below:

$$V_1(t) = a_1 \cos(2\pi f t) + n_1(t) \quad (6.2)$$

$$V_2(t) = a_2 \cos[2\pi f(t - \tau)] + n_2(t) \quad (6.3)$$

where  $a_i$  is the amplitude of the received signal,  $\tau$  is the geometric time delay, and  $n_i$  is the noise from the corresponding receiving channel. With the help of Figure 6.1,  $\tau$  can be calculated as:

$$\tau = \frac{D \sin \theta}{c} \quad (6.4)$$

where  $D$  is defined as the baseline of a pair of receiving antennas,  $c$  is the speed of light, and  $\theta$  is the angle of the object off the broadside of the antennas. Since noise signals are

uncorrelated with each other, as well as input signals, the visibility function can be reduced as below:

$$r(\tau) = a_1 a_2 \cos(2\pi f t) \cos[2\pi f (t - \tau)] \quad (6.5)$$

$$r(\tau) = \frac{a_1 a_2}{2} \cos[2\pi f (2t - \tau)] + \frac{a_1 a_2}{2} \cos[2\pi f \tau] \quad (6.6)$$

In our system, the RF frequency is 94 GHz, so the first term of Eq. 6.6 will be located at 188 GHz, which will be naturally filtered by the receiving circuits. Therefore the visibility function further reduces to:

$$r(\tau) = \frac{a_1 a_2}{2} \cos[2\pi f \tau] = r(\theta) = \frac{a_1 a_2}{2} \cos\left[2\pi f \frac{D \sin \theta}{c}\right] = \frac{a_1 a_2}{2} \cos\left[2\pi \frac{D \sin \theta}{\lambda}\right] \quad (6.7)$$

By substituting Eq. 6.4 into Eq. 6.7, the visibility function of an interferometer can be expressed as a function of  $\theta$  and  $D$ . Eq. 6.7 is also called the fringe function, the pattern of which is generated by different baseline lengths, as shown in Figure 6.2.

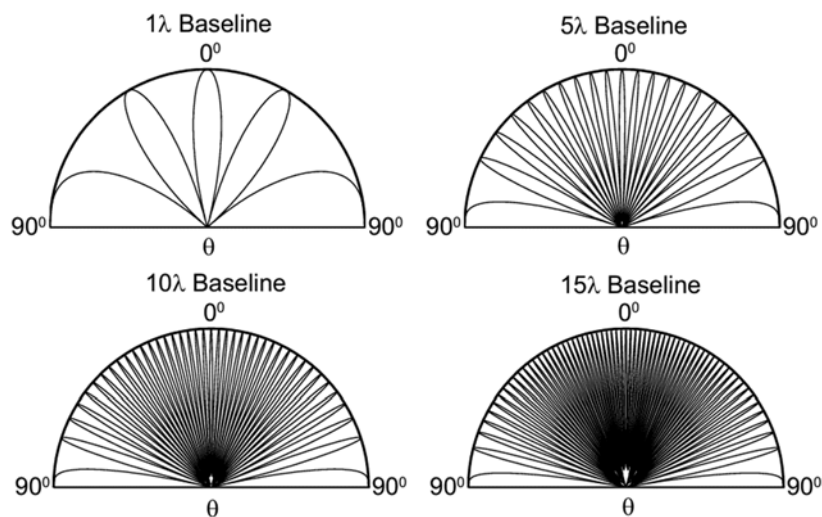


Figure 6.2 Fringe pattern of an interferometric correlator for various baselines  
(Figure adapted from [NAN12])

The patterns in Figure 6.2 resemble antenna radiation patterns, the same purpose for which our interferometer is designed. Separate receivers are used to synthesize a larger aperture than what can be achieved using only a single antenna, thereby producing better angular resolution. In fact, the patterns in Figure 6.2 are simply narrow-band responses. The actual synthesized patterns would be further modulated by the real antenna radiation and bandwidth patterns. However, in this chapter, we will only be evaluating our receiver, which does not have an antenna array on the front-end of it. Therefore, the modulation from antenna patterns can be ignored for this work. In addition, all our evaluations will be performed on RF excitations at a single frequency, therefore modulation of the fringe patterns from bandwidth patterns can also be disregarded. If our prototype array works properly with multiple excited channels, we will be able to recreate fringe patterns in both simulation and experiments similar to those shown in Figure 6.2.

### 6.3 Recreation of Fringe Pattern using Simulation Data

#### 6.3.1 Mathematical Derivation

To obtain the correlation between any two channels in our system, we should first know what output signals are expected. Revisiting our system in Figure 6.3 (highlighted in yellow), in the RF to IF path, each input signal is modulated by a unique code modulated phase setting (Modulator 1-4), joined by three other RF signals and down-converted to the IF output. The IF output will be further down-converted to the baseband and demodulated by the interferometer processors, which give the correlation for each pair of the input signals.

The modulation and demodulation code logic was designed by Mr. Chauhan. Therefore at the IF port, we expect four code modulated signals jointly. In the RF to power detector path, the input signal phase will not be shifted by code modulation, rather the phase is fixed at one of the 16 phase settings, after joining with the other three inputs. The total power can be written by the square-law power detector.

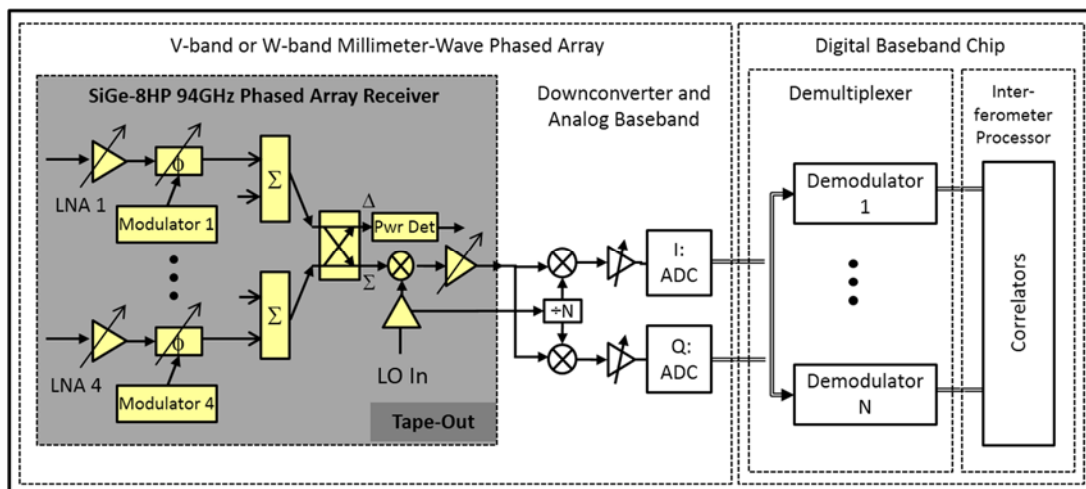


Figure 6.3 Concept illustration of the interferometer system in its entirety

Since the baseband demodulating circuits have not been developed, nor is our lab equipped to measure frequency converted phase information, the RF to IF path cannot be used in our evaluation. However, the square-law power detector, as designed and measured in Chapter 4 and 5, can give a DC voltage reading which is proportional to the power at its input. For example:

- If only CH1 is excited, only  $V_1$  will be presented at the power detector's input and

$$\text{thus: } V_{OUT} \propto (V_1)^2;$$

- If CH1 and CH2 are excited,  $(V_1 + V_2)$  will be presented at the power detector's input, thus:  $V_{OUT} \propto (V_1 + V_2)^2$ ;
- If CH1 and CH3 are excited,  $(V_1 - V_3)$  will be presented at the power detector's input, thus:  $V_{OUT} \propto (V_1 - V_3)^2$ ;
- If CH3 and CH4 are excited,  $(V_3 + V_4)$  will be presented at the power detector's input, thus:  $V_{OUT} \propto (V_3 + V_4)^2$ .

Recall from the visibility function,  $r_{ij}(\tau)$  is essentially the multiplication of input signals from the  $i^{\text{th}}$  and  $j^{\text{th}}$  channel, therefore we can follow Eq. 6.8 to obtain the visibility function of each pair of channels.

$$(V_i + V_j)^2 - (V_i - V_j)^2 = 4V_iV_j \quad (6.8)$$

We use several, simple two-channel cases below for illustrative purposes. As shown in Figure 6.4, the baseline length,  $D$  and the angle off the broadside,  $\theta$ , causes the geometric delay.

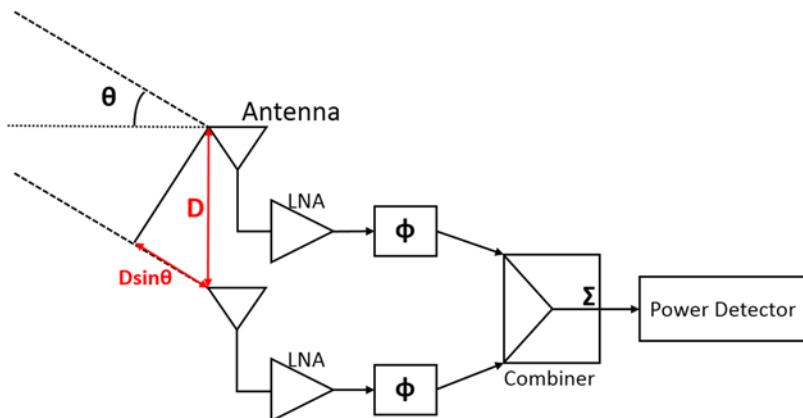


Figure 6.4 Illustration of a simple, two-channel interferometric radiometer

In our experiment, we can manually create the geometric delay by providing signals with known phase delay,  $\phi$ .

Case1:

1. Both CH1 and CH2's phase shifters set to  $0^\circ$ :

$$V_{OUT1} = C(V_{1\_0} + V_{2\_0})^2 \quad (6.9)$$

2. CH1's phase shifter is set to  $0^\circ$ , while CH2's is set to  $180^\circ$ :

$$V_{OUT2} = C(V_{1\_0} + V_{2\_180})^2 = C(V_{1\_0} - V_{2\_0})^2 \quad (6.10)$$

3. If we subtract Eq. 6.10 from 6.9, we get:

$$V_{12\_0} = V_{OUT1} - V_{OUT2} = 4C(V_{1\_0}V_{2\_0}) \quad (6.11)$$

where  $C$  is a constant.  $V_{12\_0}$  denotes the correlator voltage output when CH1 and CH2 are excited and their signals are in phase, meaning there is no geometric delay between the two channels.

Case2:

1. CH1's phase shifter is set to  $0^\circ$ , while CH2's is set to  $90^\circ$ :

$$V_{OUT1} = C(V_{1\_0} + V_{2\_90})^2 \quad (6.12)$$

2. CH1's phase shifter is set to  $0^\circ$ , while CH2's is set to  $270^\circ$ :

$$V_{OUT2} = C(V_{1\_0} + V_{2\_270})^2 = C(V_{1\_0} - V_{2\_90})^2 \quad (6.13)$$

3. If we subtract Eq. 6.13 from 6.12, we get:

$$V_{12\_90} = V_{OUT1} - V_{OUT2} = 4C(V_{1\_0}V_{2\_90}) \quad (6.14)$$

where  $C$  is a constant.  $V_{12\_90}$  denotes the correlator voltage output when CH1 and CH2 are excited and their signals are  $90^\circ$  out of phase.

In summary, when CH2's settings are  $\phi^\circ$  and  $(\phi + \pi)^\circ$ , the difference between their corresponding output voltages is proportional to the visibility, and the phase delay from CH1 is  $\phi$ . To obtain all correlation information between CH1 and CH2, it is only necessary to fix CH1 and gradually shift CH2 for  $360^\circ$ . However, in order to plot a fringe pattern, the angle off the broadside,  $\theta$ , is more of interest to us rather than  $\phi$ . Thus a transition between  $\phi$  and  $\theta$  is derived below and illustrated in Figure 6.5:

- When the baseline is  $\lambda$ , the phase delay ranges from 0 to  $2\pi$ , therefore only one possible geometric delay exists that corresponds to a phase delay of  $\phi$  out of  $2\pi$ ;
- When the base line is  $2\lambda$ , the phase delay ranges from 0 to  $4\pi$ , thus there are two possible geometric delays that give phase delays of  $\phi$  and  $\phi+2\pi$ .

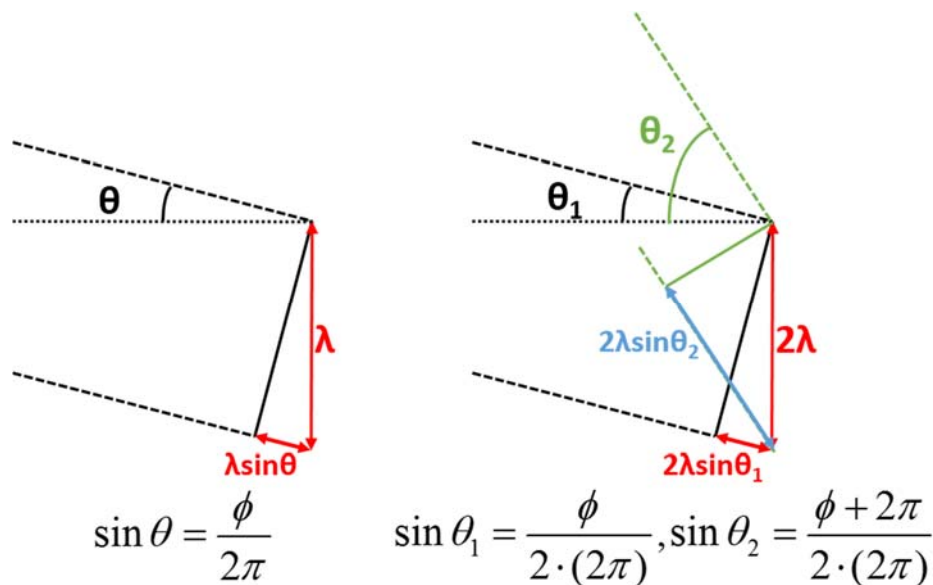


Figure 6.5 Transition between the phase delay,  $\phi$ , and the broadside angle,  $\theta$

The same logic applies when the baseline is equal to a higher number of wavelengths, and therefore a general equation can be derived below:

$$\theta_i = \sin^{-1}\left(\frac{\phi + (i-1)\pi}{2n\pi}\right), i = 1, 2, 3, \dots, n \quad (6.15)$$

where  $n = D/\lambda$ .

### 6.3.2 Simulation Model and Results

Initially, all real circuit models with extracted parasitics were used for the simulation. To find the DC output voltage in response to the RF input, long transient analysis had to be performed on each phase setting case, making the analysis impractical with regards to time and computational power. Therefore a simplified model, as illustrated in Figure 6.6, was used for simulation, which allowed a large number of phase settings to be swept in a reasonable amount of time.  $V_1$  and  $V_2$  are set to 67 GHz with relatively low power to avoid compression in the power detector. Delay of  $V_2$  was swept from 0 to  $4\pi$  with 200 evenly distributed data points. The simulated DC output voltage for the power detector is shown in Figure 6.7.

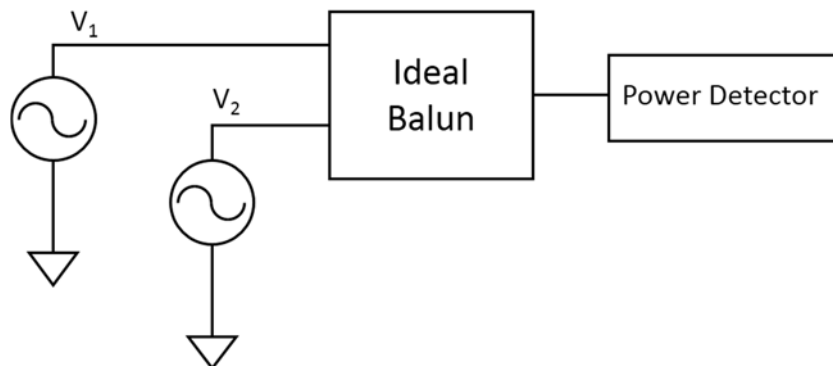


Figure 6.6 Simple setup for the simulation of a two-channel phase-switched interferometer

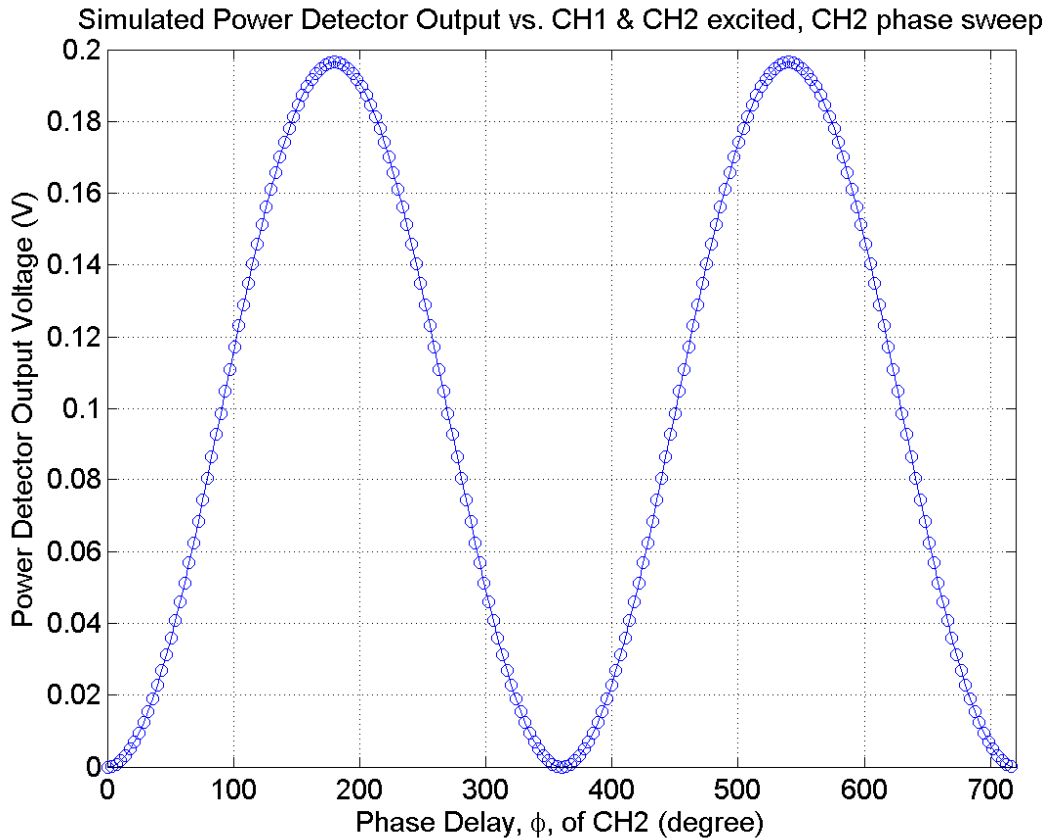


Figure 6.7 Simulated power detector output when CH1 and CH2 excited, and the CH2 phase is swept from 0 to 720°

After processing the output voltages as in Eq. 6.9-6.15, and translating  $\phi$  to  $\theta$ , polar plots for the four cases were generated using MATLAB, as shown in Figures 6.8 and 6.9. The blue curve is the ideal fringe function,  $r(\tau) = 2 \cos \left[ 2\pi \frac{D \sin \theta}{\lambda} \right]$ , while the red circles are the simulated data normalized to the same level of the ideal function. The simulation matches the theoretical equation, which is expected since everything preceding the power detector in the simulation (phase and power setting in both channels) was modeled ideally. Also, in Chapter 5, the power detector itself was proven to be linear as a function of input power.

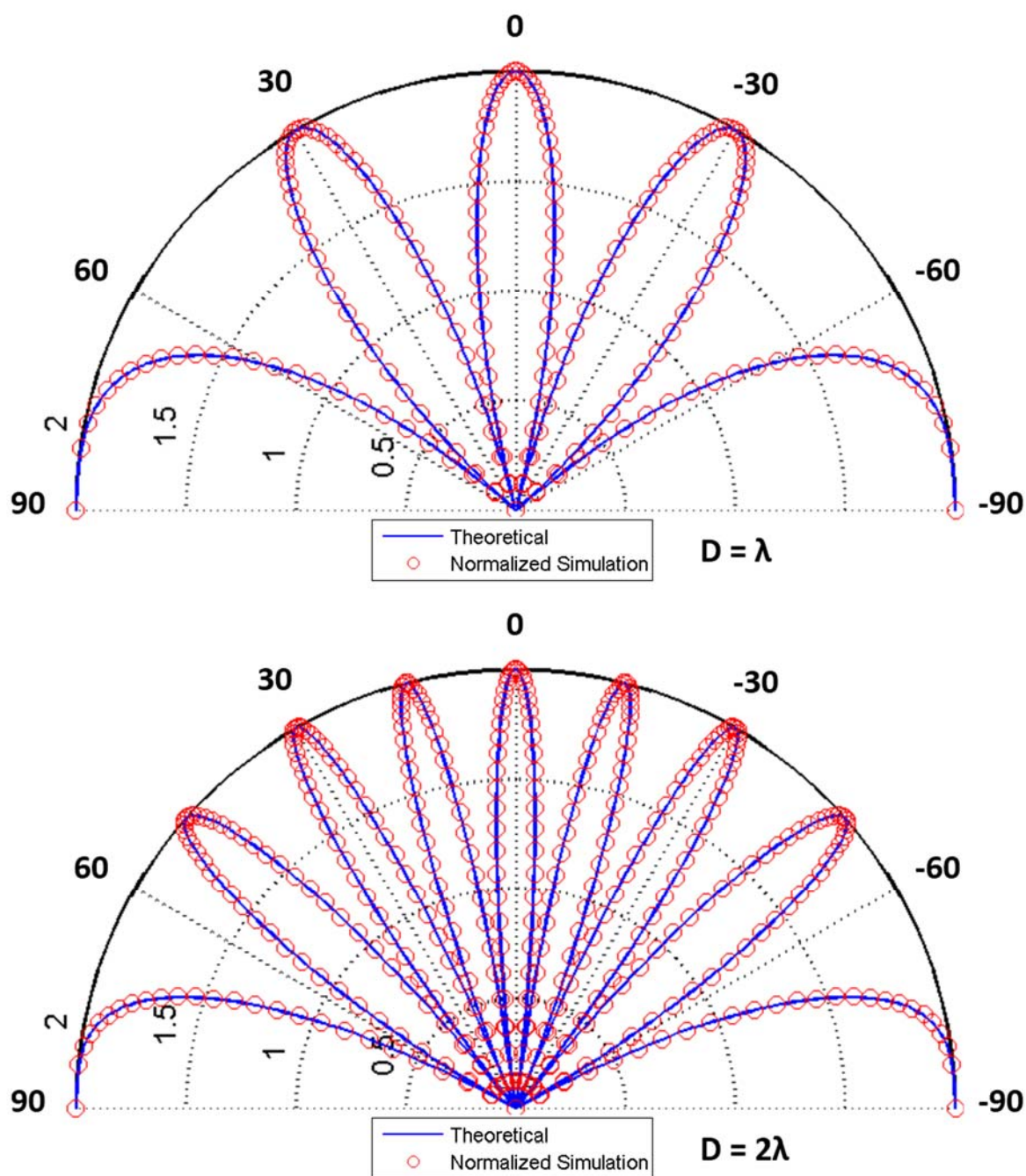


Figure 6.8 The fringe pattern produced by simulated data, top:  $D = \lambda$ ; and bottom:  $D = 2\lambda$

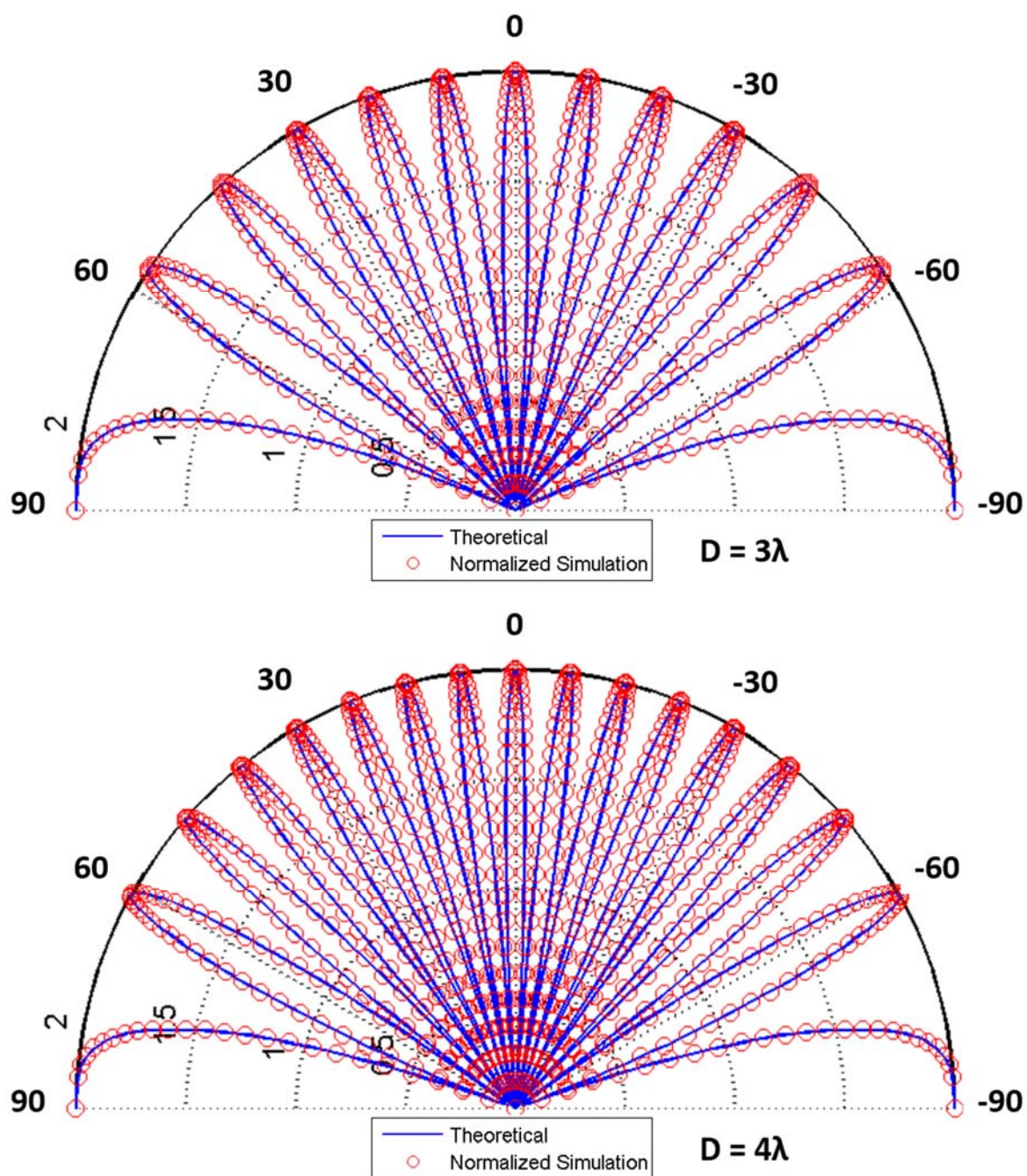


Figure 6.9 The fringe pattern produced by simulated data, top:  $D = 3\lambda$ ; and bottom:  $D = 4\lambda$

## 6.4 Recreation of Fringe Pattern using Measured Data

### 6.4.1 Measurement Setup

Recall from the single-channel measurement in Chapter 5 that the prototype array has two peaks in responsivity: one at 94.3 GHz, which is as designed, and the other at 68.1 GHz, which is due to the double resonance in the LNA frequency response. To measure the two-channel response of our array, a differential probe with an adjustable pitch was needed at the RF input side. Our lab has only two of these and they are both V band probes which only cover up to 67 GHz. Therefore the 67 GHz band was our only option to test the chip with two-channel inputs. The responsivity of one channel at 67 GHz was measured, producing a value of about 6000 V/W, therefore we are confident that the chip's RF to power detector path will work at this lower frequency.

On the other hand, due to lack of an external signal splitter, we must use two separate sources: (1) an Agilent E8361C PNA for one channel; and (2) an Agilent E8257D signal generator for the other channel. To ensure the received signals can combine constructively or destructively, it was crucial that the input sources were coherent (their frequencies and relative phases match) [KEY14]. However, our lab's available equipment did not have the function to lock with each other with regards to phase. Therefore, two-channel interferometry with external source phase shifting (as we did for the simulation in Section 6.3) was not feasible. One last resort was to use the chip's internal phase shifter to control the channels and implement what was accomplished in Section 6.3, but the phase shifting for this device was very sparse, where only one data point could be taken in every  $1/16$  of  $2\pi$ .

The actual lab setup is illustrated in Figure 6.10 and the detailed measurement steps are described below (these steps will be referred to as the “guideline” in the following sections):

1. The equipment was setup in accordance with Figure 6.10. The pitch within the RF probe was adjusted to the following levels: 444  $\mu\text{m}$  for adjacent channels, and 888  $\mu\text{m}$  for CH1 and CH3 or CH2 and CH4 combinations.

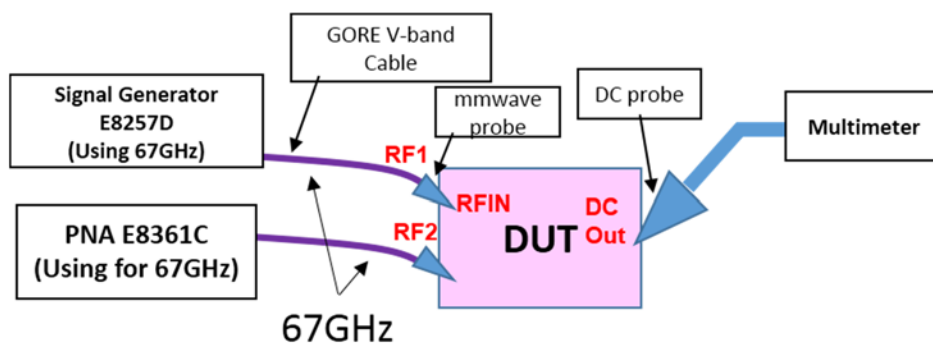


Figure 6.10 Illustration of the lab setup for the two-channel measurement

2. Due to path loss mismatch, the input source power was individually swept. An appropriate power level for each source was chosen so that the actual power at the two RF probe tips was the same. Thus, when the two input signals are in phase, the DC output reaches a maximum. When the two input signals are  $180^\circ$  out of phase, the DC output should approach a minimum. This was an important step, since our equipment does not allow us to monitor the relative phase between sources, nor can we lock their relative phase. The only real-time feedback we can get is the DC output voltage. Therefore the output voltage was closely monitored throughout the test even as data was taken automatically using LabVIEW programs.

3. The phase of the first channel (RF1) was set to 1000, which corresponds to the maximum frequency response amplitude among the 16 settings. The phase of the second channel (RF2) was set to 0100, which is  $180^\circ$  from RF1. The RF inputs were then ramped upwards. Only when the output voltage equaled zero (*i.e.* the phases of the 2 RF channels matched), did we proceed with the measurement; otherwise, step three was repeated.
4. RF2's phase was swept from 0000 to 1111 while the data was recorded. At each phase setting, about 10 to 20 measurements were taken and averaged. After several phase settings, RF2 was shifted back to 0100 for us to check if the two channels' phases still matched. If the phases no longer matched, the measurement was restarted from step three.
5. After successful measurement, the data in each phase setting was averaged and the voltage versus phase setting was plotted (similar to Figure 6.7). Polar plots were also generated using the same method described in Section 6.3.2 to compare experimental results with the theoretical fringe patterns and simulated results.

#### 6.4.2 Measured Results

Following the guideline described in the previous section, over ten tests were performed on the same chip sample. The RF input power level was varied, while different channel combinations were tested. Two sets of channel combinations, which include four separate tests are presented below, where both sets of results are very representative.

### 6.4.2.1 Test 1

Test 1 selected CH3 and CH4 for measurement. Referring to Figure 4.3, CH3 and CH4 are two identical channels, so when their inputs are in phase, the maximum output voltage should be achieved. When the same two channels are  $180^\circ$  out of phase, the minimum output voltage should appear. In this setup, the phase of CH4 was fixed (as RF1 in the guideline) and the phase of CH3 (as RF2 in the guideline) was swept over  $360^\circ$ , in step sizes of approximately  $22.5^\circ$ . Two separate sweeps were performed, one at a lower input power (Test 1a); the other sweep at a higher input power (Test 1b). The output voltage versus CH3 phase delay is plotted in Figure 6.11. Using the measured data points along with their corresponding phase delay, fringe patterns were plotted in red circles and shown in Figures 6.12-6.15, with ideal interferometer fringe patterns (blue curve) normalized to similar power levels.

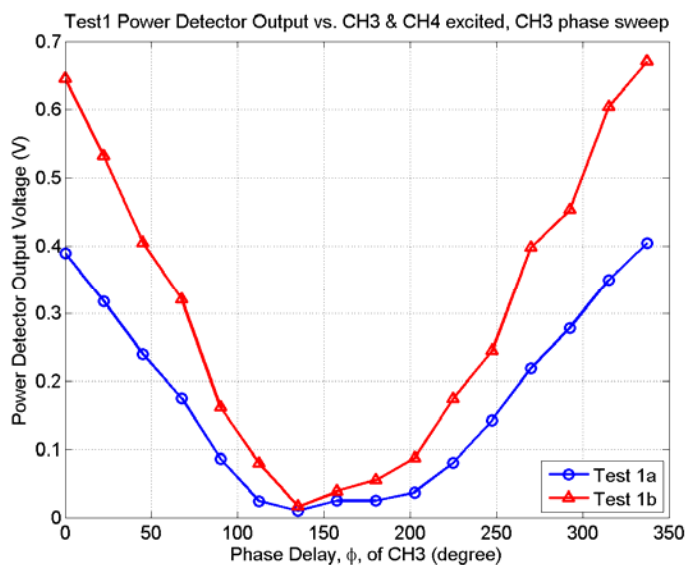


Figure 6.11 Test 1: the power detector output voltage vs. the CH3 phase delay

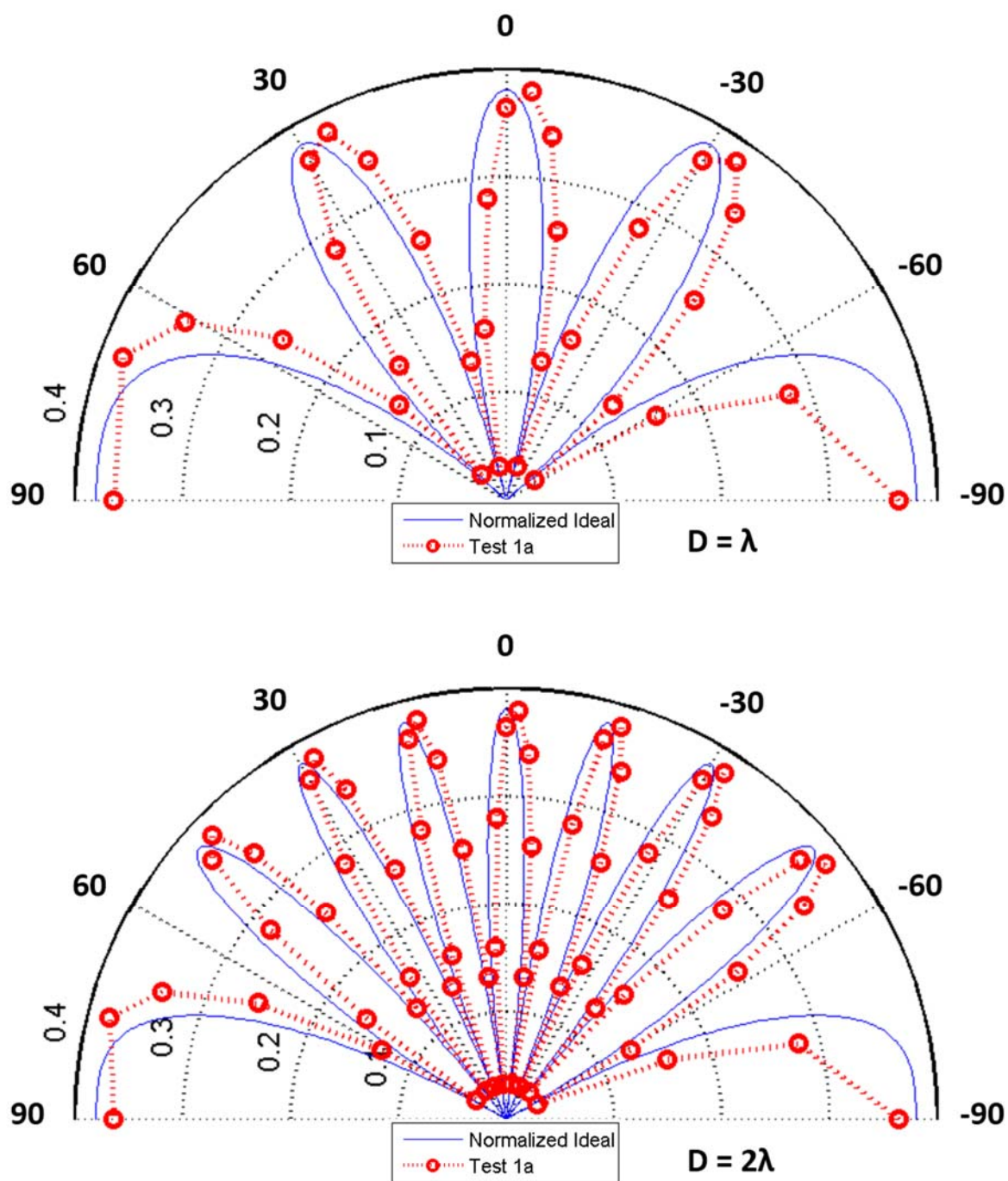


Figure 6.12 The fringe patterns of the Test 1a data, top:  $D = \lambda$ ; and bottom:  $D = 2\lambda$

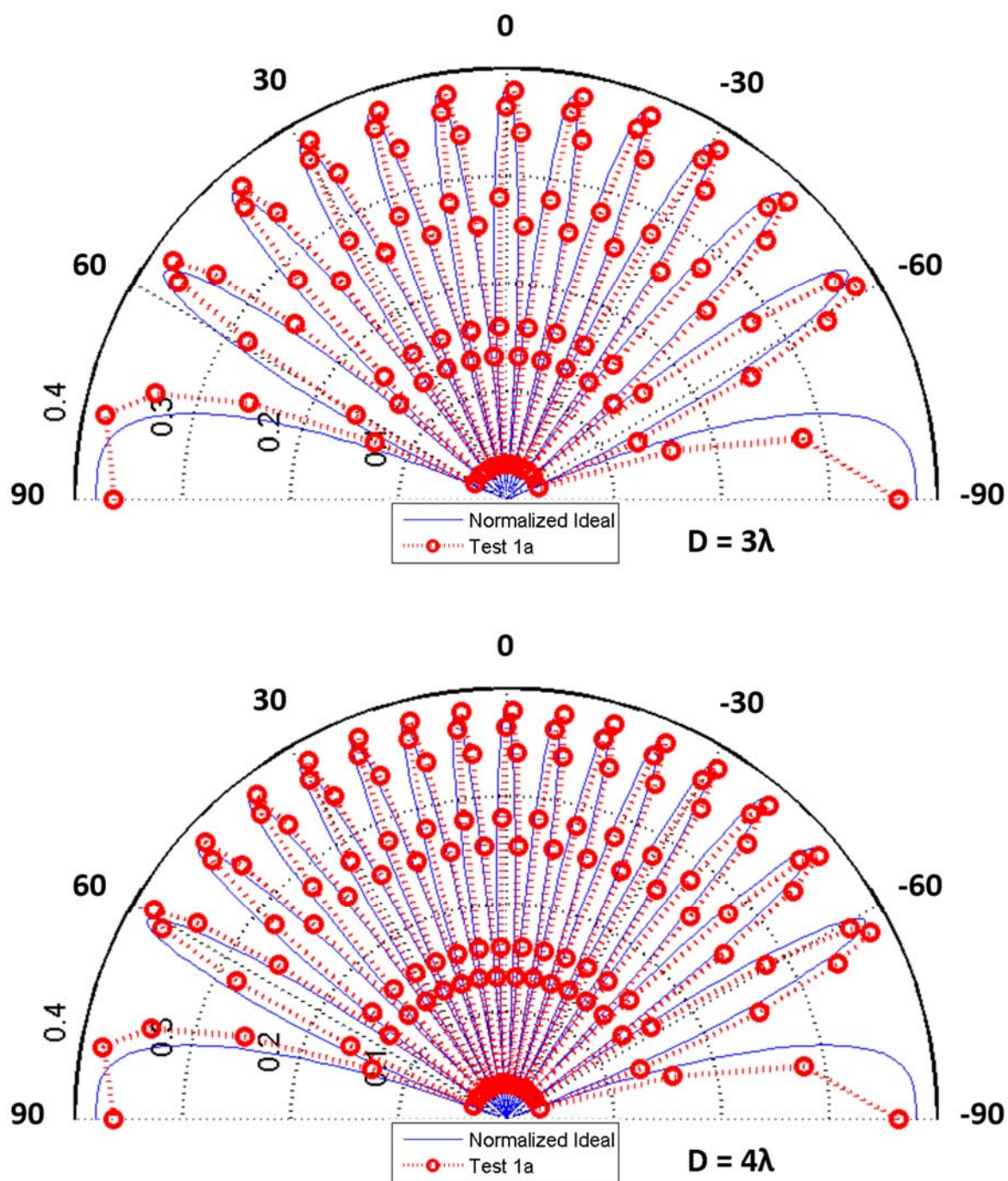


Figure 6.13 The fringe patterns of the Test 1a data, top:  $D = 3\lambda$ ; and bottom:  $D = 4\lambda$

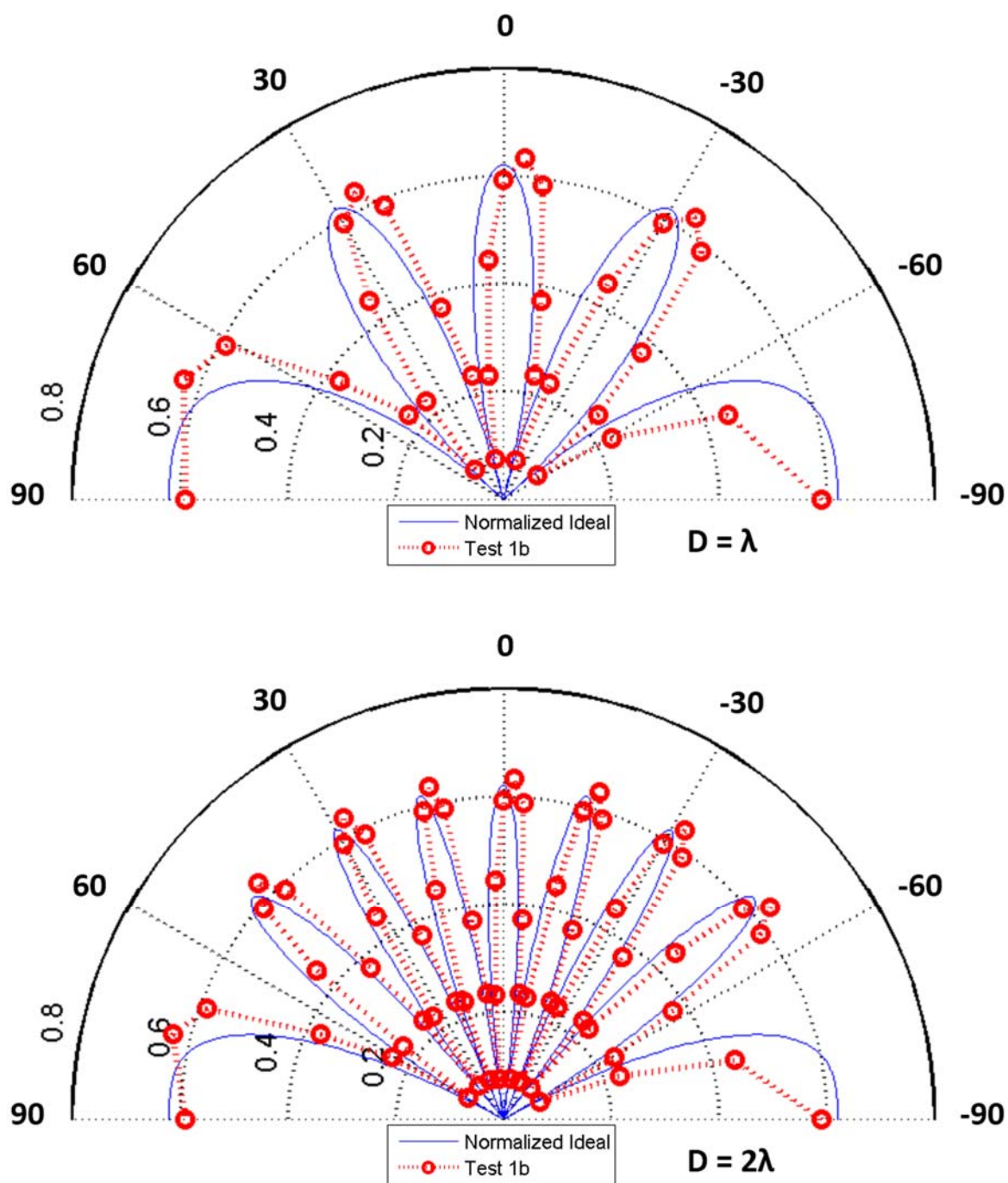


Figure 6.14 The fringe patterns of the Test 1b data, top:  $D = \lambda$ ; and bottom:  $D = 2\lambda$

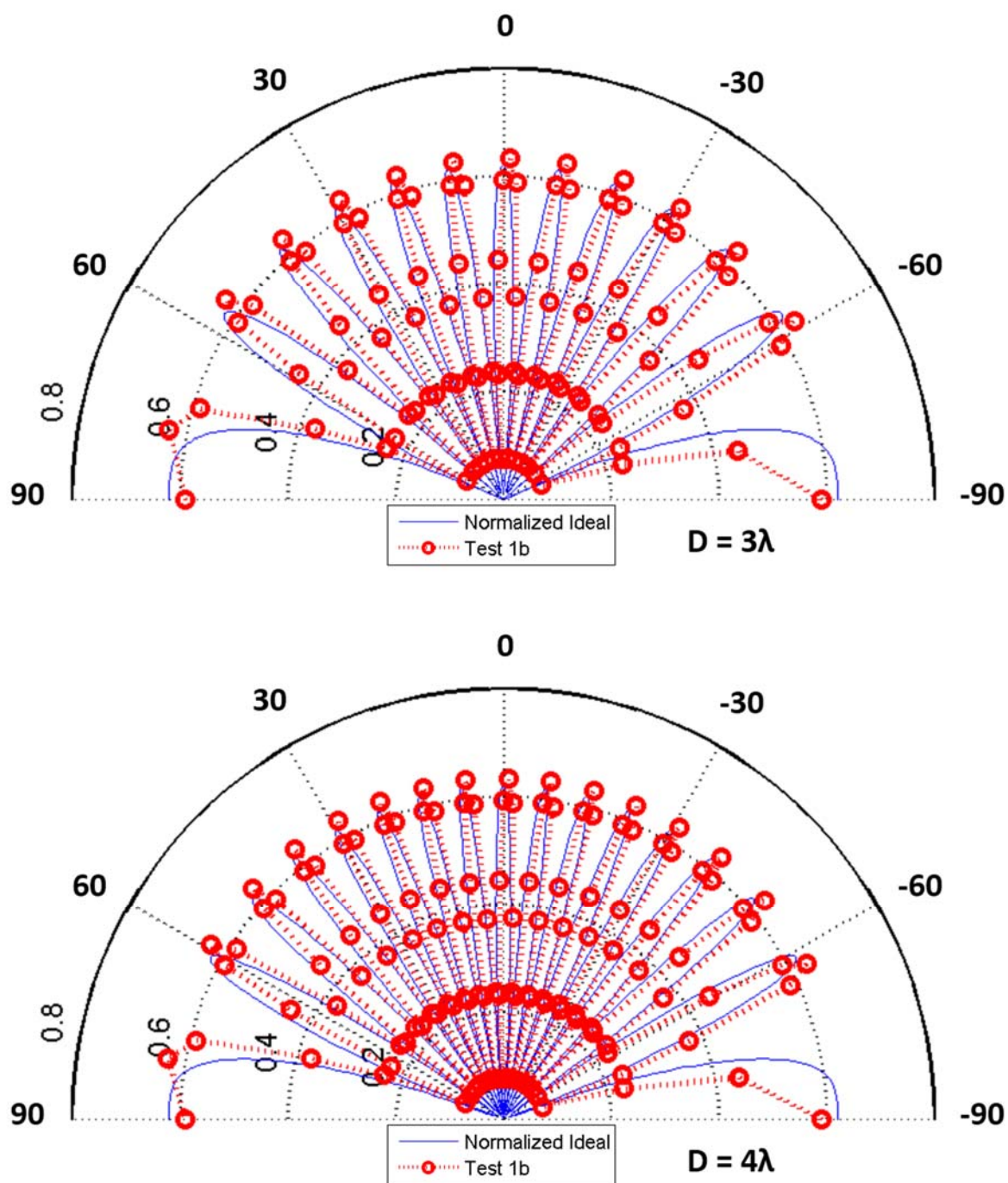


Figure 6.15 The fringe patterns of the Test 1b data, top:  $D = 3\lambda$ ; and bottom:  $D = 4\lambda$

### 6.4.2.2 Test 2

As opposed to Test 1, in which the two input channels were identical, we chose CH1 and CH3 for Test 2. CH1 and CH3 are joined by the ring hybrid coupler by its differential input ports, therefore when CH1 and CH3 are in phase, the minimum output voltage should be seen. When these two channels are  $180^\circ$  out of phase, the maximum output voltage should be present. In this particular setup, the phase of CH3 was fixed (as RF1 in the guideline) and the phase of CH1 (as RF2 in the guideline) was swept over  $360^\circ$  by a step size of approximately  $22.5^\circ$ . Similar to Test 1, two separate sweeps were performed, one at a lower input power (Test 2a); the other at a higher input power (Test 2b). The output voltage versus CH1 phase delay is plotted in Figure 6.16. The corresponding fringe patterns are plotted from Figures 6.17-6.20, and compared with the ideal interferometer fringe patterns, normalized to a similar power level.

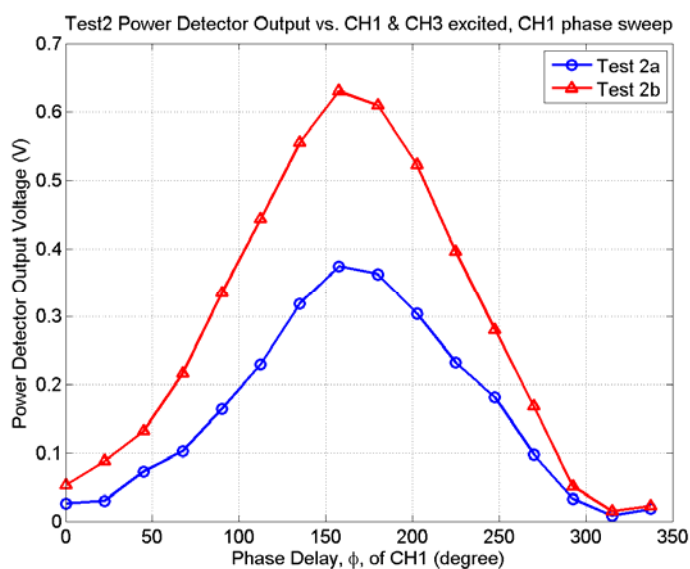


Figure 6.16 Test 2: the power detector output voltage vs. the CH1 phase delay

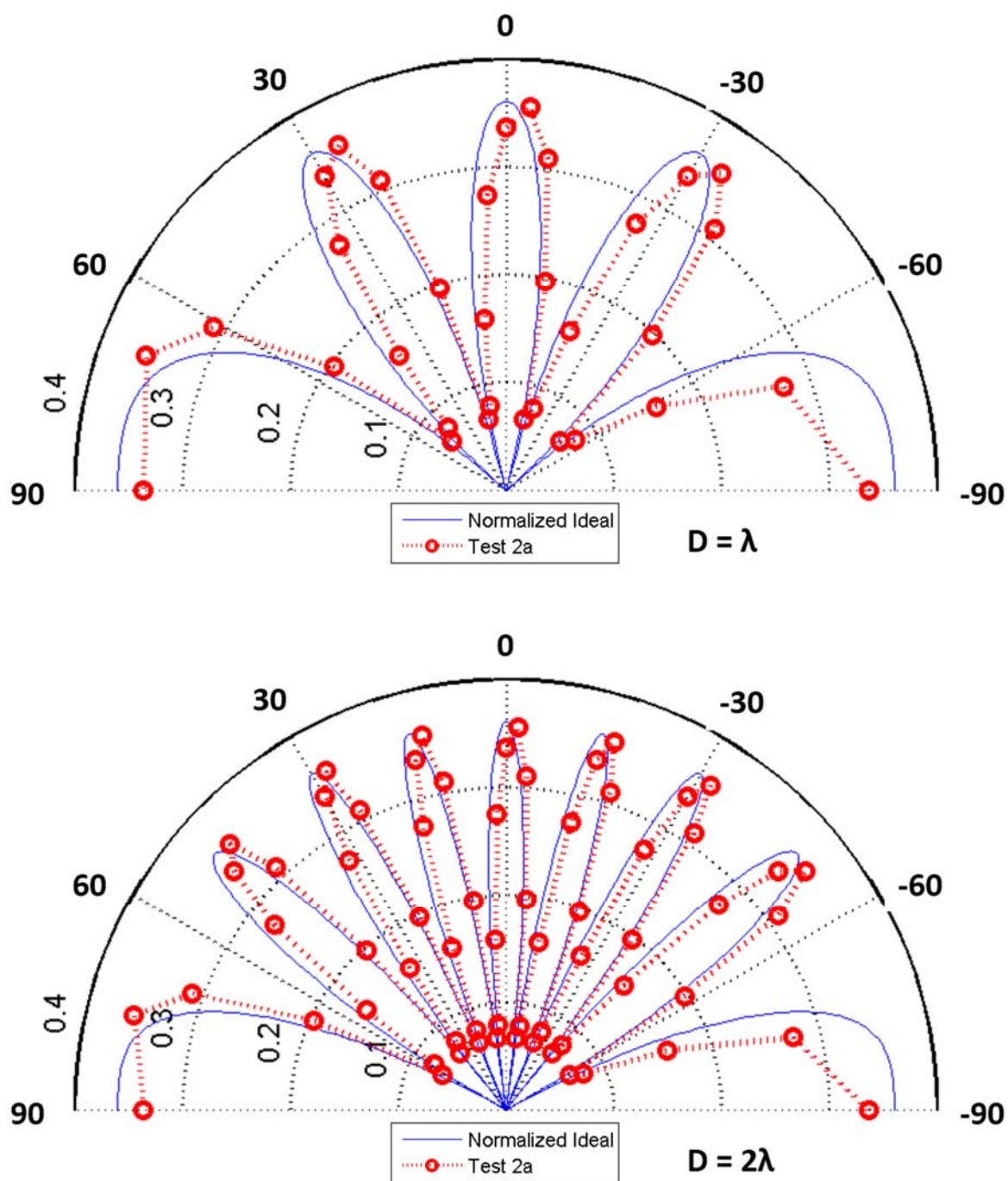


Figure 6.17 The fringe patterns of the Test 2a data, top:  $D = \lambda$ ; and bottom:  $D = 2\lambda$

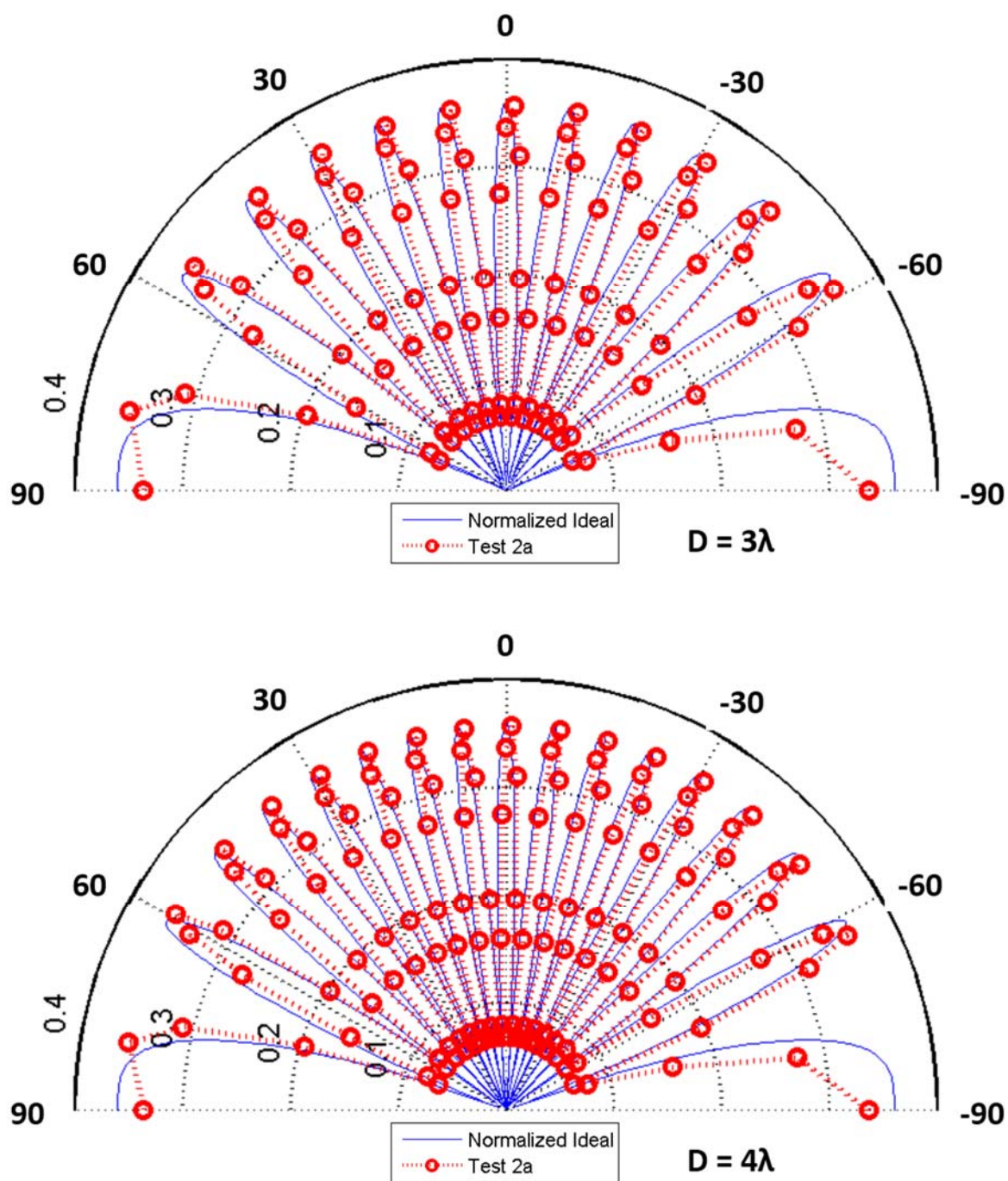


Figure 6.18 The fringe patterns of the Test 2a data, top:  $D = 3\lambda$ ; and bottom:  $D = 4\lambda$

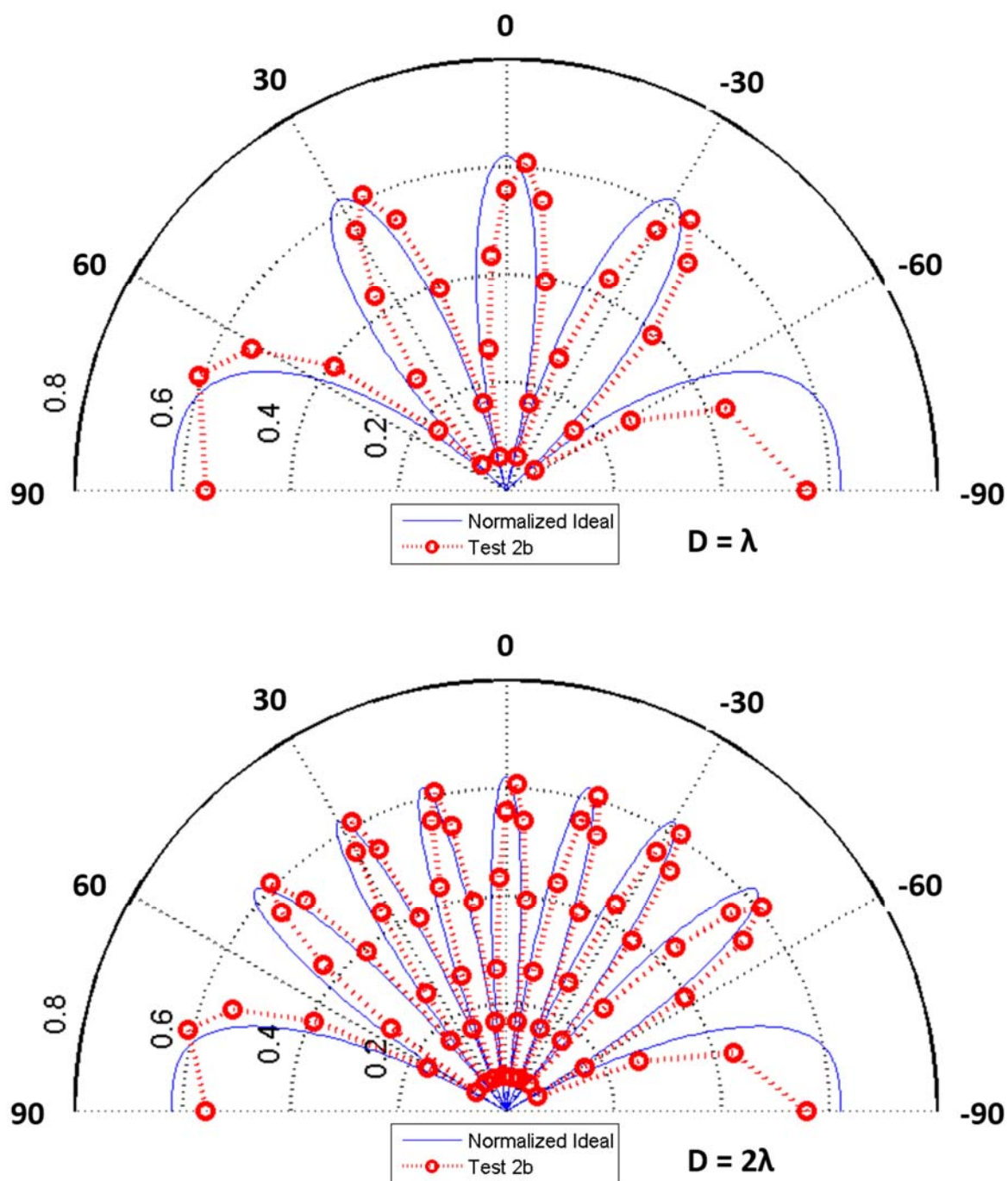


Figure 6.19 The fringe patterns of the Test 2b data, top:  $D = \lambda$ ; and bottom:  $D = 2\lambda$

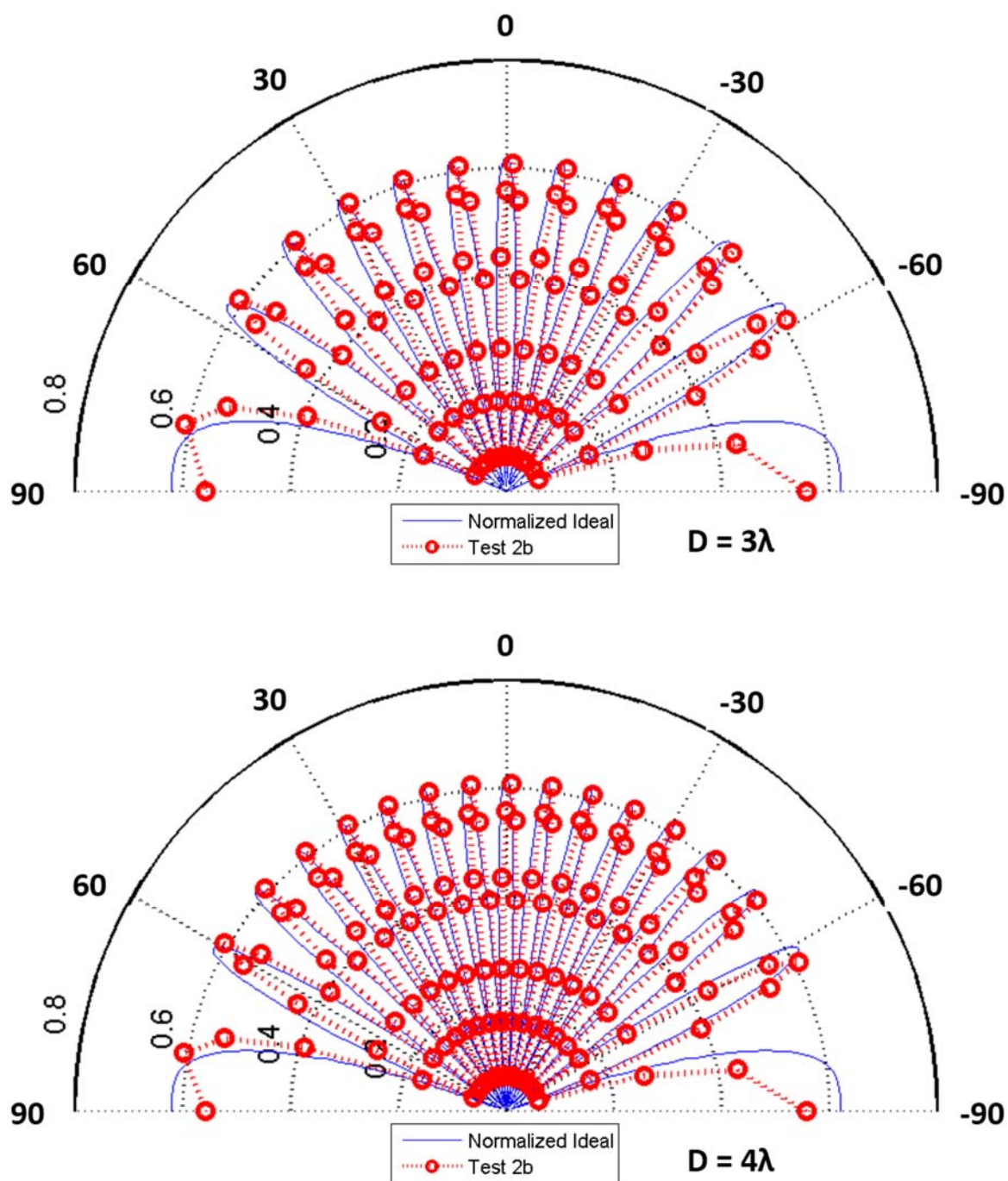


Figure 6.20 The fringe patterns of the Test 2b data, top:  $D = 3\lambda$ ; and bottom:  $D = 4\lambda$

## 6.5 Discussion

As we can observe from the measured voltage data in Figures 6.11 and 6.16, “test a” had an input power approximately 3 dB below that of “test b.” The measured output voltages for “test a” for every phase delay were unanimously about half of that of “test b.” Therefore, the power detector responds to RF inputs linearly in both “test a” and “test b”.

The fringe patterns created from the measured data can be fit into the ideal interferometric fringe pattern (from Eq. 6.7 with a normalization factor) without much discrepancy. This means the right hand side of Eq 6.8, “ $4V_iV_j$ ” can be correctly obtained from measured data “ $(V_i + V_j)^2$ ” and “ $(V_i - V_j)^2$ .” Thus, we can conclude that there are two possible outcomes:

1. Both “ $(V_i + V_j)$ ” and “ $(V_i - V_j)$ ” carry correct values in the signal path, therefore giving a correct “ $4V_iV_j$ ” value. If this case stands, then the signal at the array’s IF output, “ $(V_i + V_j)$ ”, is correct and ready for correlation processes.
2. Neither “ $(V_i + V_j)^2$ ” nor “ $(V_i - V_j)^2$ ” carries the correct value, but their difference still gives the correct value of “ $4V_iV_j$ ”. If this case stands, then there must be distortions  $d_i$  and  $d_j$  modifying  $V_i$  and  $V_j$  respectively. So the measured signals become:

$[(V_i + d_i) + (V_j + d_j)]^2$  &  $[(V_i + d_i) - (V_j + d_j)]^2$ , while their difference is  $4V_iV_j$ .

$$\begin{aligned} & [(V_i + d_i) + (V_j + d_j)]^2 - [(V_i + d_i) - (V_j + d_j)]^2 \\ &= 4(V_i + d_i)(V_j + d_j) = 4(V_iV_j + V_id_j + V_jd_i + d_id_j) = 4V_iV_j \end{aligned}$$

$$\therefore V_id_j + V_jd_i + d_id_j = 0$$

$$\therefore -\frac{d_j}{V_j} = \frac{d_i}{V_i + d_i}$$

Since “channel i” and “channel j” are identical but independent input channels, i and j can be interchanged. Therefore we have:

$$-\frac{d_j}{V_j} = \frac{d_i}{V_i + d_i} = \frac{d_j}{V_j + d_j} \Rightarrow d_j^2 + 2d_jV_j = 0$$

$$\therefore d_j = 0 \text{ or } -2V_j, \text{ and similarly } d_i = 0 \text{ or } -2V_i.$$

Distortions might come from noise and mismatch in the circuit, which is not proportional to the input signals. Therefore, the second solution is ignored and  $d_i = d_j = 0$ .

In the second case, we prove there is no such distortion that could distort the input signal, while in the meantime we keep the  $4V_iV_j$  unchanged. Therefore, the only reason we get a correct  $4V_iV_j$  value is because both “ $(V_i + V_j)$ ” and “ $(V_i - V_j)$ ” are correct and ready for correlation processes.

## 6.6 Investigation of the Four-Channel Interferometer

In previous sections, the visibility of a two-channel system was derived and demonstrated through both simulations and experiments, with good agreement between both. Unfortunately, measuring three or four input signals was not feasible in our lab. Therefore, in this section we used only simulation to demonstrate the generation of visibility for six different baselines using four-channel data. A comparison will be made between the ideal and simulated fringe pattern.

Figure 6.21 illustrates a four-channel interferometer with six different baselines. A 1-D array was used to facilitate the setup for simulation. As with our prototype array, four front-end receivers were present in this system, with the antennas aligned in a 1-D fashion, separated by one, two and four wavelengths. Therefore the corresponding baselines were:  $L_{ab} = 1\lambda$ ;  $L_{bc} = 2\lambda$ ;  $L_{ac} = 3\lambda$ ;  $L_{cd} = 4\lambda$ ;  $L_{bd} = 6\lambda$ ; and  $L_{ad} = 7\lambda$ .

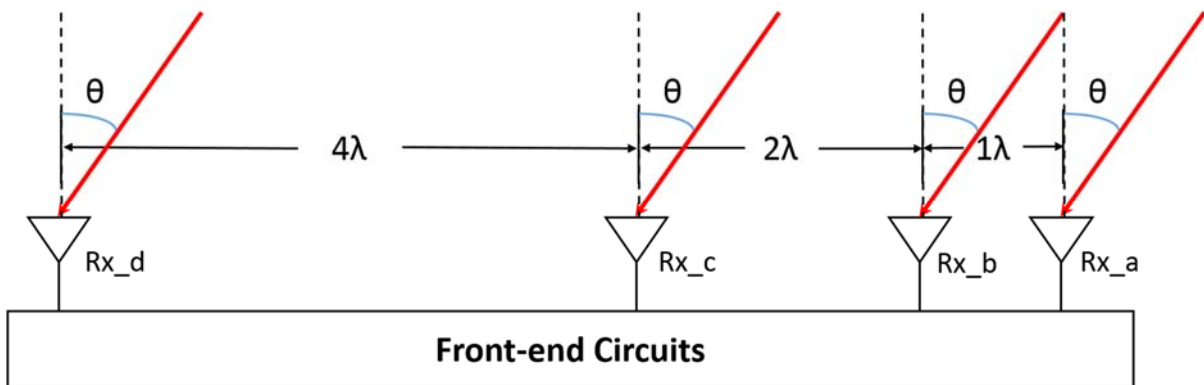


Figure 6.21 The four-channel setup for demonstration of the prototype array

The objective of this demonstration is to show a generalized method to utilize data from 16 sets of data and obtain the visibility of the aforementioned six baselines at the same time. In the meantime, the incident angle,  $\theta$ , will also be swept to generate a fringe pattern for all baselines. As demonstrated in previous sections, the output voltage of the power detector is proportional to its input voltage, while the voltage of a four-channel system is defined as:

$$V = aV_a + bV_b + cV_c + dV_d \quad (6.16)$$

where  $V_a$ ,  $V_b$ ,  $V_c$ , and  $V_d$  are the input voltage at each channel; and  $a$ ,  $b$ ,  $c$ , and  $d$  are the phase settings (in our case, either +1 or -1, indicating a phase setting of  $0^\circ$  or  $180^\circ$ ). There are two

possible outcomes for each channel, giving 16 combinations for four channels, thus 16 possible output voltages for the power detector, defined as  $V_{out}$ .

$$V_{out\_i} \propto (a_i V_a + b_i V_b + c_i V_c + d_i V_d)^2 \quad i = 1, 2, \dots, 16 \quad (6.17)$$

where the subscript,  $i$ , indicates any of the 16 combinations. The difference between any pair of  $V_{out\_i}$  and  $V_{out\_j}$  is then:

$$\Delta V_{out\_ij} = V_{out\_i} - V_{out\_j} \quad (6.18)$$

$$\Delta V_{out\_ij} \propto 2(a_i b_j V_a V_b + b_i c_j V_b V_c + a_i c_j V_a V_c + c_i d_j V_c V_d + b_i d_j V_b V_d + a_i d_j V_a V_d) \quad (6.19)$$

With proper combination of these 16  $V_{out}$ , five of the six terms on the right hand side of Eq. 6.19 can be eliminated, which leaves only the remaining term, the baseline visibility formed by a pair of receivers. The combination of the 16  $V_{out}$  are shown below, while the resulting coefficients of the combinations are tabulated in Table 6.1.

- ab: [15 + 14 + 13 + 12 + 3 + 2 + 1 + 0] - [11 + 10 + 9 + 8 + 7 + 6 + 5 + 4]
- ac: [15 + 14 + 11 + 10 + 5 + 4 + 1 + 0] - [13 + 12 + 9 + 8 + 7 + 6 + 3 + 2]
- ad: [15 + 13 + 11 + 9 + 6 + 4 + 2 + 0] - [14 + 12 + 10 + 8 + 7 + 5 + 3 + 1]
- bc: [15 + 14 + 9 + 8 + 7 + 6 + 1 + 0] - [13 + 12 + 11 + 10 + 5 + 4 + 3 + 2]
- bd: [15 + 13 + 10 + 8 + 7 + 5 + 2 + 0] - [14 + 12 + 11 + 9 + 6 + 4 + 3 + 1]
- cd: [15 + 12 + 11 + 8 + 7 + 4 + 3 + 0] - [14 + 13 + 10 + 9 + 6 + 5 + 2 + 1]

Table 6.1 denotes the numbered codes used in the above combinations. For example:

- code 0 =  $(-V_a - V_b - V_c - V_d)$
- code 7 =  $(-V_a + V_b + V_c + V_d)$
- code 12 =  $(+V_a + V_b - V_c - V_d)$

Table 6.1 Phase settings and the corresponding combinations

code	a	b	c	d	ab	ac	ad	bc	bd	cd
15	+1	+1	+1	+1	+1	+1	+1	+1	+1	+1
14	+1	+1	+1	-1	+1	+1	-1	+1	-1	-1
13	+1	+1	-1	+1	+1	-1	+1	-1	+1	-1
12	+1	+1	-1	-1	+1	-1	-1	-1	-1	+1
11	+1	-1	+1	+1	-1	+1	+1	-1	-1	+1
10	+1	-1	+1	-1	-1	+1	-1	-1	+1	-1
9	+1	-1	-1	+1	-1	-1	+1	+1	-1	-1
8	+1	-1	-1	-1	-1	-1	-1	+1	+1	+1
7	-1	+1	+1	+1	-1	-1	-1	+1	+1	+1
6	-1	+1	+1	-1	-1	-1	+1	+1	-1	-1
5	-1	+1	-1	+1	-1	+1	-1	-1	+1	-1
4	-1	+1	-1	-1	-1	+1	+1	-1	-1	+1
3	-1	-1	+1	+1	+1	-1	-1	-1	-1	+1
2	-1	-1	+1	-1	+1	-1	+1	-1	+1	-1
1	-1	-1	-1	+1	+1	+1	-1	+1	-1	-1
0	-1	-1	-1	-1	+1	+1	+1	+1	+1	+1
Baseline		Separation			Resulting Coefficient					
ab		1 $\lambda$			16	0	0	0	0	0
ac		3 $\lambda$			0	16	0	0	0	0
ad		7 $\lambda$			0	0	16	0	0	0
bc		2 $\lambda$			0	0	0	16	0	0
bd		6 $\lambda$			0	0	0	0	16	0
cd		4 $\lambda$			0	0	0	0	0	16

To get the visibility of all six baselines, only one sweep across the 16-phase combinations was needed. We swept the phase combinations and used this data to create the fringe pattern for all six baselines of different lengths. The results are shown in Figures 6.22-6.27. The blue curve indicates the theoretical fringe pattern of the corresponding baseline, while the red dots are the simulated data after linear normalization. For demonstration purposes,  $\theta$  was only sparsely swept every  $5^\circ$ , from  $-90^\circ$  to  $+90^\circ$ .

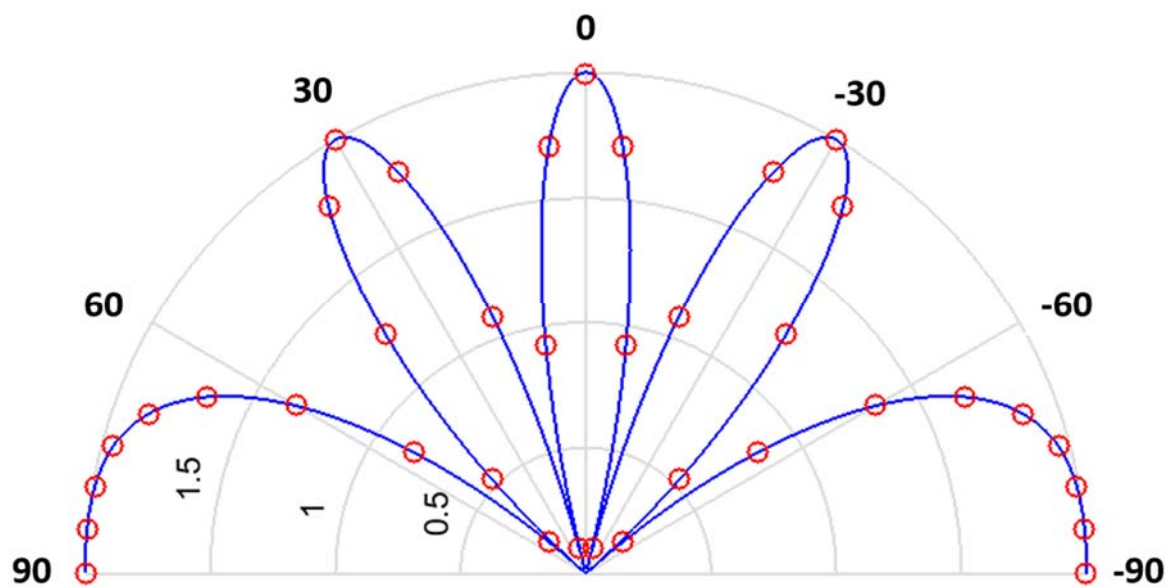


Figure 6.22 The fringe pattern of the baseline,  $L_{ab} = 1\lambda$

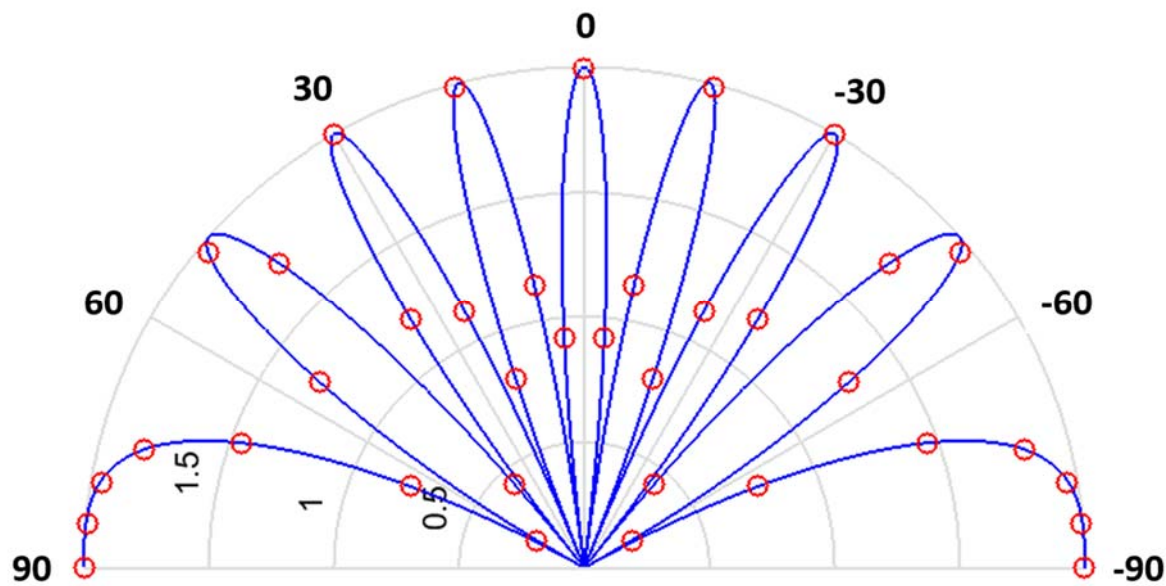


Figure 6.23 The fringe pattern of the baseline,  $L_{bc} = 2\lambda$

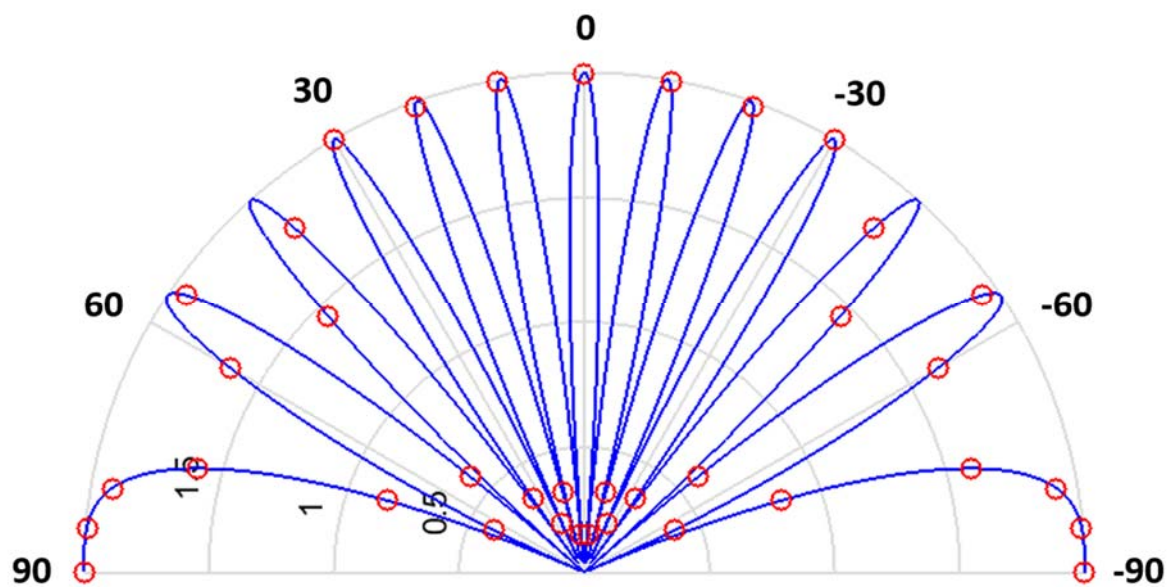


Figure 6.24 The fringe pattern of the baseline,  $L_{ac} = 3\lambda$

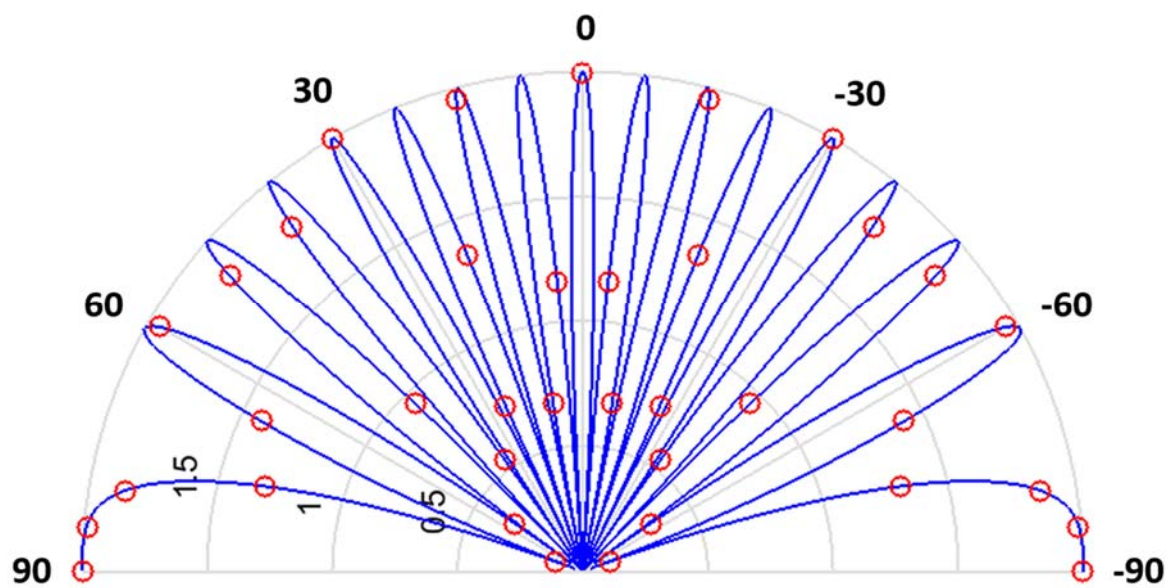


Figure 6.25 The fringe pattern of the baseline,  $L_{cd} = 4\lambda$

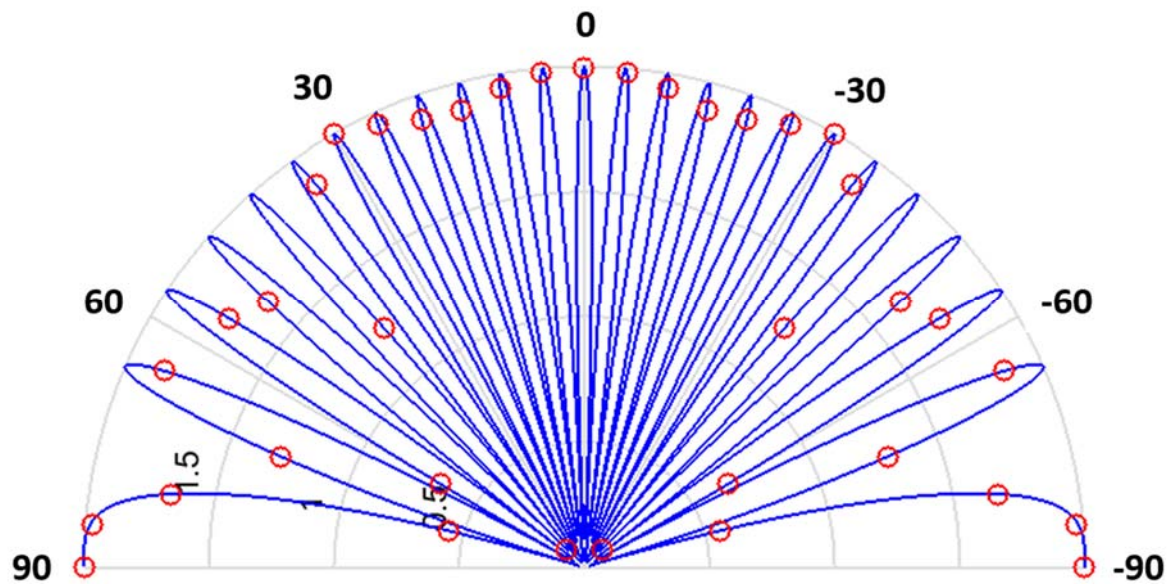


Figure 6.26 The fringe pattern of the baseline,  $L_{bd} = 6\lambda$

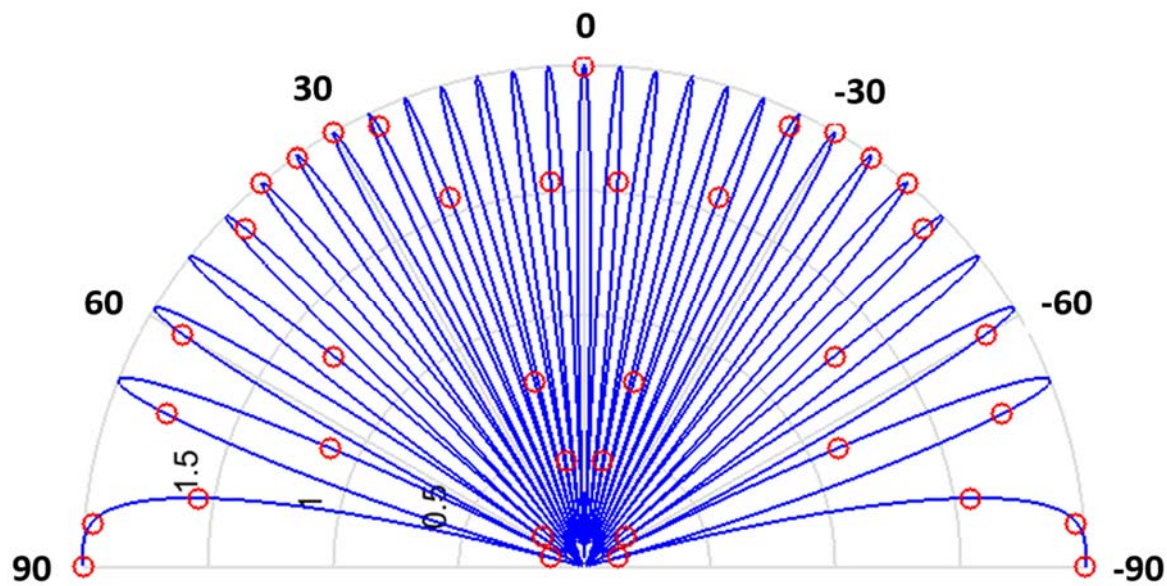


Figure 6.27 The fringe pattern of the baseline,  $L_{ad} = 7\lambda$

For all six baselines presented above, the swept simulated data can be perfectly fit into the fringe patterns of their corresponding visibility functions. This indicates a successful reconstruction of all baselines' visibility using one single sweep across 16 phase settings. The method proposed is based on the linear combination of radiometer voltage output, which is very easy to follow and generalized with increasing number of receivers. Such an algorithm could be easily implemented through digital circuits once the received analog signal is converted through ADC.

### 6.7 Summary

In summary of Chapter 6, the prototype array is evaluated for its potential of working as an interferometer front-end. Since no direct baseband processing circuit is available, nor do we have enough equipment to measure phase in frequency conversion circuit, we came up with an indirect method to prove the circuit is able to provide joined signal from any two input channels. The joined signal carries correct information, so that subsequent stages can correlate the signals from input channels and consequently obtain the visibility of a baseline. In addition, we demonstrated the reconstruction of the visibility function from the simulated output voltage data for a four-channel interferometer. All six baselines' visibility functions could be reconstructed through a single sweep, suggesting this prototype array fully functions as a phase-switched interferometer.

## **CHAPTER 7 CONCLUSIONS AND FUTURE WORK**

### 7.1 Summary of Work

This dissertation addresses the health, size and cost of contemporary MMW imaging systems. The primary goal was to build a low-cost, highly-integrated, silicon-based passive (no illumination provided) MMW imaging system, for applications related to security (for the detection of concealed objects), and biomedical testing (for the diagnosis of dermal burn wounds).

During the course of the research, both EM wave, image-forming phenomenology, and the physiological characteristics of skin burns were extensively studied. Different degrees of burn were quantitatively analyzed and found to be potentially diagnosable by PMMW imagers. We designed and fabricated the first silicon chip for interferometric SAR-based PMMW imaging. The design process of this device included:

- Design of the system architecture;
- Development of the specifications customized to the specific applications;
- Simulation and fabrication of the individual circuit components and prototype array;
- Fully test the hardware and verification of its functionality.

Although hardware-to-model mismatch was observed, every component functioned as expected, yet had performance deficits from the simulated figures of merit. Two-channel interferometry function was also tested and demonstrated that the chip carries the correct

signals that can be used to reproduce the visibility function and create images of objects in terms of their brightness. Simulation was used to verify that the brightness function of all baselines in a four-channel interferometer system can be reconstructed at once, with only one sweep over 16 phase settings, suggesting the prototype array a fully functional phase-switched interferometer.

### 7.2 Key Contributions

Our work has made several unique contributions to the field of PMMW imaging. We quantitatively described the different degrees of severity for human skin burns and concluded that PMMW imaging has potential for burn diagnosis. We also created the first interferometric SAR PMMW imaging front-end circuitry on a silicon chip and validated its functionality. Successful implementation of a PMMW imaging system with good scalability is an important step toward the future development of low-cost, highly-integrated and high-resolution imagers.

### 7.3 Future Work

As we have observed in our measured results, some individual hardware components did not perform up to the simulated figures of merit, causing the whole array to underperform. To correct these issues and improve the prototype array's function, the following a circuit level improvements should be made in the near future:

- Adjust the staggered tuned stages in the LNA to align its resonant frequency for optimal gain and noise performance;
- Optimize the layout of the phase shifter to minimize imbalance in the circuit to reduce the difference in the transmission coefficient under different phase settings;
- Re-evaluate all the passive EM components in the chip with a trusted simulator, such as HFSS, or possibly individually tape-out some of the components to rule out the behavioral discrepancies between the hardware and model;
- Optimize the LO buffer for greater LO swing to improve the conversion gain of the mixer. The IFVGA should also be optimized to increase the chip's gain.

In terms of future application of the prototype array, since the gold code generator designed by Vikas Chauhan was also embedded, more functionality and proof of concept measurements could be performed with the chip for further development of code-modulated interferometric imaging phased array.

The possibility of adding antennas to the array and constructing a fully functional, phased-array should also be considered. The ultimate goal of this work is to perform an *in vivo* test with the array, therefore the IF to baseband circuitry and signal processing algorithm should also be explored in the future to make the PMMW imager a highly integrated system.

## REFERENCES

- [AGI14] Agilent Technology, Appl. Note 57-2, pp. 5-11
- [ALA03] C.M. Alabaster, "Permittivity of Human Skin in Millimetre Wave Band," *Electron. Lett.*, 39, pp. 1521-1522, 2003.
- [ALE07] S.I. Alekseev, M.C. Ziskin, "Human Skin Permittivity Determined by Millimeter Wave Reflection Measurements," *Bioelectromagnetics*, 28, pp. 331-339, 2007.
- [ALV08] Alvarado, J.; Kornegay, K.T.; Welch, B.P.; Wang, Y.W., "W-band SiGe LNA using unilateral gain peaking," *Microwave Symposium Digest, 2008 IEEE MTT-S International*, vol., no., pp.289-292, 15-20 June 2008.
- [AND97] D.Andreuccetti, R.Fossi and C.Petrucci: An Internet resource for the calculation of the dielectric properties of body tissues in the frequency range 10 Hz - 100 GHz. Website at <http://niremf.ifac.cnr.it/tissprop/>. IFAC-CNR, Florence (Italy), 1997. Based on data published by C.Gabriel et al. in 1996
- [APP99] Roger Appleby, Rupert N. Anderton, Sean Price, Neil A. Salmon, Gordon N. Sinclair, Peter R. Coward, Andrew R. Barnes, P. D. Munday, M. Moore, Alan H. Lettington and Duncan A. Robertson, "Mechanically scanned real-time passive millimeter-wave imaging at 94 GHz", *Proc. SPIE 5077*, 1 (2003).
- [APP07] Appleby, R.; Wallace, H.B., "Standoff Detection of Weapons and Contraband in the 100 GHz to 1 THz Region," *Antennas and Propagation, IEEE Transactions on*, vol.55, no.11, pp.2944-2956, Nov. 2007.
- [BAB06] A. Babakhani, X. Guan, A. Komijani, A. Natarajan, and A. Hajimiri, "A 77-GHz 4-element phased array receiver with on-chip dipole antennas in silicon," in *IEEE ISSCC Dig. Tech. Papers*, Feb. 2006, pp.180-181.
- [BAL89] Balanis, C. A., "Advanced Engineering Electromagnetics," Hoboken, NJ: John Wiley & Sons, 1989
- [BJA04] Bjarnason, J.E., T.L.J. Chan, A.W.M. Lee, M.A. Celis, and E.R. Brown, "Millimeter-Wave, Terahertz, and Mid-Infrared Transmission through Common Clothing," *Applied Physics Letters*, Vol. 85, 2004, pp. 519-521

- [BOR99a] Born, Max, and Emil Wolf, "Principles of optics: electromagnetic theory of propagation, interference and diffraction of light," Cambridge university press, 1999.
- [BOR99b] Boric-Lubecke, O.; Nikawa, Y.; Snyder, W.; Lin, J.; Mizuno, K., "Novel microwave and millimeter-wave biomedical applications," Telecommunications in Modern Satellite, Cable and Broadcasting Services, 1999. 4th International Conference on, vol.1, no., pp.186-193 vol.1, 1999.
- [BOY92] Boylan, Anne, C. J. Martin, and G. G. Gardner. "Infrared emissivity of burn wounds." *Clinical Physics and Physiological Measurement* 13.2 (1992): 125-127.
- [CHE89] David K. Cheng, "Field and Wave Electromagnetics (2nd Edition)," Prentice Hall, 1989.
- [CHI06] Chirala, M.K.; Floyd, B.A., "Millimeter-Wave Lange and Ring-Hybrid Couplers in a Silicon Technology for E-Band Applications," *Microwave Symposium Digest, 2006. IEEE MTT-S International*, vol., no., pp.1547-1550, 11-16 June 2006
- [COL90] Cole, R.P., Shakespeare, P.G., Jones, S.G., "Thermographic assessment of burns," *Burns: Journal Of The International Society For Burn Injuries*, Vol. 16, Issue 1, p. 60, 1990
- [DAN09] Daniels, D.J., "EM Detection of Concealed Targets," Hoboken, NJ: John Wiley & Sons, 2009
- [DOA05] C. Doan, S. Emami, A. Nikenejad, and R. Brodersen, "MillimeterwaveCMOS design," *IEEE J. Solid-State Circuits*, vol. 40, no. 1, pp.144–155, Jan. 2005.
- [DOW96] Dow, G.S.; Lo, D.C.W.; Guo, Y.; Lin, E.W.; Chung, T.T.; Biedenbender, M.D.; Miromontes, O.; Marashi, A.; Yujiri, L.; Lee, P.S.C.; Shoucri, M.M.; Allen, B.R., "Large scale W-band focal plane array for passive radiometric imaging," *Microwave Symposium Digest, 1996., IEEE MTT-S International* , vol.1, no., pp.369-372 vol.1, 17-21 Jun 1996.
- [FET08] M. R. Fetterman, J. Grata, G. Jubic, W. L. Kiser, Jr., and A. Visnansky, "Simulation, acquisition and analysis of passive millimeter-wave images in remote sensing applications," *Opt. Express* 16, 20503-20515, 2008.

- [FLO05] B. Floyd, S. Reynolds, U. Pfeiffer, T. Zwick, T. Beukema, and B. Gaucher, "SiGe bipolar transceiver circuits operating at 60 GHz," *IEEE J. Solid-State Circuits*, vol. 40, no. 1, pp. 156–167, Jan. 2005.
- [FLO06] B. Floyd, "Low-Noise Millimeter-Wave Circuit Design in SiGe Technology," IBM T. J. Watson Research Center, Presentation Notes
- [FLO12] B. Floyd, "DARPA Progress, Status and Management Report, 4<sup>th</sup> Quarter 2012," North Carolina State University
- [FOR64] Forage, A.V., "Surface Temperature Measurements of Burn Wounds". *British journal of plastic surgery* (0007-1226), 17, p. 60-65, 1964
- [GAB96a] S. Gabriel, R.W. Lau, C. Gabriel, "The Dielectric Properties of Biological Tissues: I. Literature survey," *Phys. Med. Biol.*, 41, pp. 2231-2249, 1996.
- [GAB96b] S. Gabriel, R.W. Lau, C. Gabriel, "The Dielectric Properties of Biological Tissues: II Measurements in the Frequency Range 10Hz to 20GHz," *Phys. Med. Biol.*, 41, pp. 2251-2269, 1996.
- [GAB96c] S. Gabriel, R.W. Lau, C. Gabriel, "The Dielectric Properties of Biological Tissues: III. Parametric models for the dielectric spectrum of tissues," *Phys. Med. Biol.*, 41, pp. 2271-2293, 1996.
- [GAN86] O.P. Gandhi, A. Riazi, "Absorption of Millimeter Waves by Human Beings and Its Biological Implications," *IEEE Trans. Microw. Theory Tech.*, 34, pp. 228-235, 1986.
- [GAT06] Gatesman, A., "Terahertz Behavior of Optical Components and Common Materials," *Proc. SPIE*, Vol. 6212, 2006, p. 62120E
- [GOR00] Gordon N. Sinclair ; Roger Appleby ; Peter R. Coward ; Sean Price; Passive millimeter-wave imaging in security scanning. *Proc. SPIE 4032, Passive Millimeter-Wave Imaging Technology IV*, 40 (July 20, 2000);
- [GRO03] Erich N. Grossman; Aaron J. Miller; Active millimeter-wave imaging for concealed weapons detection. *Proc. SPIE 5077, Passive Millimeter-Wave Imaging Technology VI and Radar Sensor Technology VII*, 62 (August 25, 2003)
- [GUN05] S. Gunnarsson, C. Karnfelt, H. Zirath, R. Kozhuharov, D. Kuylenstierna, A. Alping, and C. Fager, "Highly integrated 60 GHz transmitter and receiver

- MMICs in a GaAs pHEMT technology,” *IEEE J.Solid-State Circuits*, vol. 40, no. 11, pp. 2174–2186, Nov. 2005.
- [GUS02] Gustrau, F.; Bahr, A., "W-band investigation of material parameters, SAR distribution, and thermal response in human tissue," *Microwave Theory and Techniques, IEEE Transactions on*, vol.50, no.10, pp.2393-2400, Oct 2002
- [HEC01] E. Hecht, “Optics (4th ed.),” Pearson Education, pp. 120, 2001
- [HWA03] H. Hwang, J. Yim, J.W. Cho, C. Cheon, Y. Kwon, “110GHz Broadband Measurement of Permittivity on Human Epidermis Using 1mm Coaxial Probe,” *IEEE Int. Micro. Symp. Digest*, 1, pp. 399-402, 2003.
- [JAM05] James, William; Berger, Timothy; Elston, Dirk, “Andrews' Diseases of the Skin: Clinical Dermatology (10th ed.),” Saunders, 2005, Pages 1, 11–12
- [JUN09] M. Jung; Y. Chang; S. Kim; W.G. Kim; Y.H. Kim; , "Development of passive millimeter wave imaging system at W-band," *Infrared, Millimeter, and Terahertz Waves, 2009. IRMMW-THz 2009. 34th International Conference on*, vol., no., pp.1-2, 21-25 Sept. 2009.
- [KAM11] D. G. Kam, D. Liu, A. Natarajan, S. Reynolds, H.-C. Chen, and B. A. Floyd, “LTCC packages with embedded phased-array antennas for 60-GHz communications,” *IEEE Microwave Comp. Letters*, vol. 21, no. 3, pp. 142-144, Mar. 2011.
- [KAN08] Kangaslahti, P.; Tanner, A.; Gaier, T.; Lambbrigtsen, B.; O'Dwyer, I.; Pukala, D.; , "Millimeter wave synthetic thinned aperture radiometer," *Infrared, Millimeter and Terahertz Waves, 2008. IRMMW-THz 2008. 33rd International Conference on*, vol., no., pp.1-2, 15-19 Sept. 2008.
- [KAP12] B. Kapilevich, B. Litvak, M. Anisimov, D. Hardon, and Y. Pinhasi, “Complex Permittivity Measurements of Textiles and Leather in a Free Space: An Angular-Invariant Approach,” *International Journal of Microwave Science and Technology*, vol. 2012, Article ID 375601, 7 pages, 2012
- [KEY14] Keysight Technologies Appl. Note, “Signal Source Solutions for Coherent and Phase Stable Multi-Channel Systems,” 2014.
- [KIM11] Kim, Won-Gyum; Moon, Nam-Won; Chang, Yu-Shin; Lee, Mun-Kyo; Jung, Sang-Won; Choi, Jun-Ho; Jung, Jin-Mi; Kim, Yong-Hoon; , "System design of focal plane array based Millimeter-wave Imaging radiometer for concealed

- weapon detection," Geoscience and Remote Sensing Symposium (IGARSS), 2011 IEEE International , vol., no., pp.2258-2261, 24-29 July 2011.
- [KOJ09] M. Kojima, et al., "Acute Ocular Injuries Caused by 60-GHz Millimeter-Wave Exposure," *Health Phys.*, 97, pp. 212–218, 2009.
- [KUE99] H.A. Kues, S.A. D'Anna, R. Osiander, W.R. Green, J.C. Monahan, "Absence of ocular effects after either single or repeated exposure to 10 mW/cm<sup>2</sup> from a 60 GHz source," *Bioelectromagnetics*20:463–473, 1999.
- [LAS10] Mitchel Laskey (2010-03-17). "An Assessment of Checkpoint Security: Are Our Airports Keeping Passengers Safe?" House Homeland Security Subcommittee on Transportation Security & Infrastructure Protection.
- [LET03] A.H. Lettington, D. Dunn, M. Attia, I.M. Blankson, "Passive millimeter-wave imaging architectures," *J. Opt. A: Pure Appl. Opt.* 5, S103-S110, 2003.
- [LET05] A.H. Lettington, D. Dunn, N.E. Alexander, A. Wabby, B.N. Lyons, R. Doyle, J. Walshe, M.F. Attia and I. Blankson, "Design and development of a high-performance passive millimeter-wave imager for aeronautical applications", *Opt. Eng.* 44, 093202, 2005.
- [LI11] Chen-Ming Li; Chun-Yen Huang; Li-Yuan Chang; Ya-Chung Yu; Chin-Chung Nien; Jenn-Hwan Tarn; Chih-Chien Chiang; Tzu-Yu Tseng; Shyh-Jong Chung, "Development of a compact total power passive millimeter-wave imaging system," *Radio-Frequency Integration Technology (RFIT)*, 2011 IEEE International Symposium on , vol., no., pp.153,156, Nov. 30 2011-Dec. 2 2011
- [LOV94] J.A. Lovberg, R.C. Chou and C.A. Martin, "Real-time millimeter-wave imaging radiometer for avionic synthetic vision", *Proc. SPIE* 2220, 234 (1994).
- [MAD08] Madhow, U., "MultiGigabit millimeter wave communication: System concepts and challenges," *Information Theory and Applications Workshop*, 2008, vol., no., pp.193-196, Jan. 27 2008-Feb. 1 2008.
- [MAS05] Massoud, Mahmoud, "Engineering Thermofluids: Thermodynamics, Fluid Mechanics, and Heat Transfer," Springer, pp. 568, 2005
- [MAY09] J. W. May, and G. M. Rebeiz, "High-Performance W-Band SiGe RFICs for Passive Millimeter-Wave Imaging," *IEEE Radio Frequency Integrated Circuits Symposium, RFIC 2009*, pp. 437-440, June 2009.

- [MAY10] May, J.W.; Rebeiz, G.M., "Design and Characterization of W -Band SiGe RFICs for Passive Millimeter-Wave Imaging," *Microwave Theory and Techniques, IEEE Transactions on* , vol.58, no.5, pp.1420-1430, May 2010.
- [MEY95] Meyer, R.G., "Low-power monolithic RF peak detector analysis," *Solid-State Circuits, IEEE Journal of* , vol.30, no.1, pp.65,67, Jan 1995
- [MIL07] R.E. Miles, X.-C. Zhang, H. Eisele, A. Krotkus, "Terahertz Frequency Detection and Identification of Materials and Objects," Dordrecht, The Netherlands: Springer, c2007, pp. 225-240
- [MIZ05] Mizuno, K.; Matono, H.; Wagatsuma, Y.; Warashina, H.; Sato, H.; Miyanaga, S.; Yamanaka, Y., "New applications of millimeter-wave incoherent imaging," *Microwave Symposium Digest, 2005 IEEE MTT-S International* , vol., no., pp. 4 pp., 12-17 June 2005.
- [NAN12] J. A. Nanzer, *Microwave and Millimeter-Wave Remote Sensing for Security Applications*. Norwood, MA: Artech House, 2012.
- [NAT06] A. Natarajan, A. Komijani, X. Guan, A. Babakhani, Y. Wang, and A. Hajimiri, "A 77-GHz phased array transmitter with local LO-path phase shifting in silicon," in *IEEE ISSCC Dig. Tech. Papers*, Feb. 2006, pp. 182–183.
- [NIK08] A. M. Niknejad and H. Hashemi (editors), *mm-Wave Silicon Technology: 60 GHz and Beyond*, Springer, 2008.
- [OJE08] E. Öjefors, and U. Pfeiffer, "A 94-GHz Monolithic Front-End for Imaging Arrays in SiGe:C Technology," *IEEE 38th European Microwave Conference, EuMC 2008*, pp. 422-425, October 2008.
- [OKA08] S. Oka, H. Togo, N. Kukutsu, and T. Nagatsuma, "Latest trends in millimeter-wave imaging technology," *Progress In Electromagnetics Research Letters*, Vol. 1, 197-204, 2008.
- [OLE82] B. W. Olesen, "Thermal Comfort," *Bruel & Kjaer, Technical Review*, No. 2, pp. 1 43, (1982)
- [OTS02] Otsuka, K.; Okada, S.; Hassan, M.; Togawa, T., "Imaging of skin thermal properties with estimation of ambient radiation temperature," *Engineering in Medicine and Biology Magazine, IEEE* , vol.21, no.6, pp.49,55, Nov.-Dec. 2002

- [PER08] Albert Pergande, "Unintended illumination for PMMW systems", Proc. SPIE 6948, 69480A (2008).
- [PER10] A.N. Pergande, L.A. Mirth, L.T. Anderson, M.A. Tomcsak, W.S. McKinley, "Illumination Source for Millimeter Wave Imaging," U.S. Patent 7 642 949 B2, Jan. 5, 2010.
- [PON03] Ponchak, G.E.; Papapolymerou, J., "180 degree hybrid (rat-race) junction on CMOS grade silicon with a polyimide interface layer," Silicon Monolithic Integrated Circuits in RF Systems, 2003. Digest of Papers. 2003 Topical Meeting on, vol., no., pp.96-99, 11-11 April 2003
- [POW08] J. Powell, H. Kim, and C. G. Sodini, "SiGe Receiver Front Ends for Millimeter-Wave Passive Imaging," IEEE Trans. Microwave Theory & Tech., vol. 56, no. 11, pp. 2416-2425, November 2008.
- [RAZ05] B. Razavi, "A 60 GHz direct-conversion CMOS receiver," in IEEEISSCC Dig. Tech. Papers, Feb. 2005, pp. 400–401.
- [REY06] Reynolds, S.K.; Powell, J.D., "77 and 94-GHz Downconversion Mixers in SiGe BiCMOS," Solid-State Circuits Conference, 2006. ASSCC 2006. IEEE Asian, vol., no., pp.191-194, 13-15 Nov. 2006.
- [SAK08] Sakai, F.; Suzuki, H.; Sato, H.; Sawaya, K.; Mizuno, K., "High resolution millimeter-wave imaging radar using inline Tx/Rx antennas," Radar Conference, 2008. EuRAD 2008. European, vol., no., pp.156-159, 30-31 Oct. 2008.
- [SAR14] Sarkar, Anirban; Greene, Kevin; Floyd, Brian, "A power-efficient 4-element beamformer in 120-nm SiGe BiCMOS for 28-GHz cellular communications," Bipolar/BiCMOS Circuits and Technology Meeting (BCTM), 2014 IEEE, vol., no., pp.68-71, Sept. 28 2014-Oct. 1 2014
- [SEV10] Severino, R.R.; Taris, T.; Deval, Y.; Belot, D.; Begueret, J.B., "A SiGe:C BiCMOS LNA for 94GHz band applications," Bipolar/BiCMOS Circuits and Technology Meeting (BCTM), 2010 IEEE , vol., no., pp.188-191, 4-6 Oct. 2010.
- [SHE07] Sheen, D.M.; McMakin, D.L.; Hall, T.E., "Near Field Imaging at Microwave and Millimeter Wave Frequencies," Microwave Symposium, 2007. IEEE/MTT-S International, vol., no., pp.1693-1696, 3-8 June 2007.

- [SHE09] Sheen, D.M.; McMakin, D.L.; Hall, T.E.; Severtsen, R.H., "Active millimeter-wave standoff and portal imaging techniques for personnel screening," *Technologies for Homeland Security, 2009. HST '09. IEEE Conference on*, vol., no., pp.440-447, 11-12 May 2009.
- [SHE10] D. Sheen, D. McMakin, and T. Hall, "Near-field three-dimensional radar imaging techniques and applications," *Appl. Opt.* 49, E83-E93 (2010).
- [SKO06] N. Skou, D.M. Le Vine, "Microwave Radiometer Systems: Design and Analysis, 2<sup>nd</sup> Edition," Norwood, MA: Artech House, 2006, pp. 197-217.
- [TAN06] Tanner, A.; Lambrigsten, B.; Gaier, T.; Torres, F., "Near Field Characterization of the GeoSTAR Demonstrator," *Geoscience and Remote Sensing Symposium, 2006. IGARSS 2006. IEEE International Conference on*, vol., no., pp.2529-2532, July 31 2006-Aug. 4 2006.
- [TAN07] Tanner, A.B.; Wilson, W.J.; Lambrigsten, B.H.; Dinardo, S.J.; Brown, S.T.; Kangaslahti, P.P.; Gaier, T.C.; Ruf, C.S.; Gross, S.M.; Lim, B.H.; Musko, S.B.; Rogacki, S.; Piepmeier, J.R., "Initial Results of the Geostationary Synthetic Thinned Array Radiometer (GeoSTAR) Demonstrator Instrument," *Geoscience and Remote Sensing, IEEE Transactions on*, vol.45, no.7, pp.1947-1957, July 2007.
- [TAN08] Tanner, A.B.; Gaier, T.C.; Lambrigtsen, B.H., "GeoSTAR Performance Demonstration," *Aerospace Conference, 2008 IEEE*, vol., no., pp.1-6, 1-8 March 2008.
- [THO01] Thompson, A.R., Moran, J.M. & Swenson, G.W., "Interferometry and Synthesis in Radio Astronomy, 2nd ed.," Wiley-Interscience, 2001.
- [TIN10] Tintinalli, Judith E., "Emergency Medicine: A Comprehensive Study Guide" New York: McGraw-Hill Companies, 2010, pp. 1374–1386
- [TOG89] Tatsuo Togawa, "Non-contact skin emissivity: measurement from reflectance using step change in ambient radiation temperature," *Clinical Physics and Physiological Measurement* 10.1 (1989): 39-48
- [TON09] Z. Tong, "SARs and Temperature Increase Induced by MRI Fields in a Model of the Human Head with Retinal Implants," unpublished.
- [UCH88] Uchinuma, E; Koganei, Y; Shioya, N; Yoshizato, K (1988). "Biological evaluation of burn blister fluid". *Annals of plastic surgery* 20 (3): 225–30

- [VAL10] A. Valdes-Garcia, S. Nicolson, J.-W. Lai, A. Natarajan, P.-Y. Chen, S. Reynolds, J.-H. Zhan, D. Kam, D. Liu, and B. Floyd, "A 16-element, SiGe BiCMOS phased-array transmitter for 60-GHz communications," *IEEE J. Solid-State Circuits*, vol. 45, no. 12, pp. 2757-2773, Dec. 2010.
- [VOW81] Vowinkel, B.; Peltonen, J.K.; Reinert, W.; Gruner, K.; Aumiller, B., "Airborne Imaging System Using a Cryogenic 90-Ghz Receiver," *Microwave Theory and Techniques, IEEE Transactions on*, vol.29, no.6, pp. 535- 541, Jun 1981.
- [WIK01] "Image Resolution," in *Wikipedia: The Free Encyclopedia*; (Wikimedia Foundation Inc., updated 5 Feb. 2015, 19:50 UTC) [encyclopedia on-line]; available from [http://en.wikipedia.org/wiki/Image\\_resolution](http://en.wikipedia.org/wiki/Image_resolution); Internet; retrieved 6 Feb. 2015.
- [WIK02] "Human skin," in *Wikipedia: The Free Encyclopedia*; (Wikimedia Foundation Inc., updated 13 Nov. 2011, 01.26 UTC) [encyclopedia on-line]; available from [http://en.wikipedia.org/wiki/Human\\_skin](http://en.wikipedia.org/wiki/Human_skin); Internet; retrieved 20 Nov. 2011.
- [WIK03] "Lens (optics)," in *Wikipedia: The Free Encyclopedia*; (Wikimedia Foundation Inc., updated 20 Nov. 2011, 12:53 UTC) [encyclopedia on-line]; available from [http://en.wikipedia.org/wiki/Lens\\_\(optics\)](http://en.wikipedia.org/wiki/Lens_(optics)); Internet; retrieved 20 Nov. 2011.
- [WIK04] "Wien approximation" in *Wikipedia: The Free Encyclopedia*; (Wikimedia Foundation Inc., updated 9 Aug. 2014, 15:11 UTC) [encyclopedia on-line]; available from [http://en.wikipedia.org/wiki/Wien\\_approximation](http://en.wikipedia.org/wiki/Wien_approximation)
- [WIK05] "Subcutaneous tissue" in *Wikipedia: The Free Encyclopedia*; (Wikimedia Foundation Inc., updated 19 Nov. 2014, 14:30 UTC) [encyclopedia on-line]; available from [http://en.wikipedia.org/wiki/Subcutaneous\\_tissue](http://en.wikipedia.org/wiki/Subcutaneous_tissue)
- [WIN08] Winkler, W.; Borngraber, J.; Korndorfer, F.; Scheytt, C., "94 GHz Amplifier in SiGe Technology," *Microwave Conference, 2008. EuMC 2008. 38th European*, vol., no., pp.167-170, 27-31 Oct. 2008.
- [XIA08] Zelong Xiao; Jianzhong Xu; Taiyang Hu, "Research on the transmissivity of some clothing materials at millimeter-wave band," *Microwave and Millimeter Wave Technology, 2008. ICMMT 2008. International Conference on*, vol.4, no., pp.1750-1753, 21-24 April 2008
- [YEO11] S. Yeom, D.S. Lee, J.Y. Son, M.K. Jung, Y.S. Jang, S.W. Jung, and S.J. Lee, "Real-time outdoor concealed-object detection with passive millimeter wave imaging," *Opt. Express* 19, 2530-2536 (2011).

- [YUJ03] Yujiri, L.; Shoucri, M.; Moffa, P.; , "Passive millimeter wave imaging," Microwave Magazine, IEEE , vol.4, no.3, pp. 39- 50, Sept. 2003.
- [YUJ06] Yujiri, L.; "Passive Millimeter Wave Imaging," Microwave Symposium Digest, 2006. IEEE MTT-S International, vol., no., pp.98-101, 11-16 June 2006.
- [ZHA11] M. Zhadobov, et al., "Millimeter-wave interactions with the human body: state of knowledge and recent advances," International Journal of Microwave and Wireless Technologies, 3, pp 237-247, 2011.
- [ZHA05] Tao Zhang; Eisenstadt, W.R.; Fox, R.M., "20 GHz bipolar RF RMS power detectors," Bipolar/BiCMOS Circuits and Technology Meeting, 2005. Proceedings of the, vol., no., pp.204-207, 9-11 Oct. 2005
- [ZHA06] Tao Zhang; Eisenstadt, W.R.; Fox, R.M.; Qizhang Yin, "Bipolar Microwave RMS Power Detectors," Solid-State Circuits, IEEE Journal of , vol.41, no.9, pp.2188-2192, Sept. 2006